

**Paleobiological Studies on the Early Eocene Equid *Hyracotherium* (Perissodactyla, Mammalia) from the Clarks Fork and Northwestern Bighorn Basins, Wyoming**

by

Aaron Robert Wood

A dissertation submitted in partial fulfillment  
of the requirements for the degree of  
Doctor of Philosophy  
(Geology)  
in The University of Michigan  
2009

Doctoral Committee:

Professor Philip D. Gingerich, Chair  
Professor Daniel C. Fisher  
Professor Kyger C. Lohmann  
Professor Philip Myers  
Associate Research Scientist Miriam Leah Zelditch

©

Aaron Robert Wood  
All rights reserved

2009

To my family, for their love, encouragement, and never questioning (explicitly) why anyone would ever want to study tiny horses.

## Acknowledgments

I thank my committee members: Philip D. Gingerich, for introducing me to the geology and paleontology of the beautiful Clarks Fork and Bighorn Basins and being confident in my abilities even when I wasn't; Miriam Leah Zelditch, for always challenging me to think in new ways about fossils and evolution and showing me that work is fun if you do it right; Dan Fisher, for all of his greatly appreciated advice and teaching me the importance of thinking deeply and carefully about my work; Kacey Lohmann, for being a great teacher and fostering my interest in geology despite me being inundated with bones and teeth; and Phil Myers, for all of his insightful comments and criticisms and encouraging me at the beginning to pursue this line of research.

I am indebted to the following friends and colleagues: Bill Sanders, for teaching me the art and science of fossil preparation and conservation; Gregg Gunnell, for trusting me with the incredible collection under his care; Carly Manz, for her extraordinary fossil-hunting skills without which there would not be a Chapter 2; and Dustin Hensley, for his humor and tireless efforts in excavating UM115547. I thank Jerry DeSilva for introducing me to the use of the Next Engine 3D scanner and Ryan Bebej for his expertise in scanning specimens and all his help in making the beautiful figures in Chapter 2. I am very grateful for Bonnie Miljour, who taught me finesse in making the figures included in this dissertation, and I greatly appreciate the hard work of Dana Begun, who is responsible for the  $\mu$ CT data shown in Chapter 2.

I am so thankful for the community of faculty, staff, and students at the University of Michigan Museum of Paleontology, past and present, who, through daily interactions, sitting in on practice talks, and insightful conversations, significantly contributed to my dissertation work: Catherine Badgley, Tom Baumiller, Natasha Beranek, Robyn Burnham, Devapriya Chattopadhyay, Mike D'Emic, Tom Eiting, Al Fagerstrom, Brady Foreman, John Graf, Takehito Ikejiri, Alex Janevski, Dan Miller, Shanan Peters, Bill Sanders, Ross Secord, Jerry Smith, Katy Smith, Cindy Stauch, John Whitlock, Jeff Wilson, and Iyad Zalmout. I am especially grateful for the friendship and immeasurable help of Ryan Bebej, Carly Manz, and Adam Rountrey. Their reliable insight, guidance, and intellectual and moral support were absolutely integral to the success of this dissertation.

I am also grateful for the help and advice of Franek Hasiuk, George Junne, Matthew Mihlbachler, Dave Sheets, and Bruce Wilkinson. Lastly, I thank the Churchill family of Powell, Wyoming, for their hospitality and generosity during fieldwork in the Clarks Fork and Bighorn Basins. I am particularly indebted to Tom Churchill for his friendship and all of the times he towed my vehicle out of the badlands (just twice, so far).

Collections studied in this dissertation were made with support from the National Science Foundation, mostly recently grant EAR-0125502 awarded to Philip D. Gingerich. Fieldwork was partially supported by a grant from the Petroleum Research Fund of the American Chemical Society (46858-AC8) awarded to Philip D. Gingerich.

## Table of Contents

Dedication .....	ii
Acknowledgments.....	iii
List of Tables .....	vii
List of Figures.....	ix
List of Appendices.....	xii
Abstract.....	xiii
Chapter 1: Introduction.....	1
Geographic and Geological Setting .....	4
North American <i>Hyracotherium</i> .....	5
<i>Hyracotherium</i> Body Size and Climate Change During the Early Eocene .....	9
Objectives .....	12
Figures.....	15
References.....	17
Chapter 2: Postcranial Functional Morphology of <i>Hyracotherium grangeri</i> : New Insights into the Locomotory Capabilities of Early Eocene Equids.....	23
Occurrence and Preservation .....	26
Axial Skeleton.....	27
Description of Forelimb Elements .....	49
Description of Hindlimb Elements .....	54
Discussion.....	60
Figures.....	67
References.....	88
Chapter 3: The Effects of Dental Wear on Tests of Evolutionary Dynamics.....	91
Methods.....	95
Results.....	116
Discussion.....	122
Tables.....	125
Figures.....	134
References.....	145
Chapter 4: Dental Wear and the Evolution of Dental Morphology in the <i>Hyracotherium</i> Lineage from the Clarks Fork and Northwestern Bighorn Basins, Wyoming.....	148
An Early Eocene <i>Hyracotherium</i> Lineage? .....	148

Evolutionary Time Series of Dental Size and Shape .....	151
Evolutionary Implications of Dental Wear .....	153
Methods.....	154
Results.....	161
Discussion.....	171
Tables.....	129
Figures.....	199
References.....	221
Chapter 5: <i>Hyracotherium</i> Evolution within the Context of Climatic and Environmental Change: Summary and Conclusions .....	224
Methods.....	225
Results.....	226
Discussion.....	227
Overall Conclusions.....	231
Tables.....	235
Figures.....	236
References.....	237
Appendices.....	239

## List of Tables

Table 3.1 Top five linear models generated by overall wear index search program, listing measurements included in principal components analysis (PCA) and associated $R^2$ value.....	125
Table 3.2 Parameters for simulated evolutionary time series.....	126
Table 3.3 The amount of lower second molar (m2) shape variance produced by sampling from worn m2 shapes in the static and directional wear simulations. ....	127
Table 3.4 Results of the tests of evolutionary mode in the directional selection simulations. ....	129
Table 4.1 Top five regression models for the lower fourth premolar (p4) positional wear index with associated $R^2$ values.....	179
Table 4.2 Top five regression models for the lower first molar (m1) positional wear index with associated $R^2$ values.....	180
Table 4.3 Top five regression models for the lower second molar (m2) positional wear index with associated $R^2$ values.....	181
Table 4.4 Top five regression models for the lower third molar (m3) positional wear index with associated $R^2$ values.....	182
Table 4.5 Multivariate shape regression results in which Procrustes superimposed coordinates of buccal and lingual shapes were regressed onto the relevant positional wear index and the overall wear index.....	183
Table 4.6 Angles between vectors of shape change with increasing dental wear in <i>Hyracotherium grangeri</i> and <i>Hyracotherium aemulor</i> .....	184
Table 4.7 Reduced major axis (RMA) results for all pairwise regressions of positional wear indices for <i>Hyracotherium grangeri</i> . ....	185
Table 4.8 Reduced major axis (RMA) results for all pairwise regressions of positional wear indices for <i>Hyracotherium aemulor</i> . ....	186



Table 4.9 Reduced major axis (RMA) results for all pairwise regressions of overall wear indices for <i>Hyracotherium grangeri</i> .	187
Table 4.10 Reduced major axis (RMA) results for all pairwise regressions of overall wear indices for <i>Hyracotherium aemulor</i> .	188
Table 4.11 Results for tests of evolutionary mode applied to total time series and subset time series of lower fourth premolar (p4) buccal shape.	190
Table 4.12 Results for tests of evolutionary mode applied to total time series and subset time series of lower fourth premolar (p4) lingual shape.	191
Table 4.13 Results for tests of evolutionary mode applied to total time series and subset time series of lower first molar (m1) buccal shape.	192
Table 4.14 Results for tests of evolutionary mode applied to total time series and subset time series of lower first molar (m1) lingual shape.	193
Table 4.15 Results for tests of evolutionary mode applied to total time series and subset time series of lower second molar (m2) buccal shape.	194
Table 4.16 Results for tests of evolutionary mode applied to total time series and subset time series of lower second molar (m2) lingual shape.	195
Table 4.17 Results for tests of evolutionary mode applied to total time series and subset time series of lower third molar (m3) buccal shape.	196
Table 4.18 Results for tests of evolutionary mode applied to total time series and subset time series of lower third molar (m3) lingual shape.	197
Table 5.1 Cross-correlation results between the pedogenic carbonate isotopic time series and morphological time series of dental size and shape.	235

## List of Figures

Figure 1.1 Schematic map of the sampled early Eocene localities in the Clarks Fork and northwestern Bighorn Basins, Wyoming.....	15
Figure 1.2 Comparison of patterns in <i>Hyracotherium</i> lower first molar size and various paleoclimatic proxies from the Clarks Fork and Bighorn Basins.....	16
Figure 2.1 Map of the University of Michigan Museum of Paleontology vertebrate fossil locality SC-16 in the Clarks Fork Basin of northwestern Wyoming.....	67
Figure 2.2 <i>Hyracotherium grangeri</i> (UM115547) shown post-exhumation and before substantial preparation (right manus and left dentary not shown).....	68
Figure 2.3 Cervical vertebrae of <i>Hyracotherium grangeri</i> (UM115547).....	69
Figure 2.4 Anterior trunk vertebrae and ribs of <i>Hyracotherium grangeri</i> (UM115547).....	71
Figure 2.5 Mid-column vertebrae, sacrum, and proximal caudal vertebrae of <i>Hyracotherium grangeri</i> (UM115547).....	73
Figure 2.6 Second lumbar (L2) – first sacral (S1) vertebrae of <i>Hyracotherium grangeri</i> (UM115547).....	75
Figure 2.7 Representative $\mu$ CT slices and surface scans of the lumbus in <i>Hyracotherium grangeri</i> (UM115547).....	77
Figure 2.8 Scapula and humerus of <i>Hyracotherium grangeri</i> (UM115547).....	79
Figure 2.9 Forelimb elements of <i>Hyracotherium grangeri</i> (UM115547).....	80
Figure 2.10 Pelvis of <i>Hyracotherium grangeri</i> (UM115547).....	82
Figure 2.11 Hindlimb elements of <i>Hyracotherium grangeri</i> (UM115547).....	84
Figure 2.12 Reconstructed right pes of <i>Hyracotherium grangeri</i> (UM115547) in medial, anterior, and lateral views.....	85
Figure 2.13 Skeletal reconstruction of <i>Hyracotherium grangeri</i> (UM115547).....	87

Figure 3.1 Outline of methods used in Chapter 3. ....	134
Figure 3.2 Buccal, lingual, and occlusal views of the lower second molar of <i>Hyracotherium</i> exhibiting size measurements, landmarks, and semi-landmarks used to calculate the overall wear index and to produce simulated morphological time series. ....	135
Figure 3.3 Simulated lower second molar (m2) shapes and variances. ....	137
Figure 3.4 Representative worn <i>Hyracotherium</i> lower second molars in buccal and occlusal view and associated overall wear index values. ....	139
Figure 3.5 Distributions of overall wear index values for lower second molars (m2) of <i>Hyracotherium</i> . ....	140
Figure 3.6 Minimal shape variance due to simulated directional selection detected by the excursion, angular, and Monte Carlo LRI tests plotted against the amount of shape variance due to sampled dental wear. ....	141
Figure 3.7 Principal components results for directional selection simulations. ....	143
Figure 3.8 Principal components results for stasis simulations. ....	144
Figure 4.1 Buccal, lingual, and occlusal views of the lower second molar of <i>Hyracotherium</i> exhibiting size measurements, landmarks, and semi-landmarks included in the positional and overall wear index calculations and in the respective analyses of shape. ....	199
Figure 4.2 Comparison of morphological time series characteristics of dental size and shape. ....	201
Figure 4.3 Stratigraphic plot of log-transformed crown areas of the lower fourth premolar (p4) and first through third lower molars (m1-3) in Clarks Fork and northwestern Bighorn Basin <i>Hyracotherium</i> taxa. ....	203
Figure 4.4 Stratigraphic distribution of anterior trigonid foveae in <i>Hyracotherium</i> . ....	205
Figure 4.5 Stratigraphic distribution of lower fourth premolar (p4) entoconids in <i>Hyracotherium</i> . ....	207
Figure 4.6 Log-rate-interval (LRI) test results for the lower fourth premolar (p4) crown area time series. ....	209
Figure 4.7 Log-rate-interval (LRI) test results for the lower first molar (m1) crown area time series. ....	211

Figure 4.8 Log-rate-interval (LRI) test results for the lower second molar (m2) crown area time series.....	213
Figure 4.9 Log-rate-interval (LRI) test results for the lower third molar (m3) crown area time series.....	215
Figure 4.10 PC2 scores versus PC1 scores for predicted unworn buccal and lingual shapes for the lower fourth premolar (p4) and the first through third lower molars (m1-3) of Clarks Fork and northwestern Bighorn Basin <i>Hyracotherium</i> taxa. ....	217
Figure 4.11 Principal components results for lower third molar lingual shape in <i>Hyracotherium</i> .....	219
Figure 4.12 Bar graph showing the cusp distribution of exposed dentin sites among the lower fourth premolar (p4) and the first through third lower molars (m1-3) in the Clarks Fork and northwestern Bighorn Basin <i>Hyracotherium</i> taxa. ....	220
Figure 5.1 Comparison of morphological time series of dental size and shape in the <i>Hyracotherium</i> lineage exhibiting heterogeneous evolutionary dynamics.....	236

## List of Appendices

Appendix 1: R Code for Dental Wear Index Search Program.....	239
Appendix 2: R Code for Directional Selection Simulation Including Excursion and Angular Test.....	241
Appendix 3: R Code for Stasis Simulation Module.....	246
Appendix 4: R Code for Directional Dental Wear and Directional Selection Simulation Module .....	248
Appendix 5: R Code for Directional Dental Wear and Stasis Simulation Module .....	250
Appendix 6: R Code for Variance Test of Directional Selection Module.....	252
Appendix 7: R Code for Variance Test of Stasis Simulation Module.....	254
Appendix 8: R Code for Monte Carlo LRI Test for Directional Selection Simulation Module .....	256
Appendix 9: R Code for Monte Carlo LRI Test for Stasis Simulation Module .....	260
Appendix 10: R Code for “Moving Window” LRI Test Module .....	264

## ABSTRACT

### **Paleobiological Studies on the Early Eocene Equid *Hyracotherium* (Perissodactyla, Mammalia) from the Clarks Fork and Northwestern Bighorn Basins, Wyoming**

by

Aaron Robert Wood

Chair: Philip D. Gingerich

The early Eocene equid *Hyracotherium*, the first North American horse, is an ideal taxon for investigating links between mammalian evolution and climatic/environmental change due its dense fossil record and the high-resolution stratigraphic and paleoenvironmental framework developed in the Clarks Fork and Bighorn Basins. Documentation of dental and post-cranial morphological time series is necessary to understand how these early horses evolved in response to changing environmental conditions during the early Eocene.

A new, nearly complete skeleton of *Hyracotherium grangeri* (UM115547), including a well-preserved vertebral column, provides a foundation for understanding the post-cranial evolution of early horses. The posterior thorax and lumbus of UM115547 are divided into facultatively and obligately dorsostable regions, allowing for dynamic positioning of the center of mass during acceleration and maximizing energetic efficiency of vertebral stabilization during locomotion, respectively. The wide range of movement allowed at the hip and shoulder joints contrasts with the restricted parasagittal movement

at distal limb articulations, representing an evolutionary compromise between energetic efficiency and maneuverability in the complicated terrain of *Hyracotherium*'s habitat.

Dental wear can potentially obscure evolutionary patterns in dental morphology and limit sample sizes available for tests of evolutionary dynamics. Simulated morphological time series, in which teeth with various amounts of dental wear were sampled, show that dental wear imposes a time-independent source of variation that asymmetrically hinders the ability to detect directional trends. To mitigate this asymmetric bias, continuous, quantitative indices of dental wear were used to predict unworn dental morphologies to mitigate this asymmetric bias.

Time series of *Hyracotherium* dental morphology over a ~1.5 million year interval exhibit heterogeneous evolutionary dynamics in size (i.e. noncontemporary directional change and stasis) in contrast to homogeneous evolutionary stasis in dental shape. Lower third molar (m3) lingual shape represents an exception in which a shift in optimal morphology occurs between two segments of evolutionary stasis. Coordinated shifts in evolutionary dynamics indicate three intervals of changing selective pressures requiring further investigation.

An adaptive hypothesis involving decreasing atmospheric pCO<sub>2</sub> and changing proportions of fruit and foliage in the diet of *Hyracotherium* is discussed to explain correlations between stable carbon isotope records and dental time series.

## **Chapter 1**

### **Introduction**

The fossil and extant horses (Family Equidae, Order Perissodactyla) of North America have served as the quintessential example of macroevolutionary change since the late 19<sup>th</sup> century (Marsh, 1879; Simpson, 1951; MacFadden, 2005). This is due to the long, 55 million-year phylogenetic history of Equidae, their abundant occurrence in the fossil record, and the appeal of their modern representatives. Since the 19<sup>th</sup> century, fossil horses have been included in studies investigating myriad subjects in paleontology and geology, ranging from paleoecological interactions and niche partitioning (Janis, 1976; MacFadden et al., 1999b), to paleoenvironmental/climatic change (Wang et al., 1994; Secord et al., 2008a), and uplift history of mountain ranges (Crowley et al., 2008).

Data used in the majority of studies involving fossil horses are derived primarily from dentitions. This is due to their high preservation potential and high information density. Dental morphology is indicative of overall body size (MacFadden, 1987; Gingerich, 2003), dietary preferences (Radinsky, 1969; Solounias and Semprebon, 2002), phylogenetic relationships (Evander, 1989; Froehlich, 2002), and the biomechanics of food acquisition and processing (Radinsky, 1984; Rensberger et al., 1984). Stable isotope analysis of dental material not only assists in further resolving dietary preferences



among taxa (Feranec and MacFadden, 2006) but also helps resolve environmental and climatic changes in the geologic past (McFadden et al., 1999a; Passey et al., 2002). Additionally, the long temporal duration of Equidae combined with distinctive changes in their dental morphology make them particularly useful for biostratigraphical purposes [see Woodburne (2004) for examples].

Fossil horses and their dentitions have been integral in understanding the environmental and climatic changes that occurred during the Miocene of North America. The independent evolution of high-crowned dentitions (hypsodonty) during the early Miocene in Equidae and other ungulate lineages has been used as an indicator of the spread of grassland or savanna environments across North America (Simpson, 1951; Janis, 1984; MacFadden, 2005). Hypsodonty increases the functional life of dentitions by providing more dental material available for wear (Janis and Fortelius, 1988), which is necessary when grazing in open environments due to the ingestion of silica-rich grasses and grit. Furthermore, stable carbon isotope data derived from fossil horse enamel indicate the expansion of C<sub>4</sub> grasses during the late Miocene, concurrent with a significant drop in atmospheric CO<sub>2</sub> levels and a reduction in mean annual temperature (MAT) (Wang et al., 1994; Passey et al., 2002). It should also be noted that the post-cranial skeletons of fossil equids further support a transition to more open habitats in exhibiting more numerous cursorial adaptations during the Miocene. Cursorial adaptations providing greater stamina and speed during locomotion would be advantageous for accessing the patchy distribution of resources in an open habitat (Janis and Wilhelm, 1993).

Horse fossils have been used to address Paleogene environment and climate change in North America (Bryant et al., 1996; Gingerich, 2003; Secord et al., 2008a,b). However the small number of studies attempting this is surprising given the long, nearly continuous Paleogene stratigraphic sequences present in North America and their associated rich equid fossil records, such as the Eocene strata of the Clarks Fork and Bighorn Basins, Wyoming, and the Oligocene White River Fauna of South Dakota, Nebraska, and Wyoming.

In the case of the Clarks Fork and Bighorn Basins, a high-resolution climate record for the latest Paleocene and earliest Eocene is emerging, following the recognition of the Paleocene-Eocene thermal maximum (PETM) as preserved in the terrestrial realm (see below). Several studies have demonstrated a direct link between biotic turnover and climate/environmental change in the Clarks Fork and Bighorn Basins (Clyde and Gingerich, 1998; Gunnell 1998, Wing et al. 2005, Chew 2009), but few have explicitly compared the evolutionary history of single lineages to the paleoclimate and paleoenvironment records (Gingerich, 2003; Wood et al., 2007).

The overall goal of this dissertation is to develop a high-resolution morphological time series of the *Hyracotherium* lineage, an early Eocene equid from the Clarks Fork and northwestern Bighorn Basins. Before the link between evolutionary and climatic/environmental change can be addressed within a fossil lineage, one must document which aspects of the lineages morphology change with time and which do not. The resulting morphological time series will be used to 1) describe the evolutionary dynamics exhibited by these early equids, and 2) determine if evolutionary patterns exhibited by *Hyracotherium* coincide with previously documented patterns of

climate/environmental change. The temporal and spatial control provided by examining records of morphological and climatic/environmental change from the same strata and localities will enable adaptive hypotheses that can be rigorously tested in future work.

### **Geographic and Geological Setting**

The contiguous Clarks Fork and Bighorn Basins are located in northwest Wyoming, bordered by the Bighorn Mountains to the east, the Beartooth and Absaroka ranges to the west, the Owl Creek Mountains to the south, and the Pryor Mountains to the northeast. These basins are part of a greater Laramide structural basin with a northwest-southeast trending axis that extends into southern Montana. Thick, synorogenic deposits of Late Cretaceous through early Eocene sediment are exposed today, including nearly 4500 meters of Paleogene strata (Gingerich, 1983).

Strata of Eocene age in the Clarks Fork and northwestern Bighorn Basins are limited to the Willwood Formation, a ~ 700 meter thick alluvial formation deposited by meandering rivers. Kraus (1996, 2001) characterized the Willwood Formation as consisting of three lithologic elements representing distinctive depositional settings: 1) multi-story sheet sandstone complexes representing trunk river channels, 2) mudstones with well-developed paleosols representing pedogenically-altered distal floodplain deposits, and 3) heterolithic packages containing ribbon sandstones and weakly pedogenically-altered mudstones. The heterolithic packages are interpreted as avulsion belt deposits that formed as river channels avulsed and became abandoned (Kraus and Aslan, 1993; Kraus, 1996; Kraus and Wells, 1999). Vertebrate fossils collected in the Willwood Formation are generally found weathering out of the weakly pedogenically-

altered mudstones (Bown and Kraus, 1981), at the irregular, erosional contacts between paleosol packages, and, to a minor extent, in carbonate-nodule conglomerates (Wood et al., 2008). No significant depositional hiatuses, and, therefore, no significant gaps in the mammalian fossil record, occur in the Willwood formation, which is conducive for generating high-resolution morphological time series.

*Hyracotherium* specimens used in this dissertation were selected from the Sand Coulee (SC) vertebrae fossil locality series collection at the University of Michigan Museum of Paleontology (Fig. 1.1). The majority of the SC localities are located along Polecat Bench, a Pleistocene river terrace near Powell, Wyoming, and in the Sand Coulee area, a series of continuous badland exposures northwest of Polecat Bench. The SC localities have been given assigned meter levels within a composite stratigraphic section (0 m = Cretaceous-Tertiary boundary) and biozone designations within the Wasatchian North American Land Mammal Age (NALMA) in the case of early Eocene localities (Gingerich, 1982; 1991; 2003). Only the first two-thirds of Wasatchian time is represented in the SC localities, including the Wa-0 through Wa-5 biozones of Gingerich (1991).

### **North American *Hyracotherium***

The first perissodactyls in North America, represented by *Hyracotherium*, appeared at the Paleocene/Eocene boundary at approximately 55.8 Ma. They appear as part of a Holarctic dispersal of modern orders of mammals, including the first primates and artiodactyls (Gingerich, 2006). This cosmopolitan modern fauna, originally distributed across the northern hemisphere, became subdivided by the North Atlantic at

the end of the early Eocene and subsequently evolved in isolation (Hooker, 1994). The North American equoids evolved into the family Equidae, which later dispersed into the Old World during the Miocene, whereas the European equoids evolved into the Palaeotheriidae, a radiation of horse-like taxa that eventually went extinct during the early Oligocene (Rose, 2006).

The similarity of North American and European equoids led to synonymy of the taxa during the late 19<sup>th</sup> century under the genus *Hyracotherium* first named by Owen (1841) for the taxon *Hyracotherium leporinum* (Froehlich, 2002). Since then, the paraphyly of *Hyracotherium* has been recognized, and the original inclusion of *Hyracotherium leporinum* within Equidae has been questioned. Recent phylogenetic studies (e.g. Hooker, 1994; Froehlich, 1999; 2002) have placed *H. leporinum* with basal tapiromorphs, which would make the genus name *Hyracotherium* inappropriate for early equid genera. Froehlich (2002) provided new generic names for North American Eocene equids, including those early Eocene equids of the Clarks Fork and Bighorn Basins, that are slowly gaining acceptance in the literature (e.g. Secord et al., 2008b; Chew, 2009). However, no general consensus has been reached, and the name *Hyracotherium* continues to be applied to North American Eocene equids (Rose, 2006). *Hyracotherium* will be used here to avoid confusion in the context of the extensive work on North American equids from the early Eocene.

*Hyracotherium* has been interpreted to have a body mass that ranged from 5-35 kg, depending on the species (MacFadden, 1987; Gingerich, 2003). *Hyracotherium* possessed four and three digits on its forelimbs and hindlimbs, respectively, and lived in open canopy forests in the Bighorn and Clarks Fork Basins (Secord et al., 2008b) and

elsewhere. Dental microwear indicates that *Hyracotherium* was a fruit browser similar to the modern yellow-back duiker, *Cephalophus silvicultor* (Solounias and Semprebon, 2002). The post-cranial skeleton exhibits many features associated with cursoriality, such as long distal limb elements and proximally-place muscle attachment sites, making *Hyracotherium* one of the most cursorially-adapted taxa of the early Eocene (Kitts, 1956; Rose, 2006). Sexually dimorphic cranial and canine morphologies combined with a male/female ratio of 1:1.5-2 estimated from a death assemblage suggest that *Hyracotherium* may have had a polygynous social structure (Gingerich, 1981).

The dentition of *Hyracotherium* is low-crowned (brachydont) with weakly to moderately developed transverse crests between the buccal and lingual molar cusps. The premolars show incipient molarization, characteristic of Equidae, but only to a degree arguably greater than their phenacodontid condylarth ancestors. The lower third molars are elongate with a well-developed hypoconulid and hypoconucristid that would have occluded with the hypocone and metaloph on the upper third molar, increasing the occlusal area available for mastication (Radinsky, 1966). Wear facets on the cheek teeth indicate that mastication in *Hyracotherium* included substantial shearing and compressive components (Radinsky, 1969; Rensberger et al. 1984), characteristic of primitive mammalian herbivores that incorporate fruit, seeds, and tender leaves in their diets.

Gingerich (1991) used a stratophenetic approach to identify 4 species of *Hyracotherium* in the Wa-0 to Wa-4 strata of the Clarks Fork Basin: *H. sandrae*, *H. grangeri*, *H. aemulor*, and *H. pernix* (Fig. 1.2). The oldest and smallest species, *H. sandrae*, ~ 5-6 kg body mass, first appears at the Paleocene/Eocene boundary and occurs throughout the Wa-0 biozone. *H. sandrae* differs from the younger 3 Clarks Fork species

primarily in body size (15-20% smaller than *H. grangeri* and *H. pernix*; 25-30% smaller than *H. aemulor*). Gingerich (1991) provided additional dental characters to distinguish *H. sandrae* from younger Wasatchian equids of similar size [e.g., *H. index* of Cope (1873) and *H. seekinsi* of Morris (1968), renamed *Minippus index* and *Eohippus angustidens*, respectively, by Froehlich (2002)], such as the presence of an anterior trigonid fovea formed by a continuous paracristid and premetacristid on the lower molars. Froehlich (2002) renamed this taxon *Sifrihippus sandrae*, claiming that an anterior trigonid fovea is autapomorphic to genus.

*H. grangeri*, an equid of intermediate body size (~ 8-10 kg), occurs throughout the Wa-1 through Wa-3a biozones. Again, Gingerich (1991) distinguished *H. grangeri* from preceding and succeeding Clarks Fork *Hyracotherium* via body size (15-20% larger than *H. sandrae*; 14% smaller than *H. aemulor*). *H. grangeri* differs from the similar sized *H. pernix* (Wa-4) by possessing more weakly-developed lophs and more rounded cusps. Although a few specimens of *H. grangeri* have been collected from the surfaces of Wa-0 strata at Polecat Bench, these Wa-0 *H. grangeri* show taphonomic characteristics atypical of Wa-0 fossil material and are likely fossil contaminants weathered from overlying Wa-1 strata (Wood et al., 2008).

*H. aemulor* is the largest species in the Clarks Fork Basin, with an estimated body mass of 12-16 kg, whose first appearance marks the beginning of the Wa-3b biozone. Gingerich (1991) described the dental morphology as nearly identical to that of *H. grangeri*, with the exception of overall size, which suggested to him an ancestor-descendant relationship between *H. grangeri* and *H. aemulor*. One stratigraphic level in the Wa-3a biozone exhibits a population of *H. grangeri* intermediate in size between

preceeding *H. grangeri* and *H. aemulor* [see Fig. 12 of Gingerich (1991) or Fig. 6 of Gingerich (2003)], providing further support for an ancestor-descendant relationship. The diastema between the lower canine and first premolar of *H. aemulor* was described by Gingerich (1991) as being disproportionately longer than that in *H. grangeri*, but Froehlich (2002) noted that this character is highly variable within taxa. Furthermore, Chew (2005) described *H. aemulor* as lacking a distinct entoconid on the lower fourth premolar to distinguish this taxon from other early Eocene equids. The stratigraphic range of *H. aemulor* does not extend into the Wa-4 biozone in the Clarks Fork Basin.

*H. pernix* is an intermediately-sized equid (~ 8-10 kg), whose first appearance indicates the beginning of the Wa-4 biozone. Gingerich (1991) noted that not only is *H. pernix* 15% smaller than the preceding *H. aemulor*, it also possesses the most well-developed hypoconid-entoconid crests (hypolophid) among the four Clarks Fork *Hyracotherium* taxa. There is no discussion of an ancestor-descendant relationship between *H. aemulor* and *H. pernix* by either Gingerich (1991) or Froehlich (2002), but both authors, however, maintained each species as con-generic. It should also be noted that no specimens intermediate in size between *H. aemulor* and *H. pernix* were described or figured by Gingerich (1991, 2003) near the Wa-3b/Wa-4 boundary.

### ***Hyracotherium* Body Size and Climate Change during the Early Eocene**

The first equids appeared in North America at the Paleocene/Eocene boundary as part of the Wa-0 fauna coincident with the Paleocene-Eocene Thermal Maximum. The PETM is a global warming event (~3-7 °C increase in temperature) that occurred at ~55.8 Ma and is associated with a massive influx of isotopically light carbon to the atmosphere



as evident via a negative carbon isotope excursion ( $\sim 6 \text{ ‰}$ ) (Zachos et al., 1993; Gingerich, 2003; Koch et al., 2003; Gradstein et al., 2005). Precipitation patterns in the Bighorn and Clarks Fork Basins were also affected during the PETM. Paleofloral data indicate that mean annual precipitation decreased by 40% (138 cm to 80 cm) at the onset of the PETM and recovered to previous values near the end of the event (Wing et al., 2005). In addition, geochemical data derived from the paleosol PETM record suggest alternating wet/dry cycles of lesser magnitude during the event (Kraus and Riggins, 2007).

Many taxa of the mammal Wa-0 fauna are remarkably smaller than immediately preceding or succeeding related taxa, including the first equid to appear in the Bighorn and Clarks Fork Basin record, *Hyracotherium sandrae* (Fig. 1.2). Gingerich (2003, 2006) has suggested that climate induced changes in vegetation may have affected the growth of herbivores during the PETM. Specifically, elevated temperature and pCO<sub>2</sub> levels have been shown to decrease the nutritional quality and digestibility of plant materials via an increase in the amounts of lignin and cellulose without a concurrent increase in the digestible portions of the plant cells (e.g. Wilson et al., 1991; Tuchman et al. 2003). This explanation does not fully account for the small body sizes of the Wa-0 fauna, because Wa-0 carnivorous mammals also show a reduction in body size (Heinrich et al., 2008). Regardless, it appears that climate change during the PETM may have elicited an adaptive response from the mammalian fauna.

Climate events later in the Wasatchian may have also affected the mammalian fauna of the Bighorn and Clarks Fork Basins. Schankler (1980) described two distinctive episodes of mammalian turnover, Biohorizons A and B, in the post-PETM Wasatchian of

the central Bighorn Basin that he suggested to be related to climatic and/or ecological change. Biohorizons A and B have been subsequently associated with the Wa-3/Wa-4 and Wa-4/Wa-5 boundaries, respectively. Chew (2009) reassessed Biohorizons A and B in light of recent documented paleoclimatic variation and found that Biohorizon A coincided with an apparent decrease in MAT of 5-8 °C whereas Biohorizon B coincided with a 5-8 °C recovery in MAT.

The Wa-3/Wa-4 cooling event and subsequent Wa-4/Wa-5 warming have been documented using independent paleoclimatic proxies (Fig. 1.2): leaf margin analysis (Wing et al., 2000) and stable oxygen isotope analysis of pedogenic hematite (Bao et al., 1999). Leaf margin MAT estimates show that across the Wa-3/Wa-4 temperatures dropped from  $16.4 \pm 2.7$  °C to  $10.8 \pm 3.3$  °C and then returned to previous values ( $15.8 \pm 2.2$  °C) following the Wa-4/Wa-5 boundary (Table 6 of Wing et al., 2000).  $\delta^{18}\text{O}$  values derived from pedogenic hematite, an indicator of surface water  $\delta^{18}\text{O}$ , show a negative shift across the Wa-3a/Wa-3b boundary (Table 2 of Bao et al., 1999). Prior to the boundary,  $\delta^{18}\text{O}$  values varied between -12 to -14 ‰ (VSMOW), suddenly shifting to -15 to -17 ‰ (VSMOW) values in the Wa-3b biozone. Bao et al. (1999) interpreted this shift in  $\delta^{18}\text{O}$  as indicative of a 6 °C maximum decrease in surface temperatures. Combining these two paleoclimatic records suggests that climatic cooling in the Bighorn and Clarks Fork Basins began near the Wa-3a/Wa-3b boundary and intensified across the Wa-3b/Wa-4 boundary.

The stratigraphic ranges of the *Hyracotherium* taxa from the Clarks Fork and northwestern Bighorn Basins correlate with the cooling events at the Wa-3a/Wa-3b and Wa-3b/Wa-4 boundaries (Fig. 1.2). At the Wa-3a/Wa-3b boundary, during the initial

cooling, the intermediately-sized *H. grangeri* is replaced by (or evolved into) the large *H. aemulor*. *H. aemulor* is subsequently replaced by the smaller and more lophodont *H. pernix* as the cooling intensifies across the Wa-3b/Wa-4 boundary. These observations, combined with the post-PETM transition of *H. sandrae* to *H. grangeri*, are highly suggestive of a link between variations in climate and equid evolution/turnover in the Clarks Fork and northwestern Bighorn Basin record.

At this point, it is uncertain whether these transitions in *Hyracotherium* taxa reflect adaptive responses to climate and environmental change. As described above, the Bighorn and Clarks Fork *Hyracotherium* are primarily distinguished by overall dental size. Although size is an important factor relevant to many aspects of function and physiology, understanding changes in dental shape will enable functional interpretations that can be more rigorously tested as adaptive responses to climate/environmental change. Furthermore, the subtle differences in dental morphology, such as inclination and orientation of cusps, cristids, and lophs, that make it difficult to dentally diagnose *Hyracotherium* taxa can be quantified via geometric morphometric techniques and described as temporal subsets of continuous dimensions of variance. Quantifying both dental size and shape allows application of statistical tests on all aspects of dental morphology to: 1) determine evolutionary dynamics exhibited by morphology and 2) detect statistically-significant correlations with climate change.

## **Objectives**

The overall goal of this dissertation is to generate and study a high-resolution morphological time series of *Hyracotherium* taxa from the Clarks Fork and northwestern

Bighorn Basins. Some aspects of *Hyracotherium* morphology, such as the post-cranial skeleton, exhibit a dense record of isolated elements that have not been rigorously studied within and among *Hyracotherium* taxa at finer stratigraphic intervals. A more complete understanding of the post-cranial functional morphology is a vital prerequisite for producing such a high-resolution time series. In addition, dental morphology is subject to biases imposed by dental wear that potentially obscure evolutionary patterns. Mitigating the effects of dental wear is therefore necessary to better resolve such evolutionary patterns. Thus, secondary goals of this dissertation are to fulfill these prerequisites for generating morphological time series.

The objective of Chapter 2 is to provide a foundation for studying the post-cranial evolution of *Hyracotherium* via a description of a new, nearly complete skeleton of *Hyracotherium grangeri* (UM115547). This specimen includes complete limbs and vertebral column, permitting a functional investigation of the complete locomotory apparatus of *Hyracotherium*. Questions that are addressed include the following. 1) What is the extent of cursorial adaptations in *Hyracotherium*? 2) What is the role of the vertebral column of *Hyracotherium* during locomotion, and how does that role differ from that of more modern equids? 3) How does the locomotory ability of *Hyracotherium* relate to its environment during the early Eocene?

The objectives of Chapter 3 are to investigate how dental wear affects observations of dental evolution and present methods for mitigating the effects of dental wear on dental morphological time series. Empirically-derived shape data from *Hyracotherium* dentitions are used to produce simulated evolutionary time series of dental shape, which are subsequently subjected to tests of evolutionary mode. The effect

of sampling worn dentitions is determined by documenting the change in test statistics as the amount of dental wear sampled increases. The following questions are addressed in this chapter. 1) Is dental wear a substantial source of variation in dental morphologies, and if so, is there a consistent trajectory of shape change with increasing dental wear? 2) Does dental wear differentially obscure modes of evolution (e.g. directional selection, evolutionary stasis, etc), and if so, how? 3) How do the statistical powers of standard tests of evolutionary dynamics vary with increased sampling of worn dentitions?

The objective of Chapter 4 is to produce a morphological time series of the lower dentition in *Hyracotherium* in order to answer the following questions. 1) How does dental shape vary among the four *Hyracotherium* taxa in the Clarks Fork and northwestern Bighorn Basins? 2) Do patterns of dental wear vary between *Hyracotherium* taxa, and if so, what does this imply about masticatory function? 3) What is the predominant mode of dental evolution exhibited by *Hyracotherium*? 4) Are the evolutionary dynamics of dental size and shape consistent? In addition, the observed differences in dental morphology are used to comment on recent taxonomic work concerning *Hyracotherium* and assess the likelihood of a single lineage of *Hyracotherium* in the Clarks Fork and northwestern Bighorn Basins.

The final chapter summarizes the results of previous chapters, especially those of Chapter 4, in the context of previously documented climatic and environmental change in the Clarks Fork and northwestern Bighorn Basins. Adaptive hypotheses are presented concerning coincident patterns of morphological and climatic/environmental changes. Finally, future work is outlined that will be used to test these adaptive hypotheses.

Figure 1.1 Schematic map of the sampled early Eocene localities in the Clarks Fork and northwestern Bighorn Basins, Wyoming. Black contours represent approximate biozone boundaries as exposed on present day surface. Locality map modified from Gingerich and Klitz (1985). Wyoming state map taken from [www.google.maps.com](http://www.google.maps.com) (accessed 10/7/2008).

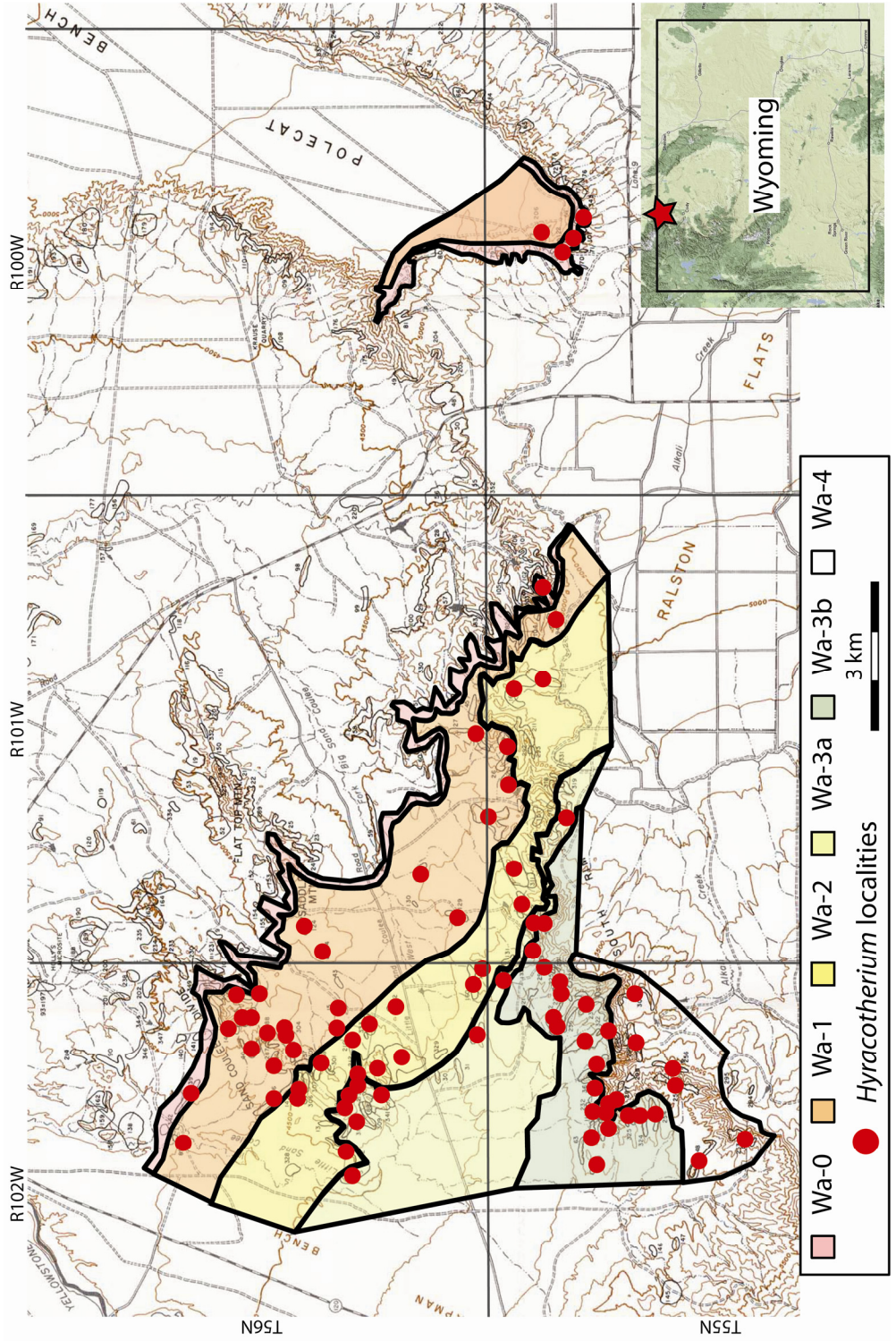
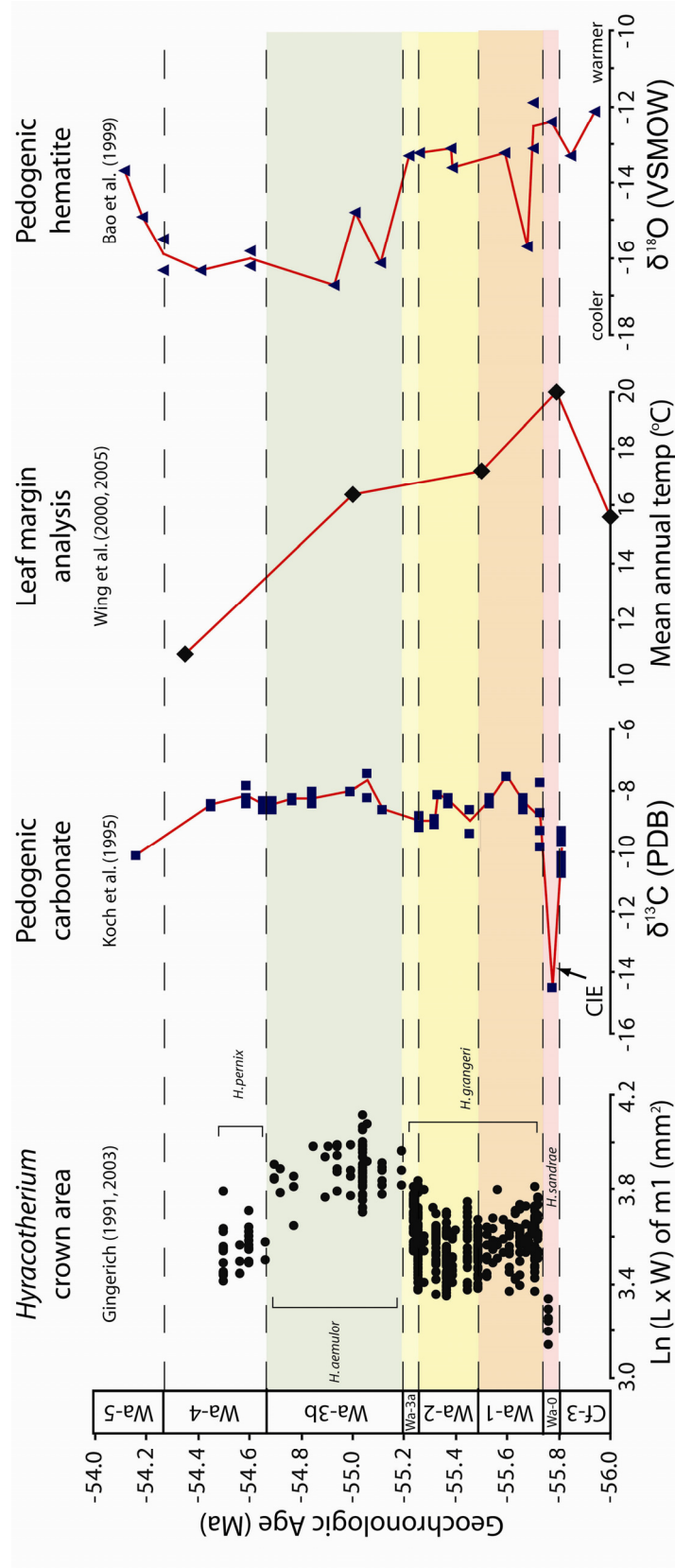


Figure 1.2 Comparison of patterns in *Hyracotherium* lower first molar size and various paleoclimatic proxies from the Clarks Fork and Bighorn Basins. The stratigraphic ranges of *Hyracotherium* taxa are indicated on the crown area plot. The *H. sandrae*/*H. grangeri* transition immediately follows the carbon isotope excursion (CIE) associated with the PETM. Initiation of regional cooling and subsequent intensification are coincident with the *H. grangeri*/*H. aemulor* (Wa-3a/Wa-3b) and *H. aemulor*/*H. pernix* (Wa-3b/Wa-4) transitions, respectively.



## References

- Bao, H., P. L. Koch, and D. Rumble III. 1999. Paleocene-Eocene climatic variation in western North America: Evidence from the  $\delta^{18}\text{O}$  of pedogenic hematite. *GSA Bulletin* 111: 1405-1415.
- Bown, T. M. and M. J. Kraus. 1981. Vertebrate fossil-bearing paleosol units (Willwood Formation, lower Eocene, northwest Wyoming, U.S.A.): Implications for taphonomy, Biostratigraphy, and assemblage analysis. *Palaeogeography, Palaeoclimatology, Palaeoecology* 34: 31-56.
- Bryant, J. D., P. N. Froelich, W. J. Showers, and B. J. Genna. 1996. Biologic and climatic signals in the oxygen isotopic composition of Eocene-Oligocene equid enamel phosphate. *Palaeogeography, Palaeoclimatology, Palaeoecology* 126: 75-89.
- Chew, A. 2005. Biostratigraphy, paleoecology, and synchronized evolution in the early Eocene mammalian fauna of the central Bighorn Basin, Wyoming. Ph.D. dissertation. Johns Hopkins University.
- Chew, A. 2009. Paleoecology of the early Eocene Willwood mammal fauna from the central Bighorn Basin, Wyoming. *Paleobiology* 35: 13-31.
- Clyde, W. C. and P. D. Gingerich. 1998. Mammalian community response to the latest Paleocene thermal maximum: An isotaphonomic study in the northern Bighorn Basin, Wyoming. *Geology* 26: 1011-1014.
- Cope, E. D. 1873. Fourth notice of extinct Vertebrata from the Bridger and the Green River Tertiaries. *Palaeontological Bulletin* 17: 1-4.
- Crowley, B. E., P. L. Koch, and E. B. Davis. 2008. Stable isotope constraints on the elevation history of the Sierra Nevada Mountains, California. *GSA Bulletin* 120: 588-598.
- Evander, R. L. 1989. Phylogeny of the family Equidae. Pp. 130-150. *in* D. R. Prothero and R. M. Schoch, eds. *The evolution of perissodactyls*. Oxford University Press, Oxford.
- Feranec, R. S. and B. J. MacFadden. 2006. Isotopic discrimination of resource partitioning among ungulates in C3-dominated communities from the Miocene of Florida and California. *Paleobiology* 32: 191-205.
- Froelich, D. J. 1999. Phylogenetic systematic of basal perissodactyls. *Journal of Vertebrate Paleontology* 19: 140-159.



- 2002. Quo vadis eohippus? The systematic and taxonomy of the early Eocene equids (Perissodactyla). *Zoological Journal of the Linnean Society* 134: 141-256.
- Gingerich, P. D. 1981. Variation, sexual dimorphism, and social structure in the early Eocene horse *Hyracotherium* (Mammalia, Perissodactyla). *Paleobiology* 7: 443-455.
- 1982. Time resolution in mammalian evolution: Sampling, lineages, and faunal turnover. *Proceedings of the Third North American Paleontological Convention* 1: 205-210.
  - 1983. Paleocene-Eocene faunal zones and a preliminary analysis of Laramide structural deformation in the Clarks Fork Basin, Wyoming. *Wyoming Geological Association Guidebook, Thirty-fourth Annual Field Conference* 34: 185-195.
  - 1991. Systematics and evolution of early Eocene Perissodactyla (Mammalia) in the Clarks Fork Basin, Wyoming. *Contributions from the Museum of Paleontology, University of Michigan* 28: 181-213.
  - 2003. Mammalian responses to climate change at the Paleocene-Eocene boundary: Polecat Bench record in the northern Bighorn Basin, Wyoming. *In* P. D. Gingerich, B. Schmitz, E. Thomas, and S. L. Wing, eds. *Causes and consequences of globally warm climates in the early Paleogene*. *Geological Society of America Special Paper* 369: 463-478.
  - 2006. Environment and evolution through the Paleocene-Eocene thermal maximum. *Trends in Ecology and Evolution* 21: 246-253.
- Gingerich, P. D. and K. Klitz. 1985. Paleocene and early Eocene fossil localities in the Fort Union and Willwood Formations, Clarks Fork Basin, Wyoming. *University of Michigan Museum of Paleontology, Miscellaneous Contributions*, 1 sheet (map).
- Gradstein, F. M., J. G. Ogg, and A. G. Smith. 2005. *A geologic time scale 2004*. Cambridge University Press, New York.
- Gunnell, G. F. 1998. Mammalian faunal composition and the Paleocene/Eocene Epoch/Series boundary: Evidence from the northern Bighorn Basin, Wyoming. Pp. 409-427 *in* M.-P. Aubry, S. G. Lucas, and W. A. Berggren, eds. *Late Paleocene – Early Eocene Biotic and Climatic Events in the Marine and Terrestrial Records*. Columbia University Press, New York.
- Heinrich, R. E., S. G. Strait, and P. Houde. 2008. Earliest Eocene Miacidae (Mammalia: Carnivora) from northwestern Wyoming. *Journal of Paleontology* 82: 154-162.

- Hooker, J. J. 1994. The beginning of the equoid radiation. *Zoological Journal of the Linnean Society* 112: 29-63.
- Janis, C. M. 1976. The evolutionary strategy of the Equidae and the origins of rumen and cecal digestion. *Evolution* 30: 757-774.
- 1984. The use of fossil ungulate communities as indicators of climate and environment. Pp. 85-104 *in* P. Brenchley, ed. *Fossils and Climate*. Wiley, London.
- Janis, C. M. and M. Fortelius. 1988. On the means whereby mammals achieve increased functional durability of their dentitions with special reference to limiting factors. *Biological Reviews of the Cambridge Philosophical Society* 63: 197-230.
- Janis, C. M. and P. B. Wilhelm. 1993. Where there mammalian pursuit predators in the Tertiary? Dances with wolf avatars. *Journal of Mammalian Evolution* 1: 103-125.
- Kitts, D. B. 1956. American *Hyracotherium* (Perissodactyla, Equidae). *Bulletin of the American Museum of Natural History* 110: 1-60.
- Koch, P. L., W. C. Clyde, R. P. Hepple, M. L. Fogel, S. L. Wing, and J. C. Zachos. 2003. Carbon and oxygen isotope records from paleosols spanning the Paleocene-Eocene boundary, Bighorn Basin, Wyoming. P. D. Gingerich, B. Schmitz, E. Thomas, and S. L. Wing, eds. *Causes and consequences of globally warm climates in the early Paleogene*. Geological Society of America Special Paper 369: 49-64.
- Koch, P. L., J. C. Zachos, and D. L. Dettman. 1995. Stable isotope stratigraphy and paleoclimatology of the Paleogene Bighorn Basin (Wyoming, USA). *Palaeogeography, Palaeoclimatology, Palaeoecology* 115: 61-89.
- Kraus, M. J. 1996. Avulsion deposits in lower Eocene alluvial rocks, Bighorn Basin, Wyoming. *Journal of Sedimentary Research* 66: 354-363.
- 2001. Sedimentology and depositional setting of the Willwood Formation in the Bighorn and Clarks Fork Basins. *In* P. D. Gingerich, ed. *Paleocene-Eocene Stratigraphy and Biotic Change in the Bighorn and Clarks Fork Basins, Wyoming*. University of Michigan Papers on Paleontology 33: 15-28.
- Kraus, M. J. and A. Aslan. 1993. Eocene hydromorphic paleosols: Significance for interpreting ancient floodplain processes. *Journal of Sedimentary Petrology* 63: 453-463.

- Kraus, M. J. and S. Riggins. 2007. Transient drying during the Paleocene-Eocene Thermal Maximum (PETM): Analysis of paleosols in the Bighorn Basin, Wyoming. *Palaeogeography, Palaeoclimatology, Palaeoecology* 245: 444-461.
- Kraus, M. J. and T. M. Wells. 1999. Recognizing avulsion deposits in the ancient stratigraphical record. *In* N. D. Smith and J. Rogers, eds. *Fluvial sedimentology VI. Special Publication of the International Association of Sedimentologists* 28: 251-268.
- MacFadden, B. J. 1987. Fossil horses from “*Eohippus*” (*Hyracotherium*) to *Equus*: Scaling, Copes law, and the evolution of body size. *Paleobiology* 12: 355-369.
- 2005. Fossil horses – evidence for evolution. *Science* 307: 1728-1730.
- MacFadden, B. J., T. E. Cerling, J. M. Harris, and J. Prado. 1999. Ancient latitudinal gradients of C<sub>3</sub>/C<sub>4</sub> grasses interpreted from stable isotopes of New World Pleistocene horse (*Equus*) teeth. *Global Ecology and Biogeography* 8: 137-149.
- MacFadden, B. J., N. Solounias, and T. E. Cerling. 1999. Ancient diets, ecology, and extinction of 5-million-year-old horses from Florida. *Science* 283: 824-827.
- Marsh, O. C. 1879. Polydactyle horses, recent and extinct. *American Journal of Science* 17: 499-505.
- Morris, W. J. 1968. A new early tertiary perissodactyl, *Hyracotherium seekinsi*, from Baja California. *Los Angeles County Museum Contributions in Science* 151: 1-11.
- Owen, R. 1841. Descriptions of the fossil remains of a mammal (*Hyracotherium leporinum*) and of a bird (*Lithornis vulturinus*) from the London Clay. *Transactions of the Geological Society, London* 6: 203-208.
- Passey, B. H., T. E. Cerling, M. E. Perkins, M. R. Voorhies, J. M. Harris, and S. T. Tucker. 2002. Environmental change in the Great Plains: An isotopic record from fossil horses. *Journal of Geology* 110: 123-140.
- Radinsky, L. 1966. The adaptive radiation of the phenacodontid condylarths and the origin of the Perissodactyla. *Evolution* 20: 408-417.
- 1969. The early evolution of the Perissodactyla. *Evolution* 23: 308-328.
- 1984. Ontogeny and phylogeny in horse skull evolution. *Evolution* 38: 1-15.
- Rensberger, J. M., A. Forsten, and M. Fortelius. 1984. Functional evolution of the cheek tooth pattern and chewing direction in Tertiary horses. *Paleobiology* 10: 439-452.

- Rose, K. D. 2006. The beginning of the age of mammals. Johns Hopkins University Press, Baltimore.
- Secord, R., S. Chester, J. Bloch, D. Boyer, and J. Krigbaum. 2008. The first North American equids: A high resolution stratigraphic study in the Paleocene-Eocene Thermal Maximum. *Journal of Vertebrate Paleontology* 28, no. 3 suppl: 140A.
- Secord, R., S. L. Wing, and A. Chew. 2008. Stable isotopes in early Eocene mammals as indicators of forest canopy structure and resource partitioning. *Paleobiology* 34: 282-300.
- Schankler, D. 1980. Faunal zonation of the Willwood Formation in the central Bighorn Basin, Wyoming. *In* P. D. Gingerich, ed. Early Cenozoic paleontology and stratigraphy of the Bighorn Basin, Wyoming. University of Michigan Papers on Paleontology 24: 99-114.
- Simpson, G. G. 1951. Horses: The story of the horse family in the modern world and through sixty million years of history. Oxford University Press, Oxford.
- Solounias, N. and G. Semprebon. 2002. Advances in the reconstruction of ungulate ecomorphology with application to early fossil equids. *American Museum Novitates* 3366: 49 pp.
- Tuchman, N. C., K. A. Wahtera, R. G. Wetzel, and J. A. Teeri. 2003. Elevated atmospheric CO<sub>2</sub> alters leaf litter quality for stream ecosystems: An *in situ* leaf decomposition study. *Hydrobiologia* 495: 203-211.
- Wang, Y., T. E. Cerling, B. J. MacFadden, and J. D. Bryant. 1994. Fossil horses and carbon isotopes: New evidence for Cenozoic dietary, habitat, and ecosystem changes in North America. *Palaeogeography, Palaeoclimatology, Palaeoecology* 107: 269-280.
- Wilson, J. R., B. Deinum, and F. M. Engels. 1991. Temperature effects on anatomy and digestibility of leaf and stem of tropical and temperate forage species. *Netherlands Journal of Agricultural Science* 39: 31-48.
- Wing, S. L., H. Bao, and P. L. Koch. 2000. An early Eocene cool period? Evidence for continental cooling during the warmest part of the Cenozoic. Pp. 197-237 *in* B. T. Huber, K. G. MacLeod, and S. L. Wing, eds. Warm climates in earth history. Cambridge University Press, Cambridge.
- Wing, S. L., G. J. Harrington, F. A. Smith, J. I. Bloch, D. M. Boyer, and K. H. Freeman. 2005. Transient floral change and rapid global warming at the Paleocene-Eocene boundary. *Science* 310: 993-996.

- Wood, A. R., M. J. Kraus, and P. D. Gingerich. 2008. Downslope fossil contamination: Mammal-bearing fluvial conglomerates and the Paleocene-Eocene faunal transition (Willwood Formation, Bighorn Basin, Wyoming). *Palaios* 23: 380-390.
- Wood, A. R., M. L. Zelditch, A. N. Rountrey, T. P. Eiting, H. D. Sheets, and P. D. Gingerich. 2007. Multivariate stasis in the dental morphology of the Paleocene-Eocene condylarth *Ectocion*. *Paleobiology* 33: 248-260.
- Woodburne, M. O., ed. 2004. Late Cretaceous and Cenozoic mammals of North America: Biostratigraphy and geochronology. Columbia University Press, New York.
- Zachos, J. C., K. C. Lohmann, J. C. Walker, and S. W. Wise. 1993. Abrupt climate change and transient climates during the Paleogene: A marine perspective. *Journal of Geology* 101: 191-213.

## Chapter 2

### **Postcranial Functional Morphology of *Hyracotherium grangeri*: New Insights into the Locomotory Capabilities of Early Eocene Equids**

The purpose of this chapter is to describe a new, nearly complete skeleton of *Hyracotherium grangeri* (UM115547) from the earliest Wasatchian of the Clarks Fork Basin of northwestern Wyoming. The importance of UM115547 is threefold. First, this new *Hyracotherium* specimen provides the best understanding to date of the primitive morphology of Equidae due to it being complete, in near articulation, and its occurrence in the Wa-1 biozone of the Clarks Fork and Bighorn Basins, ~ 200,000 years after the first appearance of Perissodactyla at the Paleocene/Eocene boundary. Second, the completeness of UM115547 provides a context for interpreting the often fragmentary postcranial fossil record of *Hyracotherium*, and when combined with the high-resolution biostratigraphic and collection techniques employed by various workers and institutions in the Clarks Fork and Bighorn Basins, there is the opportunity to study the postcranial evolution of these early horses at a scale finer than previously attempted. Finally, by possessing a complete vertebral column in addition to complete fore- and hindlimbs, UM115547 allows the first investigation of the complete locomotory apparatus of *Hyracotherium*.

Despite its abundance in the Eocene fossil record of the Clarks Fork and Bighorn Basins and elsewhere, very little comprehensive work has been done on the post-cranial morphology of *Hyracotherium*. The first post-cranial description and reconstruction of *Hyracotherium* was made by Cope (1884) based on specimens collected from the Eocene of New Mexico and Wyoming, and was followed much later by the detailed work of Kitts (1956), who made the observation that despite the numerous species named in the genus since Cope (1884) the post-cranial morphology had been almost neglected. Since Kitts (1956), the limb elements of *Hyracotherium* have been described comparatively to better understand the primitive postcranial morphology of Perissodactyla (Rose 1996), the phylogenetic relationships of basal perissodactyls (Froehlich 1999, 2002; Holbrook, 2001), and the evolution of locomotory function within Equidae (Camp and Smith 1942, Hussain 1975). Kitts (1956), however, remains as the most complete description and interpretation of the post-cranial morphology of this early equid.

The morphology of the vertebral column in *Hyracotherium*, especially the lumbus and posterior thorax, and its role in locomotion is virtually unknown. The lumbar vertebral sample of Kitts (1956) was limited to two fragmentary vertebrae, one with only a complete post-zygapophysis and the other with a partial spinous process. Based on these two vertebrae and comparisons with the Oligocene horse *Mesohippus*, Kitts (1956) reconstructed the posterior thorax and lumbus as dorsostable with embracing zygapophyses, a highly derived condition similar to extant horses. Subsequent post-cranial studies of *Hyracotherium* did not include new vertebral specimens in their descriptions and were often limited to interpreting the functional morphology of individual bones or limbs in isolation from the rest of the locomotory apparatus (e.g.

Hussein, 1975; Rose, 1996). Hussein (1975), in studying the functional morphology of the hindlimb in fossil and extant horses, concluded that joint stability and posture of *Hyracotherium* was unlike those of younger fossil taxa, and since vertebral morphology is indicative of the forces applied by limb function and locomotion (Slijper, 1946; Zhou et al., 1992), the differences in posture and joint stability should also be reflected in the vertebral morphology of *Hyracotherium*.

In this chapter, emphasis is placed on providing detailed descriptions of the vertebral morphology of *Hyracotherium* and the role of the vertebral column in locomotion. Descriptions of skull morphology are not included here, because the preserved state of the UM115547 skull (i.e. sheared, compressed, and fragmented) bears no new information on the morphology and proportions of the skull in *Hyracotherium* as described by previous authors (e.g. Kitts, 1956; Gingerich, 1981; Radinsky 1984, etc). Previous descriptions of limb morphology and function will be supplemented via detailed descriptions of muscle attachment sites and muscle-scarring in order to discuss the differential importance of limb musculature. Dog anatomy (Evans, 1993) is used as context for interpretation of muscle attachment sites and muscle function, because *Hyracotherium* resembles modern canines in general skeletal morphology, proportions, and presumed limb posture. Where the skeleton of *Hyracotherium* differs significantly from canines (i.e. pelvic and femoral morphology), the morphology of UM115547 was compared directly to extant horses (Budras et al., 2003) to reconstruct muscle positions and functions.



## **Occurrence and Preservation**

UM115547 was collected from SC-16, one of the University of Michigan Museum of Paleontology Sand Coulee vertebrate localities in the Clarks Fork Basin of northwestern Wyoming (Fig. 2.1). SC-16 is late Wa-1 in age, ~200,000 years after the Paleocene/Eocene transition. The locality consists of two well-developed, orange paleosols separated by a weakly-cemented, light gray sandstone, ~0.5 m in thickness. UM115547 was discovered near the base of the sandstone. The contact between the sandstone and the underlying paleosol is sharp and irregular. Near its base the sandstone is poorly sorted, containing a mixture of very fine-medium sand grains, mudclasts, and detrital biotites. The sandstone fines upward, grading into the C horizon of the overlying paleosol. The two paleosols typically produce carbonate encrusted mammalian dental fragments whereas the sandstone contains dental and postcranial fragments of fish, squamates, crocodylians, and mammals. The lithological characteristics and fossil content of the sandstone suggests a proximal channel depositional environment, such as a ponded or point bar deposit.

UM115547 was preserved in near articulation with its anterior portion of its skeleton oriented in right-lateral view and the posterior portion oriented in dorsal view (Fig. 2.2). The skull is compressed, sheared, and plastically deformed. Post-cranial elements show slight compression depending on their preserved orientation in the sandstone. Distal limb elements were found disarticulated, and the majority of the caudal vertebrae were not recovered. No taphonomic indicators of predation were found on the specimen, but UM115547 was preserved alongside a semi-articulated agumorph

squamate and the disarticulated limb and dental elements of an insectivore (*Palaeoryctes* sp.) that may have died near UM115547 while foraging on scavenger insects.

## **Axial Skeleton**

### Cervical vertebrae description

There are seven cervical vertebrae, labeled C1-7, in *Hyracotherium grangeri*. The first six cervical vertebrae were preserved either in near-articulation (C1-3) or in complete articulation (C3-6). C3-6 were not disarticulated during preparation in order to prevent unnecessary damage. C6 and C7 were disarticulated during burial/compaction as the glenoid of the right scapula was pressed between them. Only the cranial portion of C7 shows damage and deformation due to contact with the glenoid.

*C1 (Atlas; Fig. 2.3A-E).* — The atlas is complete except for the two atlantal wings and the ventral tubercle, which are broken and missing. The preserved proportions of the atlas is typical in being wider than tall, and the cranial articulations are deeply concave and renal in shape. The caudal articulations are fairly flat and possess a straight medial edge and a rounded lateral edge. The vertebral foramen is round in cross-section with a slight constriction ventrally. There is a shallow groove on the cranial side of the neural arch, whose edges meet at a slight rounded protuberance at the dorsal midline. Only one pair of transverse foramina is preserved at the lateral edge of the caudal articulations, but there is a small notch preserved on the right side, just lateral to the one foramen, suggesting the presence of a secondary foramen on the atlantal wing. The diameter of the lateral foramina near the cranial end of the atlas is nearly twice that of the preserved

transverse foramina. The mastoid processes of the skull are short and rounded, suggesting that the rectus capitis lateralis muscle is fairly diminutive. This further suggests that the atlantal wings most likely did not project far in the lateral direction. This contrasts with the contemporaneous tapiromorph *Cardiolphus radinskyi*, which possesses wide, laterally projecting atlantal wings and long, well-developed mastoid processes.

*C2 (Axis; Fig. 2.3A-E).* — The cranial articulations of C2 face cranially with a slight lateral component to the orientation and are deltoid in shape. The caudal articulation of the centrum is heart-shaped with the point convergent with the hypapophysis. The post-zygapophyses are reniform and face ventro-laterally. The transverse processes are relatively small and project caudally with a small lateral component to their orientation. The spinous process is broad and rounded in lateral view, identical to the condition described by Kitts (1956), but the vertical extent is not known due to a broken and missing apex. The anterior portion of the spinous process projects beyond the neural arch, and the ventral half of this projection is broad and somewhat rugose. The posterior portion of the spinous process projects and overlaps at least the third cervical vertebra, and the ventral portion of this projection exhibits a weak ridge that extends into the space between the post-zygapophyses. The centrum of C2 is roughly rectangular in shape in ventral view with a well-developed keel along the midline. The hypapophysis is well-developed, deltoid in shape, and possesses 3 longitudinal ridges with the central ridge in line with the ventral keel. The diameter of the transverse foramina is nearly twice that of the transverse foramina of the atlas.

*C3-5 (Fig. 2.3C-E)*. — These 3 vertebrae are nearly identical and only differ slightly in overall proportions, spinous process length and orientation, and development of the hypapophysis. The pre-zygapophyses are ovoid in shape and are oriented dorsomedially with a greater dorsal component. The post-zygapophyses are also ovoid in shape and are oriented ventrolaterally with a greater ventral component. Both cranial and caudal articulations of the centra are obliquely oriented with respect to the long axis and are heart-shaped with the point convergent with the ventral keel or hypapophysis, respectively. The transverse processes are broad, project ventrolaterally with a greater ventral component, and possess a cranial and caudal projection. The cranial projections of the transverse processes are broad and round, the thickness of the ventral edge is slightly inflated. Only C4 possesses a well preserved caudal projection of the transverse process, and this projection is more narrow and pointed than the cranial projection.

The lengths, widths, and heights of these 3 vertebrae gradually increase from C3 to C5. The spinous processes increase in breadth, width, and height from C3 to C5, and cranial orientation of the spinous processes also increases from C3 to C5, such that the spinous process of C3 is nearly vertical and the process of C5 is oriented cranially at nearly a 45° to the long axis of the centrum. The ventral keel of the centrum is deeper in C3-4 than in C5. The hypapophysis of C3 possesses three longitudinal ridges similarly to C2, but the hypapophyses of C4-5 possesses only 2, so that it appears as if the ventral keel bifurcates upon convergence with the hypapophysis.

*C6 (Fig. 2.3C-E).* — The sixth cervical vertebra differs from C3-5 by possessing a round caudal articulation on the centrum, a weak ventral keel on the centrum, and accessory processes that project laterally from the transverse processes near the transverse foramina. The cranial and caudal projections of the transverse processes also differ from those of C3-5 in that the cranial projections are narrow and somewhat angular and the caudal projections are broad and rounded. The spinous process is incomplete, yet appears to be more robust than the spinous processes of C3-5. Based on the preserved articulation of C5-6, the length of the spinous process of C6 was not much greater than that of C5, or, otherwise, it would have impinged onto the dorsal surface of C5. C6 also differs from C3-5 in lacking a hypapophysis. The transverse foramina appear to be the widest on C6.

*C7 (Fig. 2.4A).* — As noted above, the processes and zygapophyses of C7 were significantly damaged and deformed by compaction with the right scapula. Only the left post-zygapophysis is complete and is nearly identical to the post-zygapophyses of C3-6. Although incomplete, the transverse process appears to be short, rounded, and lacks the cranial and caudal projections exhibit by C3-6. No transverse foramina are present. The spinous process is complete, substantially longer than the spinous processes of all preceding cervical vertebrae, and has a vertical orientation with a slight caudal component. Along its height, the spinous process is widest in the middle and rapidly thins to a bladelike anterior and posterior edge. The apex of the spinous process is shallowly concave. The centrum has a square shape in ventral view and is shallowly concave on

either side of the midline. There is a small indentation on the caudal articulation of the centrum for articulation with the capitulum of the first rib.

#### Functional interpretation of cervical vertebrae

The broad and tall spinous process of the axis and the height of the spinous process of C7 provide substantial attachment sites for the nuchal ligament. The short spinous processes on C3-5 indicate that the nuchal ligament did not attach to these vertebrae. The broken spinous process of C6 is much broader at its base than those of C3-5, but most likely did not have a length sufficient to serve as an attachment site for the nuchal ligament. A nuchal ligament with attachment sites only at C2, C7, and T1 would have allowed substantial ventral flexion of the neck, as suggested by a similar case in *Pachyaena ossifraga* by Zhou et al. (1992).

The expanded and ventrally oriented transverse processes of C3-6 and the well developed hypapophyses of C2-5 provide large attachment sites for musculature (e.g. m. longis capitus, m. longis colli, and m. scalenus) used to ventrally flex the cervical region. Furthermore, the ventral orientation of the transverse processes would provide little leverage for muscles, like the m. scalenus, for lateral flexion of the neck and increase the leverage for ventral flexion.

Although the zygapophyseal articulations of the cervical region most likely did not prevent lateral flexion of the neck, there are few muscle attachment sites that would provide significant leverage for lateral flexion. The accessory projections on the transverse processes of C6 are the only attachment sites that project laterally, but these projections most likely served as an attachment site for the m. intertransversarii ventrales

cervicis, a muscle primarily used for ventral flexion. The broad spinous process of the axis would have provided a large attachment site for epaxial musculature, like the m. biventer cervicis and m. multifidus cervicis, that when used unilaterally can flex the neck and head laterally, but these muscles can also stabilize the head and neck when used bilaterally.

#### Thoracic vertebrae description

There are seventeen thoracic vertebrae, labeled T1-17, in *Hyracotherium grangeri*. The first three thoracic vertebrae are preserved in articulation with the last cervical vertebra right lateral side up, but these vertebrae were damaged by impaction of the left and right scapulae. T4-8 are also preserved in articulation with the right lateral side up, separately from C7-T3, but the left side was damaged by impaction of the left scapula. The ninth and tenth thoracic vertebrae were preserved in near articulation with T4-8, but T11-16 were found scattered in various orientations near the articulated vertebrae. The seventeenth and last thoracic vertebrae were preserved with its dorsal surface up in near articulation with the first lumbar vertebra. T9-17 show a minimum amount of damage incurred during burial and during preparation.

*T1-3 (Fig. 2.4A).* — The first thoracic vertebra possesses a complete spinous process and complete processes and zygapophyses on the left side. The post-zygapophyses are separated by a distinctive notch similarly to the condition in the cervical vertebrae. Both pre- and post-zygapophyses appear to be ovoid in shape. The pre-zygapophyses are oriented dorsomedially with a greater dorsal component, and the post-zygapophyses are

oriented ventrolaterally with a greater ventral component. The transverse process is robust, projects ventrolaterally, and possesses a deeply concave diapophysis for articulation with the tubercle of the first rib. The length of the transverse process is greater than half the centrum width in ventral view and arises from the side of the centrum. The anterior portion of the transverse process exhibits slight muscle scarring. The centrum has a square shape in ventral view, similar to C7, and has large parapophyses. The centrum is shallowly concave on either side of the midline in ventral view.

The spinous process is longer and more robust than all preceding or succeeding spinous processes, with the possible exception of T2, which does not have a complete spinous process. Along its height, the spinous process is widest in the middle and thins to a bladeliike anterior and posterior edge. Unlike C7, the apex of the spinous process of T1 is expanded into a square shape in lateral view, and the width the apex is somewhat dilated in dorsal view by comparison.

T2 is heavily damaged and preserves only a pre-zygapophysis, a partial transverse process, and the middle of the spinous process. The pre-zygapophysis is identical to the pre-zygapophysis of T1 in shape, but slightly smaller in size. The transverse process does not appear to be as robust as the transverse process of T1. The preserved portion of the spinous process is identical to that of T1, suggesting it was similar in size and shape when complete.

T3 is nearly complete, but was plastically deformed by impaction with the glenoid of the left scapula. The pre-zygapophysis is identical to the pre-zygapophyses of T1-2 in shape and is the same in size as that of T2. The post-zygapophyses are round in shape



and are separated by a very shallow notch. The transverse process of T3 is less robust than that of T1 and possesses a deeply concave diapophysis. The centrum is not as square in ventral view as the centrum of T1 and appears to be approaching the spindle shape exhibited by more posterior thoracic vertebrae. The anterior and posterior parapophyses are not preserved sufficiently to merit description. The caudal articulation surface of the centrum exhibits a rounded heart shape that is more dorso-ventrally compressed than the caudal surface of the cervical centra. The spinous process is identical to the spinous process of C7, except that it is slightly more caudally oriented and the apex is convex and a little wider.

*T4-10 (Fig. 2.4A & 2.5A).* — The fourth through tenth thoracic vertebrae show few differences among them. The pre-zygapophyses are oblong in shape, face anteriorly and dorsally with a minor lateral component, and barely project beyond the cranial articulation of the centra. The post-zygapophyses are also oblong in shape, face posteriorly and ventrally with a minor medial component, and are convergent with the neural arch, instead of being separated by a narrow notch as in the anterior thoracics. The transverse processes are less robust than those of more anterior thoracics, possess short metapophyses, and bear concave diapophyses that become increasingly shallow from T4-8. The metapophyses of T9-10 are slightly more robust than those of T4-8, and the diapophyses of T9-10 are nearly flat and face ventrolaterally. The transverse processes of T4-10 arise from the pedicle and project anteriorly and laterally at about 45° from the long axis of the centrum in dorsal view. The length of the transverse processes decreases from T4-10.

In ventral view, the centra are spindle-shaped and are slightly wider at the parapophyses. A ventral keel appears on T8 and is better developed on T9-10. The posterior parapophyses project farther from the centrum than the anterior parapophyses and are slightly more concave, exhibiting a slight bony lip that would wrap around the capitulum of the associated rib. The spinous processes decrease in length from T4-10, become more caudally oriented from T4-10, and possess apices of variable shape. For example, T4, T6, and T9 have posteriorly-pointing acute apices whereas T5 and T10 possess squared apices. The apices of T7-8 are broken and missing. The spinous process of T4 is the widest and broadest whereas widths and breadths of the spinous processes of T5-10 are nearly equivalent.

*T11-14 (Fig. 2.5A).* — T11-14 differ from T4-T10 with respect to the spinous processes, transverse processes, and rib articulations. The caudal orientation of the spinous processes decreases from T11-13, and the spinous process of T14 (anticlinal vertebra) is vertical. Kitts (1956) described T16 as being the anticlinal vertebra, but it is unclear whether this difference is due to an evolutionary change [the specimen Kitts (1956) describes is a late Wasatchian *Hyracotherium*] or a misidentification of the vertebral position [Kitts (1956) refers to his vertebral specimens as “poorly preserved”]. The lengths and widths of the spinous processes also decrease from T11-14. The diapophyses decrease in size from T11-14 and become increasingly separated from the metapophyses by a thin strut of bone, creating a concavity on the posterior side of the transverse processes. The metapophyses, however, increase in size from T11-14 and begin to curve dorsally and medially on T13-14. The height of the centra gradually decreases from T11-

14, and a ventral, midline keel is present on the centra. The concavity of the posterior parapophysis becomes increasingly shallow from T11-14 until it equals the concavity of the anterior parapophysis. The centrum of T14 is more square-shaped in ventral view than spindle-shaped, whereas T11-13 remain spindle-shaped.

*T15-17 (Fig. 2.5A).* — T15-17 differ significantly from the first 14 thoracic vertebrae in completely lacking transverse processes and in having proportions more similar to lumbar vertebrae. The pre-zygapophyses of T15 are oblong in shape and face anteriorly and dorsally with a minor lateral component similarly to the condition in the anterior thoracics, but the post-zygapophyses are deltoid in shape and are oriented ventrolaterally, instead of ventromedially. This condition defines T15 as the diaphragmatic vertebra. T16-17 have concave, deltoid-shaped pre-zygapophyses that are oriented dorsomedially and convex, deltoid-shaped post-zygapophyses that are oriented ventrolaterally. A notch separates the left and right post-zygapophyses in T15-17, and the size of this notch increases from T15 to T17. There is a distinctive fovea where the post-zygapophyses meet in T17.

The metapophyses of T15-17 are large and widen near their apices. The metapophyses of T16 are oriented vertically whereas the metapophyses of T15 and T17 are oriented dorsolaterally. Laterally-projecting ridges appear on the base of the pedicles of T15-17, and the ridge of T15 possesses a narrow process that projects away from the pedicle to the same extent as the metapophysis. The spinous processes of T15-T17 are broad, are oriented cranially, and do not taper near their apices. Instead, the spinous processes possess wide, shelf-like apices with small concave pits at the posterior margin.

In ventral view, the centra are square in shape, possess a midline keel, and have deep concavities on either side of the midline. The cranial and caudal articular surfaces of the centra are heart-shaped (although the surfaces of T17 could be arguably described as reniform), and the length and width of the centra gradually increases in T15-17 without an increase in centrum height. The parapophyses are much smaller and less concave in T15-17 than in any other thoracic vertebra. T17 does not possess a posterior parapophysis.

#### Function interpretation of the thoracic vertebrae

Whereas the anterior thoracic region likely bore substantial musculature for head, neck, and shoulder girdle movement, the majority of the thoracic vertebral region was involved in stabilizing the trunk via muscles and ligaments without significantly decreasing the flexibility of the vertebral column. The orientation of individual spinous processes indicates the direction of the resultant force applied by attached musculature (Slijper 1946). In general, a caudally-oriented spinous process experiences more muscular force from the caudal direction, a cranially-oriented process experiences more force from the cranial direction, and a vertical process experiences force equally from the cranial and caudal directions.

The tall, broad, and nearly vertical spinous processes of T1-3, in addition to the spinous process of C7, indicate that this region supported a large splenius muscle for lifting the head and neck. A large splenius muscle working in conjunction with the substantial musculature used in ventral flexion (described above) would greatly stabilize the head during locomotion, while still allowing flexibility of the cervical region during

browsing. The spinous processes of T1-3 would also support a large rhomboideus muscle, which assists in moving the forelimb in the parasagittal plane.

Features of the intermediate and posterior thoracic vertebrae suggest the presence of strong musculature used in stabilizing and extending the trunk. The long and caudally oriented spinous processes of T4-10 combined with the increasing size of the metapophyses starting with T9 provided significant leverage for the transversospinalis system of epaxial musculature for stabilizing the trunk. Furthermore, the increasing sizes of the transverse process caudal concavities from T11-14 and the ridges and/or accessory processes on the pedicles of T15-17 suggest the presence of large longissimus musculature in this region, used for both extending and stabilizing the back. When T4-11 are articulated, the spinous processes are tightly spaced, limiting the available space for intraspinal musculature. However, such tight spacing suggests the presence of short intraspinal and supraspinal ligaments between vertebrae, which would require great force to extend, further stabilizing this region of the back.

The presence of a distinctive anticlinal vertebra (T14) several positions anterior to the thoracic-lumbar junction and the presence of cranially-oriented spinous processes on T15-17 suggests that the posterior thorax comprised the most sagittally-flexible region of the trunk (Slijper 1946, Zhou et al. 1992). The longer length of the centra in this region would provide greater translation of individual vertebrae than shorter centra at the same amount of angular displacement. The greater sagittal component to the zygapophyseal articulations would prevent torsion without preventing sagittal flexion and extension. The spacing between the spinous processes widens between the posterior thoracic vertebrae, lengthening intraspinal and supraspinal ligaments and requiring less force

to extend them. The single-headed ribs attached to this region of the thorax may have moved more independently with respect to their associated vertebrae in comparison to the anterior double-headed ribs, further suggesting that ventral flexion would not have greatly impinged on the ability to inhale and exhale.

#### Lumbar vertebrae description

There are seven lumbar vertebrae, labeled L1-7, in *Hyracotherium grangeri*. The first lumbar vertebra was preserved in near articulation with the posterior thoracic vertebrae and the remainder of the lumbar vertebrae. L2-6 were preserved in tight articulation with each other and the first sacral vertebra, dorsal side up. The majority of the vertebral processes are intact, except that the transverse processes were plastically deformed by impaction with the left innominate and femur, and the right transverse processes were damaged during exhumation of the specimen.

*L1-2 (Fig. 2.5A, 2.6, & 2.7).* — The first lumbar is complete and well-preserved, except for a damaged right transverse process and a left metapophysis that was apparently deformed post-burial. The morphology of L1 is similar to last thoracic vertebra, except that it possesses short transverse processes that lack rib articulations. The pre-zygapophyses are concave, deltoid in shape, and oriented dorsomedially with a minor cranial component. The post-zygapophyses are deltoid in shape, separated by a wide notch, and are convex to the extent that significant portions of the articular surfaces are oriented ventrally (nearly parallel to the coronal plane) and laterally (nearly parallel to the sagittal plane). L1 also possesses a fovea at the intersection of the post-zygapophyses.

The transverse processes are short, arise from the side of the centrum, are oriented ventrolaterally, and project slightly beyond the cranial articulation of the centrum. The metapophyses are robust with slightly expanded apices, and the pedicle bears two linear muscle scars on each side, one between the pre- and post-zygapophyses and one near the base of the pedicle, similarly to the condition in T15-17. The spinous process is broad and cranially-oriented to the extent that it would overhang T17 nearly half its centrum length. The apex of the spinous process is expanded into a broad shelf, with a rounded cranial projection and a fovea at its posterior edge. The articular surfaces of the centrum are both renal in shape and are of equal width. The centrum also possesses a ventral keel along its midline and deep concavities on either side of the midline.

The second lumbar vertebra lacks a complete left transverse process, but is otherwise complete. The pre-zygapophyses are concave, ovoid in shape, and oriented equally in the dorsal and medial directions. The medial component is nearly parallel to the sagittal plane. The post-zygapophyses of L2 are identical to those of L1. The metapophyses are longer than those of L1 and possess expanded apices. The transverse processes stem from the centrum and are twice as long as those of L1. The transverse processes are oriented ventrolaterally, but less ventrally than L1. Two linear muscle scars are present on the pedicle, but are weakly developed in comparison to L1. The spinous process is broad with a shelf-like apex, but it is less cranially-oriented than the spinous process of L1 to the extent that it would overhang less than half the centrum length of L1. The articular surfaces of the centrum are renal in shape, and in ventral view, possess the deepest concavities and the strongest midline keel out of all the lumbar vertebrae.

*L3-7 (Fig. 2.6 & 2.7).* — L3-6 exhibit gradational changes that progress posteriorly, both in the orientation and length of the processes and the development of the zygapophyseal articulations. The pre-zygapophysis of L3 is identical to that of L2 in possessing a well-developed dorsal and sagittal articular surface, but the concavity of the pre-zygapophyses on L4 is increased such that the sagittal surface curves medially, slightly overhanging the post-zygapophyses of L3. The concavity of the prezygapophyses and the portion that curves cranially and medially over the adjacent post-zygapophyses progressively increases in size from L4-L7.

There is a concurrent change in the morphology of the post-zygapophyses, with the post-zygapophysis of L3 exhibiting a weak hemi-cylindrical shape, L4-5 exhibiting a well-developed hemi-cylindrical shape, and L6-7 exhibiting a well-developed hemi-cylindrical shape that continues onto and indents into the dorsal surface of the post-zygapophysis. The embracing nature of the L3-6 zygapophyseal articulations can be seen best in the microCT slices shown in Fig. 2.7. It should be noted that the post-zygapophyses of L6-7 are more elongate than preceding post-zygapophyses and form a shallow dorsal arc in lateral view. L6-S1 also appear to be preserved in dorsal flexion such that the posterior portion of the post-zygapophysis articulation surfaces are exposed.

Although the transverse processes of L5 are broken and missing, the length of the transverse processes appears to increase progressively from L3-6. The preserved transverse process of the L7 is the shortest of all the lumbar transverse processes, likely to accommodate the long, cranially-projecting iliac crests. The transverse process of L3 stills retains a slight ventral component to its orientation, but the processes of L4, L6, and



L7 are horizontal. The cranial orientation of the transverse processes also decreases from L3-6, to the point that the process of L6 is nearly perpendicular to the long axis of the centrum. The transverse process of L7 is significantly cranially-oriented, but again, this is most likely for accommodating the long iliac crests. There are no distinguishable muscle scars on the pedicles of L3-7, and the preserved metapophyses show no remarkable change in length or width from L3-7.

The cranial orientation of the spinous processes also decreases from L3-L7, such that the spinous process of L7 is nearly vertical. The height of the spinous processes also increases from L3-L6, although L5 lacks a complete spinous process. The spinous process of L7 is only slightly shorter than the process of L6. Only L3 and L6 possess complete spinous process apices, suggesting that the overall length of the apices and the length of the rounded cranial projection of the apices may decrease progressively from L3-7. The spinous processes of L3, L4, L6, and L7 do expand into shelf-like apices, but the widths of these shelves decreases from L3-L7. There are no foveae on the posterior margins of the spinous process apices of L3-7, unlike those of the posterior thoracics and L1-2.

The centra of L3-L7 gradually change in shape from a spindle-shape (L3) to a broad, nearly rectangular shape (L7). This change in shape is manifested by a gradual weakening of the ventral midline keel and parallel ventral concavities and a gradual increase in the width of the centra. Although, the articular surfaces of the centra are not visible on the specimen, microCT slices show that the articular surfaces gradually change from a renal shape to an ovoid shape. The centra also become increasingly

opisthocoelous from L3-7, and the centra of L6-7 are significantly dorso-ventrally compressed than preceding lumbar.

#### Functional interpretation of the lumbar vertebrae

Kitts (1956) described fragmentary lumbar vertebrae of *Hyracotherium* in which only one post-zygapophysis and one spinous process were preserved from different individuals. The preserved post-zygapophysis was described by Kitts (1956) as belonging to the fifth lumbar and exhibiting a “nearly semicircular” articular surface, identical to the morphology for L5 described above. This suggested to Kitts (1956) that at least some of the lumbar vertebrae possessed embracing zygapophyseal articulations, which would limit the flexibility of the lumbus. Kitts (1956) described the preserved spinous process as only slightly cranially inclined, which suggests that it belonged to any of the last four lumbar vertebrae based on the above description. The lack of a strong cranial inclination of the spinous process suggested that the longissimus muscle was fairly weak in the lumbus further implying decreased flexibility in the lumbus.

UM115547 provides a much more complicated functional interpretation of the lumbus in *Hyracotherium*. L1-2 are a continuation of the post-diaphragmatic thoracic vertebral morphology, except for the presence of the transverse processes, suggesting that the anterior lumbus was somewhat flexible in the sagittal plane. The large sagittal component of the zygapophyses would prevent torsion of the vertebrae, the cranial inclination of the spinous processes would prevent hyper-extension or dorsal flexion of the column, yet neither would prevent ventral flexion. Furthermore, the cranial orientation of the spinous processes and transverse processes of L1-2 would have

provided substantial leverage to the longissimus system of epaxial musculature for extending the vertebral column. Again similarly to the condition of T15-17, the muscle scars on the pedicles, the broad spinous processes, and robust metapophyses of L1-2 suggest the presence of strong muscles of the transversospinalis system of epaxial musculature, which would have been important for stabilizing this region of the vertebral column. Finally, L1-L2 possess the broadest spinous process apices, which implies the presence of a thick aponeurosis onto which strong muscle fibers and tendons could attach.

The increasing embraced character of the zygapophyseal articulations from L3-L7 suggests that flexibility decreased in this region with the possible exceptions of the L6-7 and lumbosacral joints. The decreasing cranial inclination of the spinous and transverse processes indicates decreased leverage for muscles that extend the back, yet the robust metapophyses and tall spinous processes indicate similar or greater leverage for the transversospinalis system in comparison to T15-L2. Furthermore, the horizontal orientation of the transverse processes would have positioned the iliocostalis system of epaxial musculature in such a way that nearly all of its force would have acted in the horizontal plane (i.e. no ventral or dorsal components of force for flexion or extension of the column).

The L6-7 and lumbosacral joints may have been more flexible than the L3-L6 joints for the following reasons. Preservation of L6-S1 in dorsal flexion without noticeable deformation suggests that these vertebrae were capable of dorsal flexion and possibly ventral flexion in life. The shallow arc of the post-zygapophyses in lateral view may define an arc of rotation for these joints, and the dorso-ventrally compressed

opisthocoelous centra may have acted as hinges that further restricted movement to the sagittal plane. Furthermore, it is reasonable to assume that *Hyracotherium* was flexible at these two joints because the lumbosacral joint is capable of sagittal flexion in dorsomobile mammals and is the only flexible joint in the posterior vertebral columns of dorsostable mammals (Slijper 1946, Zhou et al. 1992).

#### Sacrum description (Fig. 2.5 & 2.6)

The sacrum consists of 5 vertebrae, labeled S1-5, the last four of which are completely fused, except for the distal portions of the spinous processes. The majority of the auricular surface is on S1 with a minor component on S2, and although S1 and S2 are not fused at the centra, their corresponding portions of the auricular wings show interfingering, unfused sutures. When articulated, the auricular surface is dorso-laterally oriented and ovate in shape. In dorsal or ventral view, the sacrum forms an acute wedge that quickly tapers to less than a quarter of its anterior width. The prezygapophyses of S1 are identical to those of L7, but bear acute, cranially-inclined metapophyses instead of robust, elongate metapophyses. The centrum of S1 is rectangular in shape and is more dorso-ventrally compressed than the preceding lumbar. The cranial articular surface of the S1 centrum is strongly convex whereas the caudal articular surface is flat.

The spinous process and neural arch were broken by impaction with the left ilium, but the length of the S1 spinous process appears to be slightly shorter than the spinous process of L7. The second and third sacral vertebrae possess partial spinous processes that are equal in breadth to the spinous processes of the posterior lumbar and are inclined caudally. The orientation of the bases of the S4-5 spinous processes suggests

that these spinous processes were also caudally inclined. The intermediate sacral crests, made up by the fused zygapophyses and metapophyses, are fairly short and poorly developed. The left lateral sacral crest is well-preserved and exhibits distinctive muscle-scarring along its length.

#### Caudal vertebrae description (Fig. 2.5)

Only the first two caudal vertebrae, labeled Ca1-2, were found in association with UM115547. Ca1 was preserved in articulation with the sacrum and possesses a complete left transverse process, complete zygapophyses, and one metapophysis. Ca2 was preserved in near articulation with Ca1 and possesses a complete right transverse process, complete right zygapophyses, and well-preserved centrum articular surfaces. The pre-zygapophyses of Ca1-2 are both ovoid in shape and are oriented dorsomedially. The post-zygapophyses are also ovoid and are oriented ventrolaterally with a minor posterior component to their orientation. The articular surface of the Ca2 pre-zygapophyses is much larger than the corresponding articular surface of the Ca1 post-zygapophysis. The metapophysis of Ca1 is a thin projection that points cranially and dorsally.

The transverse process of Ca1 arises from the side of the centrum, is oriented laterally and cranially, and possesses a small cranial projection. The transverse process of the Ca2 also arises from the centrum, but is rounded and projects caudally. The tip of the transverse process of Ca2 bears a flattened surface that is oriented ventrolaterally. The broken base of the Ca2 spinous process suggests that the spinous process was oriented nearly vertically. The pedicle of Ca1 extends almost the entire centrum length whereas the pedicle of Ca2 is restricted to the anterior 2/3 of the centrum length, leaving

a wide opening for caudal nerves. The cranial articular surface of the Ca2 centrum is heart-shaped with point down whereas the caudal articular surface is heart-shaped with the point up. The ventral border of the caudal articulation surface of the Ca2 centrum bears two facets, most likely for articulation with a hemal arch.

#### Functional interpretation of the sacrum and caudal vertebrae

Since the spinous process of S1 is not preserved in its proper orientation, its role in positioning muscles for the extension and fixation of the lumbosacral joint cannot be determined. However, the relatively tall and caudally-oriented spinous processes of S2-3 suggest that muscles, like the sacrocaudalis dorsalis, had substantial leverage for extension and lateral flexion of the tail. When the sacrum is articulated with the pelvis, the first two caudal vertebrae remain within the borders of the ischium. This positioning, in conjunction with the presence of a distinctive notch on the ischial spine of the pelvis and broad transverse processes on the proximal caudal vertebrae, suggests the presence of a large coccygeus muscle, which would have been used for pressing the tail down against the anus. Although the total length of the tail in *Hyracotherium* is unknown, its proximal end would have presented a very muscular mass.

Finally, the distinctive muscle scar on the lateral sacral crest and the robust transverse processes of Ca1-2 would have provided a large attachment site for the gluteus superficialis, a muscle used for extending the hip joint. The lateral sacral crest and the caudal transverse processes would extend the origin of the gluteal muscles to the full length of the pelvis starting from the anterior-most portion of the iliac crest to a position on the proximal caudals that overhangs the posterior extent of the ischium. This

condition suggests powerful extension of the hip joint with a significant amount of rotation. This will be discussed further in the context of the hindlimb morphology.

#### Ribs and sternbrae

Seventeen ribs on each side, labeled R1-17, were preserved in UM115547 in various conditions. Figure 2.4B shows the most complete and undeformed right ribs. The first 14 ribs bear distinctive heads and tubercles that articulate with their corresponding thoracic vertebrae whereas R15-17 bear only heads that articulate with vertebral parapophyses. The tubercles of R15-17 are reduced to small bumps near the rib heads, serving only as sites for muscle attachment. The heads and tubercles of R1-3 are separated by relatively long necks and are larger than those of succeeding ribs. Rib neck length gradually decreases on succeeding ribs. The first rib possesses a robust cylindrical shaft that widens at its distal end. R2-5 are distinctively compressed mediolaterally and relatively broad anteroposteriorly, which, when articulated with the thoracic vertebrae, would have produced a shallow concavity on either side of the anterior thorax roughly the size of the scapulae.

The length and curvature of the ribs rapidly increases from R1-7, is relatively constant from R7-10, and gradually decreases from R10-17. The diameter of the concave distal ends, which serve as attachment sites for costal cartilage, is more or less constant from R2-10 and gradually decreases from R11-17. This pattern suggests that the costal cartilages of R11-17 did not directly insert onto the sternbrae and instead either formed a costal arch that attached to the cartilage of R10 or were floating ribs.

Five sternbrae were preserved in various orientations near the ribs and were partially covered in what appeared to be weakly ossified cartilage. Each sternbra is roughly rectangular in shape, compressed dorso-ventrally, and possesses a shallow groove on their dorsal and ventral surfaces. The articulating ends of the sternbrae are shallowly concave and do not possess well-developed surfaces for cartilage attachment. All of the preserved sternbrae are similar in size and shape, and, therefore do not appear to be either the manubrium or xiphoid sternbrae.

### **Description of Forelimb Elements**

#### **Scapula (Fig. 2.8A)**

The scapular blades of UM115547 were severely fragmented by impaction with the cervical and thoracic vertebrae. The right scapular spine and the distal portions of the left and right blades, however, remain intact and are consistent with the morphology described by Kitts (1956). Consequently, the blade appearing in Fig. 2.8A was reconstructed following Plate 2, Fig. 1 of Kitts (1956).

The blade has a convex border anteriorly, a straight posterior border, and is weakly concave medially. The spine projects an equal distance from the blade for the distal 4/5 of its length and rapidly tapers, becoming confluent with the blade proximally. The distal end of the spine continues onto the neck proximal to the glenoid. In contrast to Kitts (1956), there is no distinctive infraglenoid tubercle on the posterior edge of the glenoid, although the posterior edge of the neck shows slight muscle scarring. There is a small protuberance on the lateral side of the neck just proximal of the glenoid, likely for attachment of the teres minor (shoulder flexion) and triceps (elbow extension). A



prominent supraglenoid tubercle is preserved on the left scapula, which bore the biceps brachii muscle (elbow flexion and shoulder extension/stabilization). The coracoid process projects anteriorly from the glenoid and bends medially at nearly a right angle. The outer edge of that right angle and the medial tip of the coracoid process are slightly inflated, providing attachment sites for the biceps brachialis and coracobrachialis (shoulder extension and adduction) muscles, respectively.

#### Humerus (Fig. 2.8B)

The humeral head is evenly rounded and merges with a shallow and wide bicipital groove on the anterior shaft of the humerus, similarly to the description of Kitts (1956). The greater tuberosity is as long as the diameter of the humeral head and curves medially without overhanging the bicipital groove. There is a continuous, distinctive muscle scar that runs from the lateral edge of the humeral head, for attachment of the triceps muscle, and continues onto the dorsal surface of the greater tuberosity and onto its anterior edge, likely for attachment of the supraspinatus muscle (extension and stabilization of the shoulder). A circular fovea with a raised rim is present on the lateral side of the greater tuberosity and was likely an insertion site for the infraspinous muscle (rotation, extension, and stabilization of the shoulder). The deltopectoral crest appears as a very weak muscle scar on the lateral edge of the bicipital groove just distal of the greater tuberosity. The lesser tuberosity is low and bears a short muscle scar for insertion of the subscapularis (adduction and extension of the shoulder) and deep pectoral muscles (extension of the shoulder). A weak muscle scar on the medial side of the bicipital

groove just distal of the lesser tuberosity may have served as an attachment site for the coracobrachialis and the triceps muscles.

Distally, the axis of the humeral condyles is oriented obliquely to the transverse plane defined by the humeral shaft in neutral position, such that the lateral portion is oriented anteriorly out of the transverse plane and the medial portion is oriented posteriorly. This orientation of the distal humerus causes the face of the joint to point antero-medially. The medial condyle of the humerus possesses a sharp rim that is extends farther than the capitulum height and, subsequently, a greater arc length of rotation than the capitulum. The humeral trochlea is shallow, and the capitulum is constricted mediolaterally. A lateral articular shelf is confluent with the dorso-lateral surface of the capitulum and, in conjunction with the radial fossa, defines the extent of elbow flexion. The radial fossa is perforated by the supracondylar foramen, making it contiguous with the triangular ulnar fossa.

Although both epicondyles are relatively small, the medial epicondyle projects farther than the lateral epicondyle and bears a circular fovea with a raised rim on its posterior surface for attachment of the pronator teres muscle. There is also a smaller fovea below the medial epicondyle that may have served as an attachment site for manual flexor muscles. The lateral epicondyle bears two small foveae for manual extensor muscles. The anterior face of the supinator crest is narrow and exhibits slight muscle scarring, for attachment of the extensor carpi radialis muscle, whereas the posterior face is smooth and broader, for attachment of the anconeus muscle (extension of the elbow).

## Ulna (Fig 2.9A)

The olecranon possesses a well-developed, lunate muscle scar on its weakly concave medial surface, a notch on its distal end, and a short, poorly-developed muscle scar on its lateral surface, which are likely attachment sites for the triceps muscle. The lateral surface of the olecranon also exhibits a low, angular scar for attachment of the anconeus muscle. A low ridge is present along the length of the ulna in lateral view that separates the posterior attachment sites for the digital flexor muscles and the anterior sites for digital extensor muscles. The distal end of the ulna tapers to a narrow styloid process with two oblong articular facets, one oriented ventrally and the other oriented ventro-posteriorly.

Kitts (1956) describes the distolateral portion of the trochlear notch as being greatly expanded, further indicating considerable rotation of the radius and ulna with respect to the humerus during extension and flexion of the elbow. In UM115547, the medial and lateral halves of the trochlear notch are equal in width, distally and proximally, but the orientation of the notch is medially oblique to the long axis of the ulna. When the radius and ulna are articulated, however, the trochlear notch is aligned with the long axis of the radius. There is still considerable rotation possible at the elbow during flexion and extension, but this is facilitated by the greater arc length of the medial condylar surface, not the trochlear notch.

Kitts (1956) also describes the radial facet, or radial notch, of the ulna as being flat and restricted in length proximal to the trochlear notch, contrasting this with the radial facet of *Mesohippus* that extends distally along most of the ulnar length. In UM115547, the portion of the radial facet adjacent to the trochlear notch is shallowly

concave, accommodating the convex posterior surface of the proximal radius. Distally, the radial facet tapers rapidly to a thin, distinctive trough that ends just proximal of the styloid process. Furthermore, the anteromedial surface of the styloid process is notched to accommodate the ulnar facet, or ulnar notch, of the radial styloid process.

#### Radius (Fig 2.9A)

The radius of UM115547 is identical to the descriptions of Kitts (1956) and Rose (1996), with the following additions. There are distinctive facets on the proximal and distal radius, corresponding to the proximal portion of the radial facet and the styloid notch of the ulna, respectively. There is not, however, a distinctive facet along the length of the radius that corresponds to the thin distal radial facet of the ulna. This configuration suggests that compressive forces experienced between the radius and ulna are concentrated at the joints and less so along the shafts.

Rose (1996) describes the distal articular surface of the radius as two separate concavities for articulation with the scaphoid and lunar carpal bones. In UM115547, the articular surfaces are continuous, forming a shallow, concave trough, oriented mediolaterally. This trough, although shallow, defines a hinge-like joint, that may have prevented medial and lateral flexion of the carpus.

#### Manus (Fig. 2.9B)

Camp and Smith (1942) and Kitts (1956) present excellent descriptions of the manual elements of *Hyracotherium*, but there are three features apparent in the manus of UM115547 that are not discussed by either study. Firstly, the proximal surfaces of the

scaphoid, lunar, and cuneiform, for a continuous, weakly convex, linear surface that articulates with the shallow trough of the distal radius and ventral oblong facet of the ulna, completing the hinge-like joint described above. Secondly, the pisiform, which articulates with the cuneiform and the posteroventral facet of the ulna, possesses a relatively long tuber that expands distally. Such a large tuber would have provided an attachment site for a substantial flexor carpi ulnaris tendon. In addition to flexing the manus posteriorly, this tendon could have also been used to store strain energy when stretched by anterior flexion of the manus. Finally, the second metacarpal possesses a third articular facet postero-medially on its proximal end that is not accounted for by articulation with the trapezoid or trapezium. This facet is triangular in shape and is similar to the facet on the fourth metatarsal for articulation with the preserved vestigial fifth metatarsal, suggesting that UM115547 may have possessed a vestigial first digit on its manus.

### **Description of Hindlimb Elements**

#### **Pelvis (Fig. 2.10)**

The shape and proportions of the pelvis of *Hyracotherium* has been described by Kitts (1956) and Hussain (1975), who both paid particular attention to the iliac blade just dorsal to the auricular surface. Both authors discussed how this broad blade would have provided significant leverage for the medial gluteus muscle for extending the hip joint during locomotion. UM115547 exhibits remarkable muscle scarring and tubercles on its pelvis which were not mentioned by either author and merit further study.

In lateral view, the ilium possesses a broad, laterally concave blade just dorsal of the auricular surface and a tapered, cranio-laterally projecting process. The dorsal extremity of the iliac blade widens and shows slight muscle scarring. The cranial process of the ilium possesses a shallow concavity on its anterior-most extremity, likely for attachment of the iliocostalis muscles, and a long, flattened shelf on its ventro-lateral border with slight muscle scarring that runs halfway to the acetabulum, possibly for attachment of hip flexor muscles (e.g. sartorius muscle). The medial surface of the cranial process is concave and faces cranio-medially, providing a large attachment site for longissimus muscles. The ilium also exhibits a large tubercle on its ventro-lateral border adjacent to the acetabulum for attachment of the rectus femoris portion of the quadriceps (knee extension) and a smaller tubercle on its ventro-medial surface adjacent to the pubis for attachment of psoas minor tendon (ventral flexion of the lumbus).

The pubis possesses a well-developed ridge along the anterior border of the pubic symphysis, producing a shallow, ventral concavity just anterior of the obturator foramen for attachment of the adductor longus muscle (hindlimb adduction). This ridge is confluent with a weak muscle scar near the postero-medial edge of the ilium to which the pectineus muscle (hindlimb adduction) may have attached. The ischium possesses a low ischial spine for attachment of the deep gluteus muscle. There is a small notch on the posterior edge of the ischial spine that may have served as attachment site for the coccygeus muscle (see above). The ischial tuberosity bears two obliquely-oriented ridges on its ventral surface: an anterior, weaker ridge for attachment of the quadratus femoris muscle (hip extension) and a stronger posterior ridge for attachment of the semimembranosus muscle (hip extension and knee flexion). The postero-lateral surface

of the ischial tuberosity exhibits substantial muscle-scarring likely for attachment of the semitendinosus muscle (hip extension).

### Femur (Fig. 2.11A)

The tall, medially-inclined greater trochanter of the femur bears extensive muscle scarring on its antero-dorsal surface that begins on the edge of the femoral head and wraps onto the lateral surface of the femur marking a very angular boundary between it and the smoother femoral shaft. The muscle scarring extends distally only to the level of the femoral neck base and extends up and over the prominence of the greater trochanter. In posterior view, muscle scarring is restricted to the trochanter crest that leads from the greater trochanter to the third trochanter. There is a distinctive protuberance distal to the trochanter prominence at the level of the femoral neck. The muscle scarring and protuberance mark the very proximal attachment of the medial and deep gluteus muscles and femoral origination of the quadriceps muscles.

The third trochanter is positioned slightly distal to the distal end of the lesser trochanter and possesses an expanded prominence that is ovoid in shape and projects anteriorly. The ovoid prominence and the trochanter crest proximal to it mark the insertion of the superficial gluteus muscle. Slight muscle scarring is restricted to the posterior portion of the lesser trochanter, likely as an attachment site for the quadratus and adductor muscles.

Distally, the femoral condyles are nearly equal in size and shape, but in posterior view the medial condyle extends farther distally than the lateral condyle. This condition causes the axis of rotation at the knee to be oblique to the long axis of the femur. The

medial rim of the patellar groove is higher and sharper than the lateral rim. In posterior view, the medial surface just proximal of the medial condyle is shallowly concave and bordered by a strong medial supracondylar ridge. There is slight muscle scarring proximal to the lateral condyle in ventral view, but no lateral ridge is present. A large gastrocnemius sesamoid is preserved on the right femur of UM115547 adjacent to the posterior supracondylar concavity.

### Patella

The patella is ovate in overall shape with a flat dorsal surface and a ventral apex. There are two low ridges on the anterior surface that begin medially on the dorsal surface and radiate laterally to small projections on the medial and lateral surfaces. When articulated, the larger lateral projection extends beyond the lateral rim of the patellar groove. In posterior view, the articular surface has a convex, asymmetrical shape, where the area that articulates with the medial rim of the patellar groove is smaller than the area that articulates with the lateral rim.

### Tibia (2.11 B)

The proximal articular surface of the tibia forms a scalene triangular shape in which the lateral articular surface and the shelf-like fibular articulation form the most acute apex. The medial condyle is slightly broader and positioned lower than the lateral condyle. The intercondyloid tubercles are roughly equal in height although Kitts (1956) described the lateral intercondylar tubercle as higher than the medial tubercle. A deep, transverse groove is present on the anterior surface of the proximal tibia that likely served



as the attachment site for a large patellar ligament. The fibular facet is deeply concave, oblong in shape, and has a thickened anterior border with a small bony protuberance.

The anterior tibial crest extends distally 1/3 the length of the tibial shaft and borders a linear concavity on the lateral side of the tibia, which serves as an attachment site for the cranial tibialis muscle (tarsus flexion). The medial surface of the proximal tibia possesses a short longitudinal ridge that extends distally from the surface of the medial condyle for distal insertion of the semimembranosus muscle. The posterior surface of the proximal tibia is deeply concave with sharp medial and lateral border and likely served as attachment sites for digital flexor muscles and the popliteus muscle.

The lateral surface of the distal tibia possesses a rugose, triangular fibular facet with a prominent anterior border. The medial malleolus, the anterior process of the intermediate cochlear ridge, and the posterior border of the medial cochlear groove extend distally to an equal distance. The medial malleolus possesses a large fovea that faces ventro-medially and likely served as an attachment site for the medial collateral ligament.

#### Fibula (2.11 B)

Kitts (1956) described the fibula of *Hyracotherium* as circular in cross-section and possessing slightly convex and concave proximal and distal ends, respectively, contrasting with the much more complex fibular morphology exhibited by UM115547. The proximal fibula is broad and shaped like an asymmetric trapezoid in lateral view, with an acute process projecting posteriorly and a blunter process projecting anteriorly. When articulated with the tibia, the medial surface and posterior process of the proximal

fibula continue the lateral border of the posterior tibial concavity, providing further attachment sites for digital flexor muscles. Likewise, the flattened anterior portion of the proximal fibular shaft and the anterior process of the fibular head continue the lateral border of the linear, lateral concavity of the tibia. There is a small, oblong protuberance on the lateral surface of the proximal fibula, immediately above the point where the proximal fibula narrows into the fibula shaft.

The shaft of the fibula is elliptical in cross-section and forms a half spiral between its proximal and distal ends, such that the broadest face of the shaft is oriented antero-laterally at its proximal end and is oriented postero-laterally at its distal end. This half spiral would have provided a broader area proximally for muscle attachment and greater contact between the tibia and fibula distally to provide greater stability at the ankle. The shaft is significantly medio-laterally compressed immediately above the tibial facet.

The tibial facet of the distal fibula is triangular in shape and possesses a rugose surface that fits tightly to the tibia. The astragalar facet on the distal fibula is oblong and shallowly concave. There is a small facet on the posterior edge of the ventral surface that would have articulated with the calcaneum when the pes was fully extended. The lateral surface possesses a shallow fovea and a small anteriorly-projecting protuberance, which may have both been attachment sites for the lateral collateral ligament of the tarsus.

#### Pes (Fig. 2.12)

The pes of *Hyracotherium* has been described to various extents, especially the astragalus, by several authors (e.g. Kitts, 1956; Radinsky, 1966; Hussain, 1975, Gingerich, 1991; Holbrook, 2001; Froehlich, 2002). The pes of UM115547 is consistent

with previous descriptions and requires no further comment beyond the following exception. The fourth metatarsal possesses a small triangular facet on its proximal plantar border onto which fits a small vestigial fifth metatarsal. The proximal end of the vestigial fifth metatarsal is very rugose, indicating it still participated in muscle and ligament attachment. The shaft of the vestigial metatarsal is reduced to a short point.

## **Discussion**

### Functional interpretation of the limbs

In comparison to phenacodontid condylarths, motion at the elbow, wrist, knee, and ankle in *Hyracotherium* appears to be limited to a particular plane (Radinsky 1966, Thewissen 1990, Rose 1996). Motion is limited to the parasagittal plane at the wrist, knee, and ankle, reducing the muscular force necessary to stabilize the joints during parasagittal movement of the limbs during locomotion. Motion at the elbow is limited to a plane oblique to the parasagittal plane, such that in flexion the manus is oriented in line with the humerus and in extension the manus is oriented closer to the midline. The forelimb is extended during the majority of stance phase of locomotion, in which propulsive forces are generated by the limb, and is flexed during swing phase in both horses (Hildebrand 1959) and dogs (Walter & Carrier 2007, 2009). By bringing the manus closer to the midline during the stance phase, the ground reaction force at the forelimb of *Hyracotherium* is situated closer to the animal's center of mass, minimizing the amount of force applied in the roll plane of the torso and maximizing the force applied to the sagittal plane of the torso.

Contrastingly, the shoulder and hip joints appear to be capable of a wide range of motion in *Hyracotherium* as indicated by the rounded humeral and femoral heads and their corresponding rounded glenoid and acetabular articular surfaces. This morphology contrasts significantly with the morphology of *Equus* and the majority of extant artiodactyls, in which the most convex surfaces of the humeral and femoral heads are oriented antero-posteriorly, constraining motion to the parasagittal plane. Kappelman (1988) demonstrated a significant relationship between femur morphology and habitat in extant bovid artiodactyls in which taxa living in open habitats possessed hemi-cylindrical femoral heads and those living in closed habitats possessed spherical femoral heads, independent of body size. Kappelman (1988) suggested that the more flexible hip joints of closed-habitat taxa are necessary for maneuverability since these taxa must traverse over more complicated and uneven terrain than open-habitat taxa. The environment of the Bighorn Basin during the early Eocene was similar to modern open canopy forests with dense undergrowth, as demonstrated by Secord et al. (2008) using stable isotopic analysis of mammalian dentitions, suggesting that *Hyracotherium* may have also required greater maneuverability at its shoulder and hip joints to navigate through its environment.

Muscle-scarring and the relative sizes of muscle attachment sites on the appendicular skeleton of *Hyracotherium* suggest a greater investment in musculature used for parasagittal flexion and extension in comparison to muscles used for adduction and abduction. On the proximal humerus, muscle attachment sites appear to be restricted to the greater and lesser tubercles mainly for muscles that extend and stabilize the shoulder joint (e.g. the supraspinatus muscle), and no well-developed muscle scars extend onto the humeral shaft. Attachment sites for muscles that rotate and adduct the forelimb

(e.g. infraspinous and subscapularis muscles) are restricted to the proximal extremities of the humerus, allowing maneuverability of the shoulder while shortening their moment arms and reducing the amount of force they can apply to the forelimb.

Muscle attachment sites do, however, extend onto the femoral shaft (i.e. lesser and third trochanters), providing longer moment arms for extensor and flexor muscle. This suggests that the hindlimb was capable of substantial force production. Likewise, the broad distribution of gluteal muscle origination sites on the pelvis and sacrum would have provided sufficient leverage throughout the stance phase for powerful propulsion, such that the medial and deep gluteal muscles would have generated force first during stance phase followed by the superficial gluteus as the femur rotates at the hip, maximizing the length of the superficial gluteus moment arm. The lesser trochanter extends distally a quarter of the femur length, increasing the moment arm for hip adductor muscles. Adduction of the flexible hip joint would abduct the greater trochanter of the femur, increasing the moment arm of the gluteal muscles for hip abduction. The amount of force produced by hip movement outside of the parasagittal plane may have been comparable to forces produced by parasagittal movement in *Hyracotherium*.

The morphology of the distal femur and its associated sesamoid bones suggests that a large component of the hindlimb propulsive force was produced by extension of the knee and ankle. The narrow and deep patellar groove in conjunction with the deep, rugose patella implies that the distal tendon of the quadriceps muscles was relatively large and raised above the distal femur, providing a long moment arm for knee extension. Similarly, the broad, medial supracondylar ridge on the posterior distal femur suggests the presence of a large gastrocnemius muscle, whose moment arm for ankle extension

was improved by the presence of a large gastrocnemius sesamoid. Walter and Carrier (2009) noted that the knee in dogs is flexed during the first strides of maximum acceleration and becomes less flexed once a gallop is attained. A large gastrocnemius sesamoid in *Hyracotherium* would have raised the gastrocnemius muscle above the femoral condyles when the knee is flexed during acceleration, providing a longer moment and increasing the output force produced via ankle extension.

#### The role of the vertebral column during locomotion

The posterior thoracic region and the lumbus are often the most flexible portions of the mammalian vertebral column, especially at the anticlinal thoracic vertebra and the lumbo-sacral articulation (Slijper, 1946; Zhou et al., 1992). In dorsostable mammals (i.e. mammals with limited or no dorso-ventral flexion during locomotion), flexibility of the vertebral column is restricted to one or both of these positions. Kitts (1956) reconstructed *Hyracotherium* as being dorsostable, similar to modern equids, based on fragmentary vertebrae in his sample.

The posterior thorax and lumbus of UM115547, however, appears to be separated into an anterior facultative dorsostable region consisting of T15-L3 and an obligate dorsostable region consisting of L3-S1, although, as discussed above, the L6-L7 and L7-S1 articulations may have been capable of dorso-ventral flexion to some extent. The facultative region is characterized by robust metapophyses, the presence of anapophyses, well-developed muscle scars, broad, cranially-oriented spinous processes, and zygapophyses with cranially and parasagittally-oriented surfaces. The zygapophyses in this region prevented torsion and lateral movement whereas the spinous processes greatly

restricted dorsal flexion, but ventral flexion may have only been constrained by soft tissues. Furthermore, the ventral component to the orientation of the L1-2 transverse processes would advantageously position the iliocostalis muscles to better antagonize ventral flexion of the vertebral column.

The obligately dorsostable region (L3-S1) is characterized by less robust metapophyses, lack of anapophyses, no noticeable muscle scars on the pedicles, more vertically-oriented spinous processes, and embracing zygapophyses. As noted above, the embracing nature of the zygapophyses increases posteriorly within this region. These features suggest an increased importance in bone-facilitated stabilization and a subsequent reduction in the role of soft tissues for overall vertebral column stabilization. The vertical orientation of the spinous processes and the horizontal transverse processes would advantageously position epaxial musculature to stabilize or fix adjacent vertebrae, but would reduce the muscles capability to antagonize ventral flexion (Slijper, 1946).

The presence of these two distinctive vertebral regions may be due to the distribution and orientation of forces generated by the hindlimb during locomotion. Parasagittal movement of the hindlimbs in trotting dogs apply horizontal and vertical torques on the pelvis, which are countered by bilateral action of the epaxial and hypaxial musculature (Fife et al., 2001; Schilling et al., 2009; Schilling and Carrier 2009). Schilling and Carrier (2009) measured epaxial activity at the T13, L3, and L6 vertebral positions in trotting dogs and found that the greatest epaxial activity occurred consistently at L6, the vertebral position nearest the sacro-iliac articulation. Licka et al. (2004) reported that the longissimus musculature is also bilaterally active in extant horses during locomotion, but is more active in the posterior thorax than in the lumbus. The difference

in position of greatest epaxial activity between horses and dogs may be due to the presence of embracing lumbar zygapophyses in horses which help resist torsional forces.

The combination of powerful hip musculature and flexible hip joints in *Hyracotherium* suggests that torque may have been applied to the pelvis in various planes oblique to the vertical and horizontal, requiring complex coordination between hindlimb, hypaxial, and epaxial musculature to prevent dislocation of the pelvis and lumbus. The embracing zygapophyses of L3-S1 would have provided a stiff posterior lumbus, minimizing the efforts of individual epaxial muscles in preventing pelvic torsion and consequently maximizing the energetic efficiency of vertebral stabilization. This hypothesis is supported by the observation that the embracing nature of the zygapophyseal articulations increases posteriorly from L3-S1.

The lack of embracing zygapophyses in the facultative dorsostable region (T15-L3) may be due to a continued need for ventral flexion in addition to reduced participation in countering torque of the pelvis. Walter and Carrier (2009) compared the pitch angle of the vertebral columns between rapidly accelerating and galloping dogs and found a statistically-significant greater absolute pitch angle during acceleration. The authors suggest that the greater pitch angle during acceleration may be necessary to advantageously position ground reaction forces produced by the hindlimb with respect to the animals center of mass. Walter and Carrier (2009) demonstrate that during the first stride of acceleration the pitch angle of the back brings the center of the mass closer to the ground, bringing it in line with the vector of ground reaction force at the hindlimb. This positioning increases the horizontal component of the propulsive force and reduces rotation of the trunk, increasing the overall efficiency of acceleration. It is likely that



maintaining a sagittally flexible posterior thorax/anterior lumbus in *Hyracotherium* would facilitate such dynamic positioning of the center of mass during acceleration (Fig. 2.13).

Figure 2.1 Map of the University of Michigan Museum of Paleontology vertebrate fossil locality SC-16 in the Clarks Fork Basin of northwestern Wyoming. SC-16 lies just below the Wa-1/Wa-2 biozone boundary. The Paleocene/Eocene boundary is indicated by the solid black line. The upper Wyoming state and regional maps were taken from [www.google.maps.com](http://www.google.maps.com) (accessed 10/7/2008). Lower locality map modified from Gingerich and Klitz (1985).



Figure 2.2 *Hyracotherium grangeri* (UM115547) shown post-exhumation and before substantial preparation (right manus and left dentary not shown). Elements of the anterior and posterior portions of the skeleton were preserved in articulation and oriented right-lateral and dorsal side up, respectively. Intermediate trunk vertebrae (T11-16) were disarticulated and preserved in various orientations. The surrounding sediment consists of poorly sorted sandstone that likely represents a near channel depositional environment.

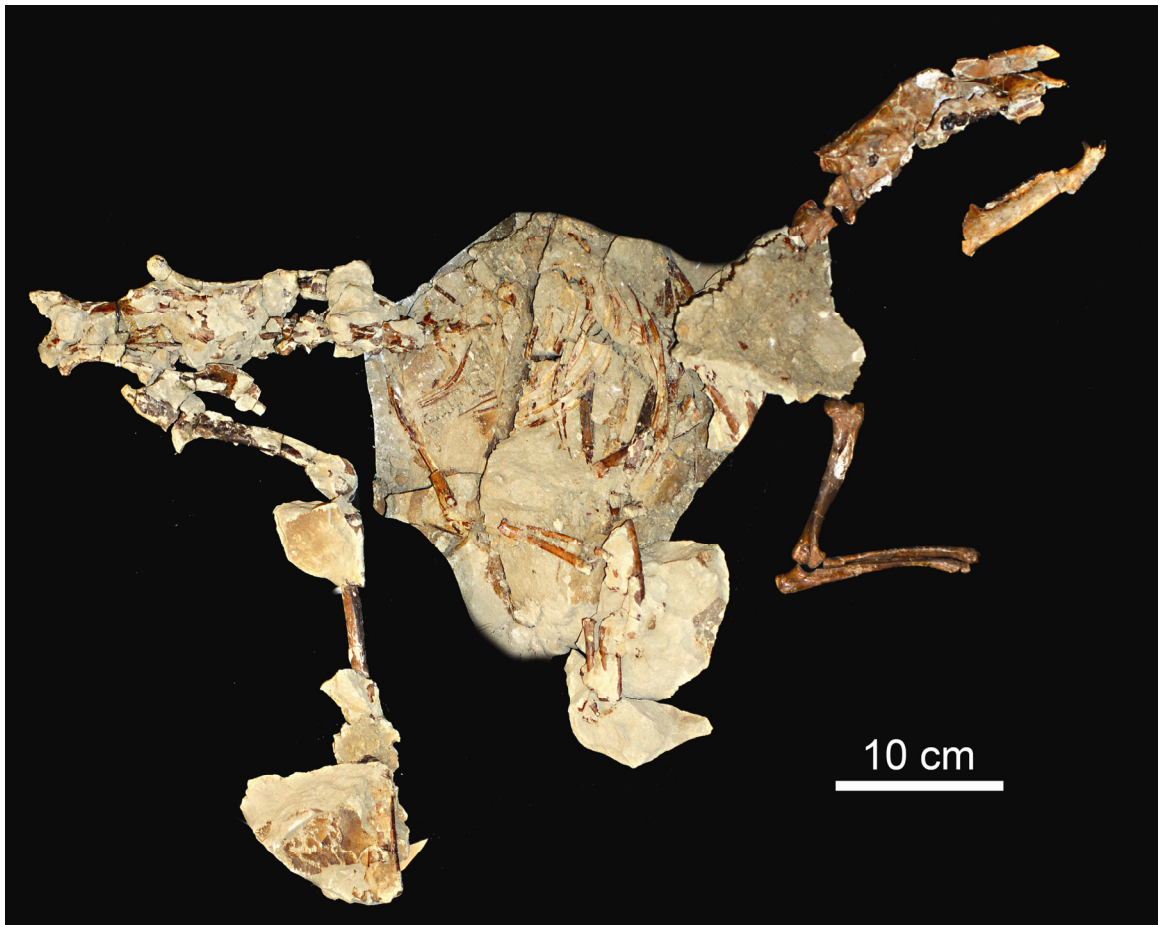


Figure 2.3 Cervical vertebrae of *Hyracotherium grangeri* (UM115547). A) Atlas and axis, cranial view. B) Atlas and axis, caudal view. C) Atlas-sixth cervical vertebra (C6), dorsal view. D) Atlas-sixth cervical vertebra (C6), left-lateral view. E) Atlas-sixth cervical vertebra (C6), ventral view.

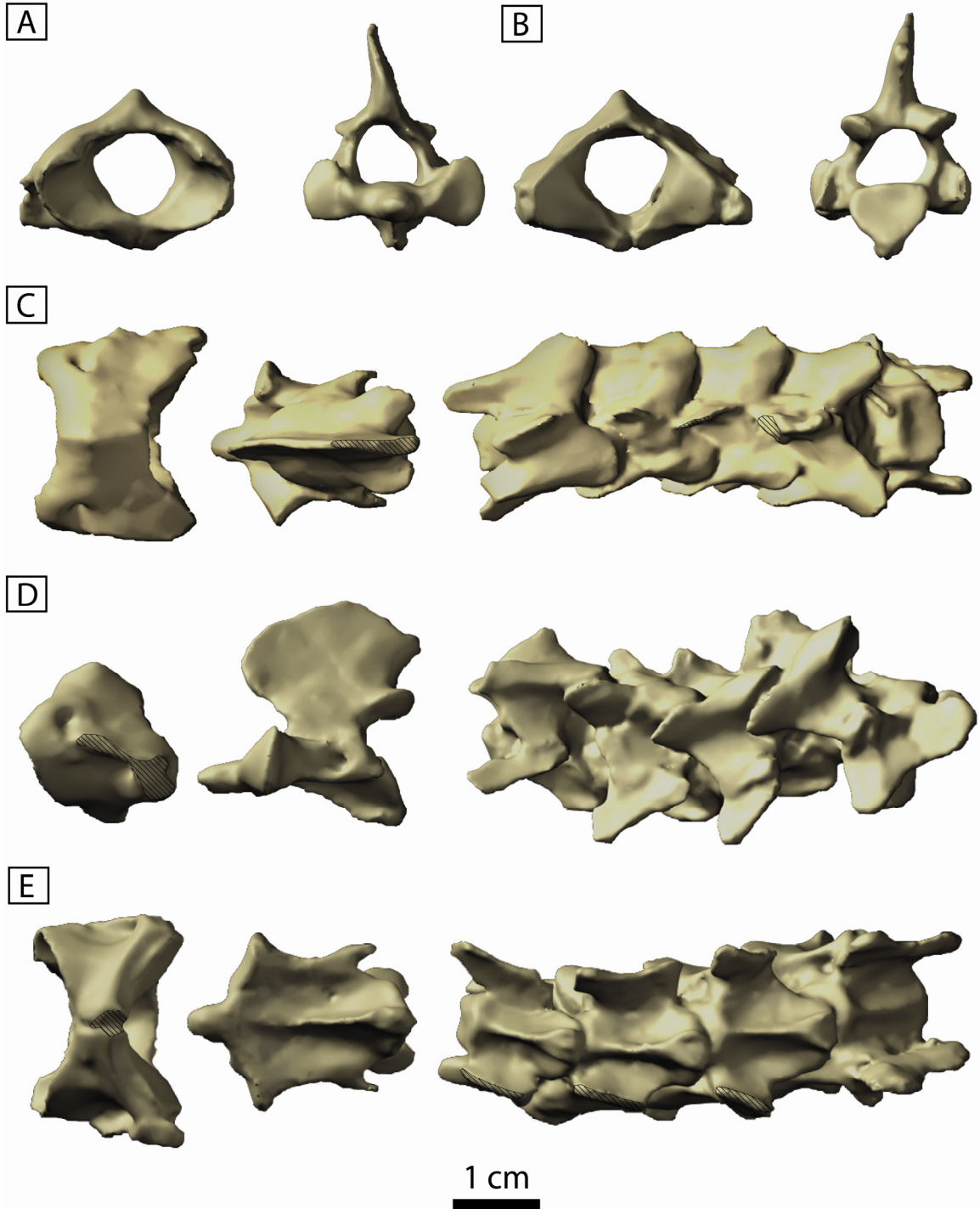
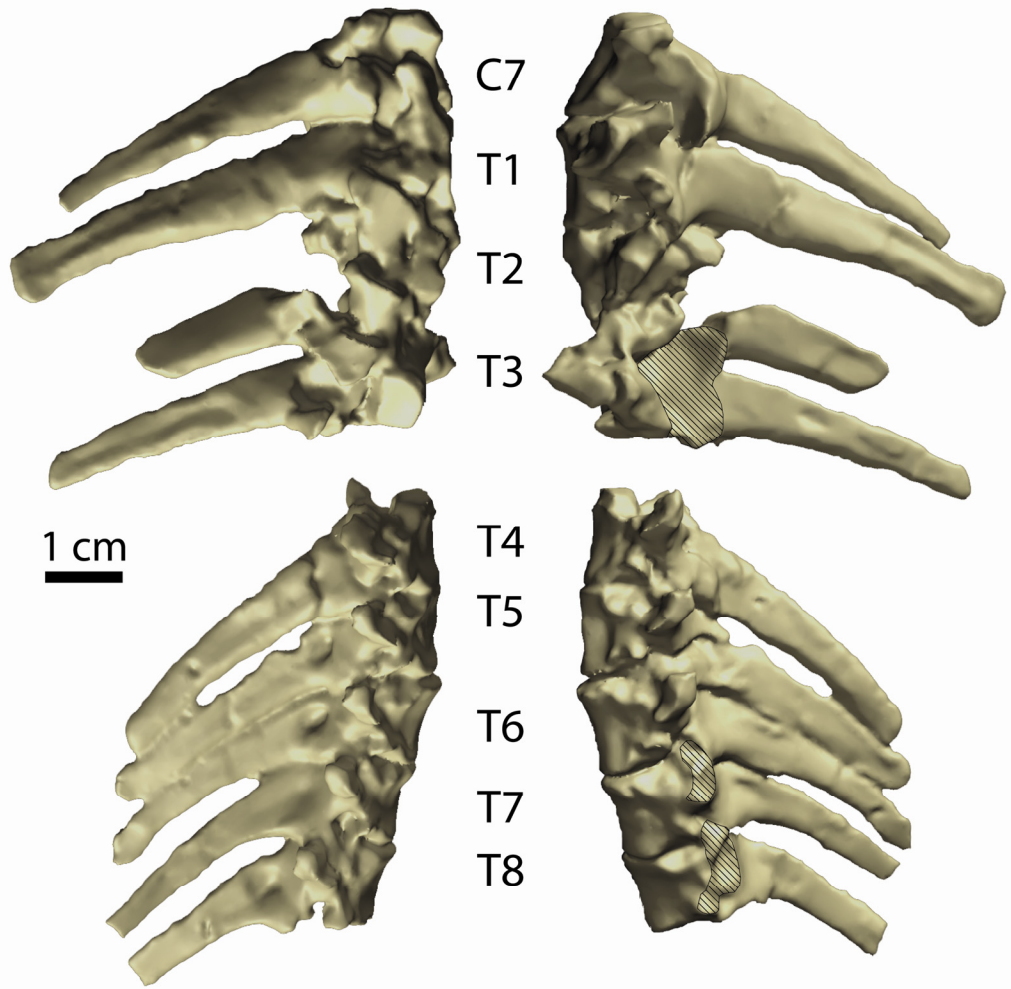


Figure 2.4 Anterior trunk vertebrae and ribs of *Hyracotherium grangeri* (UM115547).  
A) Seventh cervical (C7) – eighth thoracic (T8) in right- and left-lateral view. Note the large glenoid-shaped cavity in T2-3 produced via compaction with the left scapula. B) Representative sample of right ribs in right-lateral view. The second through fifth ribs are markedly broad anteroposteriorly and compressed mediolaterally. When articulated with the vertebrae, these ribs would have produced a shallow concavity on each side of the thorax roughly the size of the scapula.

**A**



**B**

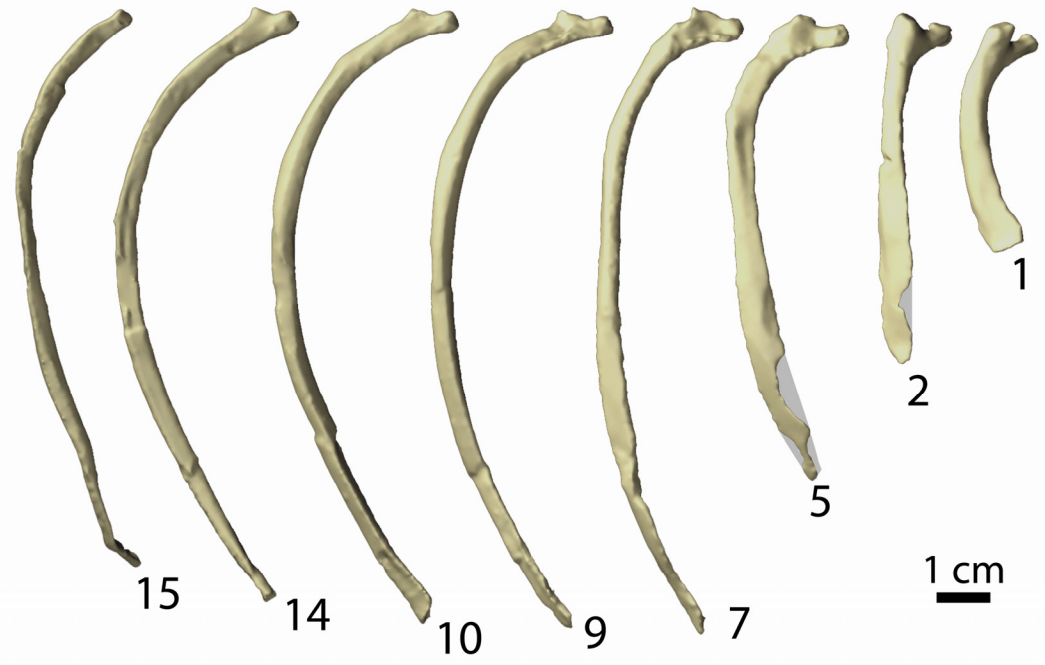


Figure 2.5 Mid-column vertebrae, sacrum, and proximal caudal vertebrae of *Hyracotherium grangeri* (UM115547). A) Ninth thoracic (T9) – first lumbar (L1) vertebrae in right- and left-lateral views. B) Second sacral (S2) – first caudal (Ca1) vertebrae in dorsal, ventral and right-lateral views, respectively. The first and second sacral were not fused in this specimen. C) Second caudal vertebra in dorsal view.

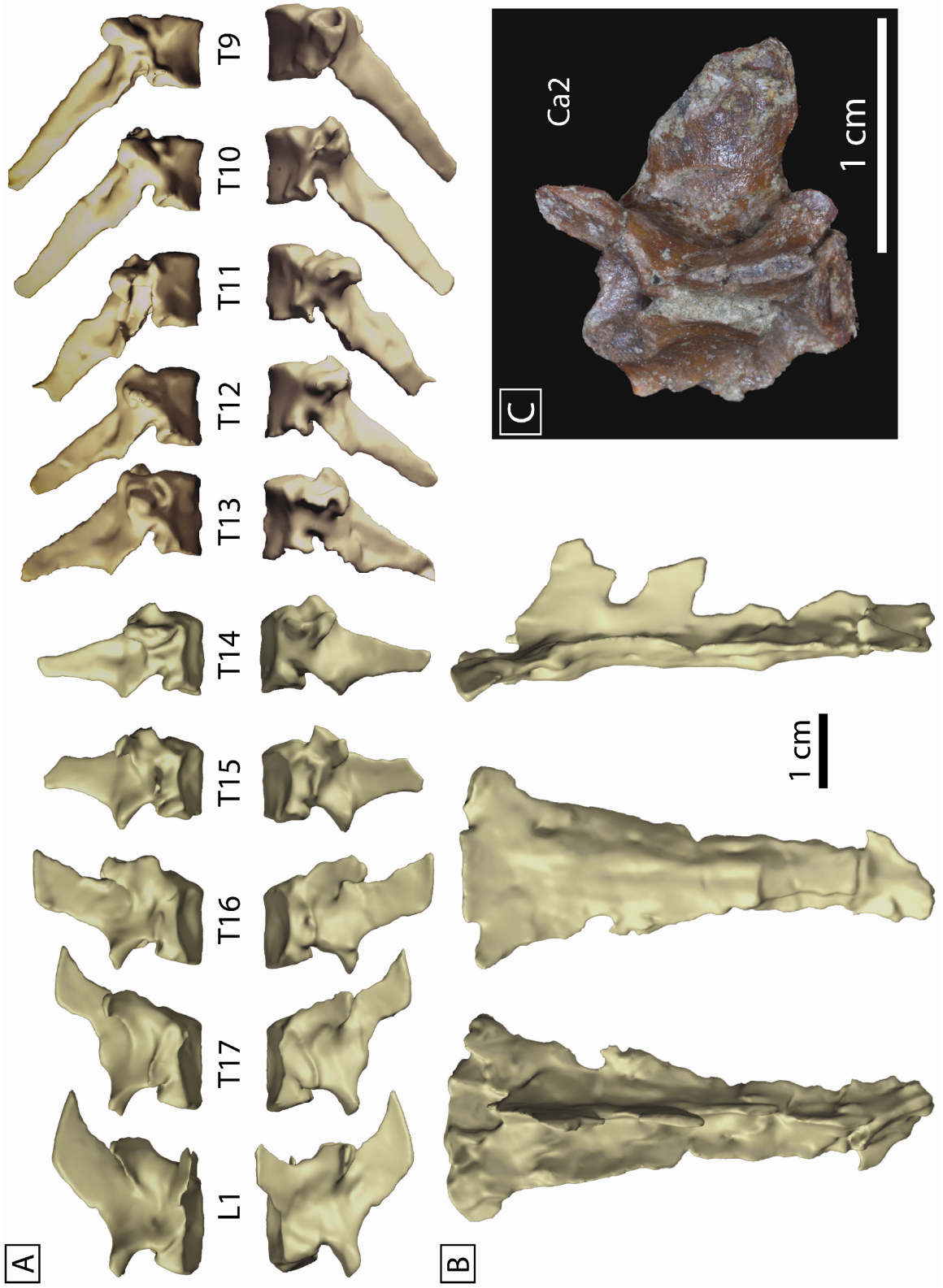


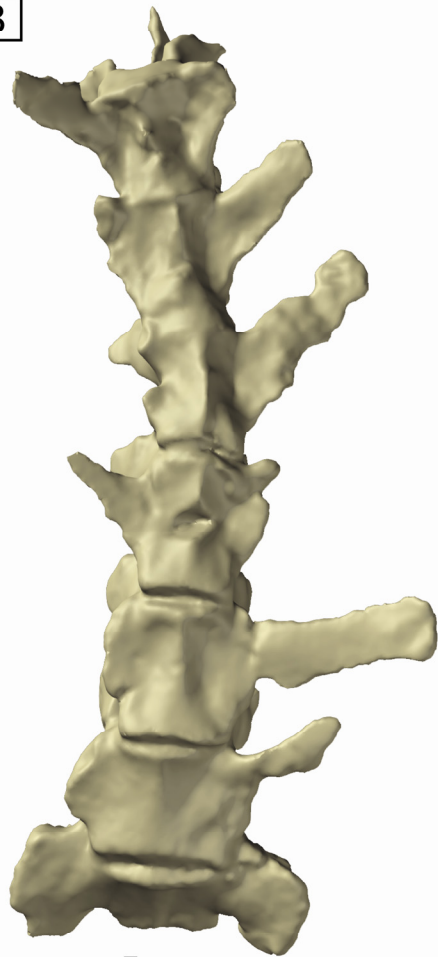


Figure 2.6 Second lumbar (L2) – first sacral (S1) vertebrae of *Hyracotherium grangeri* (UM115547). A) dorsal view, B) ventral view, C) left-lateral view, and D) right-lateral view.

A



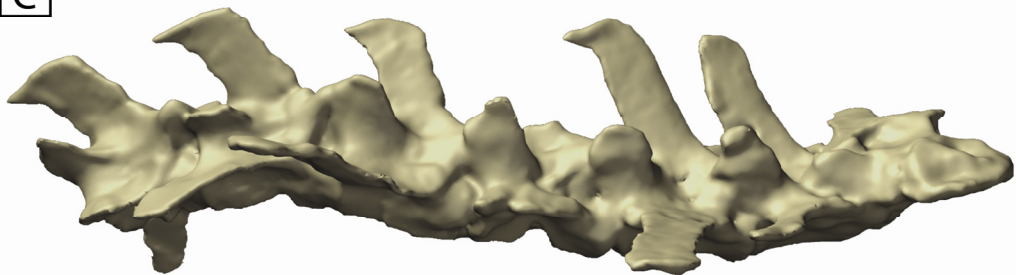
B



5 cm



C



D

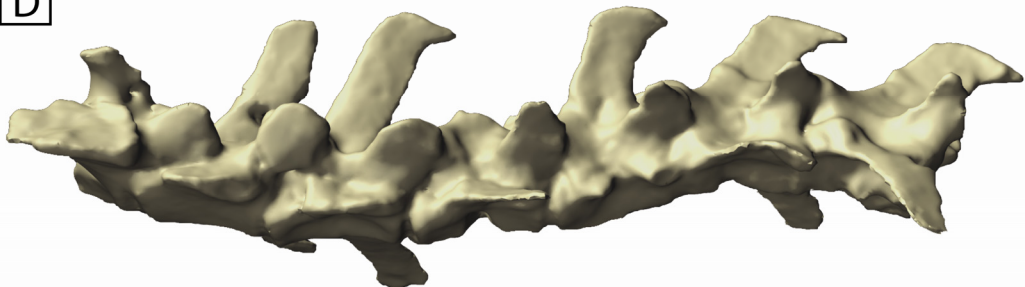


Figure 2.7 Representative  $\mu$ CT slices and surface scans of the lumbus in *Hyracotherium grangeri* (UM115547). Note how the zygapophyses at the L2-3 articulation would prevent torsion without hindering dorso-ventral flexion whereas the interlocking hemi-cylindrical zygapophyses of the remaining articulations (L3-S1) would greatly limit flexibility in the posterior lumbus.

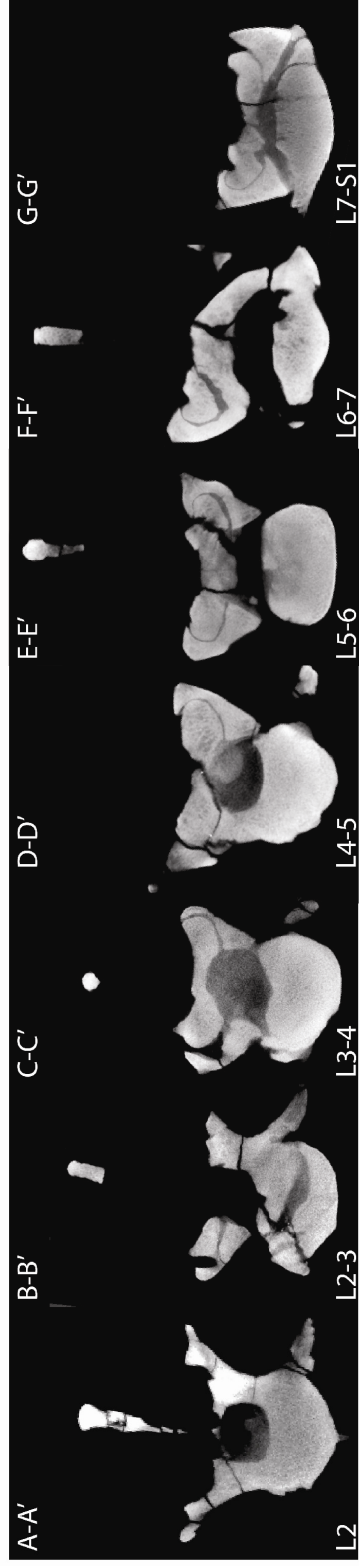
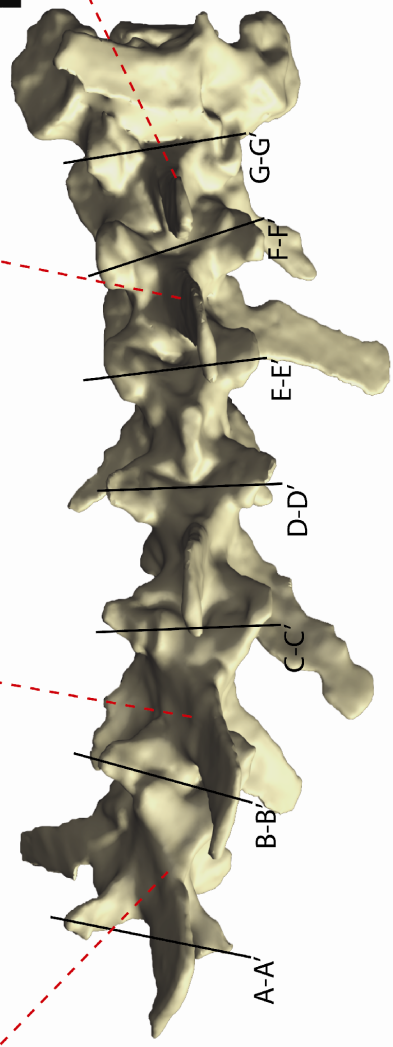
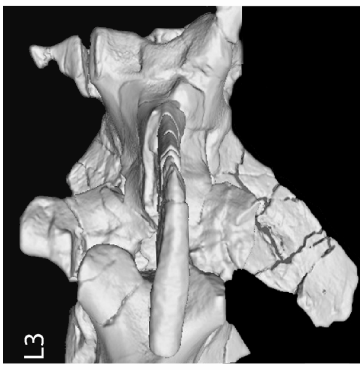
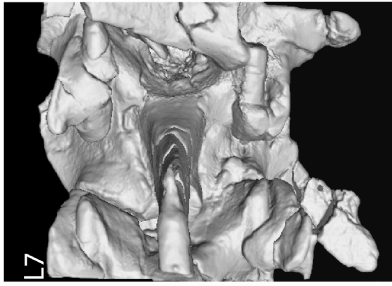
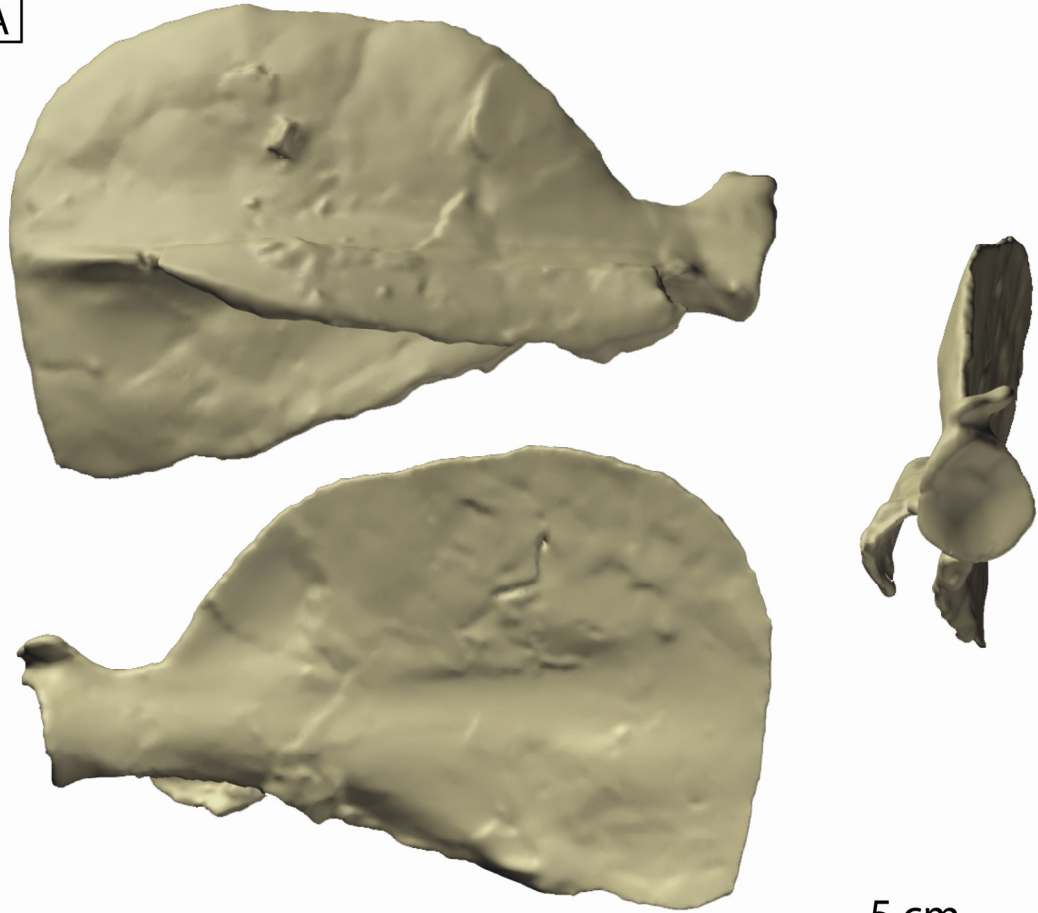


Figure 2.8 Scapula and humerus of *Hyracotherium grangeri* (UM115547). A) Reconstructed right scapula in lateral, medial, and ventral views. Proximal portion of scapular blade reconstructed following Kitts (1956). B) Right humerus in anterior, lateral, posterior, and medial views.

A



5 cm

B



Figure 2.9 Forelimb elements of *Hyracotherium grangeri* (UM115547). A) Right humerus and ulna in dorsal and lateral views. B) Reconstructed right manus in medial, anterior, and lateral views. Note the large pisiform tuber. The second metacarpal bears a triangular facet for articulation with a vestigial first metacarpal.

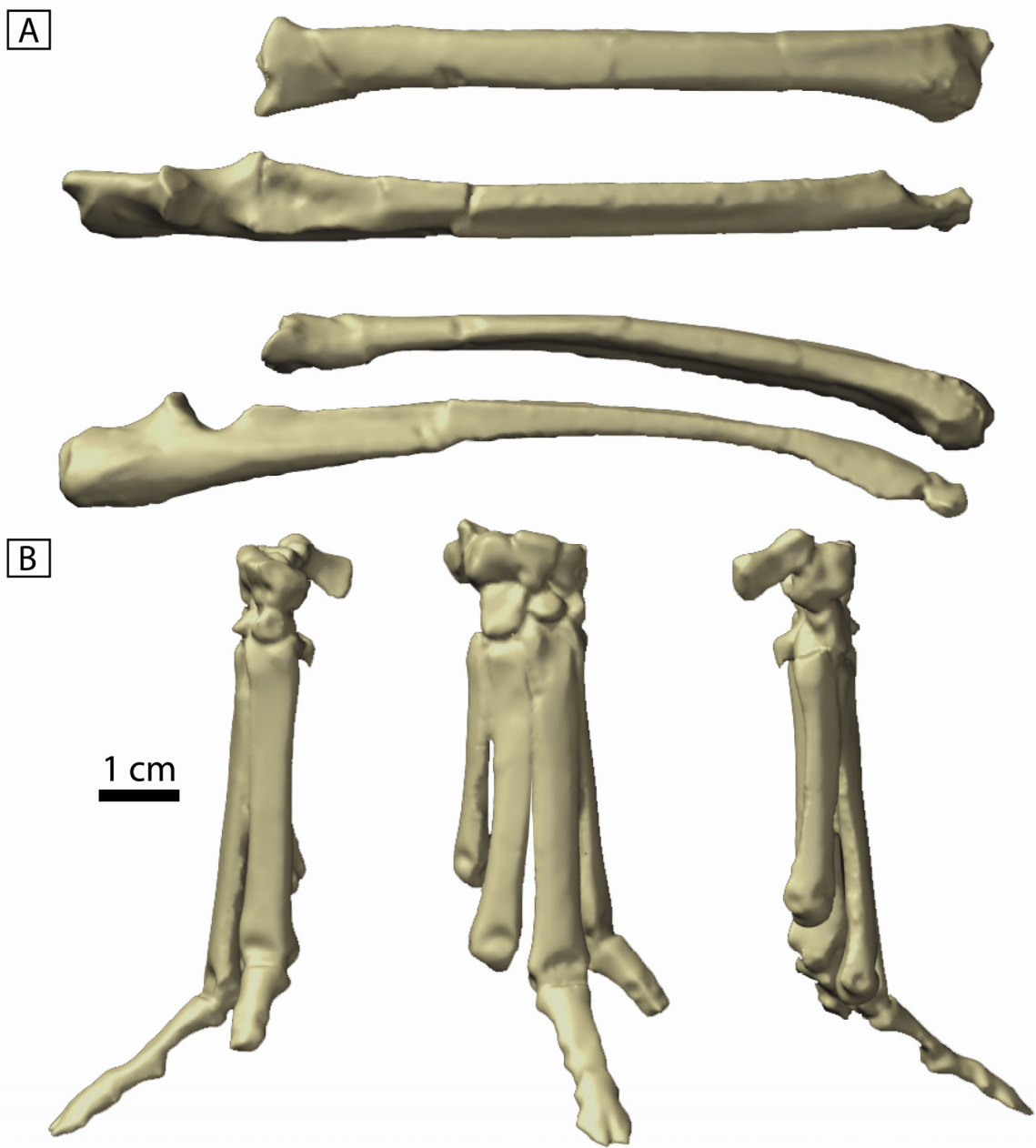


Figure 2.10 Pelvis of *Hyracotherium grangeri* (UM115547). A) dorsal view, B) ventral view, C) right-lateral view, and D) left-lateral view. The acetabulum and ischial tuberosity are better preserved on the left and right sides, respectively. Although the left ilial blade is more complete than the right, it has been plastically deformed by impaction with the sacrum.



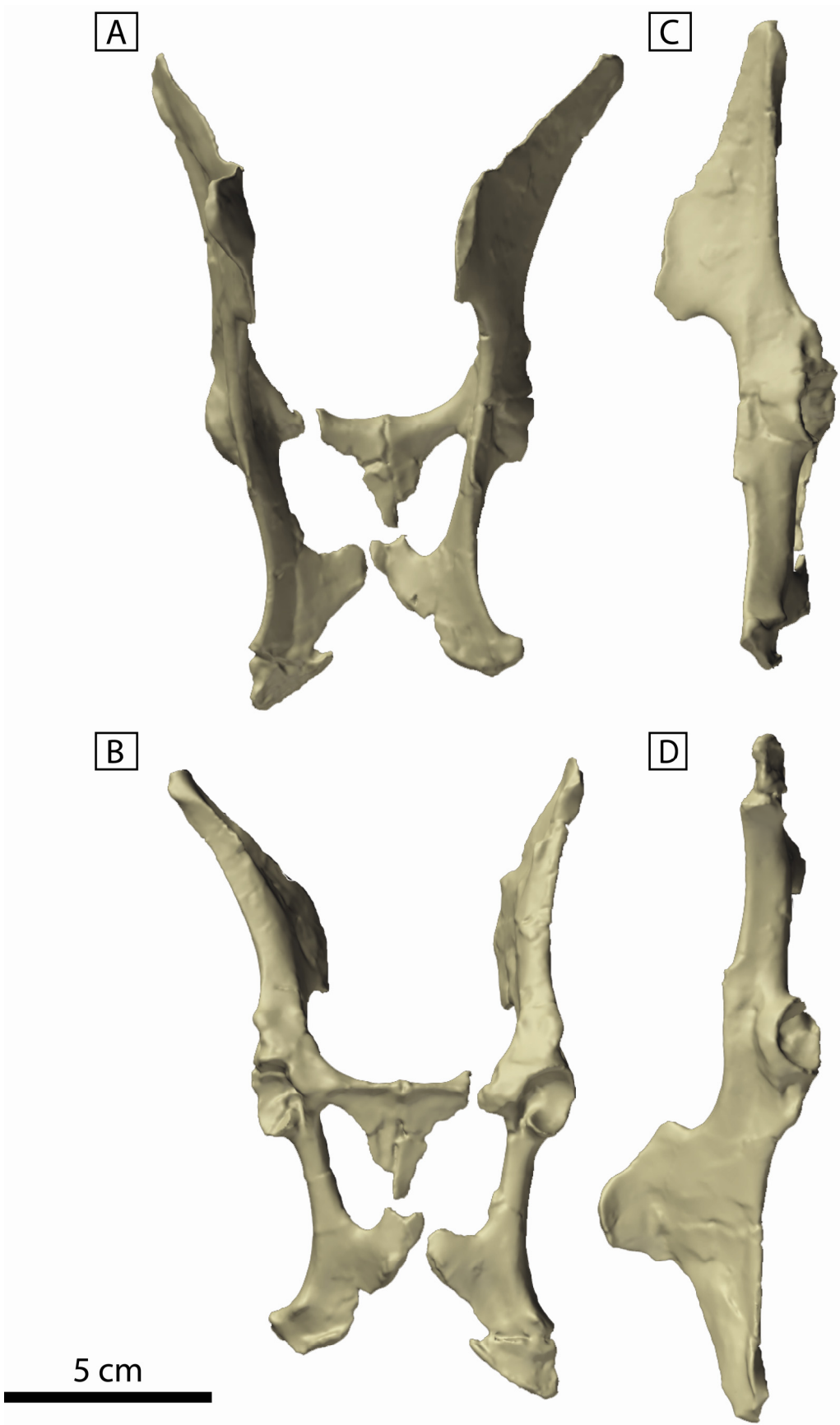


Figure 2.11 Hindlimb elements of *Hyracotherium grangeri* (UM115547). A) Right femur in anterior, lateral, posterior, and medial views, respectively. Note the presence of a large gastrocnemius sesamoid preserved in place above the femoral condyles. B) Right tibia and fibula in anterior, lateral, posterior, dorsal, and ventral views, respectively.

A



5 cm

B

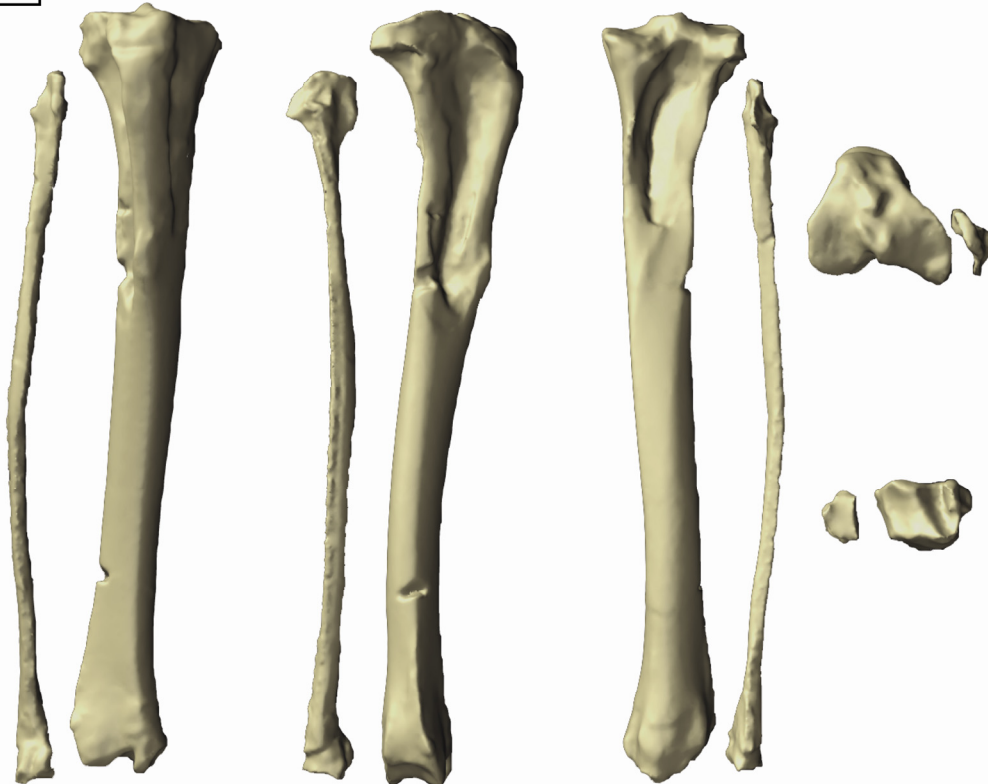


Figure 2.12 Reconstructed right pes of *Hyracotherium grangeri* (UM115547) in medial, anterior, and lateral views. Note the presence of a vestigial fifth metatarsal.

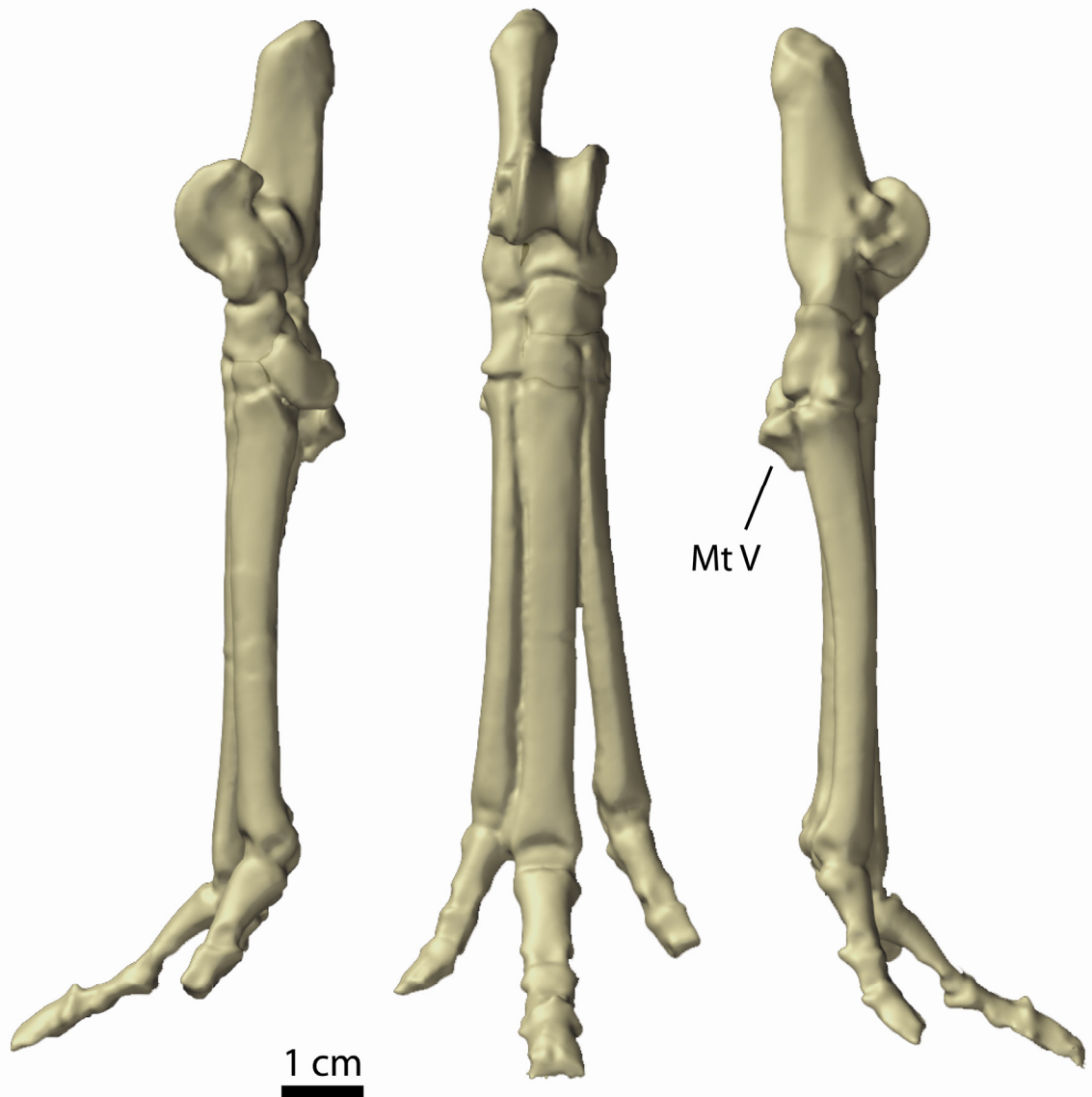
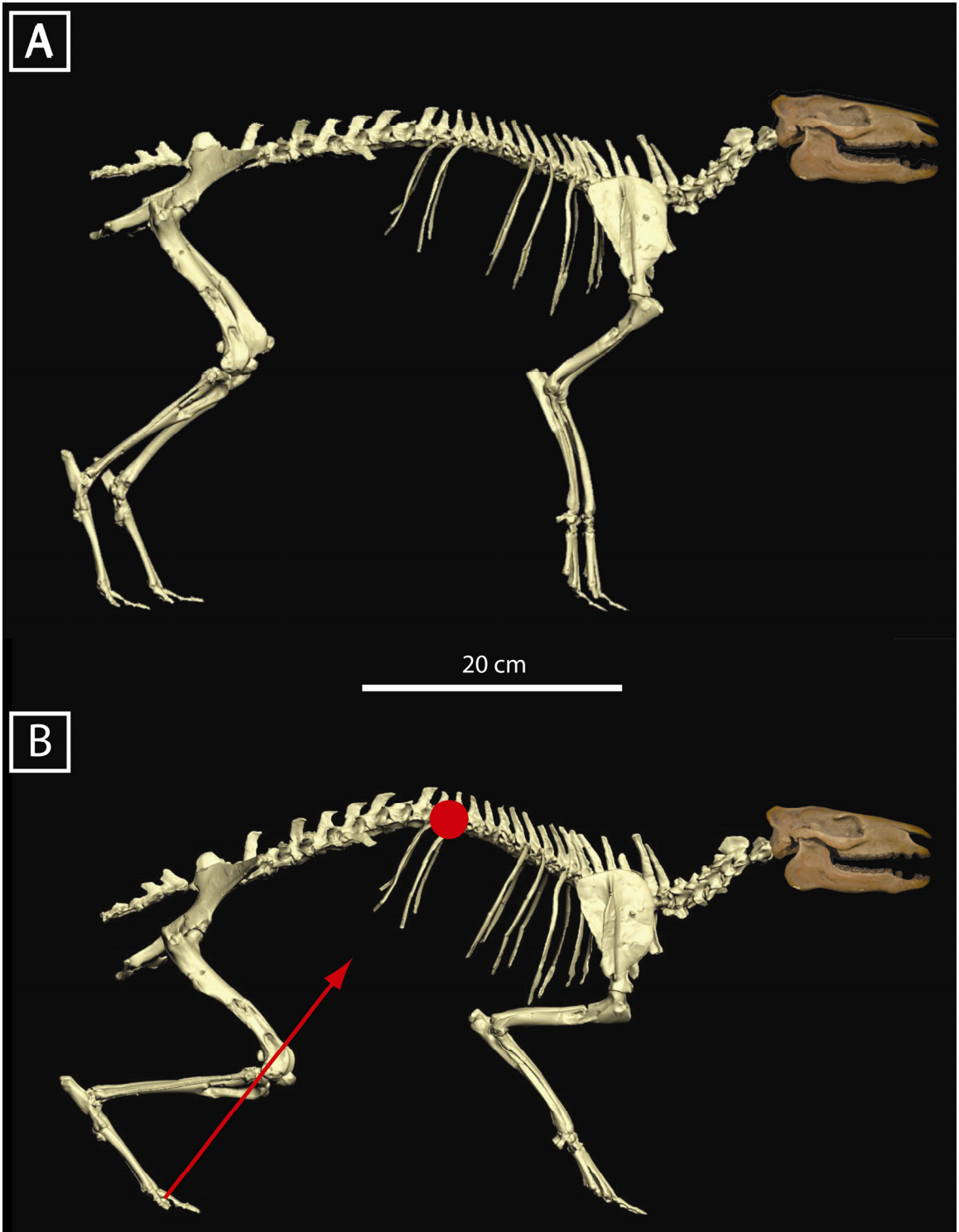


Figure 2.13 Skeletal reconstruction of *Hyracotherium grangeri* (UM115547). A) Neutral stance reconstruction. B) Hypothesized pre-acceleration stance generated by maximally flexing the knee and ankle joints and ventrally flexing the T15-L2 articulations by 2.5°. An angular displacement of 2.5° maximally flexes each vertebral articulation without dislocation (determined via dry articulation). The red arrow represents hypothetical ground reaction force produced by the hindlimb whereas the red circle indicates the hypothetical center of mass of the animal. Ventral flexion of the T15-L2 region would reposition the center of mass to intersect the ground reaction force vector. Skull included in reconstruction is *Hyracotherium venticolum* (Carnegie Museum 2315).



## References

- Budras, K. D. 2009. *Anatomy of the Horse*. Schlutersche, Germany.
- Camp, C. L. and N. Smith. 1942. Phylogeny and functions of the digital ligaments of the horse. *Memoirs of the University of California* 13: 69-124.
- Cope, E. D. 1884. The Vertebrata of the Tertiary formations of the west. Report of the United States Geological Survey of the Territories 3: 1-1009.
- Evans, H. E. 1993. *Millers Anatomy of the Dog*. Saunders, Philadelphia.
- Fife, M. M., C. L. Bailey, D. V. Lee, and D. R. Carrier. 2001. Function of the oblique hypaxial muscles in trotting dogs. *Journal of Experimental Biology* 204: 2371-2381.
- Froehlich, D. J. 1999. Phylogenetic systematic of basal perissodactyls. *Journal of Vertebrate Paleontology* 19: 140-159.
- 2002. Quo vadis eohippus? The systematic and taxonomy of the early Eocene equids (Perissodactyla). *Zoological Journal of the Linnean Society* 134: 141-256.
- Gingerich, P. D. 1981. Variation, sexual dimorphism, and social structure in the early Eocene horse *Hyracotherium* (Mammalia, Perissodactyla). *Paleobiology* 7: 443-455.
- 1991. Systematics and evolution of early Eocene Perissodactyla (Mammalia) in the Clarks Fork Basin, Wyoming. *Contributions from the Museum of Paleontology, University of Michigan* 28: 181-213.
- Gingerich, P. D. and K. Klitz. 1985. Paleocene and early Eocene fossil localities in the Fort Union and Willwood Formations, Clarks Fork Basin, Wyoming. *University of Michigan Museum of Paleontology, Miscellaneous Contributions*, 1 sheet (map).
- Hildebrand, M. 1959. Motions of the running cheetah and horse. *Journal of Mammalogy* 40: 481-495.
- Holbrook, L. T. 2001. Comparative osteology of early Tertiary tapiromorphs (Mammalia, Perissodactyla). *Zoological Journal of the Linnean Society* 132: 1-54.
- Hussain, S. T. 1975. Evolutionary and functional anatomy of the pelvic limb in fossil and recent Equidae (Perissodactyla, Mammalia). *Anatomy, Histology, Embryology* 4: 179-222.

- Kappelman, J. 1988. Morphology and locomotor adaptations of the bovid femur in relation to habitat. *Journal of Morphology* 198: 119-130.
- Kitts, D. B. 1956. American *Hyracotherium* (Perissodactyla, Equidae). *Bulletin of the American Museum of Natural History* 110: 1-60.
- Licka, T. F., C. Peham, and A. Frey. 2004. Electromyographic activity of the longissimus dorsi muscles in horses during trotting on a treadmill. *American Journal of Veterinary Research* 65: 155-158.
- Radinsky, L. 1966. The adaptive radiation of the phenacodontid condylarths and the origin of the Perissodactyla. *Evolution* 20: 408-417.
- 1984. Ontogeny and phylogeny in horse skull evolution: *Evolution* 38: 1-15.
- Rose, K. D. 1996. Skeleton of early Eocene *Homogalax* and the origin of Perissodactyla. *Palaeovertebrata* 25: 243-260.
- Schilling, N. and D. R. Carrier. 2009. Function of the epaxial muscles during trotting. *Journal of Experimental Biology* 212: 1053-1063.
- Schilling, N., T. Fischbein, E. P. Yang, and D. R. Carrier. 2009. Function of the extrinsic hindlimb muscles in trotting dogs. *Journal of Experimental Biology* 212: 1036-1052.
- Secord, R., S. L. Wing, and A. Chew. 2008. Stable isotopes in early Eocene mammals as indicators of forest canopy structure and resource partitioning. *Paleobiology* 34: 282-300.
- Slijper, E. J. 1946. Comparative biologic-anatomical investigations on the vertebral column and spinal musculature of mammals. *Verhandlingen der Koninklijke Nederlandsche Akademie van Wetenschappen, Tweede Sectie* 42: 1-128.
- Thewissen, J. G. M. 1990. Evolution of Paleocene and Eocene Phenacodontidae (Mammalia, Condylarthra). *University of Michigan Papers on Paleontology* 29: 1-107.
- Walter, R. M. and D. R. Carrier. 2007. Ground forces applied by galloping dogs. *Journal of Experimental Biology* 210: 208-216.
- 2009. Rapid acceleration in dogs: Ground forces and body posture dynamics. *Journal of Experimental Biology* 212: 1930-1939.
- Zhou, X., W. J. Sanders, and P. D. Gingerich. 1992. Functional and behavioral implications of the vertebral structure in *Pachyaena ossifraga* (Mammalia,



Mesonychia). Contributions from the Museum of Paleontology, University of Michigan 28: 289-319.

## **Chapter 3**

### **The Effects of Dental Wear on Tests of Evolutionary Dynamics**

Dental wear, the attrition and abrasion of dental surfaces, simultaneously complicates and enhances opportunities to understand the paleobiology of fossil mammals. Worn dental surfaces are the result of dental function, development, ecology, and phenotypic evolution, and understanding this system of relationships requires disentangling one aspect from the others. Using a mathematical analogy, observed dental morphology with any amount of wear is a function of selective pressures, developmental constraints, ecological parameters, phylogenetic history, and usage by the animal. Studying the individual effects of any one of these variables on overall dental morphology requires holding the remaining variables constant or minimizing their contribution to the overall morphological variation. This is often accomplished by sampling specific subsets of the total available material in which specimens vary little in the factors that are not of interest, which often limits the resolution of the study. The purpose of this chapter is to present a quantitative methodology for mitigating the effects of dental wear on dental shape in order to better resolve patterns in the evolution of shape using the total available sample of fossil material.

Teeth have the greatest preservation potential in the mammalian fossil record and are the most information-dense element of a typical mammal's body, containing information about overall body size, dietary preferences, and phylogenetic history. Not surprisingly, many studies have used dental morphologies to examine mammalian evolutionary biology, including tempo and mode of evolutionary change in mammalian lineages (e.g. Gingerich and Gunnell, 1995; Polly, 2002; Wood et al., 2007), time-dependent environmental and climatic selective pressures mammals experienced over geologic time (e.g. Gingerich, 2003; Piras et al., 2009), the morphological diversification of mammalian clades with time (e.g. Wesley-Hunt, 2005), and the role development plays in constraining or facilitating evolutionary change (e.g. Polly, 1998; Jernvall et al., 2000; Salazar-Ciudad and Jernvall, 2002). Each of these types of studies requires observations of dental morphology at a consistent level of wear. Otherwise, one risks inflating the variance of the dental morphology under study or obscuring the signal of interest by superimposing various levels of other signals.

Studying both size and shape is necessary for fully understanding the evolution of mammalian dental morphology, but size and shape possess differential susceptibilities to the effects of dental wear. Certain measures of dental size are relatively unaffected by dental wear (e.g. crown area), yet these metrics provide a limited view of the selective pressures experienced by taxa. Dental shape, on the other hand, is more closely tied to dental functional morphology and the maintenance of precise occlusion, but as dental material is removed via attrition and abrasion, dental shape is likely to change substantially throughout the life of an individual. These differential susceptibilities to dental wear can lead to highly disparate sample sizes between time series of dental size

and time series of dental shape, despite the fact these time series are derived from the same taxon and the same individuals.

Previous studies incorporating macroscopic dental wear and dental shape have focused on using wear to estimate age of fossil individuals (e.g. Scott, 1979; Roth and Shoshani, 1988; Muhlbachler, 2003; etc), to determine dietary preferences of fossil taxa (e.g. Fortelius and Solounias, 2000; Kaiser and Solounias, 2003; etc), or to better understand the mechanisms of mastication (e.g. Rensberger, 1986; Popowics and Fortelius, 1997; Evans et al., 2005; etc). None of these studies, however, have documented the continuum of shape change with increasing wear within a population or investigated how shape change with wear itself changes with time in a mammalian lineage. Hypsodont (high-crowned) molars with highly enfolded enamel experience extensive wear, yet their occlusal shapes remain largely unaffected (Fortelius and Solounias, 2000). On the other hand, brachyodont (low-crowned) dentitions exhibit substantial shape differences with wear, as documented by studies using categorical wear classes (e.g. Hillson, 1990; Ungar and Williamson, 2000; etc), but the progression of dental shape change with wear and the distribution of shape change with wear along the tooth row and among cusps and crests of individual teeth can be best understood with the use of a continuous measure of dental wear.

The goal of this chapter is to produce a continuous, quantitative index of dental wear for a lineage of fossil mammals with which to 1) study the biases imposed by sampling worn dentitions on documenting evolutionary patterns in dental morphology and 2) predict dental morphologies at any level of dental wear. Geometric morphometric data, in addition to standard size measures, from an early Eocene *Hyracotherium* lineage

are used to create simulations of evolutionary change which are subsequently subjected to variants of conventional statistical tests of evolutionary mode. All simulated morphological time series are based upon empirical observations to reduce the probability of producing biologically unrealistic simulations. The effects of sampling worn dental morphologies is determined by documenting how the individual tests statistics change as the maximum amount of dental wear sampled increases. Although the predicted *Hyracotherium* dental shapes were used in this chapter solely to design the simulated morphological time series, these methods will be used in the following chapter to investigate the actual evolutionary and ecological patterns exhibited by the Bighorn Basin *Hyracotherium* lineage.

The following methods are somewhat labor-intensive so the results of this chapter are used to devise practical guidelines for future research. Specifically, the results are used to determine the highest level of dental wear from which one can sample and still consistently and accurately detect the actual evolutionary signal. The results of this project are also used to investigate the sensitivities of the four statistical tests to complications imposed by dental wear and other possible sources of bias. Sheets and Mitchell (2001) noted that conventional univariate tests of evolutionary dynamics produce asymmetric results, disproportionately detecting evolutionary stasis over directional trends. The progression of shape change with wear and the concurrent change in shape variance are used below to explain why such asymmetry also occurs in multivariate tests of evolutionary dynamics.

## Methods

### Data collection (Step 1, Fig. 3.1)

Isolated teeth and dentary fragments bearing p4, m1, m2, and/or m3 tooth positions were selected from the Sand Coulee (SC) vertebrate fossil locality series collection at the University of Michigan Museum of Paleontology. This resulted in sample sizes of 147, 239, 286, and 294 for the respective tooth positions. Only lower dentitions were used here and in the following chapter because of the greater abundance of lower teeth in the Bighorn Basin collection and the fact that lower teeth are found intact within dentary fragments more often than upper teeth are found intact within maxillary fragments. The latter observation allows more teeth to be attributed to particular individuals with greater certainty.

Each tooth or jaw fragment was molded and cast in gray epoxy to provide a uniform color and to minimize digitizing error due to color heterogeneity. Each tooth was then photographed in occlusal, buccal, and lingual view using the following standardized orientation protocol: Each cast was affixed to a rectangular wooden block using plasticine clay and oriented with the occlusal surface facing the camera. The cast was then positioned such that 1) the metaconid and protoconid were equidistant from the tooth margin, 2) all portions of the buccal cingulid remained in the same focal plane, and 3) the long axis of the tooth was parallel to the long axis of the wooden block. In order to photograph buccal and lingual views, the rectangular wooden block was rotated 90° onto either the buccal- or lingual-facing side, providing a view 90° to the orientation used in the occlusal view. All right teeth were digitally reflected and analyzed as left teeth.

A combination of landmarks and semi-landmarks was digitized in all three views to produce coordinates for shape analysis and size measurements of various aspects of the dental morphology (Fig. 3.2). All landmarks and semi-landmarks were Procrustes superimposed to eliminate variation due to position, scale, and rotation for analysis of dental shape. Unlike landmarks, semi-landmarks are not discrete, homologous anatomical loci and are, instead, uniformly spaced points along curves or outlines of the morphology under study. Since the spacing of semi-landmarks is arbitrary, superimposition requires an additional alignment step to remove the variation in semi-landmarks due to position along the curve. The perpendicular sliding alignment method was used here. In this method, the curve of interest is modeled based on the mean shape, and the tangent of the curve at each semi-landmark is estimated. Each semi-landmark is then slid toward the normal of its respective tangent until the overall difference from the mean shape is minimized (Zelditch et al., 2004). Semi-landmark and procrustes superimposition were performed using SemiLand6 (Sheets, 2003).

In occlusal view, 20 semi-landmarks were digitized along the tooth margin using a circular fan with 20 evenly-spaced rays, positioned in the center of each tooth. The center of each tooth was found by calculating the centroid position between the metaconid, protoconid, entoconid, and hypoconid. On worn teeth with exposed dentin at the four cusps, the position of the cusp was defined as the center of the subcircular exposure of dentin. Calculation of the centroid position and application of the radial fan was performed using MakeFan (Sheets, 2005). Since the center of exposed dentin at each cusp position is not homologous to the original cusp tips, these 4 points cannot be used in shape analysis, leaving 20 semi-landmarks that can only be used to measure size

variables that are relatively unaffected by dental wear. It should also be noted that assuming the centers of exposed dentin represent the original position of the cusp tips adds a level of error to the centroid position calculation, which affects the spacing of semi-landmarks digitized and consequently the position at which size measurements were taken.

In buccal and lingual view, 5 landmarks/40 semi-landmarks and 4 landmarks/40 semi-landmarks were digitized, respectively (Fig. 3.2). The buccal landmarks consist of 1) the intersection of the cingulid and anterior edge of the trigonid, 2) the intersection of the cingulid and posterior edge of the hypoconid, and 3-5) highest point associated with the protoconid, hypoconid, and hypoconulid, respectively. The lingual landmarks consist of 1) the intersection of the cingulid and anterior edge of the metaconid, 2) the intersection of the cingulid and the posterior edge of the entoconid, and 3-4) the highest points associated with the metaconid and entoconid. Since buccal landmarks 3-5 and lingual landmarks 3-4 are not homologous points among individuals, these landmarks were used only to measure univariate variables (e.g. cusp heights) and not incorporated into the shape analysis. Forty semi-landmarks were used to model the buccal or lingual outlines during semi-landmark alignment, but 22 of these semi-landmarks were removed after superimposition, resulting in 2 landmarks/18 semi-landmarks and 2 landmarks/18 semi-landmarks in the analysis of buccal and lingual shape, respectively.

Fig. 3.2 shows the size measurements from the three views. All size measurements were derived from digitized photographs with a digitized scale. Linear measurements were taken as the distance between relevant, digitized points in TMorphGen (Sheets, 2000). Area of exposed dentin in occlusal view was estimated in



TPSdig2 (Rohlf, 1996) based on a closed, digitized outline of the exposure using the following equation:

$$Area = abs \left[ \sum_i^{n+1} (x_{i+1} - x_i) \times \frac{1}{2} (y_{i+1} + y_i) \right]$$

where n = number of points in outline;  $(x_i, y_i)$  = coordinates of point i.

Each digitized outline of exposed dentin was iteratively resampled, increasing the density of points, and adjusted to better fit the shape of the exposure until the area estimate was stable at the second decimal place. Total crown area was calculated using the length and width of each tooth in occlusal view in order to better make comparisons with previously published data. The line connecting landmarks 1 and 2 in each view was used as a baseline for measuring cusp heights (Fig. 3.2). All size measurements were log transformed before analysis.

#### Dental wear index calculation (Step 2, Fig. 3.1)

The trajectory of dental shape change with increasing dental wear can best be investigated using multivariate regression, which requires a continuous independent variable of dental wear. The area of exposed dentin is a continuous measure of dental wear but not all worn teeth exhibit exposed dentin on their crowns—well-developed wear facets in the enamel surface can be present without exposed dentin. In order to produce a wear index that includes all worn teeth, an exhaustive search was conducted for the linear combination of univariate measurements that best predicts the area of exposed dentin. That index can then be applied to worn teeth lacking exposed dentin.

A search program was written in the R statistical computing package (<http://www.r-project.org/>) that performs a principal components analysis (PCA) of all possible combinations of univariate measurements and regresses the area of exposed dentin onto scores associated with the first principal component (PC1). The program operates using the following steps, which will be explained in greater detail below: 1) Calculate individual deviations from the expected value based on overall size for each explanatory linear measurement (i.e. regression residuals), 2) produce all possible combinations of explanatory variables, 3) perform a PCA on each combination and generate PC1 scores, 4) linearly regress exposed dentin area onto each set of PC1 scores, and 5) record the five combinations of measurements whose PC1 scores produce the highest  $R^2$  values. The search program was used to produce a wear index for each individual tooth position in addition to an overall wear index that can be applied to all four positions in order to facilitate comparisons between the p4, m1, m2, and m3 positions.

Size measurements used in the search were taken only from the subset of teeth that exhibited exposed dentin (Fig. 3.2). Variation in each measurement is partially dependent on the amount of dental wear experienced by a given tooth. For example, cusp and cristid height should decrease as wear increases, and ratios of corresponding buccal and lingual cusp heights (e.g. protoconid/metaconid ratio) are also expected to decrease with wear since the buccal side of each *Hyracotherium* tooth possesses more wear facets than the lingual side (Radinsky, 1969). The centroid size of the buccal and lingual outlines should also decrease with dental wear, because the landmarks and semi-

landmarks measured along the outlines approach a minimum distance from their centroid position as each outline is flattened with increasing wear.

None of these measurements, however, are independent of each other, preventing the use of multiple regression to find the suite of explanatory variables that best predicts exposed dentin area. PCA is useful in this case, because it produces linear combinations of the original variables to explain patterns of covariance within the data. Each linear combination explains an independent axis of variance within the data, and the position of each individual on the new axis is called its score, the vector product of the individual's original variable values and the loadings of the original variables on the new PC axis. Exposed dentin area was regressed on the scores associated with the first principal component (PC1), or the linear combination that explains the largest axis of variation, in the search program. Each PCA was performed on the correlation matrix because of the heterogeneous measurement scales of the variables.

Variation in the explanatory variables due to overall size of the individual was removed by regression; more specifically, each log-transformed linear measurement from buccal and lingual views was regressed onto tooth length, and the residuals from the regression, i.e., the deviations from the expected value, were used as the data in each PCA as well as for calculating protoconid/metaconid and hypoconid/entoconid ratios. Likewise, exposed dentin areas were regressed onto total crown area to remove variation due to tooth size. The square root of the exposed dentin area residuals was used as the dependent variable in the final regression of the search program to maintain equal dimensionality between the dependent and independent variables (PC1 scores).

Regression diagnostics were performed on the resultant top five regression models to check for normality of the residuals and to identify influential points, if any. A combination of the Shapiro-Wilk test and Q-Q plots was used to detect non-normally distributed residuals, and influential points were detected using half-normal plots of the Cook's Distance statistic (Faraway, 2005). If influential points were detected via the half-normal plots for any regression model, that individual tooth was removed from the data, and the search program was ran again. If the ranking of the top five regression models did not change substantially, the model with the highest  $R^2$  value was chosen as the wear index for the given tooth position or overall index.

The above methods were used to calculate wear indices specific to particular teeth, but the analyses and simulations herein are based on the overall dental wear index. The search program calculated the overall wear index using a combination of measurements from all p4, m1, m2, and m3 teeth with exposed dentin. The use of the overall wear index allows the results and conclusions of this chapter to be applied to the other tooth positions in the following chapter. The position-specific wear indices and their implications will also be discussed in the following chapter.

Shape regression on wear index values (Step 3, Fig. 3.1)

Both the variation in dental shape explained by wear and the trajectory of dental shape change due to increasing wear can be determined via multivariate regression of the shape data onto the continuous wear index. Shape regression produces a vector of slope coefficients and a vector of intercept coefficients that enables predictions of the expected shape at any value of the independent variable (Zelditch et al., 2004). In the case of

dental wear shape, the coefficient vectors can be used to generate an expected worn dental morphology at a given level of wear, and all predicted shapes taken together represent the progression or trajectory of shape change with wear. The regression residuals, or deviations from an expected worn shape, represent individual deviations from the average trajectory of dental shape change with wear, which is most likely the result of intraspecific variation in the unworn dental phenotype in addition to wear events unique to the individual (e.g. cusp breakage, atypical occlusion, etc). It is assumed here that intraspecific variation in the unworn morphology explains the greater proportion of each individual's deviation from the morphology expected from the regression function. Thus, the unworn phenotype for an individual can be reconstructed by calculating the morphology expected at the lowest wear value and adding the individual's residual vector.

Procrustes superimposed shape coordinates were converted to partial warp and uniform scores prior to regression to avoid complications with regression statistics due to incorrect degrees of freedom. Specifically, Procrustes superimposed data has  $2K$  dimensions, where  $K$  equals the number of landmarks, but only  $2K-4$  degrees of freedom. Partial warp scores, on the other hand, have degrees of freedom equal to the number of partial warps, which is ideal for conventional statistics. Partial warps are calculated by eigenanalysis of the bending energy matrix, a matrix used to compute the minimal bending energy required to deform a reference shape into an observed shape via the thin-plate spline (Slice et al., 1996; Zelditch et al., 2004). Partial warps represent local, non-uniform shape changes relative to a reference shape, and in this case, the reference shape is the mean shape of the data. The uniform component of shape change expresses the global affine shape change (compression/dilation and shear) and affects the position of all

landmarks and semi-landmarks in the reference shape (Rohlf and Bookstein, 2003; Zelditch et al., 2004).

In the multivariate shape regression, each individual tooth is represented by a vector of partial warp and uniform scores, and each partial warp or uniform component is linearly regressed onto the independent variable (i.e. the wear index). This results in vectors of slope coefficients and intercept coefficients equal in length to the number of partial warps and uniform components. A vector of residuals is also produced for each individual in the data set, which is again equal in length to the number of partial warps and uniform components (Zelditch et al., 2004). The regression coefficient vectors and regression residuals enable predictions of the dental shape at any value of the wear index. The ability to predict an individual's shape at any value of the wear index is valuable in two ways: 1) The effects of dental wear can be removed by predicting each individual's shape at the lowest wear value, removing variation that may obscure evolutionary patterns in the dental phenotype, and 2) Artificially varying the amount of dental wear and the amount of shape change due to dental wear provides a means for understanding how dental wear obscures evolutionary patterns in the dental phenotype. Initial multivariate shape regressions on the dental wear indices were performed using TPSRegress (Rohlf, 2005) in order to conveniently calculate regression statistics (e.g. % unexplained variance, Goodall's F-statistic, etc).  $R^2$  values are estimated by subtracting the variance unexplained by the wear index, calculated by summing the squared Procrustes distance between each observed shape and its expected shape, from one. The computational steps used by TPSRegress were reproduced in an R program to more

easily manipulate predicted dental morphologies in the simulated time series discussed below.

The following methods were applied only to the second lower molar (m2) of *Hyracotherium* (N = 292) in order to investigate the effects of dental wear on evolutionary time series of dental shape. The second lower molar shape is the least variable shape for both observed and predicted unworn shapes in comparison to the p4, m1, and m3, and the wear index explains more variation in m2 shape than in the other three tooth positions (see Chapter 4, Tables 4.11-18). These characteristics imply that m2 morphology, both worn and unworn, is more constrained than the other tooth positions and may have been less responsive to sources of random noise that may obscure signals of evolutionary change and shape change with wear.

#### Simulated dental time series (Step 4, Fig. 3.1)

The results of the multivariate shape regressions were used to generate evolutionary time series of dental shape as well as time series of dental wear in buccal view. An evolutionary time series refers to evolutionary changes in the mean dental phenotype through time whereas a time series of dental wear refers to how the trajectory of dental shape change with wear changes with time. Although the simulated time series are discussed here separately from the tests of evolutionary mode (described below), they were generated within the same R program that performed the evolutionary tests.

Fifteen simulated time series exhibiting directional, gradualistic change were produced that remained constant in the direction of change but varied in selective strength. The mean predicted unworn dental shape (i.e. the predicted shape at the lowest

wear value from the regression) was used as the first mean phenotype in every simulated time series. Over 20 steps, the mean phenotype gradually changed into a target shape (described in detail in the next paragraph). The target shape was chosen from the set of predicted unworn individual shapes, meeting the following three criteria: 1) the Procrustes distance between the mean unworn buccal shape and the target shape must be similar to the mean pairwise Procrustes distance between all predicted unworn shapes, 2) the target shape must be derived from a relatively unworn tooth (i.e. possess a relatively low wear index value), and 3) reasonable exaggeration of the target shape (2-3 times the vector length) results in a biologically realistic buccal shape (e.g. the cusps do not intersect in the resultant shape).

Selective strength was varied by multiplying the residual vector of the target shape by a scalar that ranged from 0.2 to 3 by 0.2 increments for the 15 simulated directional time series. The new residual vector was then divided by the number of steps in the series to generate the amount of change applied to the mean phenotype at each step of the series. For example, if the selective strength of the time series was 1 and there are 20 steps in the series, then at each step  $1/20$  of the target shape residual vector was added to the initial shape to produce the new mean m2 shape. Fig. 3.3A shows superimposed shape configurations for target m2 shapes under different selective strengths. Randomly distributed error with zero mean and standard deviation of  $10^{-5}$  was added to the mean shape to produce a population of m2 shapes at each step of the time series. A standard deviation of  $10^{-5}$  was chosen to match the order of magnitude of the smallest value in the target shape residual vector. The amount of error applied to the residual vectors was not varied among the different time series, because the effect of randomly generated noise on



tests of evolutionary mode has been thoroughly explored by Sheets et al. (2001) and Sheets and Mitchell (2001).

Fifteen simulated time series exhibiting evolutionary stasis were generated using a single peak adaptive landscape in which the mean predicted unworn m2 shape represents the mean optimal morphology and distance along the landscape is measured by Procrustes distance. In each time series, the adaptive peak was defined as the mean predicted unworn m2 shape with radius equal to a predetermined Procrustes distance from that mean. The mean phenotype at each step was selected from the set of predicted unworn shapes derived from empirical data [an approach modified from Polly (2004)]. For example, in a static time series with an adaptive peak radius of 0.03 Procrustes distance, the mean phenotype at each time step was randomly selected from the subset of predicted unworn shapes that were within 0.03 Procrustes distance units of the mean predicted unworn shape. This selection process was implemented in the simulation by predicting all unworn m2 shapes, calculating each shape's Procrustes distance from the mean unworn shape, and associating each shape's Procrustes distance with its residual vector. The selected residual vector was then added to the mean predicted unworn m2 shape.

A maximum adaptive peak radius was chosen by selecting the SC locality with the largest *Hyracotherium* m2 sample, calculating the mean unworn shape and all individual unworn shapes for that locality, and finding the maximum Procrustes distance from the mean unworn shape. This resulted in 15 time series of evolutionary stasis with adaptive peak radii that ranged from 0.018 to 0.046 Procrustes distance by an increment of 0.002 Procrustes distance units. A population of m2 shapes was produced for each

time step by sampling from the subset of unworn shapes with replacement and adding randomly distributed error to the residual vectors with zero mean and standard deviation of  $10^{-5}$ .

Static and directionally-changing time series of dental wear were generated using the slope and intercept coefficient vectors derived from the multivariate shape regression. In the static time series of dental wear, the same coefficient vectors were used at each time step to generate worn m2 buccal shapes. In the directional wear time series, the coefficient vectors changed gradually and directionally with each time step, so that the trajectory of shape change with wear gradually diverged with increasing wear in comparison to previous time steps. The new wear trajectory starts with the same unworn m2 buccal shape as in the preceding time step yet produces increasingly divergent shapes as wear progresses.

The new trajectory of shape change with dental wear at each time step was calculated by incrementally adding a constant  $C$  to an element in the slope coefficient vector and subtracting the product of  $C$  and the minimum wear index value from the respective element in the intercept coefficient vector. Specifically, two vectors of constants,  $[C_1 C_2 \dots C_N]$  and  $[-C_1 * X_{\min} -C_2 * X_{\min} \dots -C_N * X_{\min}]$ , were incrementally added to the slope and intercept coefficient vectors, respectively, where  $N$  is the number of partial warps and uniform components and  $X_{\min}$  is the smallest observed wear value. Ten different simulated wear time series were produced by multiplying the two vectors of constants by a scalar that varied from 0.05 to 0.5. These new constant vectors represent the incremental change in the trajectory of shape change with wear at each time step of the series, such that the difference in the wear trajectories of the initial and final steps of a

20 step series would be  $1 \times [C_1 \ C_2 \ \dots \ C_N]$  and  $1 \times [-C_1 * X_{\min} \ -C_2 * X_{\min} \ \dots \ -C_N * X_{\min}]$  for the weakest directional wear series and  $10 \times [C_1 \ C_2 \ \dots \ C_N]$  and  $10 \times [-C_1 * X_{\min} \ -C_2 * X_{\min} \ \dots \ -C_N * X_{\min}]$  for the strongest directional wear series.

The constants for the first five partial warps and the two uniform components were scaled to the same order of magnitude as their respective slope values whereas the remaining constants were given values of zero. By non-uniformly changing the slope and intercept vectors, the effects of wear on buccal shape are incrementally redistributed toward a target distribution reached at the end of the time series (Fig. 3.3B). A uniform change in the slopes and intercepts with time would only lead to a uniform increase or decrease in the rate of shape change with wear.

#### Tests of evolutionary mode (Step 5, Fig. 3.1)

Four tests of evolutionary mode, each investigating different aspects of an evolutionary time series, are necessary to fully characterize patterns of phenotypic change over time: an excursion-based test, an angle- (or direction-) based test, a variance-based test, and a rate-based test (LRI method). The excursion and angle tests use Monte Carlo simulations to test the null hypothesis of a random walk, determining if observations significantly deviate from expectations of a random morphological time series. The variance test, on the other hand, uses a static trend as its null hypothesis, using a resampling technique to generate confidence intervals for the difference in total variance and interval variance of the studied time series. The log-rate-interval method of Gingerich (1993, 2001) has been modified in this project to use Monte Carlo simulations to test if LRI slopes significantly deviate from a null hypothesis of a random walk.

Although each of the above tests have been described to some extent in Gingerich (1993, 2001), Sheets et al. (2001), Wood et al. (2007), and Piras et al. (2009), they will be described here in greater detail to clarify their use in conjunction with the simulated dental time series.

The excursion test determines whether the maximum excursion observed in a morphological time series significantly deviates from the maximum excursion expected from a random walk. The use of a random walk as the null hypothesis in the excursion test is important, because it allows 1) prevention of erroneous, deterministic interpretations of the observed data and 2) the use of rigorous, unequivocal definitions of directional selection and evolutionary stasis. Limited observations of an unbiased morphological random walk have the potential to exhibit either no net change, a common definition of evolutionary stasis (e.g. Lieberman et al., 1995) or short-term directional change that can be mistakenly interpreted as the result of directional selection. Comparing the observed morphological excursion to a distribution of excursions produced by random walks in the excursion test mitigates problems imposed by limited observations of the fossil record.

In the excursion test, the shapes at each time interval are averaged, and all pairwise Procrustes distances between the mean shapes are calculated to find the maximum observed excursion. A distribution of random walks is then generated based on changes observed in the actual shape time series, using the initial mean shape in the observed series as the initial shape in each random walk. The changes between successive intervals in the observed time series are characterized by a Procrustes distance and a vector of Procrustes residuals, which, combined, describe the magnitude and direction of

shape change. Thus, each step of a random walk can be randomly sampled with replacement from a set of magnitudes and a set of directions derived from the observed time series. Whereas the direction of shape change at each step of the random walk was taken directly from the set of observed vectors of Procrustes residuals, the magnitude of shape change was drawn from a uniform distribution that ranged from zero change to the maximum Procrustes distance between consecutive steps in the observed time series.

Allowing the magnitude of shape change at each step of the random walk to be chosen separately from the vector of Procrustes residuals differs from previous forms of this test (Sheets et al., 2001; Wood et al., 2007; Piras et al., 2009). This addition to the excursion test provides a wider range of possible shape changes from which to generate a random walk, yielding a less constrained distribution of unbiased random walks. Setting the maximum of the uniform distribution to a value derived from the observed series, however, still constrains each random walk within parameters defined by the data being tested.

In the excursion test, five hundred random walks are generated for each observed or simulated time series, and all pairwise Procrustes distances are calculated for each random walk. The distribution of 500 maximum Procrustes distance is then used to produce a 95% confidence interval for the expected maximum excursion generated by a random time series. An observed maximum excursion falling above the 95% CI is indicative of a directional trend (i.e. more change than expected from an unbiased random walk) in the observed or simulated time series. An observed maximum excursion falling below the CI is indicative of stasis (i.e. less change than expected from an unbiased random walk).

In the angle test, a distribution of random walks is generated in order to determine if the average angle between consecutive steps of a time series significantly deviates from the expectation of a random walk. Similar to the excursion test, the use of a random walk as the null is important in the angle test, because a single random walk can exhibit both short-term, consistent directions of change (i.e. no angular change between consecutive time steps) as well as reversals (i.e. an angular change of  $180^\circ$ ). The expected mean angle of change in a random walk is  $90^\circ$ , since the angle of change may vary from  $0^\circ$ - $180^\circ$  with equal probability. In a directional time series the direction of change should be relatively consistent, producing an expected angle less than  $90^\circ$ . For evolutionary stasis, any deviation from the mean shape should be counter-acted by a reversal back towards the mean, producing an expected mean angle greater than  $90^\circ$ . The angles between consecutive vectors of shape change (i.e. the vectors of change between  $\text{step}_i$ - $\text{step}_{i+1}$  and  $\text{step}_{i+1}$ - $\text{step}_{i+2}$ ) are calculated by taking the dot product of their corresponding vectors (Zelditch et al. 2004), and angles are then averaged over the entire time series.

A distribution of random walks is produced in the angle test in the same way as the excursion test, but here only the direction of change is important (i.e. the vectors of Procrustes residuals scaled to unit length). The observed mean angle is then compared to the confidence interval of values derived from the random walks. An observed value above the 95% CI indicates evolutionary stasis whereas a value below the CI indicates a directional trend. The same set of Monte Carlo simulations was used to produce the CI's for the excursion and angle tests performed on each time series to provide greater computational efficiency.

The variance test compares the variance at individual time intervals to the overall variance of the time series to determine if the observed time series significantly deviates from the null hypothesis of a time series with static mean and static variance. Using a static trend as the null hypothesis in the variance test is important, because the results of the test provide insight into the magnitude of morphological constraint in the time series (Piras et al., 2009). In a random or directional morphological time series, in which the population mean changes but its variance remains constant, this test would show that the total variance of the time series is consistently greater than the variance at any particular interval. The statistical significance of the difference in variance is determined by recalculating the interval and total variances 500 times, after resampling the shapes within each with replacement, and taking the difference in variance after each resampling. This produces a distribution of differences in variance for each time interval from which a 95% confidence interval can be calculated. If the confidence interval contains the value zero for a given interval, then total variance of the time series is not significantly greater than that interval's variance. The variance test is much more limited than the excursion and angle tests, because it cannot distinguish between random walks, directional trends, and static trends with variable stabilizing selective strengths (Piras et al., 2009).

The LRI method is built on the observation that rates of evolutionary change are often inversely proportional to the interval of time over which each rate is measured (Gingerich, 1993; Clyde and Gingerich, 1994; Gingerich, 2001), which is primarily due to the occurrence of evolutionary reversals in morphological time series. In an LRI analysis, all possible pairwise rates of morphological change are regressed onto the corresponding interval of time and a confidence interval for the slope of the regression

line is generated by bootstrapping. The amount of reversals in an observed univariate time series is reflected in the steepness of the negative slope, such that a directional time series with few reversals would produce a confidence interval containing zero and a static time series with many reversals would produce a confidence interval containing the value -1. The expected slope value for an unbiased, univariate random walk is -0.5.

For multivariate shape data, the rate of change is measured by dividing the Procrustes distance between two mean shapes by the length of the time interval separating them. All pairwise Procrustes distances and all corresponding pairwise interval lengths were calculated for the simulated morphological time series, and least squares regression was used to calculate the LRI slope. Using the expected slope values for the ideal directional, static, and random morphological time series described above is not adequate for testing against a null hypothesis of a random walk since the confidence interval for an observed slope may not contain the values 0, -0.5, or -1. For example, a confidence interval of (-0.7, -0.8) could be interpreted as a random walk, a static time series, or some combination of the two patterns. Instead, the Monte Carlo techniques described above were used to generate a distribution of slopes to which the observed slopes can be compared. If the observed slope falls outside and above the 95% CI of slopes produced by random walks, the observed time series can be interpreted as a directional time series. An observed slope outside and below the 95% CI is indicative of evolutionary stasis.

Taken together, the results of these various tests can more fully characterize the pattern of evolutionary change than any one test alone. Furthermore, seemingly contradictory results between the four tests can be indicative of the spectrum of



evolutionary patterns possible in the fossil record. For example, an observed directional trend in morphology may exhibit several low-magnitude, counteracting changes due to the effects of competing selective forces, morphological constraints, and/or immigration (Roopnarine et al., 1999). In this case, the excursion, angular, variance, and LRI test results would indicate directional evolution, stasis, directional/random evolution, and random evolution, respectively. In the case of a static time series in which the strength of stabilizing selection varies with time, the four results would be stasis, stasis, directional/random, and stasis, respectively.

#### Dental wear and evolutionary tests (Step 5, Fig. 3.1)

The excursion, angular, variance, and LRI tests were applied to superimposed time series of dental phenotypic shape change and dental wear shape change to investigate how dental wear interferes with detection of evolutionary signals. Each simulated evolutionary time series was subjected to the battery of four tests of evolutionary mode 21 times, in which the first batch of tests were performed on unworn teeth and each subsequent batch of tests were performed on time series sampled from increasingly worn teeth. The distribution of wear values in each time interval was estimated using an empirically-derived skewed normal probability distribution. This distribution was derived by fitting a skewed normal distribution to the distribution of wear values at the stratigraphic level with the largest sample size of *Hyracotherium* m2's, which was performed using the sn R package with parameters provided by <http://azzalini.stat.unipd.it/SN/sn-fit.html> (Accessed February, 2009).

After performing the tests of evolutionary mode on the unworn series, the R program was allowed to sample from an increasingly larger subset of wear values and to apply the associated shape transformations to each interval's population of m2 buccal shapes. The total range of observed wear values (-1.76 to 5.47) was subdivided into 20 bins of equal width (~0.36 wear index width), so that at each iteration of the test battery the maximum wear value that could be sampled increased by 0.36. Twenty wear values per interval were sampled with replacement for each simulated time series to approximate actual sample sizes of *Hyracotherium* available in the studied stratigraphic range. Twenty replicates of each time series were ran to generate median results for each test at the various levels of wear sampling.

The variances in shape due to the evolutionary and directional wear trends were calculated in order to determine the role of variance in each test's ability to correctly detect evolutionary trends. The shape variance for each evolutionary simulation was calculated over the entire time series using only unworn shapes and averaged for each selective strength or adaptive peak radius. The shape variance due to dental wear was calculated in simulations in which the phenotype was held constant and only the amount of wear sampled was allowed to change. The variance of all 400 worn shapes produced in each simulation was averaged for each sampled range of wear values and across all directional wear strengths. The shape variance of the weakest evolutionary trend correctly identified by each test was regressed onto the amount of shape variance for each subset of dental wear values in order to measure each test's sensitivity to dental wear. Principal components analyses of representative simulated time series were also

performed to investigate the interaction of shape variance produced by phenotypic evolution and shape variance imposed by dental wear.

## Results

### Dental wear index

Table 3.1 lists the five regression models for the overall wear index that best predicted the area of exposed dentin. Each model produced normally distributed residuals with constant variance, and the rank order of the top three regression models did not change after removal of the most influential data point. The best regression model consists of a linear combination of the protoconid, hypoconid, and entoconid heights, explaining 53% and 72% of the variance in exposed dentin area over all tooth positions and over all m2 specimens, respectively. Based on this wear index, the observed range of wear values for the m2 position is -1.76 (least worn) to 5.47 (most worn) (Fig. 3.4).

The density distribution of wear index values for a given stratigraphic level shown in Fig. 3.5B, estimated using the 42 wear values observed at 1750 m stratigraphic level (Fig. 3.5A), is a skewed normal distribution (log-normal) with a median of  $\sim 0.14$  and mean  $\sim 0.40$ . Out of the 20 bins of equal wear value width used in the sampling simulations, the -1.04/-0.67 and -0.67/-0.31 bins contain the greatest number of teeth based on this distribution. Fig. 3.5C shows the actual frequency distribution of the total sample of *Hyracotherium* m2's with the contribution of teeth with and without exposed dentin shown for each bin of wear values. The total frequency distribution is nearly identical to the density distribution estimated from the 1750 m level. The -0.67/-0.31 bin is the first bin in which the majority of teeth exhibit exposed dentin. Those m2's with

exposed dentin in bins of lesser wear show subtle evidence of breakage on cusps with small areas of exposed dentin or unusual patterns of wear, such as a well-developed wear facet on a single lingual surface without a corresponding facet on the buccal side of the tooth.

#### Multivariate shape regression on wear index

There is a significant relationship between the overall dental wear index and m2 buccal shape ( $N=292$ ,  $F = 265.41$ ;  $df = 36, 10440$ ;  $p < 0.0001$ ). The percent of variance in m2 buccal shape explained by the overall wear index is 47.82% (i.e.  $R^2 \sim 1 - 0.5218$ , where 0.5218 is the proportion of variance unexplained by the wear index). Initially, the changes in buccal shape related to wear are concentrated on the apical and anterior portions of the protoconid and hypoconid, but as wear progresses, noticeable change also occurs at the hypoconulid and the posterior sides of the protoconid and hypoconid until the trigonid and talonid are worn into two low plateaus (Fig. 3.3A). The distribution of shape change with wear on tooth surfaces in both buccal and lingual view and the implications of this distribution for mastication in *Hyracotherium* are discussed in the following chapter.

As described above, the distribution of predicted unworn shapes is used to simulate a time series of phenotypic evolution. All predicted unworn buccal shapes are biologically realistic, meaning that all of the predicted buccal outlines would be functional during mastication. Removing ~47% of the variance in observed shapes due to the wear index substantially decreases the range of shapes within the 292 predicted unworn morphologies and, consequently, reduces the range of pairwise Procrustes

distances in comparison to the observed shapes (min = 0.008, mean = 0.047, max = 0.149; and min = 0.010, mean = 0.078, max = 0.238, respectively). A right m2 from SC054 (UM82228) best met the 3 criteria listed above for choosing the target shape in simulated time series of directional phenotypic change: Procrustes distance from mean unworn shape = 0.046, wear index value = -0.77, and three times the vector of shape change between UM82228 and the mean unworn shape is biologically realistic (Fig. 3.3A). The maximum observed Procrustes distance between the mean unworn shape specific to the locality with the largest sample size (SC002) and any predicted unworn shape for that locality was 0.046. This value was used as the maximum adaptive peak radius for the simulated time series of evolutionary stasis.

#### Simulated time series of evolutionary and dental wear change

Using UM82228 as the target shape in the 15 directional simulations of phenotypic change caused each directional time series to result in an m2 shape in which the buccal cusps were more acute and more closely spaced than in the initial mean shape. The total variance of each directional time series increased as a power function and the maximum excursion increased linearly with the selective strength of the simulated time series. The mean angle of change between successive time steps was invariably zero in all simulations (Table 3.2). For the evolutionary stasis simulations, both the total variance and maximum excursion increased linearly with the adaptive peak radius of the time series. The mean angle of shape change between successive steps of the stasis simulations ranged from 119.6°-121.6° with a mean of 120.88° (Table 3.2).

Biologically realistic buccal shapes were also produced by the 10 time series of directional shape change with wear, in which the distribution of wear shape change on the talonid gradually changed with each time step. Specifically, the cristid obliqua and the anterior-most portion of the hypoconid wore progressively faster than the rest of the talonid in buccal view with each successive time step (Fig. 3.3B). The differences in the distribution of wear shape change between the dental wear time series are minute at early stages of wear, but as wear progresses these differences become increasingly more noticeable. Plotting the total variance of each wear time series versus the range of wear values sampled similarly reflects more substantial shape change at later stages of wear (Fig. 3.3C, Table 3.3). Overall, the sigmoid pattern in accumulation of variance is similar between the different wear time series in which variance increases slowly at low values of wear, increases rapidly at intermediate values, and levels off at the highest values.

#### Evolutionary test results

The excursion, angular, Monte Carlo, and variance tests exhibit substantial asymmetry in their ability to detect directional selection and evolutionary stasis in morphological time series when teeth of various wear index values are sampled (Table 3.4). Each test correctly identified the 15 simulations of evolutionary stasis regardless of the amount of wear sampled or the strength of directional wear, whereas the ability of the tests to correctly identify the 15 simulated times series of directional selection varied with the amount of dental wear sampled. For each simulation of directional selection, with the exception of those simulations with the greater selective strengths, there was a range of sampled dental wear at which the null hypotheses of the 4 tests could not be rejected.

Interestingly, implementing directional dental wear in the simulations only had an effect on the variance test (i.e. more frequent occurrence of Type II error at greater directional wear strengths), whereas the powers of the excursion, angular, and Monte Carlo LRI tests were not noticeably affected (Table 3.4C). It should also be noted that the excursion test rejected the null hypothesis in favor of evolutionary stasis in directional selection simulations of low selective strengths when sampling from extreme values of dental wear.

Fig. 3.6 illustrates the differing sensitivities of the excursion, angular, and Monte Carlo LRI tests to dental wear effects in the directional selection simulations. As the amount of shape variance due to dental wear increased (x-axis), the minimum shape variance correctly identified as the result of directional selection also increased (y-axis). The slope values indicate the minimum evolutionary shape variance detected as a proportion of the dental wear variance, which differed between the 3 tests, such that the excursion test, angular test, and Monte Carlo LRI results produced slopes of 1.4, 2.1, and 1.7, respectively. This means, for example, that in order to reject the null hypothesis of the excursion test, the amount of shape variance produced by directional selection must be at least 1.4 times greater than the amount of shape variance exhibited by the sample due to dental wear. The sensitivity of the variance test to dental wear cannot be directly compared to those of the excursion, angular, and Monte Carlo LRI tests due to its usage of a static null hypothesis.

#### PCA results for simulated time series

Principal components analyses were performed on two directional selection simulations: 1) directional selective strength 0.6/static wear and 2) directional selective

strength 0.6/directional wear strength 5. PCA results of these simulations show that as the range of sampled dental wear increases, the contribution of phenotypic shape variance to the greatest dimension of overall variance (i.e. PC1) decreases (Fig 3.7). When the trajectory of shape change due to dental wear is constant across all time steps (Fig. 3.7A-E), the dimension of shape variance due to directional selection rotates through PC1/PC2 space as the range of sampled wear values increases. When no worn teeth are sampled (maximum wear value = -1.76), shape variance due to directional selection is parallel to PC1, but when extremely worn teeth are sampled (e.g. maximum wear value = 4.39), the dimension of shape variance due to directional selection lies perpendicular to PC1 (i.e. PC2). At these extreme values of dental wear, PC1 almost entirely consists of the variance of dental shape due to wear.

PCA results for the directional selection/directional wear simulation are similar, but at extreme values of sample dental wear, the signal in shape variance due to directional selection loses coherency in PC1/PC2 space (Fig. 3.7G-I). As the range of sample dental wear increases, temporal separation of dental shapes diminishes until each temporal distribution of shapes completely overlap in PC1/PC2 space. In both types of directional selection simulations, however, there is a unique minimum in the proportion of total shape variance represented by PC1 that corresponds to a particular value of the dental wear index, the value at which the majority of the evolutionary tests no longer reject the null hypothesis (Fig. 3.7F, J).

Principal components analyses were also performed on two evolutionary stasis simulations: 1) adaptive peak radius < 0.032 Procrustes distance units/static wear and 2) adaptive peak radius < 0.032 Procrustes distance units/directional wear 5. In both stasis



simulations, there was no temporal separation of shapes in PC1/PC2 space for any ranges of sampled wear (Fig. 3.8). The range of PC1 scores increased as more worn teeth were sampled, such that the distribution of shapes changed from a circular distribution in PC1/PC2 space to a highly elongate distribution at extreme wear index values.

## **Discussion**

The asymmetrical ability of the excursion, angular, Monte Carlo LRI, and variance tests to correctly distinguish evolutionary trends with the added complication of dental wear is intriguingly similar to the results of Sheets and Mitchell (2001) and Sheets et al. (2001). These studies documented the effects of random noise on detecting evolutionary trends in univariate and multivariate morphological time series, respectively. Sheets and Mitchell (2001) showed that at shorter step lengths and equal amounts of random noise, the *x*-statistic, runs, and LRI tests (univariate equivalents of the excursion, angular, and Monte Carlo LRI tests used here) were consistently more successful at detecting stabilizing selection than directional selection. When evolutionary time series of shape were subjected to the multivariate excursion and angular tests, the success rates were even more asymmetric: a 100% success rate for simulations of stabilizing selection whereas the success rate for simulations of directional selection was inversely proportional to the amount of applied noise and proportional to the number of steps in each simulation (Sheets et al., 2001).

Although the amount of dental wear sampled at each step of the simulations presented here was chosen at random, the similarity of the results presented here and those of Sheets et al. (2001) and Sheets and Mitchell (2001) is not simply the result of

applying random noise to deterministic trends. The tests of evolutionary mode are designed to distinguish time-dependent, consistent changes in morphology (i.e. directional selection) and temporally-invariable morphology (i.e. stabilizing selection) from random processes that can be either dependent or independent of time. The time dependence of directional selection means that there is a dimension of the morphological variance that is parallel with time whereas in stabilizing selection all dimensions of morphological variance are perpendicular to time. Dental wear and random noise add a dimension of morphological variance that is not parallel to time at the resolution of the sampled evolutionary time series, differentially diluting the evolutionary signal in each type of morphological time series.

The PCA results of the two directional selection simulations and the two static simulations suggest that the tests of evolutionary mode are highly sensitive to the relationship between time and the greatest dimension of morphological variance (i.e. PC1). When the null hypothesis is correctly rejected in the directional selection simulations, the PC1/PC2 plots show clear temporal separation along PC1 (i.e. the dimension of variance that is parallel to time is the greatest contributor to PC1). When the null hypothesis is not rejected, the dimension of morphological variance parallel to time is the minor contributor to PC1 (Fig. 3.7). Contrastingly, at no point was there any temporal separation along PC1 in the simulations of evolutionary stasis regardless of the amount of dental wear sampled (Fig. 3.8). These observations suggest that a strong correlation between time and the greatest dimension of morphological variance is indicative of directional selection, no correlation is indicative of stasis, and any weak correlation will not be distinguished from a random walk.

Although these results are somewhat intuitive, practical guidelines for determining whether biases, like dental wear, are effectively obscuring the evolutionary signal in dental morphological time series (i.e. occurrence of type II error) are still necessary. The simplest approach is to sample only teeth that exhibit no exposed dentin. In *Hyracotherium*, m2's with no exposed dentin make up the majority of teeth with wear values lower than -0.67. Sampling at or below this level of dental wear produced type II errors only in the directional selection simulations with weak selective strengths ( $< 0.8 * \text{the target shape}$ ).

A more rigorous approach to detect the occurrence of type II error in an evolutionary analysis of dental shape would involve estimating and comparing the amount of variance due to a hypothesized evolutionary trend and the amount of variance due to both dental wear and intraspecific variation. The variance due to a hypothesized evolutionary trend can be estimated by modeling the mean morphology at the observed temporal resolution and calculating the variance across all mean shapes. The variance due to dental wear and intraspecific variation can be estimated by calculating shape variance at a particular stratigraphic interval. Should the shape variance from the modeled evolutionary trend be less than 1.4 times the estimated variance due to dental wear and intraspecific variation (based on excursion test slope in Fig. 3.6), then the occurrence of type II error is likely. However, the failure to reject the null hypothesis of a random walk when the ratio of variances is greater than 1.4 is a strong indicator that the observed data does not exhibit directional selection.

Table 3.1 Top five linear models generated by overall wear index search program, listing measurements included in principal components analysis (PCA) and associated  $R^2$  value. Measurements were taken from p4, m1, m2, and m3 positions. The model with rank one ( $R^2 = 0.53$ ) was used as the overall index in all simulations.

<b><u>Model rank</u></b>	<b><u>Measurements included in PCA</u></b>	<b><u>R<sup>2</sup></u></b>
1	1) Ln protoconid height residuals 2) Ln metaconid height residuals 3) Ln entoconid height residuals	0.53
2	1) Ln protoconid height residuals 2) Ln metaconid height residuals 3) Ln entoconid height residuals 4) Hypoconid height/ entoconid height ratio	0.51
3	1) Ln protoconid height residuals 2) Ln hypoconid height residuals 3) Ln metaconid height residuals 4) Ln entoconid height residuals	0.48
4	1) Ln protoconid height residuals 2) Ln hypoconulid height residuals 3) Ln metaconid height residuals 4) Ln entoconid height residuals	0.46
5	1) Ln protoconid height residuals 2) Ln hypoconid height residuals 3) Ln metaconid height residuals 4) Ln entoconid height residuals 5) Hypoconid height/ entoconid height ratio	0.45

Table 3.2 Parameters for simulated evolutionary time series. In the directional selection simulations, selective strength refers to the proportion of the m2 shape change vector that each simulated lineage attained at the end of the time series. Adaptive peak radius refers to the width of the adaptive peak in which m2 morphology was allowed to vary in the evolutionary stasis simulations. Pdu = Procrustes distance units.

Selective Strength (Pdu)	Directional Evolutionary Time Series				Static Evolutionary Time Series			
	Total Shape Variance	Mean Maximum Excursion (Pdu)	Mean Angle		Adaptive Peak Radius (Pdu)	Total Shape Variance	Mean Maximum Excursion (Pdu)	Mean Angle
0.2	7.01E-06	0.009	0		0.018	2.21E-04	0.028	119.9
0.4	2.80E-05	0.018	0		0.020	2.91E-04	0.033	120.9
0.6	6.30E-05	0.027	0		0.022	3.55E-04	0.037	121.3
0.8	1.12E-04	0.037	0		0.024	4.09E-04	0.040	121.9
1.0	1.75E-04	0.046	0		0.026	4.74E-04	0.044	119.8
1.2	2.52E-04	0.055	0		0.028	5.33E-04	0.046	121.0
1.4	3.43E-04	0.064	0		0.030	5.68E-04	0.049	120.6
1.6	4.48E-04	0.073	0		0.032	6.14E-04	0.052	122.2
1.8	5.67E-04	0.082	0		0.034	6.44E-04	0.056	122.6
2.0	7.00E-04	0.092	0		0.036	7.12E-04	0.059	120.4
2.2	8.47E-04	0.101	0		0.038	7.65E-04	0.060	119.6
2.4	1.01E-03	0.110	0		0.040	8.31E-04	0.065	120.3
2.6	1.18E-03	0.119	0		0.042	8.59E-04	0.067	120.4
2.8	1.37E-03	0.128	0		0.044	8.93E-04	0.070	121.7
3.0	1.58E-03	0.137	0		0.046	9.46E-04	0.071	120.6

Table 3.3 The amount of lower second molar (m2) shape variance produced by sampling from worn m2 shapes in the static and directional wear simulations. The 1, 5, and 10 refer to scalar multipliers used to vary the length of the vectors describing how teeth wore differently between time steps of the simulations.

Static Wear Time Series	1 x Directional Wear Time Series		5 x Directional Wear Time Series		10 x Directional Wear Time Series	
	Maximum Wear Value Sampled	Total Shape Variance	Maximum Wear Value Sampled	Total Shape Variance	Maximum Wear Value Sampled	Total Shape Variance
-1.40	6.52E-06	-1.40	6.62E-06	-1.40	1.01E-05	1.13E-05
-1.04	1.92E-05	-1.04	1.88E-05	-1.04	2.37E-05	3.50E-05
-0.67	3.69E-05	-0.67	3.88E-05	-0.67	4.94E-05	7.46E-05
-0.31	6.53E-05	-0.31	6.91E-05	-0.31	9.04E-05	1.30E-04
0.04	1.08E-04	0.04	1.13E-04	0.04	1.45E-04	2.06E-04
0.40	1.71E-04	0.40	1.62E-04	0.40	2.19E-04	2.86E-04
0.77	2.27E-04	0.77	2.25E-04	0.77	2.94E-04	3.90E-04
1.13	3.16E-04	1.13	3.12E-04	1.13	3.78E-04	5.32E-04
1.49	4.05E-04	1.49	4.06E-04	1.49	4.79E-04	6.81E-04
1.85	4.82E-04	1.85	5.03E-04	1.85	5.86E-04	8.28E-04
2.21	5.74E-04	2.21	5.98E-04	2.21	7.05E-04	9.80E-04
2.58	6.49E-04	2.58	6.72E-04	2.58	7.83E-04	1.09E-03
2.94	7.18E-04	2.94	7.36E-04	2.94	8.78E-04	1.19E-03
3.30	7.90E-04	3.30	7.99E-04	3.30	9.97E-04	1.29E-03
3.66	8.41E-04	3.66	8.41E-04	3.66	1.07E-03	1.35E-03
4.02	8.94E-04	4.02	8.56E-04	4.02	1.14E-03	1.37E-03
4.39	9.06E-04	4.39	8.75E-04	4.39	1.21E-03	1.41E-03
4.75	9.31E-04	4.75	8.98E-04	4.75	1.26E-03	1.44E-03
5.11	9.54E-04	5.11	9.00E-04	5.11	1.30E-03	1.44E-03
5.47	9.51E-04	5.47	9.10E-04	5.47	1.29E-03	1.46E-03

Table 3.4 Results of the tests of evolutionary mode in the directional selection simulations. A) Results for simulations with static dental wear. Simulation parameters and the maximum dental wear sampled appear on the vertical and horizontal labels, respectively. Four test results are shown for each simulation in following order: Monte Carlo LRI, angular test, excursion test, and variance test. Color coding corresponds to the test result: Blue = directional selection, yellow = random walk, red = evolutionary stasis, and green = directional/random walk. Directional evolutionary trends and random walks cannot be distinguished using the variance test.

Wear Index Boundaries

Phen Mode	Selective Strength	Wear Mode	Wear Strength	-1.76	-1.40	-1.04	-0.67	-0.31	0.04	0.40	0.77	1.13	1.49	1.85	2.21	2.58	2.94	3.30	3.66	4.02	4.39	4.75	5.11	5.47
Dir	0.2	Static	-	Dir	Dir	Dir	Dir	Dir	Dir	Dir	Dir	Dir	Dir	Dir	Dir	Dir	Dir	Dir	Dir	Dir	Dir	Dir	Dir	Dir
Dir	0.4	Static	-	Dir	Dir	Dir	Dir	Dir	Dir	Dir	Dir	Dir	Dir	Dir	Dir	Dir	Dir	Dir	Dir	Dir	Dir	Dir	Dir	Dir
Dir	0.6	Static	-	Dir	Dir	Dir	Dir	Dir	Dir	Dir	Dir	Dir	Dir	Dir	Dir	Dir	Dir	Dir	Dir	Dir	Dir	Dir	Dir	Dir
Dir	0.8	Static	-	Dir	Dir	Dir	Dir	Dir	Dir	Dir	Dir	Dir	Dir	Dir	Dir	Dir	Dir	Dir	Dir	Dir	Dir	Dir	Dir	Dir
Dir	1.0	Static	-	Dir	Dir	Dir	Dir	Dir	Dir	Dir	Dir	Dir	Dir	Dir	Dir	Dir	Dir	Dir	Dir	Dir	Dir	Dir	Dir	Dir
Dir	1.2	Static	-	Dir	Dir	Dir	Dir	Dir	Dir	Dir	Dir	Dir	Dir	Dir	Dir	Dir	Dir	Dir	Dir	Dir	Dir	Dir	Dir	Dir
Dir	1.4	Static	-	Dir	Dir	Dir	Dir	Dir	Dir	Dir	Dir	Dir	Dir	Dir	Dir	Dir	Dir	Dir	Dir	Dir	Dir	Dir	Dir	Dir
Dir	1.6	Static	-	Dir	Dir	Dir	Dir	Dir	Dir	Dir	Dir	Dir	Dir	Dir	Dir	Dir	Dir	Dir	Dir	Dir	Dir	Dir	Dir	Dir
Dir	1.8	Static	-	Dir	Dir	Dir	Dir	Dir	Dir	Dir	Dir	Dir	Dir	Dir	Dir	Dir	Dir	Dir	Dir	Dir	Dir	Dir	Dir	Dir
Dir	2.0	Static	-	Dir	Dir	Dir	Dir	Dir	Dir	Dir	Dir	Dir	Dir	Dir	Dir	Dir	Dir	Dir	Dir	Dir	Dir	Dir	Dir	Dir
Dir	2.2	Static	-	Dir	Dir	Dir	Dir	Dir	Dir	Dir	Dir	Dir	Dir	Dir	Dir	Dir	Dir	Dir	Dir	Dir	Dir	Dir	Dir	Dir
Dir	2.4	Static	-	Dir	Dir	Dir	Dir	Dir	Dir	Dir	Dir	Dir	Dir	Dir	Dir	Dir	Dir	Dir	Dir	Dir	Dir	Dir	Dir	Dir
Dir	2.6	Static	-	Dir	Dir	Dir	Dir	Dir	Dir	Dir	Dir	Dir	Dir	Dir	Dir	Dir	Dir	Dir	Dir	Dir	Dir	Dir	Dir	Dir
Dir	2.8	Static	-	Dir	Dir	Dir	Dir	Dir	Dir	Dir	Dir	Dir	Dir	Dir	Dir	Dir	Dir	Dir	Dir	Dir	Dir	Dir	Dir	Dir
Dir	3.0	Static	-	Dir	Dir	Dir	Dir	Dir	Dir	Dir	Dir	Dir	Dir	Dir	Dir	Dir	Dir	Dir	Dir	Dir	Dir	Dir	Dir	Dir



Table 3.4 continued... B) Results for simulations with directionally changing dental wear (strength = 5). Four test results are shown for each simulation in following order: Monte Carlo LRI, angular test, excursion test, and variance test. Color coding corresponds to the test result: Blue = directional selection, yellow = random walk, red = evolutionary stasis, and green = directional/random walk.



Table 3.4 continued... C) Results for simulations with various strengths of directionally changing dental wear. Four test results are shown for each simulation in following order: Monte Carlo LRI, angular test, excursion test, and variance test. Color coding corresponds to the test result: Blue = directional selection, yellow = random walk, red = evolutionary stasis, and green = directional/random walk.



Figure 3.1 Outline of methods used in Chapter 3. Procedures and calculations used to generate output at each step are explained in detail in the methods section (pgs. 96-117).

**Step 1: Data collection**

Input: Photographs of dental casts in occlusal, buccal, and lingual views using standardized orientation

Output: 1) Univariate measures (see Fig 3.2)  
2) Procrustes superimposed shape coordinates (see Fig. 3.2)

**Step 2: Wear index calculations**

Input: Univariate measures (Step 1)

Output: 1) Continuous, quantitative index of dental wear  
2) Density distribution of wear values per stratigraphic level

**Step 3: Dental shape regression on wear**

Input: 1) Procrustes superimposed coordinates (Step 1)  
2) Wear index values (Step 2)

Output: 1) Shape regression coefficients  
2) Predicted unworn dental shapes

**Step 4: Simulated dental time series**

Input: 1) Wear index values (Step 2)  
2) Shape regression coefficients (Step 3)  
3) Predicted unworn dental shapes (Step 3)

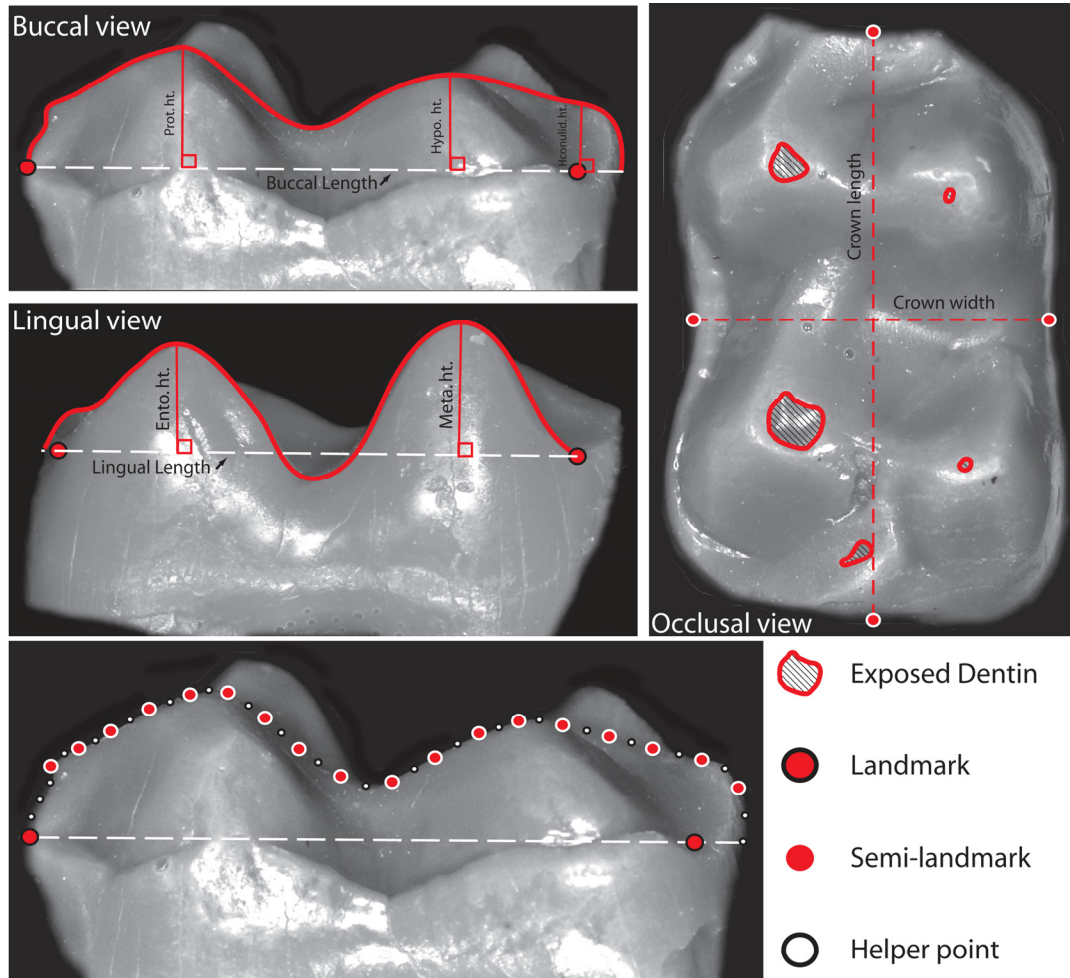
Output: 1) Directional evolutionary time series of various selective strengths (15)  
2) Static evolutionary time series of various adaptive peak widths (15)  
3) Directionally-changing trajectories of dental shape change with wear (10)  
4) Static trajectory of dental shape change with wear (1)

**Step 5: Tests of evolutionary mode**

Input: 1) Wear Index values (Step 2)  
2) Density distribution of wear values (Step 2)  
3) Output of Step 4

Output: 1) Results from Excursion, Angle, and Variance tests for simulated time series  
2) Understanding of bias imposed by sampling worn teeth on evolutionary signals of dental shape time series

Figure 3.2 Buccal, lingual, and occlusal views of the lower second molar of *Hyracotherium* exhibiting size measurements, landmarks, and semi-landmarks used to calculate the overall wear index and to produce simulated morphological time series.



### Size Measurements

#### Occlusal view:

- 1) Crown area (crown length x crown width)
- 2) Exposed dentin area (estimated from closed outlines at cusps)

#### Buccal view:

- 1) Buccal length
- 2) Protoconid height (highest point of protoconid to baseline)
- 3) Hypoconid height (highest point of hypoconid to baseline)
- 4) Hypoconulid height (highest point of hypoconulid to baseline)
- 5) Buccal centroid size (incl. all landmarks, semi-landmarks, helper points)

#### Lingual view:

- 1) Lingual length
- 2) Metaconid height (highest point of metaconid to baseline)
- 3) Entoconid height (highest point of entoconid to baseline)
- 4) Lingual centroid size (incl. all landmarks, semi-landmarks, helper points)

#### Ratios:

- 1) Protoconid height/metaconid height
- 2) Hypoconid height/entoconid height

Figure 3.3 Simulated lower second molar (m2) shapes and variances. A) Unworn m2 buccal shapes generated in the directional selection simulations. Dots on each black outline represent landmarks and semi-landmark positions generated in each simulation. B) Worn m2 buccal shapes generated in the simulations of static and directional wear. The trajectory of shape change in the static wear simulation represents the observed pattern of shape change in *Hyracotherium* with increased dental wear. C) Comparison of the increase in shape variance with increased sampling of worn teeth between simulations of static and directional wear.

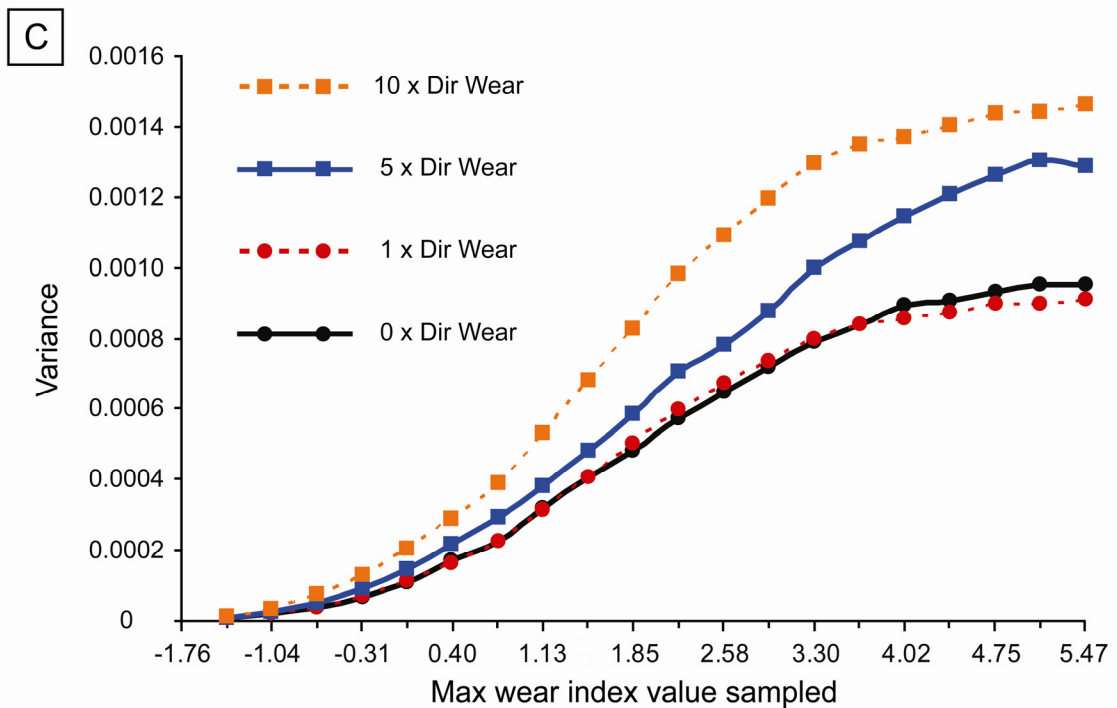
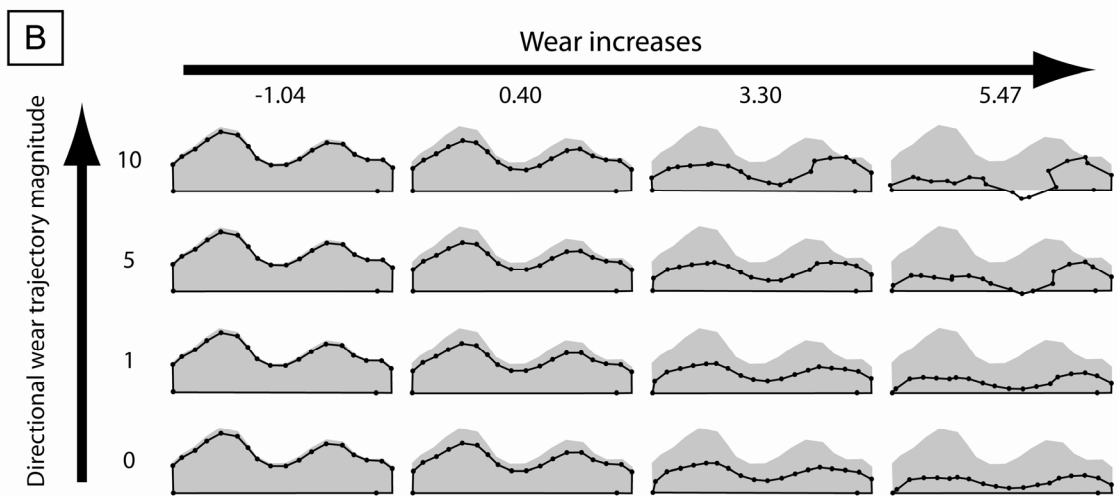
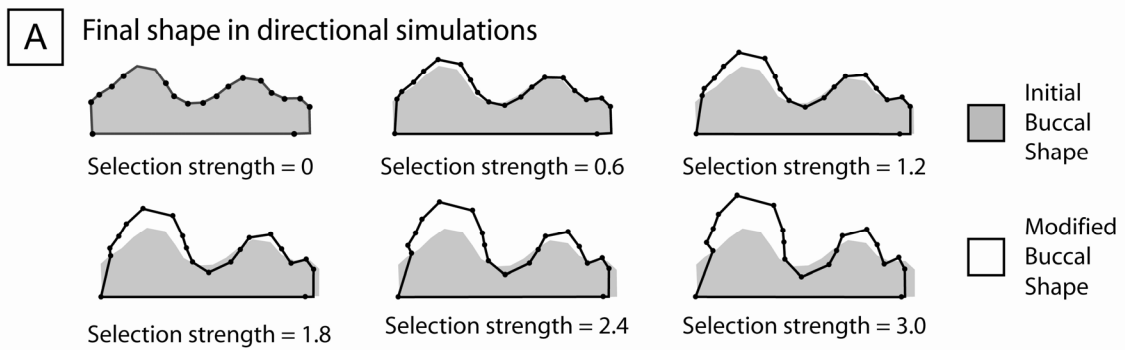




Figure 3.4 Representative worn *Hyracotherium* lower second molars in buccal and occlusal view and associated overall wear index values. The overall wear index explained 47.82% of buccal shape variance, indicating substantial, yet predictable changes in dental occlusion with increased wear.

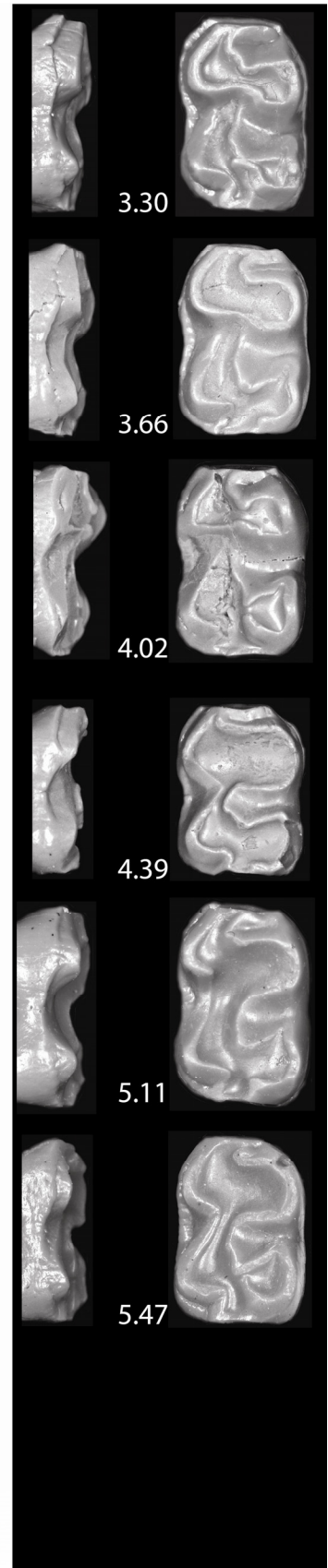
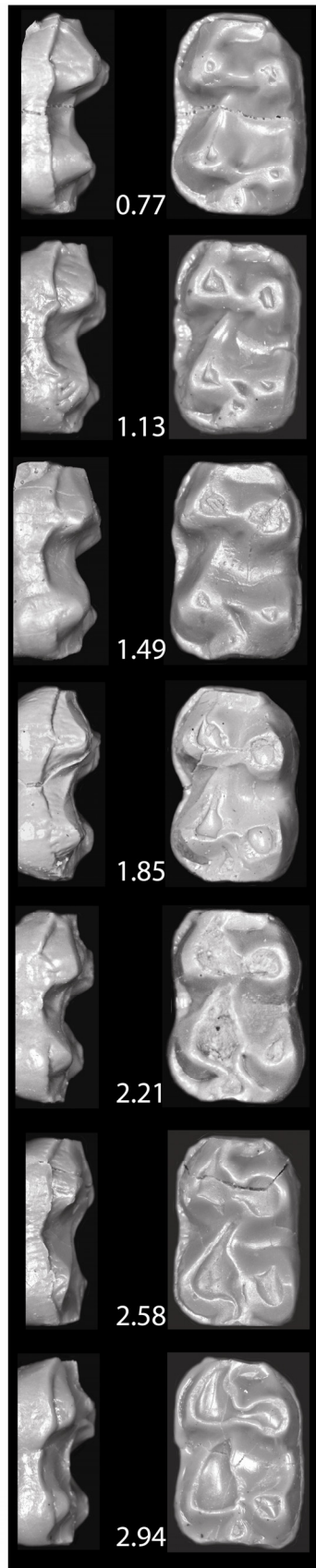
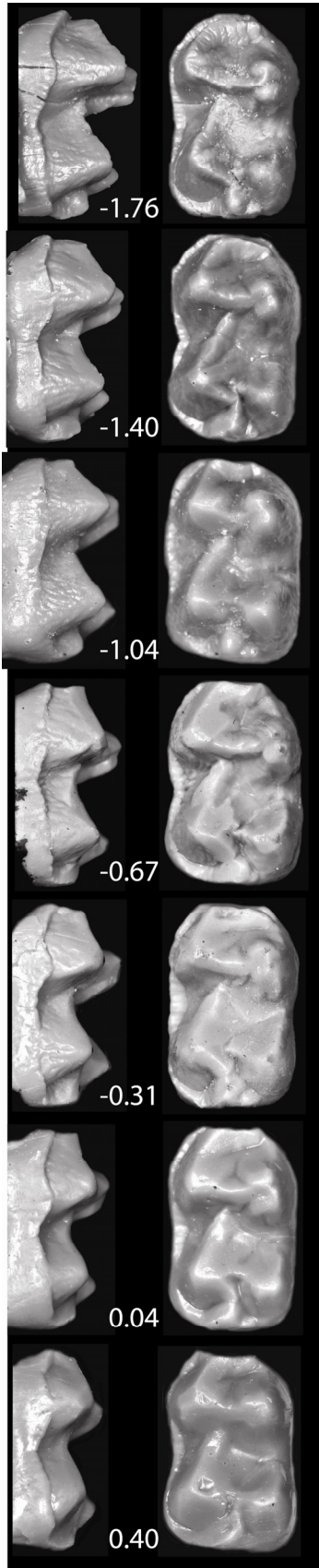


Figure 3.5 Distributions of overall wear index values for lower second molars (m2) of *Hyracotherium*. A) Observed density distribution of overall wear index values sampled from the 1750 meter stratigraphic level. B) Modeled density distribution of overall wear index values used in simulations. C) Frequency distribution of overall wear index values in total m2 sample. The (-0.67,-0.31) bin is the first in which the majority of teeth exhibit exposed dentin.

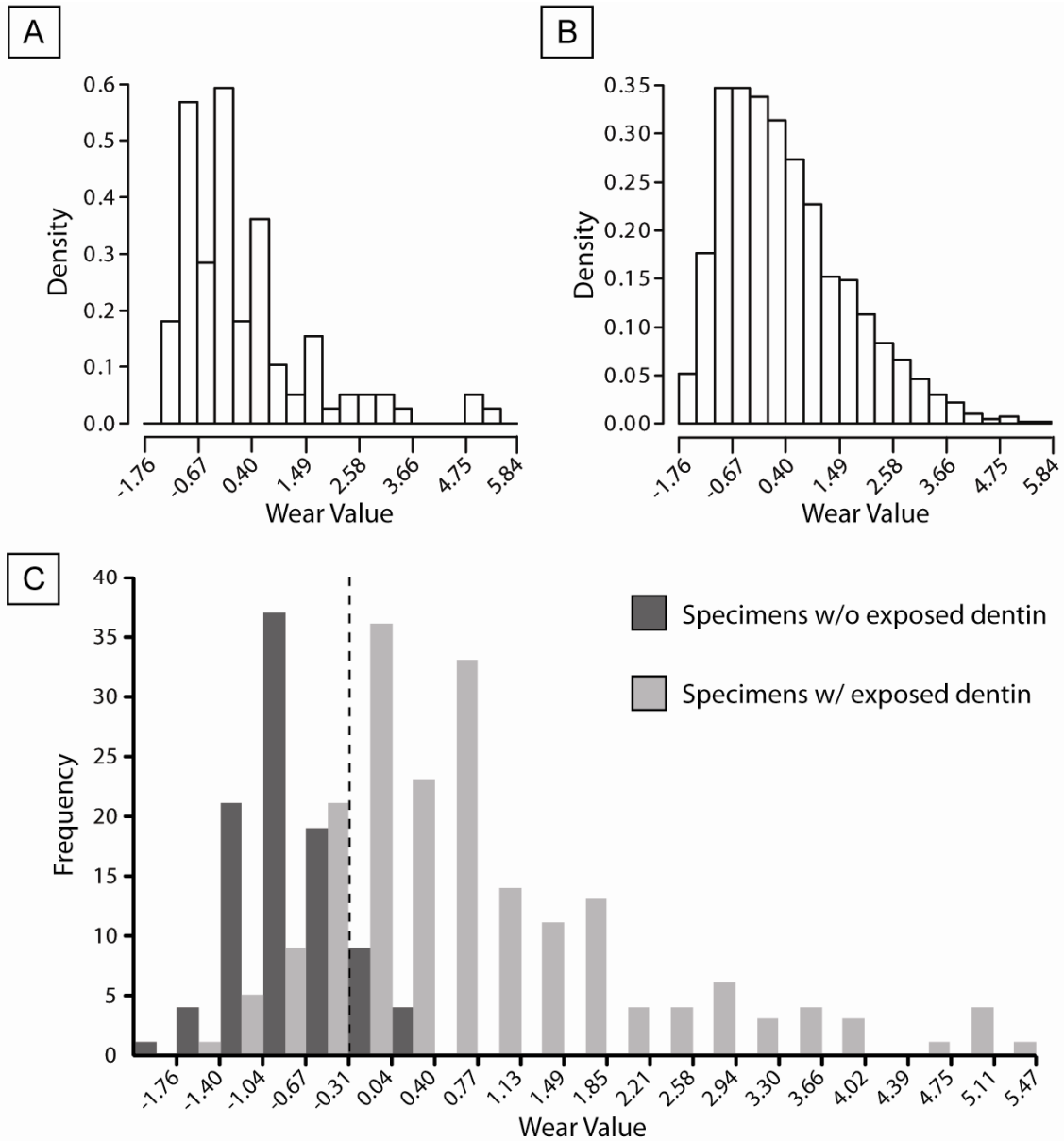


Figure 3.6 Minimal shape variance due to simulated directional selection detected by the excursion, angular, and Monte Carlo LRI tests plotted against the amount of shape variance due to sampled dental wear. Steeper slope values indicate greater sensitivity to the effects of dental wear. The excursion test consistently had a greater success rate in correctly rejecting the null hypothesis of a random walk.

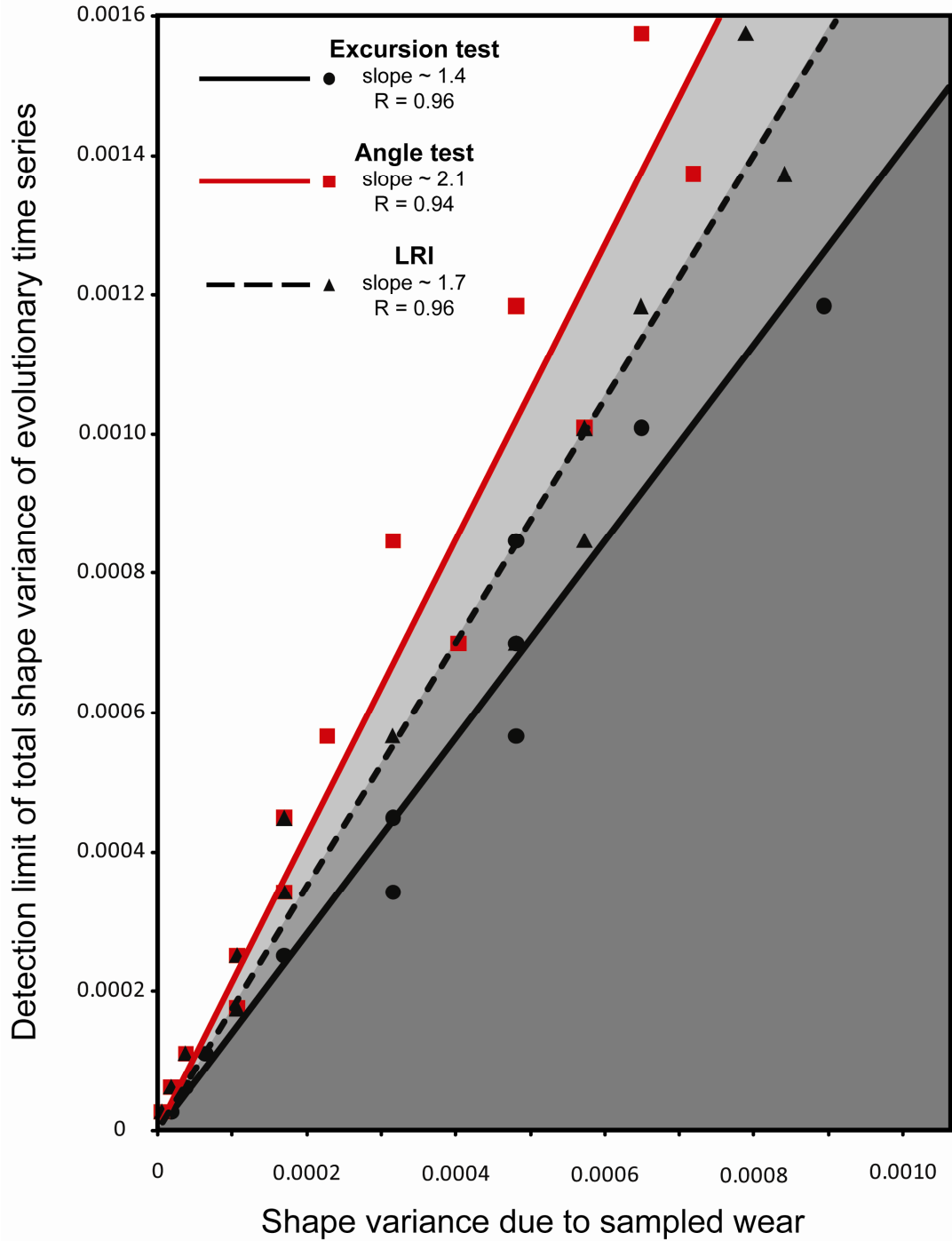


Figure 3.7 Principal components results for directional selection simulations. A-E) PC1/PC2 score distribution of m2 buccal shapes generated in the 0.6 strength directional selection simulations at different levels of sampled dental wear. Colors indicate simulated shapes belonging to specific time steps. G-H) Distribution of PC1/PC2 scores of simulated dental shapes in the 5 x directional wear simulations. F & I) Change in the percentage of overall shape variance explained by PC1 and PC2 as more dental wear is sampled in the static and directional wear simulations, respectively. Unique minimum in percent of variance explained by PC1 coincides with the amount of sampled wear at which the majority of evolutionary tests no longer directional trends.

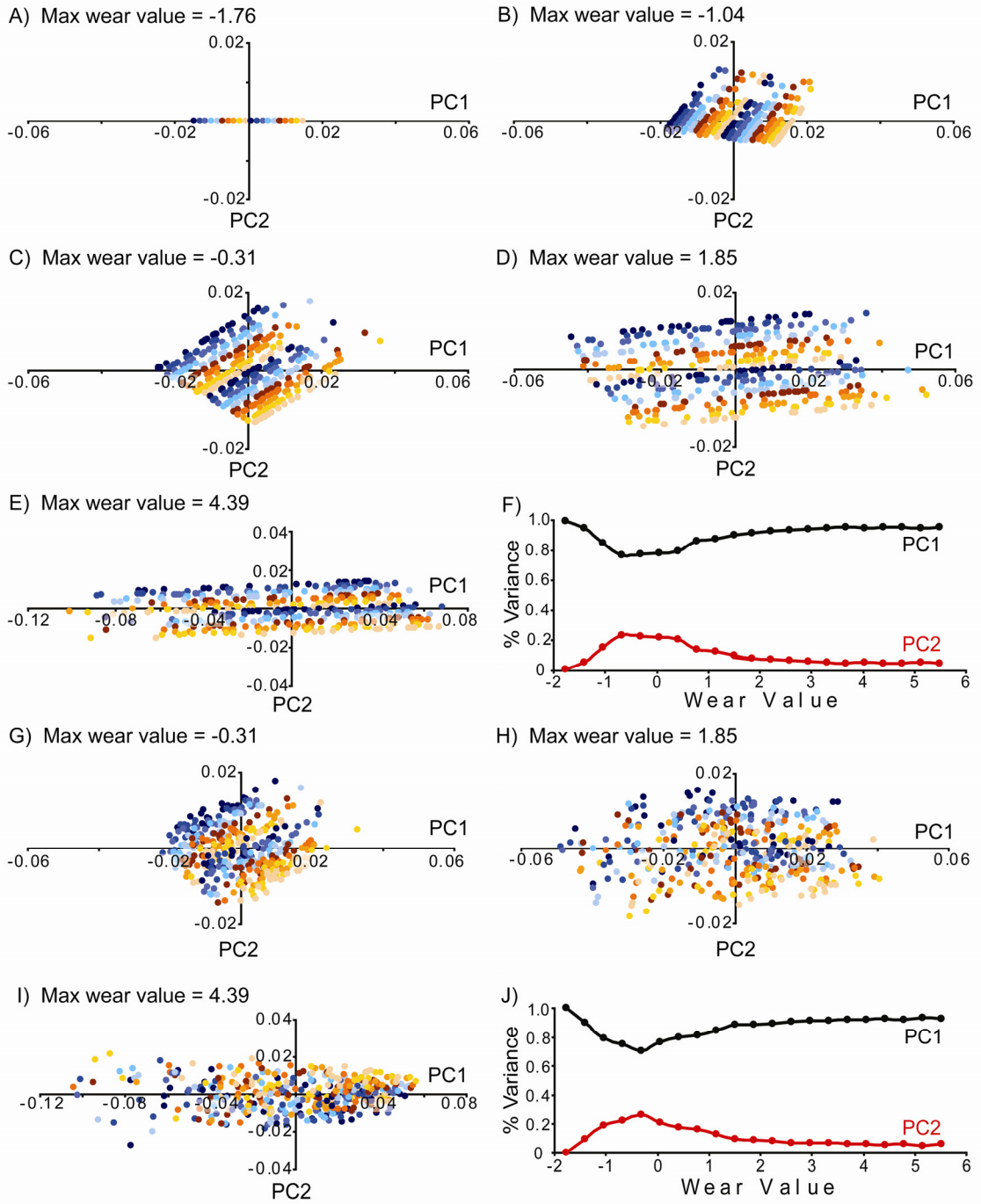
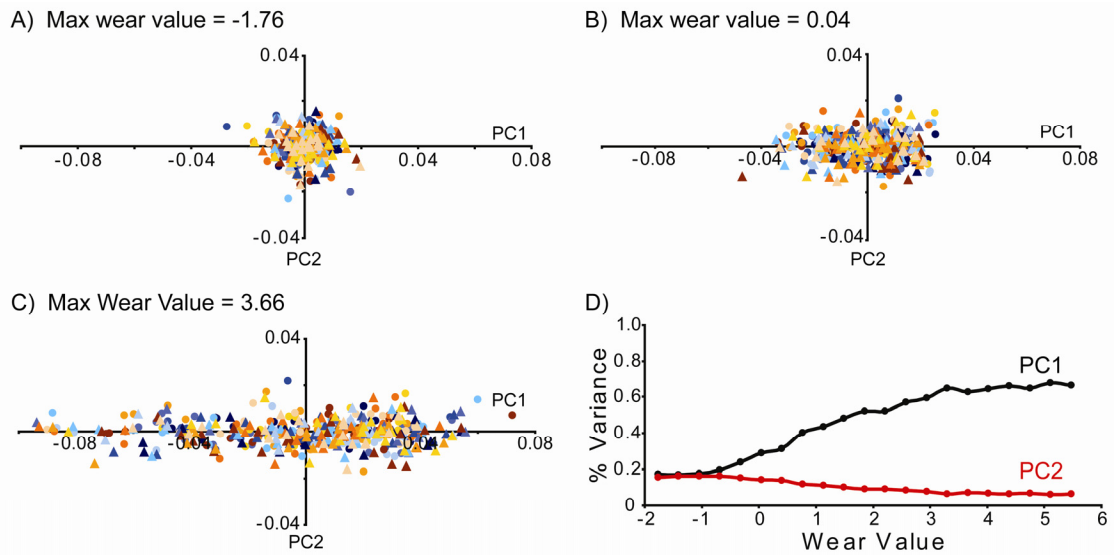


Figure 3.8 Principal components results for stasis simulations. A-C) Distribution of PC1/PC2 scores for a simulation of evolutionary stasis (adaptive peak radius = 0.032 Procrustes distance units). No temporal separation of scores occurs regardless of the amount of dental wear sampled. D) Change in the percentage of overall shape variance explained by PC1 and PC2 as more dental wear is sampled.



## References

- Clyde, W. C. and P. D. Gingerich. 1994. Rates of evolution in the dentition of early Eocene *Cantius*: Comparison of size and shape. *Paleobiology* 20: 506-522.
- Evans, A. R., J. Hunter, M. Fortelius, and G. D. Sanson. 2005. The scaling of tooth sharpness in mammals. *Annales Zoologici Fennici* 42: 603-613.
- Faraway, J. J. 2004. *Linear models with R*. Chapman and Hall, London.
- Fortelius, M. and N. Solounias. 2000. Functional characterization of ungulate molars using the abrasion-attrition wear gradient: A new method for Reconstructing Paleodiets. *American Museum Novitates* 3301: 1-36.
- Gingerich, P. D. 1993. Quantification and comparison of evolutionary rates. *American Journal of Science* 293A: 453-478.
- 2001. Rates of evolution on the time scale of the evolutionary process. *Genetica* 112: 127-144.
- 2003. Mammalian responses to climate change at the Paleocene-Eocene boundary: Polecat Bench record in the northern Bighorn Basin, Wyoming. *In* Gingerich, P. D., Schmitz, B., Thomas, E., and Wing, S. L., eds., *Causes and consequences of globally warm climates in the early Paleogene*: Geological Society of America Special Paper 369: 463-478.
- Gingerich, P. D. and G. F. Gunnell. 1995. Rates of evolution in Paleocene-Eocene mammals of the Clarks Fork Basin, Wyoming, and a comparison with Neogene Siwalik lineages of Pakistan. *Palaeogeography, Palaeoclimatology, Palaeoecology* 115: 227-247.
- Hillson, S. 1990. *Teeth*. Cambridge University Press, Cambridge.
- Jernvall, J., S. V. E. Keranen, and I. Thesleff. 2000. Evolutionary modification of development in mammalian teeth: Quantifying gene expression patterns and topography. *Proceedings of the National Academy of Science* 97: 14444-14448.
- Kaiser, T. M. and M. Fortelius. 2003. Differential mesowear in occluding upper and lower molars: Opening mesowear analysis for lower molars and premolars in hypsodont horses. *Journal of Morphology* 258: 67-83.
- Lieberman, B. S., C. E. Brett, and N. Eldredge. 1995. A study of stasis and change in two species lineages from the Middle Devonian of New York State. *Paleobiology* 21: 15-27.



- Mihlbachler, M. C. 2003. Demography of late Miocene rhinoceroses (*Teleoceras proterum* and *Aphelops malacorhinus*) from Florida: Linking mortality and sociality in fossil assemblages. *Paleobiology* 29: 412-428.
- Piras, P., F. Marcolini, P. Raia, M. T. Curcio, and T. Kotsakis. 2009. Testing evolutionary stasis and trends in first lower molar shape of extinct Italian populations of *Terricola savii* (Arvicolidae, Rodentia) by means of geometric morphometrics. *Journal of Evolutionary Biology* 22: 179-191.
- Polly, P. D. 1998. Variability, selection, and constraints: Development and evolution in viverravid (Carnivora, Mammalia) molar morphology. *Paleobiology* 24: 409-429.
- 2002. Phylogenetic tests for differences in shape and the importance of divergence times. *In* N. MacLeod and P. L. Forey, eds., *Morphology, Shape and Phylogeny: Systematics Association Special Volume Series* 64: 220-246.
- 2004. On the simulation of the evolution of morphological shape: Multivariate shape under selection and drift. *Palaeontologica Electronica* 7: 28 pp.
- Popowics, T. E. and M. Fortelius. 1997. On the cutting edge: Tooth blade sharpness in herbivorous and faunivorous mammals. *Annales Zoologici Fennici* 34: 73-88.
- Radinsky, L. 1969. The early evolution of the Perissodactyla. *Evolution* 23: 308-328.
- Rensberger, J. M. 1986. Early chewing mechanisms in mammalian herbivores. *Paleobiology*: 12: 474-494.
- Rohlf, F. J. 1996. TPSDig2 v. 2.10. Stony Brook morphometrics software series. Available at <http://life.bio.sunysb.edu/morph/>.
- 2005. TPSRegress v. 1.31. Stony Brook morphometrics software series. Available at <http://life.bio.sunysb.edu/morph/>.
- Rohlf, F. J. and F. L. Bookstein. 2003. Computing the uniform component of shape variation. *Systematic Biology* 52: 66-69.
- Roopnarine, P. D., G. Byars, and P. Fitzgerald. 1999. Anagenetic evolution, stratophenetic patterns, and random walk models. *Paleobiology* 24: 41-57.
- Roth, V. L. and J. Shoshani. 1988. Dental identification and age determination in *Elephas maximus*. *Journal of Zoology* 214: 567-588.
- Salazar-Ciudad, I. and J. Jernvall. 2002. A gene network model accounting for development and evolution of mammalian teeth. *Proceedings of the National Academy of Science* 99: 8116-8120.

- Scott, E. C. 1979. Dental wear scoring technique. *American Journal of Physical Anthropology* 51: 213-217.
- Sheets, H. D. 2000. TMorphGen v. 6. IMP series software. Available at <http://www3.canisius.edu/~sheets/morphsoft.html>.
- 2003. Semiland v. 6. IMP series software. Available at <http://www3.canisius.edu/~sheets/morphsoft.html>.
- 2005. MakeFan v. 6. IMP series software. Available at <http://www3.canisius.edu/~sheets/morphsoft.html>.
- Sheets, H. D., K. Kim, and C. E. Mitchell. 2001. A multivariate approach to random walks in the fossil record. Geological Society of America, Annual Meeting.
- Sheets, H. D. and C. E. Mitchell. 2001. Why the null matters: Statistical tests, random walks and evolution. *Genetica* 112: 105-125.
- Slice, D. E., F. L. Bookstein, L. F. Marcus, and F. J. Rohlf. 1996. A glossary for geometric morphometrics. *In* L. F. Marcus, M. Corti, A. Loy, G. J. P. Naylor, and D. E. Slice, eds., *Advances in Morphometrics* 284: 531-551.
- Ungar, P. and M. Williamson. 2000. Exploring the effects of tooth wear on functional morphology: A preliminary study using dental topographic analysis. *Palaeontologia Electronica* 3: 18 pp.
- Wesley-Hunt, G. D. 2005. The morphological diversification of carnivores in North America. *Paleobiology* 31: 35-55.
- Wood, A. R., M. L. Zelditch, A. N. Rountrey, T. P. Eiting, H. D. Sheets, and P. D. Gingerich. 2007. Multivariate stasis in the dental morphology of the Paleocene-Eocene condylarth *Ectocion*. *Paleobiology* 33: 248-260.
- Zelditch, M. L., D. L. Swiderski, H. D. Sheets, and W. L. Fink. 2004. *Geometric morphometrics for biologists: A primer*. Elsevier, London.

## Chapter 4

### **Dental Wear and the Evolution of Dental Morphology in the *Hyracotherium* Lineage from the Clarks Fork and northwestern Bighorn Basins, Wyoming**

The purpose of this chapter is to investigate the evolutionary dynamics of the lower dental morphology in the Clarks Fork and northwestern Bighorn Basin lineage of *Hyracotherium*. This investigation includes analyzing evolutionary time series of both dental size and dental shape to provide a better understanding of the evolutionary processes that affected *Hyracotherium*, as manifested via lower dental morphology, during the early Eocene. Additional objectives of this chapter are to reassess recent taxonomic work pertaining to the Clarks Fork and northwestern Bighorn Basin *Hyracotherium* and to explore what information dental wear can provide about mastication in this early Eocene equid.

#### **An Early Eocene *Hyracotherium* Lineage?**

Gingerich (1991) used a stratophenetic approach to assign species to the Clarks Fork and northwestern Bighorn Basin *Hyracotherium* based mainly on changes in m1 crown area, noting the lack of other consistent morphological differences between taxa (see Chapter 1). To summarize, *H. sandrae* (Wa-0) differed from *H. grangeri* (Wa-1 to Wa-3a) by being 15-20% smaller, *H. grangeri* differed from *H. aemulor* (Wa-3b) by

being 16% smaller, and *H. aemulor* differed from *H. pernix* (Wa-4) by being 14-15% larger (Fig. 1.2). The biostratigraphic record documented by Gingerich (1991) suggests potential ancestor-descendant relationships among *Hyracotherium* taxa, which would constitute a relatively, long continuous lineage of early Eocene equids. Recent work by Froehlich (2002) and Chew (2005, 2009), however, does not support the presence of a single lineage of *Hyracotherium* taxa during the Wasatchian, and instead suggests a more complicated history of immigration, extinction, and differential abundances of closely related taxa.

An ancestor-descendant relationship between *Hyracotherium sandrae* and *Hyracotherium grangeri* has been questioned on two accounts. Firstly, Gingerich (1991) noted that these taxa may have co-occurred during the Wa-0 biozone with *H. sandrae* being the more abundant equid. Wood et al. (2008) described consistent taphonomic differences between the Wa-0 *H. sandrae* and *H. grangeri* specimens collected from the northwestern Bighorn Basin, arguing that rare specimens of *H. grangeri* represent fossil contaminants eroded and transported from younger, overlying sediment. Wood et al. (2008) described potential source horizons for the fossil contaminants and used a vertical model of downslope contamination to conclude that the presence of *H. grangeri* in Wa-0 can be explained by contamination alone.

Secondly, the cladistic analysis of Froehlich (2002) divided the Clarks Fork and Bighorn Basin *Hyracotherium* into 2 genera, renaming the Wa-0 taxon *Sifrihippus sandrae* and the remaining taxa *Arenahippus*. This assignment was based primarily on the presence of an anterior trigonid fovea in *Sifrihippus sandrae*, with further support from secondary characters involving continuous measurements of the lower dentition.

The large sample sizes of lower dentitions available in this study will be used to determine the variability of the presence of an anterior trigonid fovea is among the *Hyracotherium* taxa to determine how informative this character is in resolving early equid taxonomy.

Chew (2005, 2009) documented the stratigraphic range of *Hyracotherium aemulor* as overlapping the ranges of *H. grangeri* and *H. pernix* in the central Bighorn Basin, precluding an ancestor-descendant relationship between *H. aemulor* and the other taxa. These species were identified by Chew (2005) via differences in m1 size, in addition to the presence of a crenulated m3 heel and the absence of a distinctive entoconid on p4 in *H. aemulor* [Appendix 4 of Chew (2005)]. No unequivocal characters were provided to distinguish *H. grangeri* from *H. pernix*. Chew (2005) further suggested that *H. grangeri* and *H. pernix* may represent a single lineage.

The difference in temporal distribution of *Hyracotherium* m1 size between northwestern and central portions of the Bighorn Basin are likely due to differences in sedimentation rates and the precision of stratigraphic correlation of fossil localities. Early Wasatchian deposits are typically thicker in the northwestern basin (Clyde, 2001), providing greater temporal resolution and lower time-averaging of faunal assemblages. The sedimentation rate in the central basin did not significantly increase and approach the sedimentation rate of the northwestern basin until the Wa-5 biozone (Chew, 2005), well above the interval of interest in this study. Furthermore, central Bighorn Basin localities are tied to three composite sections across an area of ~ 2000 km<sup>2</sup> in comparison to the single composite section in the Clarks Fork and northwestern Bighorn Basins (~ 400 km<sup>2</sup>), inherently increasing the amount of error in fossil locality correlation in the central

basin. These observations suggest that the Clarks Fork and northwestern Bighorn Basin record is more representative of the stratigraphic ranges of early Wasatchian

*Hyracotherium*.

The characters of a crenulated m3 heel and absence of a p4 entoconid proposed by Chew (2005) for *Hyracotherium aemulor* weaken the hypothesis of ancestor-descendant relationships between *H. grangeri*, *H. aemulor*, and *H. pernix*. The frequency of these characters among the *Hyracotherium* taxa, including *H. aemulor*, has not been adequately demonstrated using large, stratigraphically-organized samples. Thus, the sampled dentitions in this study will be used to determine whether these characters are limited to *H. aemulor* and therefore represent diagnostic characters for the taxon.

### **Evolutionary Time Series of Dental Size and Shape**

If the *Hyracotherium* taxa constitute a single lineage during the early Wasatchian, then the stratigraphic pattern of m1 crown area documented by Gingerich (1991, 2003) represents an evolutionary time series of morphological change (Fig. 1.2). Gingerich (1993) applied his Log-Rate-Interval (LRI) method to subsets of this time series, producing within-species LRI slopes for *H. grangeri* and *H. aemulor* which he interpreted to be indicative of evolutionary stasis. This interpretation was made by comparing a distribution of observed slope values to a single expected value for the slope generated by a random time series. Sheets and Mitchell (2001) argued, however, that the observed test statistic in an LRI analysis should be compared to a distribution of values produced under the null in order to adequately reject the null hypothesis of a random walk. In this chapter, time series of crown area are subjected to a variant of the LRI

method which produces a distribution of random walk LRI slopes using Monte Carlo techniques (see Chapter 3 for an explanation of Monte Carlo simulations).

The stratigraphic pattern in *Hyracotherium* m1 size (Fig. 1.2) is suggestive of heterogeneous evolutionary dynamics, in which the mode under which a morphology evolves changes between subsets of the time series. For example, m1 crown area may have experienced evolutionary stasis through ~ 300,000 generations of *H. grangeri*, and undergone directional selection for 13,500 generations during the *H. grangeri*/*H. aemulor* transition (Gingerich, 1993). Applying tests of evolutionary mode to subsets of a time series requires an *a priori* hypothesis of when the shift in evolutionary dynamics should occur. A heuristic search approach avoids the prerequisite of *a priori* hypotheses by estimating the optimal shifting point entirely from the data itself in an objective and rigorous manner. The variant of the LRI method used in this chapter approximates a heuristic search by viewing each size time series in a “moving window,” calculating LRI slopes for every possible subset of the time series. The intersection of windows exhibiting statistically-significant evolutionary modes can be interpreted as the shifting point in evolutionary dynamics.

Dental shape in the *Hyracotherium* lineage is also expected to respond to selective pressures imposed by climatic and environmental change during the early Eocene. Dental shape is more closely associated with dental functional morphology than size, reflecting the dietary preferences and mode of mastication of the animal. If climatic or ecological change affects the availability, material properties, or nutritional quality of plant materials, dental morphology, especially dental shape, should experience a change in selective pressures, subsequently leading to morphological change. Previous studies,

however, comparing the evolutionary dynamics of dental size and shape found a disjoint between the modes of size and shape change, indicating that dental size and shape respond differently to the same climatic and ecological perturbations (Clyde and Gingerich, 1994; Wood et al., 2007).

### **Evolutionary Implications of Dental Wear**

Dental wear, as measured using methods presented in Chapter 3, will be used to 1) predict unworn morphologies for specimens with differing amounts of dental wear and 2) study how the distribution of dental wear differs among tooth positions and among *Hyracotherium* taxa. Predicting unworn dental morphologies increases the available sample size for each evolutionary time series and removes sources of variation that may obscure the evolutionary signal in each time series. As shown in Chapter 3, sampling teeth with various amounts of dental wear has the potential to overwhelm the dimension of morphologic variance due to directional selection, leading to a higher occurrence of Type II error when comparing to a null hypothesis of a random walk. Time series exhibiting evolutionary stasis, however, are not sensitive to the variation imposed by dental wear when subjected to the multivariate tests of evolution mode. Removing the effects of dental wear is therefore necessary in order to reliably detect the directional trends in the dental shape time series.

Dental wear will also be used to determine how different portions of each tooth position wear differently in addition to assessing differential wear between positions. One prediction is that the buccal side of each tooth should experience more shape change with increasing wear than the lingual side. The buccal portion of the lower dentition of



*Hyracotherium* possesses a greater proportion of wear facets than the lingual side (Radinsky, 1969), and during the transverse chewing motion, food accumulates on the buccal side, causing any exposed dentin to wear faster and deeper than on the lingual side (Kaiser and Fortelius, 2003). Since dental wear is due to the attrition and abrasion experienced by teeth during mastication, differences in the amount of dental wear of one tooth position per unit wear of another should reflect the relative contributions of each tooth to the mastication.

Finally, comparing the trajectories of dental shape change with increasing dental wear among the *Hyracotherium* species will be used to detect differences in mastication among each. Differing trajectories of shape change could potentially reflect differences in chewing motions or differences in the distribution of enamel and dentin among taxa. If the trajectories of shape change with wear do not vary among *Hyracotherium* taxa despite changes in overall body size, this would indicate teeth maintain functional equivalency without allometric change.

## **Methods**

Specimen preparation and the landmark/semi-landmarks and size measurements taken from each specimen were described in the previous chapter. Isolated teeth and dentary fragments of *Hyracotherium* bearing p4, m1, m2, and/or m3 tooth positions were selected from the Sand Coulee (SC) vertebrate fossil locality series collection at the University of Michigan Museum of Paleontology regardless of the amount of dental wear exhibited. This resulted in sample sizes of 147, 239, 286, and 294 for the respective tooth positions. The stratigraphic distributions of the four tooth positions varied, resulting in

different numbers of time steps in the p4, m1, m2, and m3 evolutionary time series (32, 35, 39, and 36 time steps, respectively).

Each tooth was molded, cast, and photographed in occlusal, buccal, and lingual view using the standardized orientation protocol described in Chapter 3. All right teeth were digitally reflected and analyzed as left teeth. Landmarks and semi-landmarks were digitized in all three views to produce size measurements and coordinates for shape analysis (Fig. 3.2, Fig. 4.1). All landmarks and semi-landmarks were Procrustes superimposed to eliminate variation due to position, scale, and rotation for analysis of dental shape. The perpendicular-sliding semi-landmark alignment method was also used in this chapter.

The positional wear indices for p4, m1, m2, and m3 and the overall wear index used in this chapter were taken directly from work presented in Chapter 3. The wear indices were calculated by using a search program written in the R statistical computing package that performs a principal components analysis (PCA) of all possible combinations of univariate residuals and regresses residual values of exposed dentin area onto the PC1 scores associated with each suite of measurement residuals. Only measurements taken from a subset of teeth with exposed dentin were used in the search program (p4: N = 86, m1: N = 185, m2: N = 197, and m3: N = 118). The suite of measurement residuals whose PC1 scores best predicts the exposed dentin area residuals was used to generate wear index values for each tooth position (i.e. positional wear indices) and all sampled teeth (i.e. overall wear index).

Multivariate shape regression was performed for the buccal and lingual views using the methods described in Chapter 3. Partial warp scores were calculated for each

shape for a given tooth position, and each set of scores was regressed onto the appropriate wear indices to produce vectors of slope coefficients and intercept coefficients for each tooth position in addition to a vector of regression residuals for each individual tooth. Unworn buccal and lingual dental morphologies were estimated for each individual tooth using the regression coefficient vectors and the appropriate residual vector at the lowest observed wear index value for that particular tooth position.

#### Species comparisons of dental wear

A bootstrap method was used to test whether the vector of dental shape change with increasing wear is statistically different between species of the *Hyracotherium* lineage. Only *Hyracotherium grangeri* and *Hyracotherium aemulor* were compared because of inadequate sample sizes of *Hyracotherium sandrae* and *Hyracotherium pernix*. This method uses the null hypothesis of no difference between regression vectors for the two groups, and the null hypothesis can be rejected if the observed angle between observed regression vectors is significantly greater than the range of angles produced from pairs of vectors generated by resampling within each species. Each bootstrap set from a species is generated by sampling shape residuals with replacement from the original shape regression and randomly adding them to the expected shapes at the observed wear values. Each new set of shapes is regressed onto the wear index to produce two new regression vectors, and the angle between the two vectors is calculated. This procedure was performed 900 times for each species to produce a one-sided 95% CI for the angle between regression vectors. If the observed angle falls above the one-sided

95% CI for both species, it can be concluded that the progression of shape change with dental wear differs significantly between the two species.

The wear index values were also used to determine how much dental wear was experienced by one tooth position per unit wear of another position via reduced major axis (RMA) bivariate regression to further compare dentitions of *Hyracotherium grangeri* and *Hyracotherium aemulor*. Several of the sampled teeth can be attributed to individual specimens, such that the wear index value for each position along the tooth row can be measured for an individual. This subset of data was used to produce bivariate plots of wear values between every pair of tooth positions (e.g. p4 vs m1, p4 vs m2, etc), and the slope of each regression indicates how much dental wear was experienced by the tooth position plotted on the y-axis for every unit of dental wear experienced by the tooth plotted on the x-axis. RMA regression was used, because RMA assumes error in both the dependent and independent variables and fits a trend line to the data by minimizing residual values in both variables for each data point.

Confidence intervals for the slope values were produced to determine if the resultant slope significantly deviates from 1. If the slope is significantly lower than 1, than the tooth position plotted on the y-axis wears at a fraction of the dental wear rate of the tooth plotted on the x-axis. Conversely, if the slope is significantly greater than 1, then the x-axis tooth position wears at a fraction of the wear rate of the y-axis tooth position. The differences in dental wear rates between tooth positions could be the result of preferential usage of a tooth position during mastication. Furthermore, significant differences in regression coefficients between *Hyracotherium grangeri* and

*Hyracotherium aemulor* may be indicative of species-specific differences in rates of dental wear with respect to other tooth positions.

#### Tests of evolutionary dynamics

The four time series of dental size (i.e. mean crown area per stratigraphic level) were subjected to a variant of the Monte Carlo log-rate-interval (LRI) test (see Chapter 3) in which an LRI slope is calculated for all possible subsets of time steps. In a typical Monte Carlo LRI analysis, all pairwise rates of morphological change are regressed onto the corresponding interval of time, and the slope of the regression line is compared to a distribution of slopes produced by random walks to determine if the observed slope significantly deviates from the expectation of a random walk. The moving window LRI test calculates an observed LRI slope and distribution of random walk slopes in a window that varies from a minimum of 5 time steps to the length of the entire series. After each calculation, the test window shifts one time step forward in the time series and performs a new set of calculations. Once all possible consecutive subsets are tested at a given window size, the window size increases by one time step and the process is reiterated. A minimum window size of 5 time steps was chosen to provide at least 10 points for the slope calculation. Stratigraphic samples consisting of a single individual were not included in the analyzed time series.

Each subset of results generated in the “moving window” LRI test must be interpreted within the context of the other subsets. A long segment of homogeneous evolutionary dynamics is likely to produce nested subsets each exhibiting the same evolutionary dynamic. Furthermore, subsets exhibiting different evolutionary dynamics

are either likely to overlap or be separated by a series of time steps that cannot be distinguished from a random walk. In these cases, the midpoint of the overlap or random series will be interpreted as the shifting point in evolutionary dynamics.

Morphological time series of size and shape can both be characterized by a magnitude and direction of change between consecutive time steps (Fig. 4.2). The multivariate tests of evolutionary dynamics applied to shape time series are therefore extensions of typical univariate tests, such as the scaled maximum test (Bookstein, 1987; 1988) and runs test (Raup and Crick, 1981). The displacement in shape, however, is described by a vector with  $2n$  elements, where  $n$  is the number of landmarks in the shape configuration. The magnitude of shape change (i.e. Procrustes distance) and the direction of shape change between consecutive time steps (the arccosine of dot product of consecutive vectors of shape change) vary with time in a multidimensional space. Since the magnitude and direction of shape change cannot be summarized by a single value (i.e.  $\Delta x$ ), the combined results of several multivariate tests are necessary to characterize the evolution of shape.

Time series of predicted unworn buccal and lingual shapes for each tooth position were subjected to the 4 tests of evolutionary mode presented in Chapter 3: the excursion test, the angle test, the variance test, and the Monte Carlo LRI test. The excursion test determines whether the maximum excursion observed in a morphological time series significantly deviates from the maximum excursion expected from a random walk. In the angle test, a distribution of random walks is generated in order to determine if the average angle between consecutive steps of a time series significantly deviates from the expectation of a random walk.

The variance test compares the variance at individual time intervals to the overall variance of the time series to determine if the observed time series significantly deviates from the null hypothesis of a time series with static mean and static variance. Similarly to the univariate LRI test, the Monte Carlo LRI analysis of shape involves comparing the LRI slope to a distribution of slopes produced by random walks, but in this variant of the test, the morphological rates are measured in units of Procrustes distance per unit time. Refer back to the methods section of Chapter 3 (pgs 109-114) for detailed explanations of the 4 tests and their implementation.

In contrast to the dental size time series, the excursion, angular, and Monte Carlo LRI tests were applied to shape data over all possible combinations of consecutive biozones (e.g. Wa-0 to Wa-1, Wa-0 to Wa-2, Wa-2 to Wa-4, etc) in order to detect shifts in the evolutionary dynamics of tooth shape in *Hyracotherium*. Testing all possible subsets of each shape time series using the “moving window” approach would be prohibitively time-intensive due to the long processing time necessary to generate and analyze 500 Monte Carlo random walk simulations of shape change.

Estimated unworn buccal and lingual shapes for each tooth position were also subjected to principal components analyses to detect differences in shape between successive time intervals. The outcome of the 4 tests of evolutionary mode described above is dependent of the resolution of the morphological time series, such that short-term directional change between successive intervals may not be detected. PCA results may indicate a significant difference in morphology between successive intervals if the time intervals are separated along principal component axes with significantly large eigenvalues. The use of PCA will be particularly useful in detecting any shape change in

the *H. sandrae* - *H. grangeri* transition that occurs between the first two time steps in each morphological time series.

## Results

### Stratigraphic patterns in crown area

Natural log-transformed crown area of the p4, m1, m2, and m3 positions is plotted against stratigraphic level in Fig. 4.3. At each tooth position, the smallest crown areas occur in the Wa-0 biozone, followed by the intermediate crown areas in the Wa-1 to Wa-3a biozone. In the Wa-3b biozone, the crown area of each tooth position appears to gradually increase, reaching a maximum near the 1900 meter level, after which it gradually decreases to more intermediate values near the Wa-3b/Wa-4 boundary. The magnitude of size change during the Wa-3b biozone varies between the tooth positions, such that m3 exhibits the greatest magnitude of change, followed by p4 and m2. The lower first molar shows little to no size change during the Wa-3b biozone. In the Wa-4 biozone, the crown areas remain near the intermediate values attained in the Wa-1 to Wa-3a biozones. Crown area of m1 decreases slightly through the Wa-1 to Wa-2 biozones consistent with the pattern described by Gingerich (1991, 2003), but such a decrease is not evident in the p4, m2, and m3 crown area time series.

Although gradual increase and decrease in crown area is apparent through the Wa-3b biozone, the size transitions across the Wa-0/Wa-1 boundary and the Wa-2 to Wa-3b biozones appear to be abrupt changes in morphology at the scale shown in Fig. 4.3A. This is unsurprising for the Wa-0 to Wa-1 transition in which the Wa-0 taxon, *Hyracotherium sandrae*, appears in only one stratigraphic interval in the p4 and m1 time



series. There is one individual of *H. sandrae* size at the 1545 m level in the m2 and m3 series that exhibits taphonomic features indicative of Wa-1 preservation. It is unclear whether this specimen represents an intermediate form between *H. sandrae* and *H. grangeri* or is an indication that *H. sandrae* persisted into the Wa-1 biozone.

Closer inspection of the Wa-2 to Wa-3b transition (Fig. 4.3B) reveals that, for the p4 and m3 positions, the increase in crown area may be facilitated by gradual change during the Wa-3a biozone. Contrastingly, the m1 and m2 positions show a sudden increase in crown area variance, especially at the 1750 m level (0.020 and 0.014, respectively), in comparison to the average interval variance for the Wa-2 biozone (0.009 for both m1 and m2). Localities SC133 and SC310, which are included in the 1750 m stratigraphic interval, may comprise time-averaged samples, because each locality's range of crown areas span the full range of values for the entire interval, leading to an erroneous estimate of m1 and m2 variance. It should also be noted that the Wa-3a interval includes only 2 stratigraphic intervals, and at such a low temporal resolution, these observations are tenuous.

#### Temporal distribution of “diagnostic” characters

Anterior trigonid foveae are present in m1 specimens throughout the early Wasatchian (Fig. 4.4). The proportion of the sampled m1 with the anterior trigonid fovea decreases with time, making up 80% of the sample in the Wa-0 biozone, 29% in the Wa-1 biozone, 16% in Wa-2, 12% in Wa-3a, and 13% of the first half of the Wa-3b biozone. Teeth with the anterior trigonid fovea do not appear after the 1850 m level. Similar patterns in the stratigraphic distribution of this character are evident for the m2 position.

Likewise, the subset of specimens without a p4 entoconid follows the same stratigraphic pattern in p4 crown area as the subset with a distinctive entoconid (Fig. 4.5A). Also, the absence of a p4 entoconid in some *H. grangeri* specimens is not due to dental wear. The subsets of specimens with and without a p4 entoconid exhibit nearly identical distributions of wear index values, meaning that those *H. grangeri* specimens without a p4 entoconid are no more worn than those with an entoconid.

#### Regression models for wear indices

The suite of measurements whose PC1 scores best predicted the area of exposed dentin varied among the p4, m1, m2, and m3 tooth positions, producing 4 different positional indices (Tables 4.1-4.4). The protoconid height residual value was the only measurement common to all four positional indices. The top regression model for the p4 positional index produced the lowest  $R^2$  value (0.503) among the top regression models for the other tooth positions and included only the height residuals for the trigonid cusps. Adding the ratio of trigonid cusp heights to the suite of measurements led to a slightly lower correlation (0.486). The two best regression models for the m1 positional index ( $R^2 = 0.779$  and  $0.777$ , respectively) both contained all cusp height residuals, but the best model only contained the hypoconid/entoconid height ratio where the second best model contained both cusp height ratios.

The five best regression models for m2 produced the highest  $R^2$  values among all top five models of the other tooth positions, and these models only differed marginally in  $R^2$  values (0.821 and 0.820, respectively) and in the measurements incorporated (inclusion of the entoconid height residuals and talonid cusp height ratio, respectively).

The best regression model for the m3 positional wear index ( $R^2 = 0.531$ ) contained all cusp height residuals, except the metaconid residuals, as well as the ratio of trigonid cusp heights. The suite of measurements used in the overall wear index presented in Chapter 3 did not match any of the top five positional indices at any tooth position. Correlations between the individual positional indices and the overall wear index varied with tooth position (p4:  $r = 0.80$ , m1:  $r = 0.94$ , m2:  $r = 0.97$ , and m3:  $r = 0.86$ ).

#### Trajectories of shape change with dental wear

The F-statistics for all shape regressions onto the best positional and overall wear indices were statistically-significant ( $p < 0.001$ ) at each tooth position (Table 4.5). The positional index consistently explained a greater proportion of shape variance in comparison to the overall index at each tooth position and view, with m1 lingual shape as the only exception ( $R^2$  of 38.5 and 39.1, respectively). The wear indices explained the greatest proportion of shape variance at the m2 position and the lowest proportion at the m3 position for both views. Furthermore, the positional and overall wear indices consistently explained more variance in buccal shape than lingual shape at each tooth position.

The vector of shape change with increased dental wear as measured by the positional indices did not significantly differ between *Hyracotherium grangeri* and *Hyracotherium aemulor*. At each tooth position, the observed angle between the species vectors of shape change invariably fell within at least one of the species one-sided 95% CIs generated via resampling (Table 4.6). The sample sizes used to perform the species-specific shape regressions for the p4, m1, m2, and m3 positions differed substantially

(103, 185, 204, and 180, respectively, for *H. grangeri*; 32, 35, 61, and 78, respectively, for *H. aemulor*), meaning that outliers in the *H. aemulor* sample will have greater influence in calculating the vector of shape change with dental wear. The greater influence of outliers in the *H. aemulor* sample will lead to consistently larger angles between resampled vectors in comparison to the *H. grangeri* sample, potentially producing a higher occurrence of type II error. Therefore, the range of angles produced by resampling the *H. grangeri* sample may provide a more powerful test. Only the observed angle for m1 lingual shape fell outside the one-sided *H. grangeri* 95% CI, suggesting that there may be a significant difference in how m1 lingual shape changes with wear between the two species.

#### Wear rate results

The rates of dental wear exhibited by the p4, m1, and m2 positions with respect to each other were significantly different between *Hyracotherium grangeri* and *Hyracotherium aemulor* (Tables 4.7 - 4.10). The amount of p4 dental wear per unit m1 wear was significantly lower in *H. aemulor* than in *H. grangeri*, regardless of whether the overall or positional indices were used. Using the overall dental wear index, the amount of m2 dental wear per unit m1 wear was significantly lower in *H. grangeri* than in *H. aemulor*. In both species, the amount of m1 dental wear per unit p4 or m2 dental wear was significantly greater than 1, meaning the m1 position wore faster than either p4 or m2.

The slope values for each regression line with m1 dental wear as the x-variable can be used to describe the contribution of each tooth position to each masticatory stroke

relative to m1. The amount of p4 dental wear per unit m1 wear was significantly closer to 1 in *H. grangeri* than in *H. aemulor* (0.50 and 0.36, respectively) whereas the amount of m2 dental wear per unit m1 wear was significantly closer to 1 in *H. aemulor* than in *H. grangeri* (0.75 and 0.58, respectively). The slope values for the regressions involving m1 and m3 were not statistically significantly different between *H. grangeri* and *H. aemulor* (0.38 and 0.29, respectively, using the overall wear index). Thus, in *H. grangeri*, the contributions of p4, m2, and m3 to the masticatory stroke were 50%, 58%, and 38%, respectively, whereas in *H. aemulor* the contributions were 36%, 75%, and 29%, respectively.

#### Test results of dental size evolution

In p4, m1, and m2 size time series, the “moving window” LRI test detected a statistically-significant directional segment beginning with the Wa-0 (1520 m) time step. The remaining time steps in each of these directional subsets exhibit minor changes in size, such that when the Wa-0 step is not included, these steps exhibit either a random walk or evolutionary stasis. Thus, these directional subsets are not given much weight in interpretations that follow.

Two segments exhibiting evolutionary stasis are evident in the p4 size time series. The first segment spans the Wa-1/Wa-2 boundary whereas the second includes the latest Wa-1 through earliest Wa-3a biozones (Fig. 4.6). These two stasis segments overlap substantially, but no interval including both segments were found to be significantly different from a random walk. The mean p4 size in the lower and upper stasis segments differ only slightly [ $3.23 \ln(\text{mm}^2)$  and  $3.26 \ln(\text{mm}^2)$ , respectively]. The m1 size time

series exhibits a stasis segment (1645 m – 1720 m) within a directional segment (1630 m – 1895 m). The overlap midpoint occurs at the 1700-1720 m levels in the Wa-2 biozone (Fig. 4.7). The directional m1 segment spans the *H. grangeri*/*H. aemulor* transition, in which m1 size changes from 3.42 ln(mm<sup>2</sup>) to 3.88 ln(mm<sup>2</sup>).

Two directional segments (1630 m – 1910 m and 1910 m – 2110 m, respectively) and one stasis segment (1545 m – 1620 m) are evident in the m2 size time series (Fig. 4.8). The lack of overlap among these 3 segments indicates specific transition points at which the evolutionary dynamics shift within the time series (1620-1630 m and 1910 m, respectively). The mean m2 size in the stasis segment is 3.81 ln(mm<sup>2</sup>). In the lowest directional segment, mean m2 size changes from 3.81 ln(mm<sup>2</sup>) to 4.12 ln(mm<sup>2</sup>) during the *H. grangeri*/*H. aemulor* transition and then decreases to 3.78 ln(mm<sup>2</sup>) during the upper directional segment (i.e. the *H. aemulor*/*H. pernix* transition).

Similarly, the m3 size time series exhibits 2 directional segments (1630 m – 1915 m and 1895 m – 2050 m, respectively) and one stasis segment (1545 m – 1760 m) (Fig. 4.9). The overlap midpoint between the stasis segment and the lower directional segment appears at the 1695 m level during the Wa-2 biozone. The mean m3 size during the stasis segment is 4.01 ln(mm<sup>2</sup>). Lower third molar size changes from 4.00 ln(mm<sup>2</sup>) to 4.44 ln(mm<sup>2</sup>) during the lower directional segment (*H. grangeri*/*H. aemulor* transition) and decreases to 3.94 ln(mm<sup>2</sup>) during the upper segment (*H. aemulor*/*H. pernix* transition).

#### Test results of dental shape evolution

Principal components analyses of predicted unworn buccal and lingual shapes show temporal separation only for lower third molar lingual shape (Fig. 4.10). All other

tooth shapes, including m3 buccal shape, completely overlap in PC1/PC2 space at all temporal resolutions. For m3 lingual shape, the shapes corresponding to *Hyracotherium grangeri* and *Hyracotherium aemulor* completely fill the range of PC1 and PC2 scores. Shapes corresponding to *H. sandrae* (Wa-0) and *H. pernix* (Wa-4), however, are separated along PC1, with the exception of 3 outliers in the *H. pernix* sample (Fig. 4.11A). The vector of shape differences along PC1 (39% of overall variance) relates to changes in the inclination of the entoconid and height of the hypoconucristids relative to the metaconid, such that teeth with positive PC1 scores exhibit posteriorly-inclined entoconids and low hypoconucristids. Teeth with negative PC1 scores exhibit nearly vertical entoconids in lingual view and tall hypoconucristids (Fig. 4.11B).

The positive PC1 scores of two of the *H. pernix* outliers (UM67341 and UM73595) may be explained by unusual hypoconucristid morphologies. UM67341 exhibits an unusual amount of dental wear on its hypoconucristid relative to the amount of wear exhibited by the metaconid and entoconid. The orientation of the right hypoconucristid of UM73595 as photographed using the standardized protocol causes the cristid to intersect the posterior margin below the full height of the hypoconulid, leading to an apparently low-lying hypoconucristid. Consequently, the predicted unworn lingual morphologies of UM67341 and UM73595 also reflect unusually low hypoconucristids. The left m3 hypoconucristid of UM73595 does not exhibit this unusual morphology. The orientation of the entoconids in UM67341 and UM73595 is nearly vertical. Conversely, the third outlier, UM73492, possesses a tall hypoconucristid but a posteriorly-inclined entoconid.

“Moving window” LRI results for the time series of m3 lingual shape PC1 scores indicate two statistically-significant segments of evolutionary stasis. The lowest stasis segment (1545 – 1895 m) exhibits a mean PC1 score of zero whereas the upper stasis segment (1915 – 2065 m) exhibits a mean of -0.03. The stasis segments do not overlap, implying that the shift in evolutionary dynamics occurred within the 1895-1915 m interval.

The excursion, angle, and Monte Carlo LRI tests consistently rejected the null hypothesis of a random walk in favor of the alternative of evolutionary stasis for the total time series of p4, m1, m2, and m3 shapes in both buccal and lingual views (Tables 4.11 - 4.18). The maximum observed excursion for all tooth positions and views fell below the 95% CI, indicating less change in dental shape across the total time series than expected from a random walk. The maximum observed excursion in buccal view was less than the maximum excursion in lingual view for the p4, m1, and m3 positions, but the maximum observed excursions were equal in m2 buccal and lingual views (0.061 Procrustes distance units). Furthermore, m2 exhibited the lowest maximum excursions in both buccal and lingual views whereas m1 exhibited the greatest maximum excursions.

The average angle of change for each total time series were less than 180°, yet statistically significantly greater than the distribution of angles produced by random walks, which suggests nonrandom, counteracting changes between time steps of each evolutionary time series. The m2 total time series had the greatest average angle of change among all buccal and lingual shapes (124° and 122°, respectively), whereas the m3 and p4 had the lowest average angle of change among the buccal and lingual time series, respectively (113° and 117°, respectively). There was no consistent difference in



average angle of change between buccal and lingual views among the 4 tooth positions. The observed LRI slope for each total time series was statistically significantly greater than the distribution of slopes produced by random walks, indicating that each time series exhibited more reversals in dental shape than expected from a random walk. The observed LRI slopes ranged from -0.89 (m3 lingual shape) to -0.99 (p4 lingual shape), and, similarly to the angle test results, there was no consistent difference in the observed LRI slope between buccal and lingual views among the 4 tooth positions.

The excursion, angle, and Monte Carlo LRI tests, however, did not consistently reject the null hypothesis of a random walk among the subset time series of dental shape. The excursion and angular tests did not reject the null hypothesis in time series with relatively few time steps, although the angle test appeared to be less sensitive to the number of time steps than the excursion test. In contrast, the Monte Carlo LRI test rejected the random walk null hypothesis in every subset time series, regardless of the number of steps.

The null hypothesis of a static mean and static variance across the total time series was rejected in the variance test for all tooth positions and views. The Wa-0 m1-3 buccal and lingual variances were significantly lower than the total time series variances, but this result is likely due to a small sample size for each tooth position (N = 5, 5, and 12, respectively). Buccal and lingual p4 shape variance from the Wa-1 sample is significantly lower than the total time series variance. This result is relatively robust since the Wa-1 p4 sample has the greatest sample size (N = 37) among all other biozones in the p4 time series. Wa-2 m2 lingual shape variance (N=84) was also significantly lower than the total m2 time series variance. Lingual m3 shape variance was significantly lower than

the total m3 time series variance during the Wa-1 (N = 46) and Wa-3a (N = 27) biozones, but there was only a significant difference during the Wa-3a biozone in m3 buccal view.

## **Discussion**

### Comparison of wear indices

The suite of measurements that best predicted exposed dentin area and is consequently used to produce the positional wear indices is partially related to the distribution of sites of exposed dentin among the five cusps and the unworn heights of the cusps. The measurements used to generate the p4 positional index are derived solely from the trigonid, indicating that the talonid experiences little dental wear in comparison. The talonid of the lower fourth premolar of *Hyracotherium* is not as well developed as the molar talonids, possesses a low entoconid, and lacks a distinctive hypoconulid. Furthermore, the protoconid and metaconid bear the greatest proportion of the exposed dentin sites on the lower fourth premolar (Fig. 4.12). Although the hypoconid does bear a substantial proportion of the total exposed dentin sites, the absolute area of exposed dentin at the hypoconid is slight in comparison to the trigonid exposed dentin even at high levels of dental wear.

The suite of measurements used to generate the m1 and m2 positional wear indices incorporates measurements from both the trigonid and talonid, indicating that dental wear is somewhat equally distributed among the basins. The positional indices differ in that the m1 positional index includes the metaconid and hypoconulid height residuals whereas the m2 positional index does not. Exposed dentin sites are more equally distributed among the buccal and lingual cusps of m1 in comparison to m2,

suggesting more asymmetric dental wear at the m2 position (Fig. 4.12) Inclusion of the hypoconulid height residuals in the m1 positional index appears to be due to the fact that the m1 sample shows a greater range of wear values than m2 (maximum overall wear index value of 12.1 and 5.5, respectively), and at such high levels of m1 dental wear, a relatively small cusp, like the hypoconulid, can substantially contribute to the overall area of exposed dentin.

The suite of measurements used to generate the m3 positional wear index does not include metaconid height residuals and instead includes the ratio of trigonid cusp heights, suggesting asymmetrical dental wear of the trigonid. This asymmetry in dental wear between the buccal and lingual portions of m3 is also apparent in the distribution of exposed dentin sites in which the buccal cusps consistently possess a greater proportion of exposed dentin sites in comparison to their lingual counterparts (Fig. 4.12). The m3 hypoconulid is better developed than the hypoconulid of m1 and m2 and likely functioned as a protoconid of a more posterior tooth during mastication (Radinsky, 1969), explaining its inclusion in the m3 positional wear index despite the fact that m3 experiences less overall dental wear (max overall wear index of 4.2) than either m1 or m2.

The overall wear index only includes height residuals for the protoconid, hypoconid, and entoconid (see Chapter 3), also reflecting asymmetry in dental wear at the trigonid. The positional wear indices of p4 and m1 do not support such asymmetric dental wear, indicating that the large sample sizes of m2 and m3 teeth may have biased the results of the search program used to generate the overall wear index ( $N = 315$  combined for m2 and m3 compared to  $N = 271$  for p4 and m1). The overall wear index, however, appears to be a fairly robust measure of dental wear at all 4 tooth positions in

comparison to the positional indices, since the correlations between each positional index and the overall index are all relatively high ( $r = 0.80-0.97$ ).

#### Morphometric reassessment of *Hyracotherium* taxonomy

Anterior m1 and m2 trigonid foveae, crenulated m3 heels, and presence/absence of p4 entoconids are not diagnostic characters for resolving *Hyracotherium* taxonomy. Not all Wa-0 specimens of *H. sandrae* size exhibit anterior trigonid foveae, just as not all Wa-3b specimens of *H. aemulor* size lack p4 entoconids. Furthermore, the anterior trigonid fovea appears to be better developed in younger taxa that have been attributed to *H. grangeri* than in most *H. sandrae* specimens (compare the *H. grangeri* at 1545 m to the *H. sandrae* specimen at 1520 m in Fig. 4.4B). Crenulations on enamel surfaces, like the m3 heel, are quickly eroded after minor amounts of wear, and some specimens *H. grangeri* with low dental wear possess crenulated m3 heels. Teeth with these characters follow the same stratigraphic pattern in crown area as teeth without them (Fig. 4.4A & 4.5A). Instead of explaining these observations as the presence of nearly indistinguishable, contemporaneous equid taxa following the same evolutionary trends in overall body size, a much simpler hypothesis would be that trigonid foveae, crenulated m3 heels, and p4 entoconids are highly variable characters in this lineage.

PCA results for unworn buccal and lingual shapes at each tooth position provide no evidence that the Clarks Fork and northwestern Bighorn Basin *Hyracotherium* species represent separate lineages. Complete overlap of the distribution of PC1/PC2 scores for p4, m1, m2, and buccal m3 shape suggest no change in tooth shape with time. In addition, temporal separation of lingual m3 PC scores does not refute the hypothesis of a

single lineage existing in the Clarks Fork and northwestern Bighorn Basins through the Wa-0 to Wa-4 biozones and, rather, supports a hypothesis of gradual evolutionary change within a single lineage of horses. It is possible that lingual m3 shape became more variable after the first appearance of *Hyracotherium* during the Wa-1 to Wa-3b biozones and later became constrained to a morphology with greater fitness during the Wa-4 biozone. Lower third molars with vertically-oriented metaconids and entoconids are more similar to the condition exhibited by the lingual cusps of m1 and m2, realigning the transverse crests of m3 to be parallel to those of m1-2. Realignment of the transverse m3 crests would have been adaptive by lengthening the area of the molar row used for shearing and thereby increasing the amount of food processed per chewing stroke (Janis and Fortelius, 1988).

The statistically-indistinguishable trajectories of shape change with increased dental wear between *Hyracotherium grangeri* and *Hyracotherium aemulor* suggests that the role of each tooth position during mastication remained constant across the species transition, providing further support for a continuous lineage through the early Wasatchian. This result, combined with the PCA results showing complete overlap of *H. grangeri* and *H. aemulor* unworn shapes, suggests that despite changes in tooth size, functional equivalency of dental morphology was maintained without changes in tooth shape. Similar patterns have been documented for lineages of the early Eocene primate *Cantius* and phenacodontid *Ectocion* in which functional dental morphology scaled isometrically with changes in body size (Clyde and Gingerich, 1994 and Wood et al., 2007; respectively). It is possible that the trajectory of shape change with wear may be

different for *H. sandrae* or *H. pernix*, especially at the m3 position, but this cannot be tested with current sample sizes.

#### Mastication in *Hyracotherium grangeri* and *Hyracotherium aemulor*

The amount of dental wear experienced by one tooth position per unit of dental wear experienced by another position indicates the relative differences in usage of each position during mastication. The results shown in Tables 4.7 – 4.10 suggest that the contribution of each cheek tooth to food processing during each masticatory stroke varies between *Hyracotherium grangeri* and *Hyracotherium aemulor*, such that the contribution of p4 decreases and contribution of m2 increases in the *H. grangeri* - *H. aemulor* transition. In both species, the lower first molar shows the greatest amount of dental wear per unit wear of the other positions, indicating that m1 contributes the most during each masticatory stroke.

One possible reason for the fact that m1 contributes the most to each chewing stroke in *Hyracotherium* is that the lower first molar may experience the greatest occlusal force generated by the masticatory muscles, as was directly measured in humans by Spencer (1998). It is possible that in the *H. grangeri* - *H. aemulor* transition the position of greatest occlusal force moved posteriorly from being nearly equidistant from the p4 and m2 position to being closer to the m2 position. The position of greatest occlusal force is a function of masticatory muscle geometry, including cross-section thickness, fiber types, fiber orientations, etc, as well as mandibular geometry, such as relative positions of the dental arcade, temporomandibular joint, and masticatory muscle insertion sites (Weijs, 1980; Herring, 1985; Spencer, 1998; Greaves, 2000). Only mandibular

geometry can be compared between *H. grangeri* and *H. aemulor*, and based on the best preserved mandibular specimens of *H. grangeri* and *H. aemulor*, the projected length between m1 and the mandibular condyle is 3% greater in *H. aemulor* at uniform overall jaw lengths. Determining whether or not this slight change in tooth row positioning (or any other aspect of mandibular morphology) is sufficient to explain the patterns in wear rates will require larger sample sizes.

#### Evolutionary dynamics of the *Hyracotherium* lineage

The “moving window” LRI indicates heterogeneous evolutionary dynamics in dental size at all four tooth positions, implying that selection pressures on dental and overall body size varied during the duration of the *Hyracotherium* lineage. Each time series includes a static segment during portions of the *H. grangeri* stratigraphic range, indicating that selective pressures on dental and body size were relatively constant during this time. Sometime during the Wa-2 biozone, however, selective pressures changed, favoring larger tooth and body sizes as indicated by directional trends across the *H. grangeri*/*H. aemulor* transition. This directional increase in molar size reached a maximum during 1895 – 1915 m interval of the Wa-3b biozone, after which smaller dental and body sizes were selected for, especially at the m2 and m3 positions.

Constrastingly, the combined results of the excursion, angle, Monte Carlo LRI, and variance tests indicate that lower dental shape in the Clarks Fork and northwestern Bighorn Basin *Hyracotherium* lineage exhibits evolutionary stasis over the ~ 1.5 million years sampled. The mean shape changed less than expected from a random walk (i.e. excursion test results) and exhibited more reversals than expected from a random walk

(i.e. angle and Monte Carlo LRI results) over the total time series. This pattern in mean lower dental shape is also present in the subset time series with the exception of those temporal subsets with relatively few time steps.

Although the mean lower dental shape appears to be static through the *Hyracotherium* lineage, dental shape variance was not static at the p4, m2, and m3 positions, suggesting temporal change in morphological constraints at these positions. Both stabilizing selection and intrinsic constraints can account for a pattern of static mean and changing morphological variance. Under stabilizing selection, change in morphological variance can be explained by changes in the selective constraints around the optimal phenotype, such that the fitness of relatively extreme phenotypes changes with time as selective pressures relax or strengthen.

Intrinsic constraints, specifically epistatic interactions, can also explain this pattern if the genetic background of a gene is altered sufficiently via selection to subsequently promote an increase in variation of that gene's expressed effects (Hansen and Wagner, 2001; Hansen and Houle, 2004). Although development of each molar position involves the same set of 50 genes (Salazar-Ciudad and Jernvall, 2002; Workman et al., 2002), the fact that the individual tooth positions of *Hyracotherium* exhibit differing patterns in variance does not exclude changes in epistatic variation as a causal mechanism, because differential spatial expression of transcription factors common to all tooth positions is important in determining tooth identity and cusp configurations in mammalian dentitions (Salazar-Ciudad and Jernvall, 2002).

Although the time series of PC1 scores for m3 lingual shape does exhibit evolutionary stasis, the “moving window” LRI results indicates the m3 lingual shape



moved to a new optimal shape during the 1895 – 1915 m interval. This interval coincides with a shift in evolutionary dynamics in m2 and m3 crown area. If the shift in crown areas dynamics and optimal m3 lingual shape are due to the same selective pressures, then it appears that dental size and shape evolve at different rates to reach their respective optimal morphologies.

Table 4.1 Top five regression models for the lower fourth premolar (p4) positional wear index with associated  $R^2$  values. In each model, the measurements listed were subjected to principal component analysis, and the area of exposed dentin was regressed onto the resultant set of PC1 scores. The model with the highest  $R^2$  value was used as the positional wear index in all subsequent analyses.

<b><u>Model rank</u></b>	<b><u>p4 measurements</u></b>	<b><u><math>R^2</math></u></b>
1	1) Ln protoconid height residuals 2) Ln metaconid height residuals	0.503
2	1) Ln protoconid height residuals 2) Ln metaconid height residuals 3) Protoconid height/ metaconid height ratio	0.486
3	1) Ln protoconid height residuals 2) Ln hypoconid height residuals 3) Ln metaconid height residuals 4) Ln entoconid height residuals	0.459
4	1) Ln protoconid height residuals 2) Ln hypoconulid height residuals 3) Ln lingual view centroid size 4) Ln metaconid height residuals	0.435
5	1) Ln protoconid height residuals 2) Ln hypoconulid height residuals 3) Ln lingual view centroid size 4) Ln metaconid height residuals 5) Ln entoconid height residuals	0.434

Table 4.2 Top five regression models for the lower first molar (m1) positional wear index with associated R<sup>2</sup> values. The model with the highest R<sup>2</sup> value was used as the positional wear index in all subsequent analyses.

<b><u>Model rank</u></b>	<b><u>m1 measurements</u></b>	<b><u>R<sup>2</sup></u></b>
1	1) Ln protoconid height residuals 2) Ln hypoconid height residuals 3) Ln hypoconulid height residuals 4) Ln metaconid height residuals 5) Ln entoconid height residuals 6) Hypoconid height/ entoconid height ratio	0.779
2	1) Ln protoconid height residuals 2) Ln hypoconid height residuals 3) Ln hypoconulid height residuals 4) Ln metaconid height residuals 5) Ln entoconid height residuals 6) Protoconid height/ metaconid height ratio 7) Hypoconid height/ entoconid height ratio	0.777
3	1) Ln protoconid height residuals 2) Ln hypoconid height residuals 3) Ln hypoconulid height residuals 4) Ln metaconid height residuals 5) Ln entoconid height residuals 6) Protoconid height/ metaconid height ratio	0.774
4	1) Ln buccal view centroid size 2) Ln protoconid height residuals 3) Ln hypoconid height residuals 4) Ln hypoconulid height residuals 5) Ln metaconid height residuals 6) Ln entoconid height residuals 7) Protoconid height/ metaconid height ratio 8) Hypoconid height/ entoconid height ratio	0.771
5	1) Ln protoconid height residuals 2) Ln hypoconid height residuals 3) Ln hypoconulid height residuals 4) Ln lingual view centroid size 5) Ln metaconid height residuals 6) Ln entoconid height residuals 7) Protoconid height/ metaconid height ratio	0.768

Table 4.3 Top five regression models for the lower second molar (m2) positional wear index with associated R<sup>2</sup> values. The model with the highest R<sup>2</sup> value was used as the positional wear index in all subsequent analyses.

<b><u>Model rank</u></b>	<b><u>m2 measurements</u></b>	<b><u>R<sup>2</sup></u></b>
1	1) Ln protoconid height residuals 2) Ln hypoconid height residuals 3) Ln metaconid height residuals 4) Ln entoconid height residuals	0.821
2	1) Ln protoconid height residuals 2) Ln metaconid height residuals 3) Ln entoconid height residuals 4) Hypoconid height/ entoconid height ratio	0.820
3	1) Ln hypoconid height residuals 2) Ln metaconid height residuals 3) Ln entoconid height residuals 4) Protoconid height/ metaconid height ratio	0.811
4	1) Ln protoconid height residuals 2) Ln hypoconid height residuals 3) Ln hypoconulid height residuals 4) Ln metaconid height residuals 5) Ln entoconid height residuals	0.807
5	1) Ln protoconid height residuals 2) Ln hypoconid height residuals 3) Ln metaconid height residuals 4) Ln entoconid height residuals 5) Hypoconid height/ entoconid height ratio	0.795

Table 4.4 Top five regression models for the lower third molar (m3) positional wear index with associated R<sup>2</sup> values. The model with the highest R<sup>2</sup> value was used as the positional wear index in all subsequent analyses.

<b>Model rank</b>	<b>m3 measurements</b>	<b>R<sup>2</sup></b>
1	1) Ln protoconid height residuals 2) Ln hypoconid height residuals 3) Ln hypoconulid height residuals 4) Ln entoconid height residuals 5) Ln hypoconucristid height residuals 6) Protoconid height/ metaconid height ratio	0.531
2	1) Ln protoconid height residuals 2) Ln hypoconid height residuals 3) Ln hypoconulid height residuals 4) Ln entoconid height residuals 5) Ln hypoconucristid height residuals 6) Protoconid height/ metaconid height ratio 7) Hypoconid height/ entoconid height ratio	0.518
3	1) Ln hypoconid height residuals 2) Ln hypoconulid height residuals 3) Ln entoconid height residuals 4) Ln hypoconucristid height residuals 5) Protoconid height/ metaconid height ratio 6) Hypoconid height/ entoconid height ratio	0.517
4	1) Ln protoconid height residuals 2) Ln hypoconid height residuals 3) Ln hypoconulid height residuals 4) Ln lingual view centroid size 5) Ln entoconid height residuals 6) Ln hypoconucristid height residuals 7) Protoconid height/ metaconid height ratio	0.517
5	1) Ln protoconid height residuals 2) Ln hypoconid height residuals 3) Ln hypoconulid height residuals 4) Ln metaconid height residuals 5) Ln entoconid height residuals 6) Ln hypoconucristid height residuals 7) Hypoconid height/ entoconid height ratio	0.508

Table 4.5 Multivariate shape regression results in which Procrustes superimposed coordinates of buccal and lingual shapes were regressed onto the relevant positional wear index and the overall wear index. All regressions are statistically significant, and the positional indices explain more shape variance than the overall wear index, with the exception of m1 lingual shape.

<b>Tooth position/view</b>	<b>Wear index</b>	<b>% shape variance explained by wear</b>	<b>F</b>	<b>df</b>	<b>p-value</b>
p4/buccal	Position index	37.5	88.6	34, 5032	< 0.001
	Overall index	29.2	61.1	34, 5032	< 0.001
m1/buccal	Position index	44.7	192.3	36, 8640	< 0.001
	Overall index	41.7	169.0	36, 8640	< 0.001
m2/buccal	Position index	51.4	306.7	36, 10440	< 0.001
	Overall index	47.8	265.4	36, 10440	< 0.001
m3/buccal	Position index	29.6	123.4	36, 10584	< 0.001
	Overall index	22.3	84.4	36, 10584	< 0.001
p4/lingual	Position index	25.5	50.6	36, 5328	< 0.001
	Overall index	23.6	45.8	36, 5328	< 0.001
m1/lingual	Position index	38.5	149.3	36, 8640	< 0.001
	Overall index	39.1	151.9	36, 8640	< 0.001
m2/lingual	Position index	42.2	212.1	36, 10440	< 0.001
	Overall index	41.8	208.6	36, 10440	< 0.001
m3/lingual	Position index	14.4	49.7	36, 10584	< 0.001
	Overall index	12.4	41.8	36, 10584	< 0.001

Table 4.6 Angles between vectors of shape change with increasing dental wear in *Hyracotherium grangeri* and *Hyracotherium aemulor*. The observed angle between the species vectors invariably fell within at least one of the species one-sided 95% CIs generated via resampling, indicating no significance difference in how buccal and lingual shape change with wear between the species.

<b>Tooth position</b>	<b>Comparison</b>	<b>Angle between wear vectors (Buccal)</b>	<b>Angle between wear vectors (Lingual)</b>
<b>p4</b>	Between species	13.2°	24.3°
	Within <i>H. grangeri</i>	31.1°	37.3°
	Within <i>H. aemulor</i>	63.2°	73.3°
<b>m1</b>	Between species	13.1°	26.3°
	Within <i>H. grangeri</i>	23.4°	23.8°
	Within <i>H. aemulor</i>	92.0°	100.4°
<b>m2</b>	Between species	11.5°	15.2°
	Within <i>H. grangeri</i>	12.8°	15.5°
	Within <i>H. aemulor</i>	52.4°	61.0°
<b>m3</b>	Between species	14.9°	19.9°
	Within <i>H. grangeri</i>	23.8°	33.8°
	Within <i>H. aemulor</i>	40.8°	54.1°

Table 4.7 Reduced major axis (RMA) results for all pairwise regressions of positional wear indices for *Hyracotherium grangeri*. Each set of data points in the regressions is measured from the same individual, such that the resultant slope indicates the amount of dental wear experienced by one tooth position (y-axis) per unit wear of another position (x-axis). Highlighted cells indicate regression lines that are statistically-significantly different between *H. grangeri* and *H. aemulor*.

***Hyracotherium grangeri***

**Positional index**

X-value/  
Y-value

	p4	m1	m2	m3
p4	---	$y = 1.50x + 0.97$ N = 60 slope (1.26, 1.74) int (0.65, 1.29)	$y = 1.00x + 0.14$ N = 51 slope (0.82, 1.18) int (-0.14, 0.42)	$y = 1.62x - 0.47$ N = 25 slope (1.07, 2.16) int (0.02, 0.92)
m1	$y = 0.67x - 0.65$ N = 60 slope (0.56, 0.77) int (-0.88, -0.42)	---	$y = 0.76x - 0.49$ N = 113 slope (0.71, 0.82) int (-0.59, -0.39)	$y = 0.90x - 0.44$ N = 39 slope (0.70, 1.11) int (-0.75, -0.13)
m2	$y = 1.00x - 0.14$ N = 51 slope (0.82, 1.18) int (-0.42, 0.15)	$y = 1.31x + 0.64$ N = 113 slope (1.21, 1.40) int (0.50, 0.78)	---	$y = 1.21x - 0.03$ N = 73 slope (1.02, 1.22) int (-0.20, 0.14)
m3	$y = 0.62x - 0.29$ N = 25 slope (0.41, 0.83) int (-0.55, -0.03)	$y = 1.11x + 0.49$ N = 39 slope (0.86, 1.36) int (0.14, 0.84)	$y = 0.89x + 0.03$ N = 73 slope (0.81, 0.97) int (-0.13, 0.18)	---



Table 4.8 Reduced major axis (RMA) results for all pairwise regressions of positional wear indices for *Hyracotherium aemulor*. Each set of data points in the regressions is measured from the same individual, such that the resultant slope indicates the amount of dental wear experienced by one tooth position (y-axis) per unit wear of another position (x-axis). Highlighted cells indicate regression lines that are statistically-significantly different between *H. grangeri* and *H. aemulor*.

***Hyracotherium aemulor***

**Positional index**

X-value/  
Y-value

	p4	m1	m2	m3
p4	---	y = 2.29x + 1.34 N = 20 slope (1.39, 3.20) int (0.51, 2.17)	y = 2.19x + 0.58 N = 18 slope (1.22, 3.16) int (-0.26, 1.43)	y = 1.99x + 0.34 N = 8 slope (0.60, 3.39) int (-0.89, 1.57)
m1	y = 0.44x - 0.58 N = 20 slope (0.26, 0.61) int (-1.01, -0.16)	---	y = 0.95x - 0.60 N = 22 slope (0.75, 1.16) int (-0.99, -0.21)	y = 0.75x - 1.11 N = 7 slope (-0.01, 1.50) int (-3.14, 0.92)
m2	y = 0.46x - 0.27 N = 18 slope (0.25, 0.66) int (-0.67, 0.14)	y = 1.05x + 0.63 N = 22 slope (0.83, 1.27) int (0.24, 1.02)	---	y = 1.03x + 0.09 N = 21 slope (0.69, 1.37) int (-0.72, 0.90)
m3	y = 0.50x - 0.17 N = 8 slope (0.15, 0.85) int (-0.80, 0.47)	y = 1.34x + 1.49 N = 7 slope (-0.02, 2.70) int (-0.54, 3.53)	y = 0.97x - 0.09 N = 21 slope (0.65, 1.29) int (-0.88, 0.70)	---

Table 4.9 Reduced major axis (RMA) results for all pairwise regressions of overall wear indices for *Hyracotherium grangeri*. Each set of data points in the regressions is measured from the same individual, such that the resultant slope indicates the amount of dental wear experienced by one tooth position (y-axis) per unit wear of another position (x-axis). Highlighted cells indicate regression lines that are statistically-significantly different between *H. grangeri* and *H. aemulor*.

***Hyracotherium grangeri***

**Overall index**

X-value/  
Y-value

	p4	m1	m2	m3
p4	---	$y = 1.99x + 2.34$ N = 60 slope (1.68, 2.31) int (1.95, 2.74)	$y = 1.14x + 1.39$ N = 51 slope (0.95, 1.33) int (1.15, 1.63)	$y = 1.05x + 1.37$ N = 25 slope (0.71, 1.39) int (0.99, 1.76)
m1	$y = 0.50x - 1.18$ N = 60 slope (0.42, 0.58) int (-1.33, -1.03)	---	$y = 0.58x - 0.01$ N = 113 slope (0.53, 0.63) int (-0.10, 0.08)	$y = 0.38x + 0.19$ N = 39 slope (0.29, 0.47) int (0.05, 0.33)
m2	$y = 0.88x - 1.22$ N = 51 slope (0.73, 1.02) int (-1.42, -1.02)	$y = 1.72x + 0.02$ N = 113 slope (1.58, 1.86) int (-0.13, 0.17)	---	$y = 0.61x + 0.23$ N = 73 slope (0.55, 0.68) int (0.14, 0.32)
m3	$y = 0.95x - 1.31$ N = 25 slope (0.64, 1.26) int (-1.52, -1.09)	$y = 2.63x - 0.49$ N = 39 slope (2.02, 3.25) int (-0.89, -0.10)	$y = 1.63x - 0.37$ N = 73 slope (1.46, 1.81) int (-0.53, -0.21)	---

Table 4.10 Reduced major axis (RMA) results for all pairwise regressions of overall wear indices for *Hyracotherium aemulor*. Each set of data points in the regressions is measured from the same individual, such that the resultant slope indicates the amount of dental wear experienced by one tooth position (y-axis) per unit wear of another position (x-axis). Highlighted cells indicate regression lines that are statistically-significantly different between *H. grangeri* and *H. aemulor*.

***Hyracotherium aemulor***

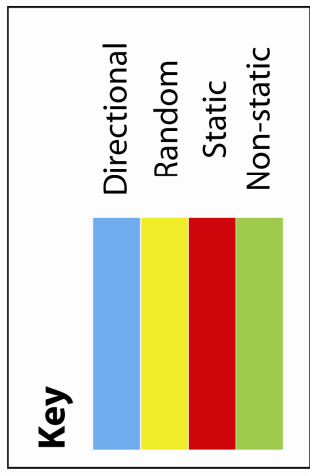
**Overall index**

X-value/  
Y-value

	p4	m1	m2	m3
p4	---	y = 2.81x + 4.57 N = 20 slope (2.03, 3.60) int (3.27, 5.87)	y = 1.68x + 2.76 N = 18 slope (1.03, 2.34) int (1.68, 3.83)	y = 0.83x + 1.05 N = 8 slope (0.35, 1.30) int (0.34, 1.76)
m1	y = 0.36x - 1.62 N = 20 slope (0.26, 0.45) int (-1.82, -1.42)	---	y = 0.75x + 0.07 N = 22 slope (0.64, 0.86) int (-0.12, 0.26)	y = 0.29x - 0.33 N = 7 slope (0.07, 0.51) int (-0.75, 0.09)
m2	y = 0.59x - 1.64 N = 18 slope (0.36, 0.83) int (-1.96, -1.32)	y = 1.34x - 0.09 N = 22 slope (1.14, 1.53) int (-0.34, 0.15)	---	y = 0.55x - 0.09 N = 21 slope (0.40, 0.69) int (-0.33, 0.15)
m3	y = 1.21x - 1.27 N = 8 slope (0.52, 1.90) int (-1.73, -0.82)	y = 3.47x + 1.14 N = 7 slope (0.78, 6.15) int (-0.19, 2.48)	y = 1.83x + 0.16 N = 21 slope (1.35, 2.31) int (-0.27, 0.59)	---

Table 4.11 Results for tests of evolutionary mode applied to total time series and subset time series of lower fourth premolar (p4) buccal shape. Observed maximum excursions, average angles, and LRI slopes highlighted in red indicate observations that significantly deviate from the null hypothesis of a random walk in favor of evolutionary stasis. Observations highlighted in yellow, usually associated with time series of relatively few time steps, do not significantly deviate from expectations of a random walk. Variance test results highlighted in red indicate interval variances that are not significantly less than the total time series. Results highlighted in green indicate interval variances significantly less than the total variance, rejecting the null hypothesis of static mean and variance for the time series.

Time series	# steps in time series	Obs max excursion	# Random walks w/ excursion less than obs	# Random walks w/ excursion greater than obs	Obs average angle	# Random walks w/ angle less than obs	# Random walks w/ angle greater than obs	Obs LRI slope	# Random walks w/ LRI slope less than obs	# Random walks w/ LRI slope greater than obs
Total	32	0.105	0	1000	119.03	1000	0	-0.94	0	1000
Wa0-Wa1	12	0.099	4	996	120.99	997	3	-0.97	0	1000
Wa0-Wa2	18	0.099	0	1000	119.40	1000	0	-0.96	0	1000
Wa0-Wa3a	20	0.099	0	1000	121.15	1000	0	-0.99	0	1000
Wa0-Wa3b	29	0.105	0	1000	118.03	1000	0	-0.90	0	1000
Wa1	11	0.065	116	884	118.91	989	11	-0.97	0	1000
Wa1-Wa2	17	0.068	3	997	118.04	999	1	-0.96	0	1000
Wa1-Wa3a	19	0.068	1	999	120.06	1000	0	-0.99	0	1000
Wa1-Wa3b	28	0.098	1	999	117.20	1000	0	-0.89	0	1000
Wa1-Wa4	31	0.098	0	1000	118.32	1000	0	-0.93	0	1000
Wa2	6	0.068	518	482	114.74	871	129	-1.12	5	995
Wa2-Wa3a	8	0.068	300	700	121.54	971	29	-1.13	1	999
Wa2-Wa3b	17	0.098	5	995	115.69	999	1	-0.90	0	1000
Wa2-Wa4	20	0.098	1	999	117.76	1000	0	-0.99	0	1000
Wa3a-Wa3b	11	0.098	94	906	111.79	976	24	-0.89	0	1000
Wa3a-Wa4	14	0.098	24	976	115.87	995	5	-1.01	0	1000
Wa3b	9	0.098	224	776	105.34	866	134	-0.97	0	1000
Wa3b-Wa4	12	0.098	62	938	112.16	980	20	-0.85	14	986



Time series	N	Variance	Var <sup>total</sup> (lower bound)	Var <sup>total</sup> (upper bound)
Total	147	2.4E-03		
Wa0	1			
Wa1	37	1.7E-03	7.1E-05	1.2E-03
Wa2	36	2.2E-03	-5.2E-04	8.2E-04
Wa3a	30	2.4E-03	-6.0E-04	6.8E-04
Wa3b	32	2.7E-03	-8.0E-04	3.3E-04
Wa4	11	3.2E-03	-1.5E-03	4.5E-04

Table 4.12 Results for tests of evolutionary mode applied to total time series and subset time series of lower fourth premolar (p4) lingual shape. See Table 4.11 caption for explanation.

Time series	# steps in time series	Obs max excursion	# Random walks w/ excursion less than obs	# Random walks w/ excursion greater than obs	Obs average angle	# Random walks w/ angle less than obs	# Random walks w/ angle greater than obs	Obs LRI slope	# Random walks w/ LRI slope less than obs	# Random walks w/ LRI slope greater than obs
Total	32	0.134	0	1000	116.99	1000	0	-0.99	0	1000
Wa0-Wa1	12	0.108	55	945	115.73	987	13	-0.97	0	1000
Wa0-Wa2	18	0.130	0	1000	115.34	999	1	-0.99	0	1000
Wa0-Wa3a	20	0.130	0	1000	117.81	1000	0	-1.02	0	1000
Wa0-Wa3b	29	0.134	0	1000	117.44	1000	0	-0.96	0	1000
Wa1	11	0.108	208	792	114.49	971	29	-0.95	0	1000
Wa1-Wa2	17	0.130	1	999	114.57	1000	0	-0.98	0	1000
Wa1-Wa3a	19	0.130	0	1000	117.28	1000	0	-1.01	0	1000
Wa1-Wa3b	28	0.134	0	1000	117.08	1000	0	-0.89	0	1000
Wa1-Wa4	31	0.134	0	1000	116.65	1000	0	-0.98	0	1000
Wa2	6	0.124	351	649	119.66	893	107	-1.14	5	995
Wa2-Wa3a	8	0.124	184	816	125.62	981	19	-1.15	0	1000
Wa2-Wa3b	17	0.134	0	1000	120.27	1000	0	-0.97	0	1000
Wa2-Wa4	20	0.134	0	1000	119.05	1000	0	-1.01	0	1000
Wa3a-Wa3b	11	0.134	25	975	116.70	981	19	-0.95	0	1000
Wa3a-Wa4	14	0.134	6	994	115.76	994	6	-0.99	0	1000
Wa3b	9	0.134	86	914	108.37	890	110	-0.87	5	995
Wa3b-Wa4	12	0.134	13	987	109.74	947	53	-0.92	0	1000

Time series	N	Variance	Var <sub>total</sub> <sup>int</sup> (lower bound)	Var <sub>total</sub> <sup>int</sup> (upper bound)
Total	147	3.9E-03		
Wa0	1			
Wa1	37	3.2E-03	3.9E-05	1.6E-03
Wa2	36	4.1E-03	-1.6E-03	1.1E-03
Wa3a	30	3.7E-03	-7.6E-04	1.3E-03
Wa3b	32	4.2E-03	-1.2E-03	8.0E-04
Wa4	11	5.3E-03	-3.0E-03	1.2E-03

**Key**

- 
 Directional
- 
 Random
- 
 Static
- 
 Non-static

Table 4.13 Results for tests of evolutionary mode applied to total time series and subset time series of lower first molar (m1) buccal shape. See Table 4.11 caption for explanation.

Time series	# steps in time series	Obs max excursion	# Random walks w/ excursion less than obs	Obs average angle	# Random walks w/ angle less than obs	# Random walks w/ angle greater than obs	Obs LRI slope	# Random walks w/ LRI slope less than obs	# Random walks w/ LRI slope greater than obs
Total	35	0.107	0	118.91	1000	0	-0.91	0	1000
Wa0-Wa1	13	0.067	2	123.38	998	2	-1.02	0	1000
Wa0-Wa2	20	0.077	0	116.26	1000	0	-1.01	0	1000
Wa0-Wa3a	22	0.077	0	117.72	1000	0	-1.01	0	1000
Wa0-Wa3b	31	0.107	0	119.87	1000	0	-0.86	0	1000
Wa1	12	0.067	70	121.64	998	2	-0.97	0	1000
Wa1-Wa2	19	0.077	17	114.82	1000	0	-0.99	0	1000
Wa1-Wa3a	21	0.077	4	116.51	1000	0	-0.99	0	1000
Wa1-Wa3b	20	0.107	0	119.12	1000	0	-0.84	0	1000
Wa1-Wa4	34	0.107	0	118.22	1000	0	-1.18	1	999
Wa2	7	0.061	570	99.32	693	307	-0.90	0	1000
Wa2-Wa3a	9	0.061	334	108.34	914	86	-1.12	0	1000
Wa2-Wa3b	18	0.107	0	117.50	1000	0	-0.84	0	1000
Wa2-Wa4	22	0.107	0	116.39	1000	0	-0.94	0	1000
Wa3a-Wa3b	11	0.095	15	124.63	994	6	-0.92	1	999
Wa3a-Wa4	15	0.097	2	120.73	1000	0	-1.06	0	1000
Wa3b	9	0.095	32	125.68	989	11	-0.96	0	1000
Wa3b-Wa4	13	0.097	3	120.69	1000	0	-1.06	0	1000

Time series	N	Variance	Var <sup>total</sup> Var <sup>interval</sup> (lower bound)	Var <sup>total</sup> Var <sup>interval</sup> (upper bound)
Total	239	2.1E-03		
Wa0	5	1.4E-03	4.5E-04	1.7E-03
Wa1	66	1.7E-03	-1.4E-04	8.3E-04
Wa2	76	1.8E-03	-2.6E-04	7.4E-04
Wa3a	43	2.5E-03	-1.3E-03	4.4E-04
Wa3b	35	2.6E-03	-1.4E-03	1.9E-04
Wa4	14	2.3E-03	-1.1E-03	9.0E-04

**Key**

- 
 Directional
- 
 Random
- 
 Static
- 
 Non-static

Table 4.14 Results for tests of evolutionary mode applied to total time series and subset time series of lower first molar (m1) lingual shape. See Table 4.11 caption for explanation.

Time series	# steps in time series	Obs max excursion	# Random walks w/ excursion less than obs	# Random walks w/ excursion greater than obs	Obs average angle	# Random walks w/ angle less than obs	# Random walks w/ angle greater than obs	Obs LRI slope	# Random walks w/ LRI slope less than obs	# Random walks w/ LRI slope greater than obs
Total	35	0.140	0	1000	119.64	1000	0	-0.93	0	1000
Wa0-Wa1	13	0.106	1	999	123.44	1000	0	-0.97	0	1000
Wa0-Wa2	20	0.106	0	1000	119.48	1000	0	-0.98	0	1000
Wa0-Wa3a	22	0.106	0	1000	116.87	1000	0	-1.01	0	1000
Wa0-Wa3b	31	0.140	0	1000	117.51	1000	0	-0.91	0	1000
Wa1	12	0.086	26	974	119.77	997	3	-0.95	0	1000
Wa1-Wa2	19	0.102	6	994	117.09	1000	0	-0.97	0	1000
Wa1-Wa3a	21	0.102	1	999	114.59	1000	0	-1.00	0	1000
Wa1-Wa3b	20	0.140	0	1000	115.99	1000	0	-0.91	0	1000
Wa1-Wa4	34	0.140	0	1000	118.38	1000	0	-0.92	0	1000
Wa2	7	0.085	336	664	116.80	96	904	-1.32	0	1000
Wa2-Wa3a	9	0.085	151	849	110.11	85	915	-1.20	0	1000
Wa2-Wa3b	18	0.140	5	995	115.07	2	998	-0.93	0	1000
Wa2-Wa4	22	0.140	0	1000	119.08	1000	0	-0.96	0	1000
Wa3a-Wa3b	11	0.140	97	903	118.94	15	985	-1.02	0	1000
Wa3a-Wa4	15	0.140	14	986	123.92	1000	0	-1.07	0	1000
Wa3b	9	0.140	184	816	114.36	939	61	-1.12	0	1000
Wa3b-Wa4	13	0.140	42	958	121.91	999	1	-1.10	0	1000

Time series	N	Variance	Var <sup>total</sup>	Var <sup>interval</sup> (lower bound)	Var <sup>interval</sup> (upper bound)
Total	239	3.7E-03			
Wa0	5	4.7E-03	-2.4E-03	2.9E-03	
Wa1	66	3.4E-03	-1.1E-03	1.6E-03	
Wa2	76	3.1E-03	-3.4E-04	1.7E-03	
Wa3a	43	3.6E-03	-1.3E-03	1.5E-03	
Wa3b	35	4.9E-03	-3.0E-03	7.2E-04	
Wa4	14	4.7E-03	-2.2E-03	1.0E-03	

**Key**

- 
 Directional
- 
 Random
- 
 Static
- 
 Non-static



Table 4.15 Results for tests of evolutionary mode applied to total time series and subset time series of lower second molar (m2) buccal shape. See Table 4.11 caption for explanation.

Time series	# steps in time series	Obs max excursion	# Random walks w/ excursion less than obs	# Random walks w/ excursion greater than obs	Obs average angle	# Random walks w/ angle less than obs	# Random walks w/ angle greater than obs	Obs LRI slope	# Random walks w/ LRI slope less than obs	# Random walks w/ LRI slope greater than obs
Total	39.00	0.061	0	1000	124.29	1000	0	-0.95	0	1000
Wa0-Wa1	13.00	0.032	17	983	124.07	999	1	-0.97	0	1000
Wa0-Wa2	21.00	0.053	0	1000	122.99	1000	0	-1.01	0	1000
Wa0-Wa3a	23.00	0.053	0	1000	122.86	1000	0	-1.02	0	1000
Wa0-Wa3b	34.00	0.061	0	1000	124.69	1000	0	-0.95	0	1000
Wa1	12.00	0.032	26	974	124.14	998	2	-0.97	0	1000
Wa1-Wa2	20.00	0.053	0	1000	122.97	1000	0	-1.02	0	1000
Wa1-Wa3a	22.00	0.053	0	1000	122.83	1000	0	-1.02	0	1000
Wa1-Wa3b	33.00	0.061	0	1000	125.73	1000	0	-0.96	0	1000
Wa1-Wa4	38.00	0.061	0	1000	124.32	1000	0	-0.95	0	1000
Wa2	8.00	0.053	58	942	121.85	981	19	-1.23	0	1000
Wa2-Wa3a	10.00	0.053	29	971	121.79	989	11	-1.16	0	1000
Wa2-Wa3b	21.00	0.061	0	1000	125.48	1000	0	-1.00	0	1000
Wa2-Wa4	26.00	0.061	0	1000	124.71	1000	0	-0.98	0	1000
Wa3a-Wa3b	13.00	0.046	8	992	128.19	999	1	-1.05	0	1000
Wa3a-Wa4	18.00	0.047	1	999	126.17	1000	0	-1.00	0	1000
Wa3b	11.00	0.046	41	959	126.92	998	2	-1.01	0	1000
Wa3b-Wa4	16.00	0.047	2	998	125.07	1000	0	-0.97	0	1000

Time series	N	Variance	Var <sup>total</sup> (lower bound)	Var <sup>total</sup> (upper bound)
Total	286	1.3E-03		
Wa0	5	7.2E-04	4.1E-04	1.1E-03
Wa1	75	1.2E-03	-1.2E-04	4.1E-04
Wa2	84	1.1E-03	-7.3E-05	4.1E-04
Wa3a	45	1.2E-03	-1.1E-04	3.9E-04
Wa3b	61	1.8E-03	-1.1E-03	4.4E-05
Wa4	15	1.3E-03	-4.9E-04	6.1E-04

**Key**

- Directional
- Random
- Static
- Non-static

Table 4.16 Results for tests of evolutionary mode applied to total time series and subset time series of lower second molar (m2) lingual shape. See Table 4.11 caption for explanation.

Time series	# steps in time series	Obs max excursion	# Random walks w/ excursion less than obs	# Random walks w/ excursion greater than obs	Obs average angle	# Random walks w/ angle less than obs	# Random walks w/ angle greater than obs	Obs LRI slope	# Random walks w/ LRI slope less than obs	# Random walks w/ LRI slope greater than obs
Total	39	0.061	0	1000	122.25	1000	0	-0.92	0	1000
Wa0-Wa1	13	0.040	30	970	117.65	996	4	-0.89	0	1000
Wa0-Wa2	21	0.050	1	999	118.95	1000	0	-0.94	0	1000
Wa0-Wa3a	23	0.050	1	999	120.02	1000	0	-0.96	0	1000
Wa0-Wa3b	34	0.060	0	1000	121.02	1000	0	-0.96	0	1000
Wa1	12	0.040	39	961	115.71	981	19	-0.89	0	1000
Wa1-Wa2	20	0.050	3	997	117.95	1000	0	-0.95	0	1000
Wa1-Wa3a	22	0.050	2	998	119.16	1000	0	-0.97	0	1000
Wa1-Wa3b	33	0.060	0	1000	120.50	1000	0	-0.96	0	1000
Wa1-Wa4	38	0.061	0	1000	121.71	1000	0	-0.93	0	1000
Wa2	8	0.050	357	643	120.80	955	45	-1.18	1	999
Wa2-Wa3a	10	0.050	224	776	123.12	988	12	-1.17	0	1000
Wa2-Wa3b	21	0.060	2	998	123.01	1000	0	-1.00	0	1000
Wa2-Wa4	26	0.061	0	1000	124.50	1000	0	-0.96	0	1000
Wa3a-Wa3b	13	0.059	62	938	122.93	998	2	-1.06	0	1000
Wa3a-Wa4	18	0.061	2	998	125.19	1000	0	-1.00	0	1000
Wa3b	11	0.059	112	888	121.77	994	6	-1.02	0	1000
Wa3b-Wa4	16	0.061	1	999	124.77	1000	0	-0.97	0	1000

Time series	N	Variance	Var <sub>interval</sub> <sup>total</sup> (lower bound)	Var <sub>interval</sub> <sup>total</sup> (upper bound)
Total	286	1.3E-03		
Wa0	5	6.1E-04	5.7E-04	1.1E-03
Wa1	75	1.3E-03	-2.7E-04	2.8E-04
Wa2	84	9.6E-04	1.1E-04	5.6E-04
Wa3a	45	1.2E-03	-2.1E-04	4.3E-04
Wa3b	61	1.8E-03	-1.1E-03	9.1E-05
Wa4	15	1.5E-03	-6.6E-04	4.1E-04

**Key**

- 
 Directional
- 
 Random
- 
 Static
- 
 Non-static

Table 4.17 Results for tests of evolutionary mode applied to total time series and subset time series of lower third molar (m3) buccal shape. See Table 4.11 caption for explanation.

Time series	# steps in time series	Obs max excursion	# Random walks w/ excursion less than obs	# Random walks w/ excursion greater than obs	Obs average angle	# Random walks w/ angle less than obs	# Random walks w/ angle greater than obs	Obs LRI slope	# Random walks w/ LRI slope less than obs	# Random walks w/ LRI slope greater than obs
Total	36	0.069	0	1000	113.06	1000	0	-0.95	0	1000
Wa0-Wa1	12	0.062	8	992	116.35	986	14	-1.08	0	1000
Wa0-Wa2	19	0.063	0	1000	115.37	1000	0	-1.06	0	1000
Wa0-Wa3a	21	0.063	0	1000	117.94	1000	0	-1.06	0	1000
Wa0-Wa3b	31	0.069	0	1000	113.25	1000	0	-0.95	0	1000
Wa1	11	0.062	15	985	114.54	976	24	-1.10	0	1000
Wa1-Wa2	18	0.063	0	1000	114.29	998	2	-1.07	0	1000
Wa1-Wa3a	20	0.063	0	1000	117.13	998	2	-1.06	0	1000
Wa1-Wa3b	30	0.069	0	1000	112.56	1000	0	-0.95	0	1000
Wa1-Wa4	35	0.069	0	1000	112.46	1000	0	-0.96	0	1000
Wa2	7	0.049	204	796	114.87	857	143	-1.22	0	1000
Wa2-Wa3a	9	0.049	83	917	122.00	965	35	-1.13	0	1000
Wa2-Wa3b	19	0.069	5	995	111.61	997	3	-0.90	0	1000
Wa2-Wa4	24	0.069	2	998	111.68	1000	0	-0.94	0	1000
Wa3a-Wa3b	12	0.057	29	971	104.33	920	80	-0.94	0	1000
Wa3a-Wa4	17	0.057	3	997	106.87	992	8	-0.98	0	1000
Wa3b	10	0.057	84	916	103.93	869	131	-0.96	0	1000
Wa3b-Wa4	15	0.057	6	994	107.00	985	15	-0.94	0	1000

Time series	N	Variance	Var <sub>total</sub> <sup>int</sup> (lower bound)	Var <sub>total</sub> <sup>int</sup> (upper bound)
Total	294	1.9E-03		
Wa0	12	1.2E-03	4.1E-04	1.1E-03
Wa1	46	1.7E-03	-2.3E-04	6.8E-04
Wa2	107	1.9E-03	-2.3E-04	3.1E-04
Wa3a	27	1.4E-03	1.9E-04	8.9E-04
Wa3b	78	2.2E-03	-5.9E-04	9.3E-05
Wa4	23	2.1E-03	-7.1E-04	4.6E-04

**Key**

- 
 Directional
- 
 Random
- 
 Static
- 
 Non-static

Table 4.18 Results for tests of evolutionary mode applied to total time series and subset time series of lower third molar (m3) lingual shape. See Table 4.11 caption for explanation.

Time series	# steps in time series	Obs max excursion	# Random walks w/ excursion less than obs	# Random walks w/ excursion greater than obs	Obs average angle	# Random walks w/ angle less than obs	# Random walks w/ angle greater than obs	Obs LRI slope	# Random walks w/ LRI slope less than obs	# Random walks w/ LRI slope greater than obs
Total	36	0.116	0	1000	120.95	1000	0	-0.89	0	1000
Wa0-Wa1	12	0.059	9	991	114.82	982	18	-1.07	0	1000
Wa0-Wa2	19	0.091	0	1000	123.94	1000	0	-0.99	0	1000
Wa0-Wa3a	21	0.091	0	1000	124.93	1000	0	-1.00	0	1000
Wa0-Wa3b	31	0.107	0	1000	121.70	1000	0	-0.94	0	1000
Wa1	11	0.059	17	983	117.35	981	19	-1.12	0	1000
Wa1-Wa2	18	0.091	0	1000	124.98	1000	0	-1.01	0	1000
Wa1-Wa3a	20	0.091	0	1000	126.76	1000	0	-1.03	0	1000
Wa1-Wa3b	30	0.107	0	1000	122.76	1000	0	-0.95	0	1000
Wa1-Wa4	35	0.116	0	1000	121.83	1000	0	-0.90	0	1000
Wa2	7	0.091	135	865	134.79	967	33	-1.29	0	1000
Wa2-Wa3a	9	0.091	48	952	136.58	996	4	-1.19	0	1000
Wa2-Wa3b	19	0.107	0	1000	124.22	1000	0	-0.98	0	1000
Wa2-Wa4	24	0.116	1	999	122.49	1000	0	-0.92	0	1000
Wa3a-Wa3b	12	0.079	366	634	115.56	984	16	-0.91	0	1000
Wa3a-Wa4	17	0.092	11	989	115.91	999	1	-0.88	0	1000
Wa3b	10	0.079	498	502	115.15	961	39	-0.89	3	997
Wa3b-Wa4	15	0.092	21	979	115.71	1000	0	-0.89	0	1000

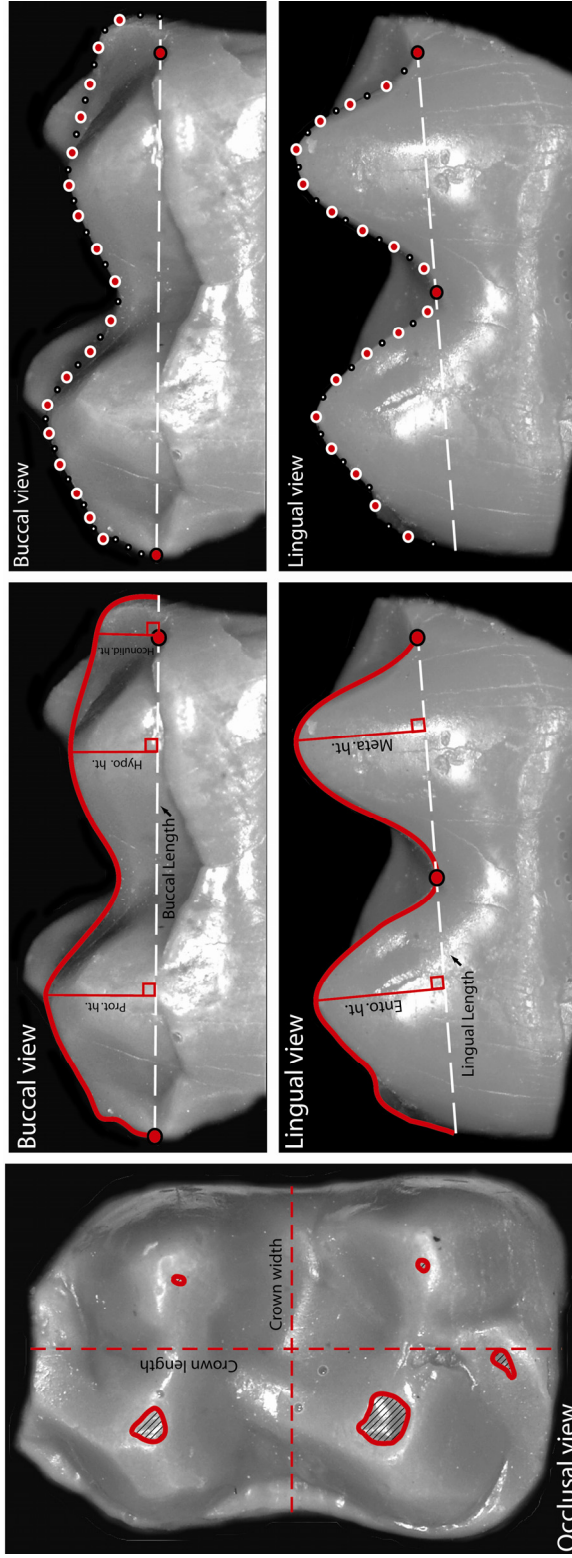
series	N	Variance	Var <sup>total</sup>	Var <sup>interval</sup> (lower bound)	Var <sup>interval</sup> (upper bound)
Total	294	2.6E-03			
Wa0	12	2.1E-03	1.6E-04	1.2E-03	1.2E-03
Wa1	46	1.9E-03	2.7E-04	1.0E-03	1.0E-03
Wa2	107	2.6E-03	-4.4E-04	5.2E-04	5.2E-04
Wa3a	27	1.9E-03	3.8E-04	1.2E-03	1.2E-03
Wa3b	78	2.7E-03	-5.9E-04	4.8E-04	4.8E-04
Wa4	23	3.0E-03	-1.4E-03	5.7E-04	5.7E-04

**Key**

- Directional
- Random
- Static
- Non-static

Figure 4.1 Buccal, lingual, and occlusal views of the lower second molar of *Hyracotherium* exhibiting size measurements, landmarks, and semi-landmarks included in the positional and overall wear index calculations and in the respective analyses of shape.



## Size Measurements

### Occlusal view:

- 1) Crown area (crown length x crown width)
- 2) Exposed dentin area (estimated from closed outlines at cusps)

### Buccal view:

- 1) Buccal length
- 2) Protoconid height (highest point of protoconid to baseline)
- 3) Hypoconid height (highest point of hypoconid to baseline)
- 4) Hypoconulid height (highest point of hypoconulid to baseline)
- 5) Buccal centroid size (incl. all landmarks, semi-landmarks, helper points)

### Lingual view:

- 1) Lingual length
- 2) Metaconid height (highest point of metaconid to baseline)
- 3) Entoconid height (highest point of entoconid to baseline)
- 4) Lingual centroid size (incl. all landmarks, semi-landmarks, helper points)

### Ratios:

- 1) Protoconid height/metaconid height
- 2) Hypoconid height/entoconid height

## Key





-  Exposed Dentin
-  Landmark
-  Semi-landmark
-  Helper point

Figure 4.2 Comparison of morphological time series characteristics of dental size and shape. Morphological change between consecutive time steps can be described by a magnitude and a direction of change in both types of time series. The difference is that shape displacement is defined by a vector with  $2n$  elements, where  $n$  is the number of landmarks in the shape configuration. The magnitude of shape displacement (i.e. Procrustes distance) and the direction of shape displacement between consecutive timesteps (i.e. arccosine of the dot product) vary with time in a multi-dimensional space, requiring the combined results of various multivariate tests of evolutionary dynamics to fully characterize the evolution of shape. Abbreviations: wrt = with respect to, mag = magnitude.

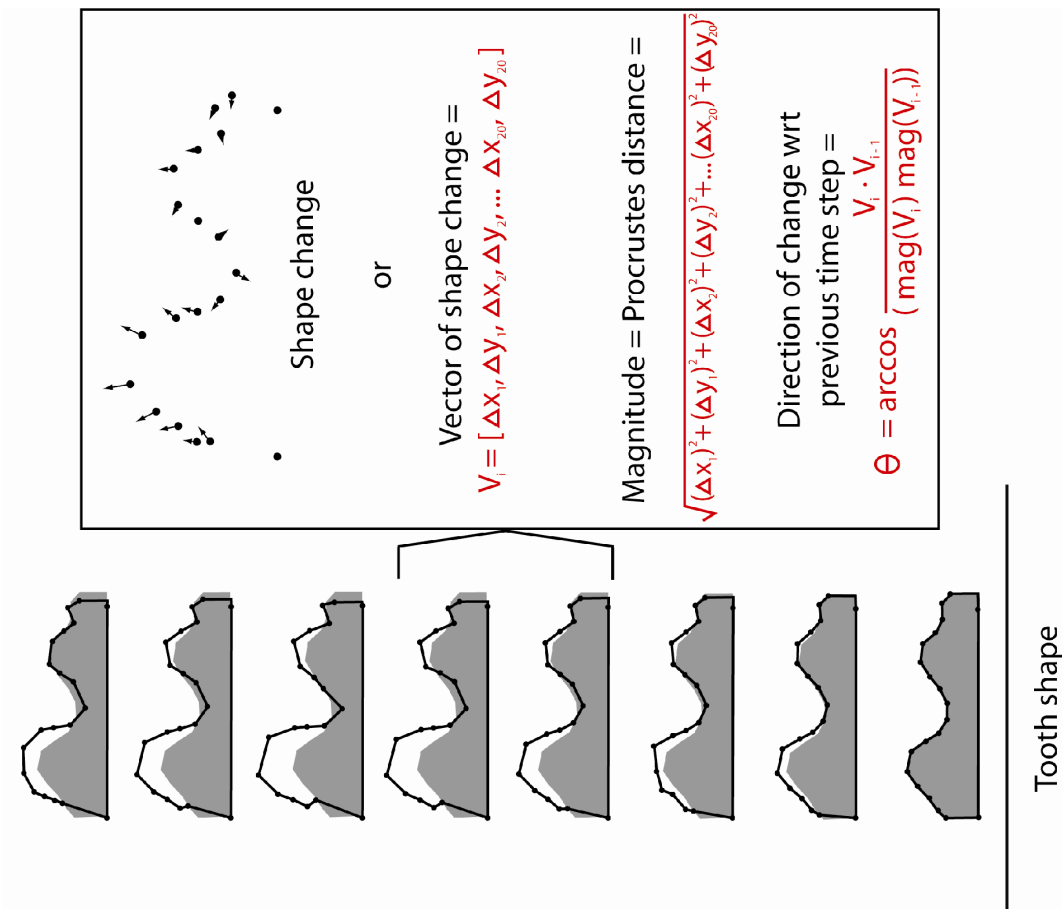
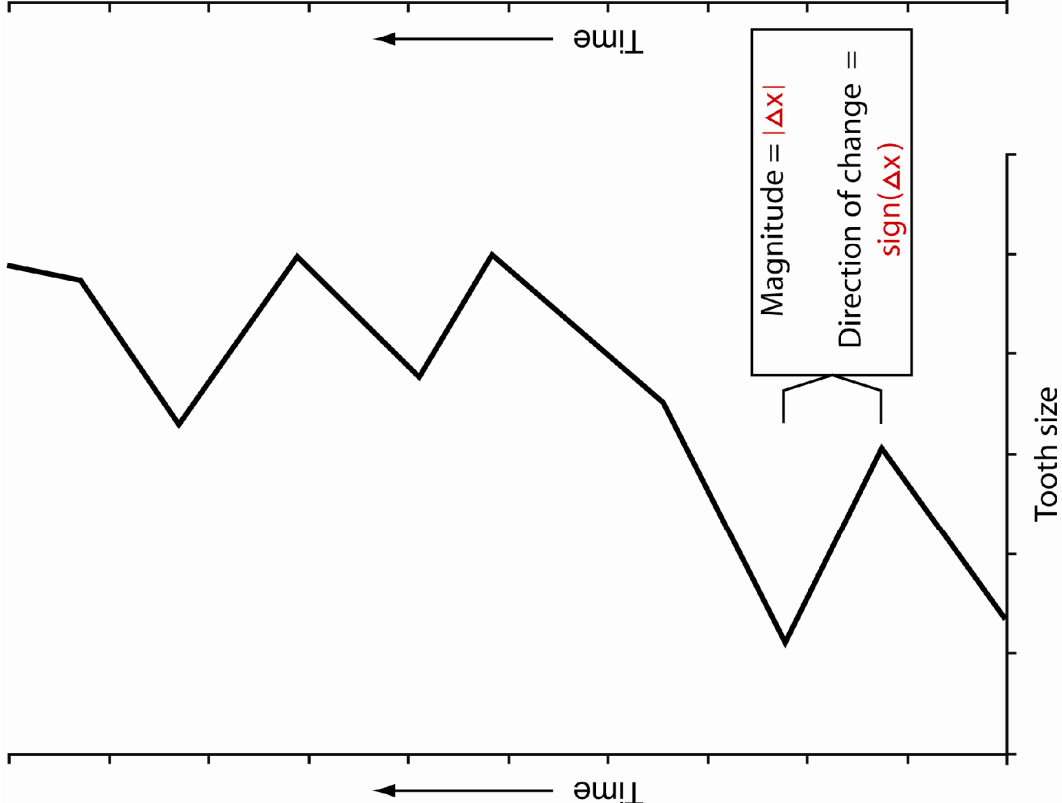




Figure 4.3 Stratigraphic plot of log-transformed crown areas of the lower fourth premolar (p4) and first through third lower molars (m1-3) in Clarks Fork and northwestern Bighorn Basin *Hyracotherium* taxa. Red lines represent position of mean shape per stratigraphic interval. A) Stratigraphic plot of the total sample through the Wa-0 – Wa-4 biozones. A similar pattern of size change is evident in all four tooth positions. Smallest tooth sizes occur during the Wa-0 biozone, followed by an increase to intermediate sizes at the Wa-0/Wa-1 boundary. Tooth sizes increase during the Wa-3 biozone, reaching a maximum near the 1900 meter level and decreasing to more intermediate sizes near the Wa-3/Wa-4 boundary. B) Close up of the Wa-2/Wa-3a and Wa-3a/Wa-3b boundaries, illustrating differential dynamics in the evolution of tooth sizes. The transition in p4 and m3 size appear to occur via a gradual increase in mean tooth size whereas the m1 and m2 size transitions occur after an increase in size variation.

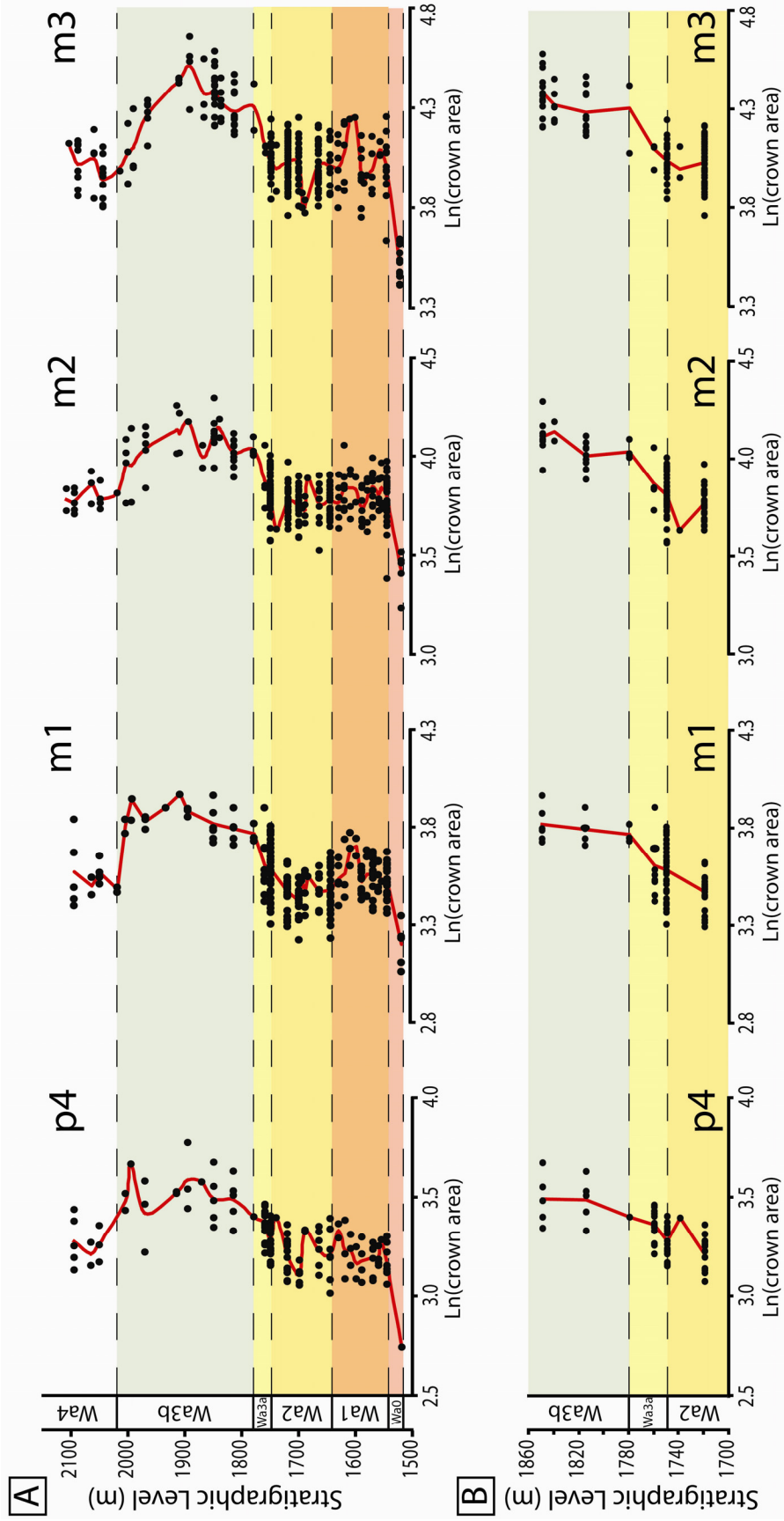


Figure 4.4 Stratigraphic distribution of anterior trigonid foveae in *Hyracotherium*. A) Stratigraphic plot of log-transformed lower first molar crown areas, exhibiting the stratigraphic distribution of anterior trigonid foveae. Anterior trigonid foveae consist of a continuous paracristid and premetacristid. Black circles represent teeth that lack the anterior trigonid fovea. Both types of m1 morphologies follow the same pattern in crown area, with a decreasing frequency of teeth exhibiting the anterior trigonid fovea with time. B) Lower first molars attributed to various species of Clarks Fork and northwestern Basin *Hyracotherium*, each exhibiting an anterior trigonid fovea. Continuous paracristids and premetacristids do not appear to be limited to the *H. sandrae* species and instead represents a highly variable portion of lower dental morphology in the *Hyracotherium* lineage.

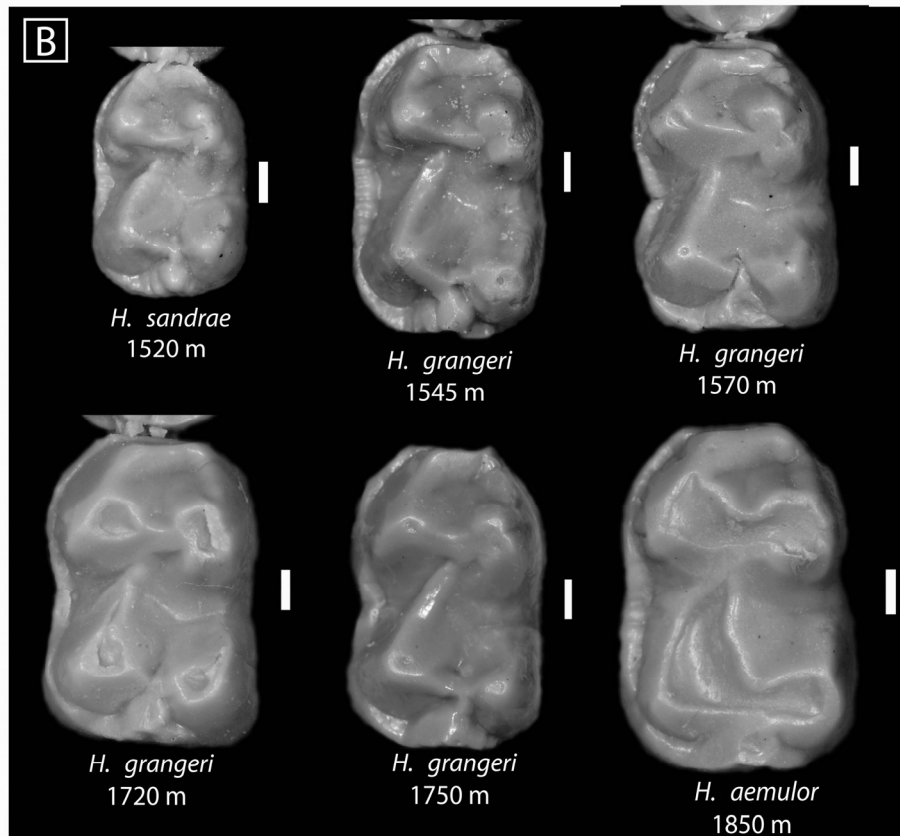
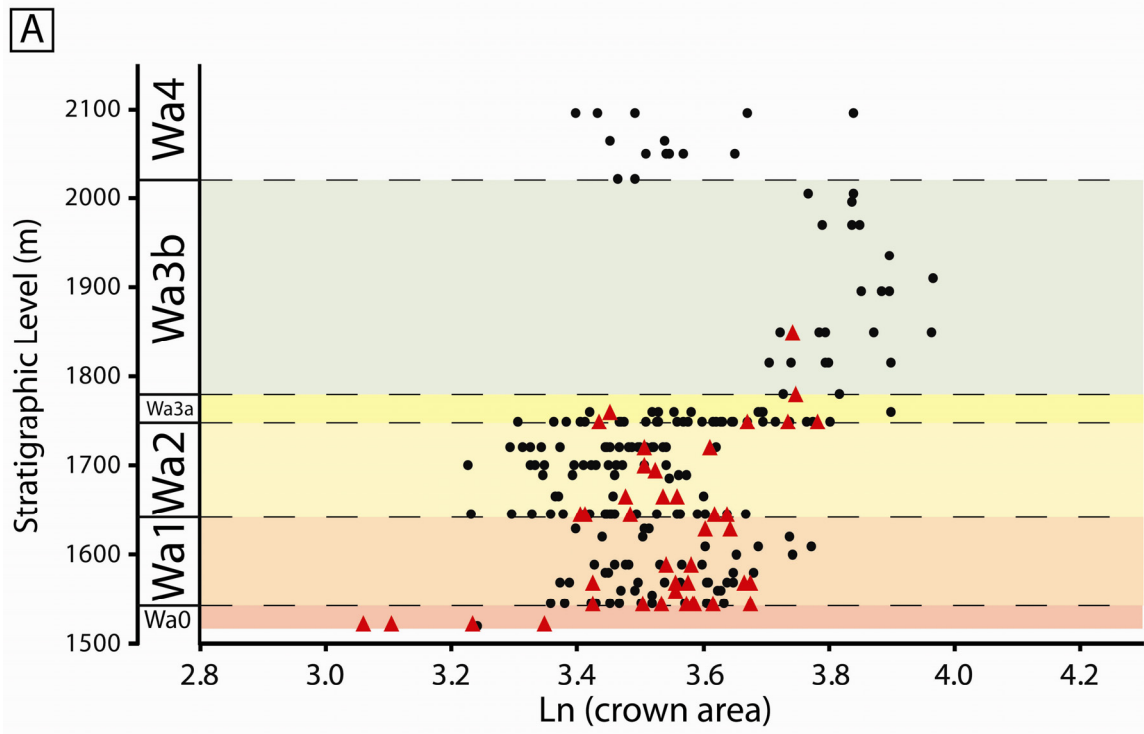


Figure 4.5 Stratigraphic distribution of lower fourth premolar (p4) entoconids in *Hyracotherium*. A) Stratigraphic plot of log-transformed lower fourth premolar crown areas, exhibiting the stratigraphic distribution of p4 entoconids. Lower fourth premolars without distinctive entoconids (red diamonds) follow the same stratigraphic pattern in crown as those with entoconids (black circles). B) Frequency distribution of p4 positional wear index values between lower fourth premolars with and without a distinctive entoconid. The distribution of wear values overlap completely, suggesting that the absence of a p4 entoconid in *H. grangeri* and *H. pernix* cannot be explained by dental wear.

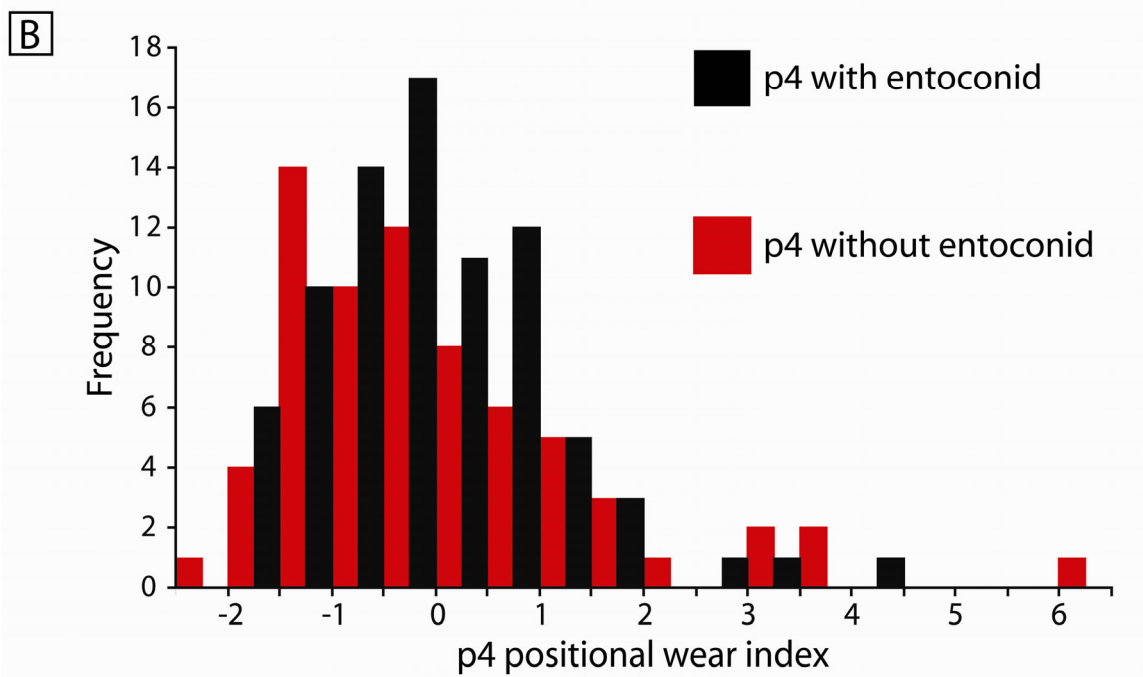
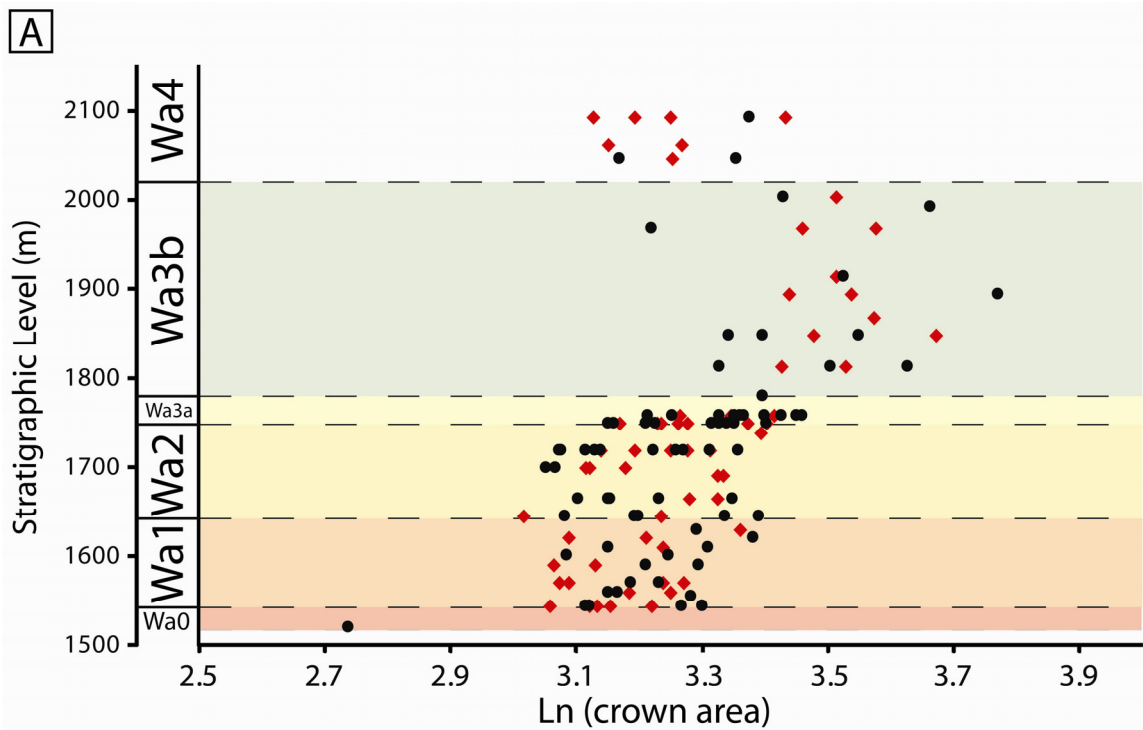


Figure 4.6 Log-rate-interval (LRI) test results for the lower fourth premolar (p4) crown area time series. A) Moving window LRI results organized by initial time step and window size for all subsets of the p4 crown area time series. Blue grid boxes correspond to test results indicating directional selection. Red grid boxes correspond to evolutionary stasis results. Darker shades indicated higher significance levels ( $\alpha = 0.10, 0.05, \text{ and } 0.01$ ). Concentrations of color indicate nested subsets exhibiting equivalent evolutionary dynamics. B) Stratigraphic plots exhibiting moving window LRI results. Test results shown correspond to the longest inclusive subset of nested subsets exhibiting the same evolutionary mode. Three segments of time steps were found to significantly differ from the expectation of a random walk. Two overlapping stasis segments occur within the stratigraphic range of *Hyracotherium grangeri* (Wa-1 – Wa-3a). The detection of a directional segment spanning the Wa-0/Wa-1 boundary in the p4, m1, and m2 series is likely due to the inclusion of dramatically small sizes in the Wa-0 interval. Exclusion of the Wa-0 interval produces either non-significant or static results.

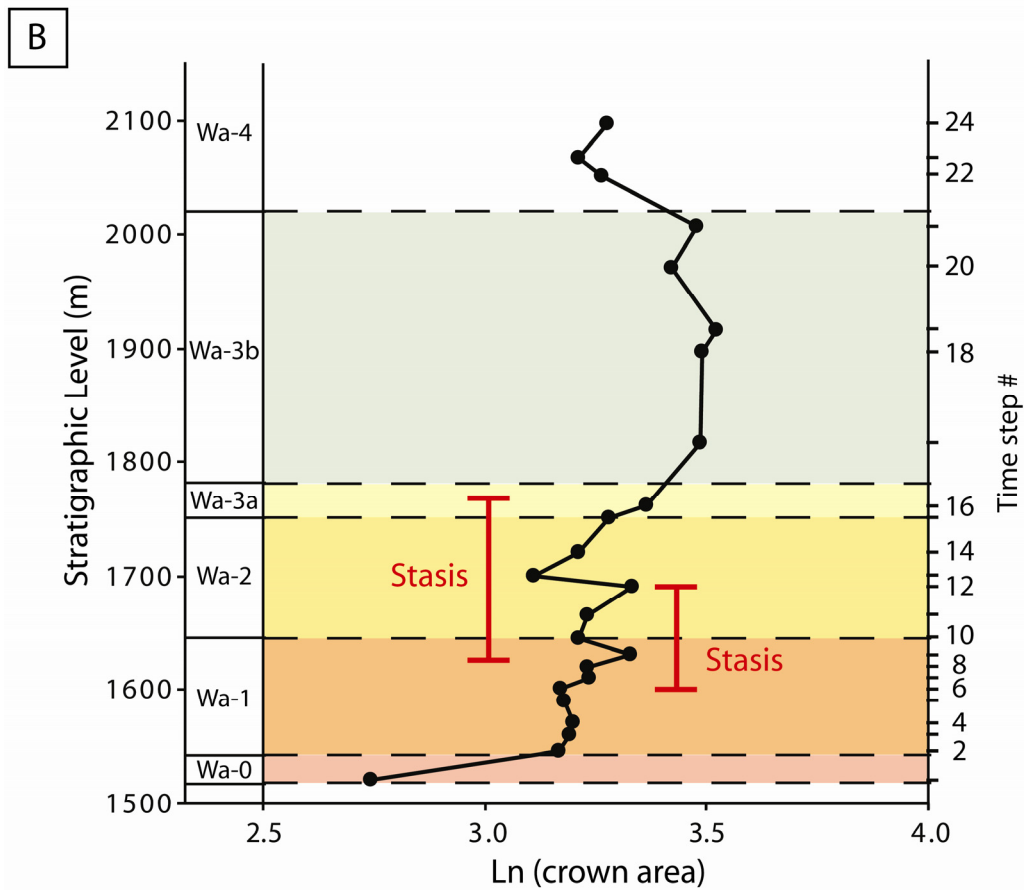
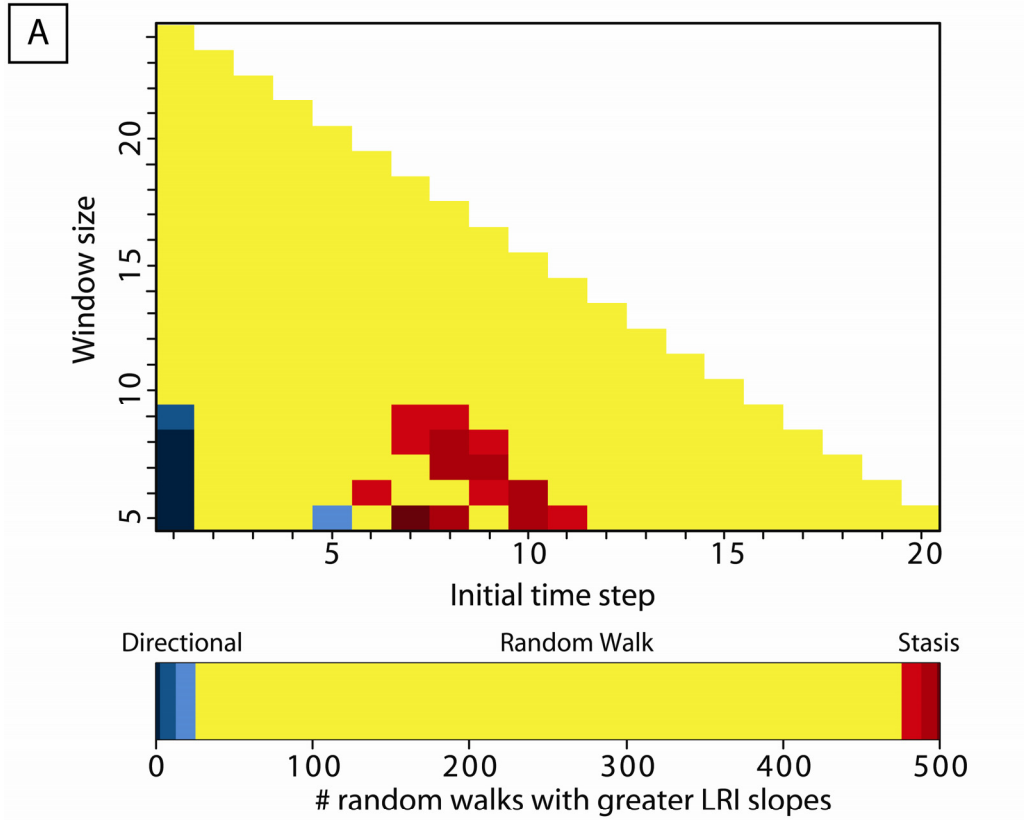




Figure 4.7 Log-rate-interval (LRI) test results for the lower first molar (m1) crown area time series. A) Moving window LRI results organized by initial time step and window size for all subsets of the m1 crown area time series. See caption for Fig. 4.6 for explanation. B) Stratigraphic plots exhibiting moving window LRI results. A stasis segment during the Wa-2 biozone is nested within a directional segment corresponding to the *Hyracotherium grangeri*/*H. aemulor* transition with an overlap midpoint between the 1700 m and 1720 m levels. The overlap midpoint may indicate that selective pressures changed during this interval to favor larger m1 sizes.

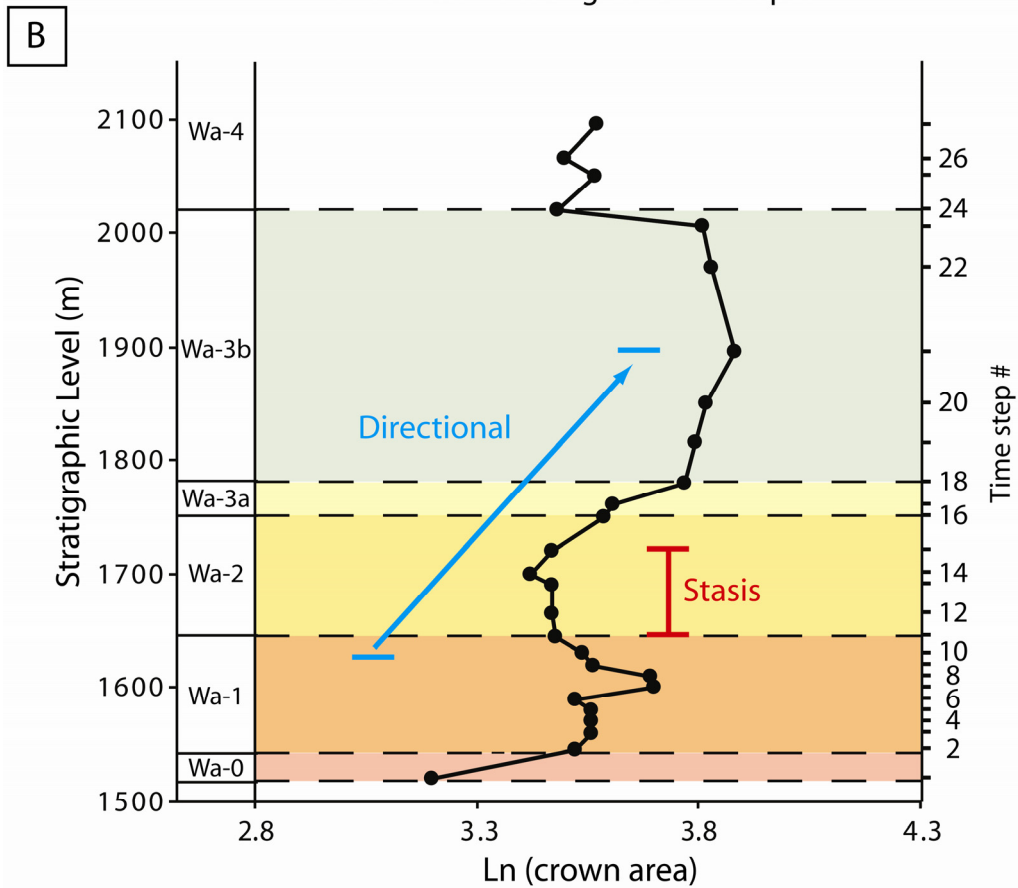
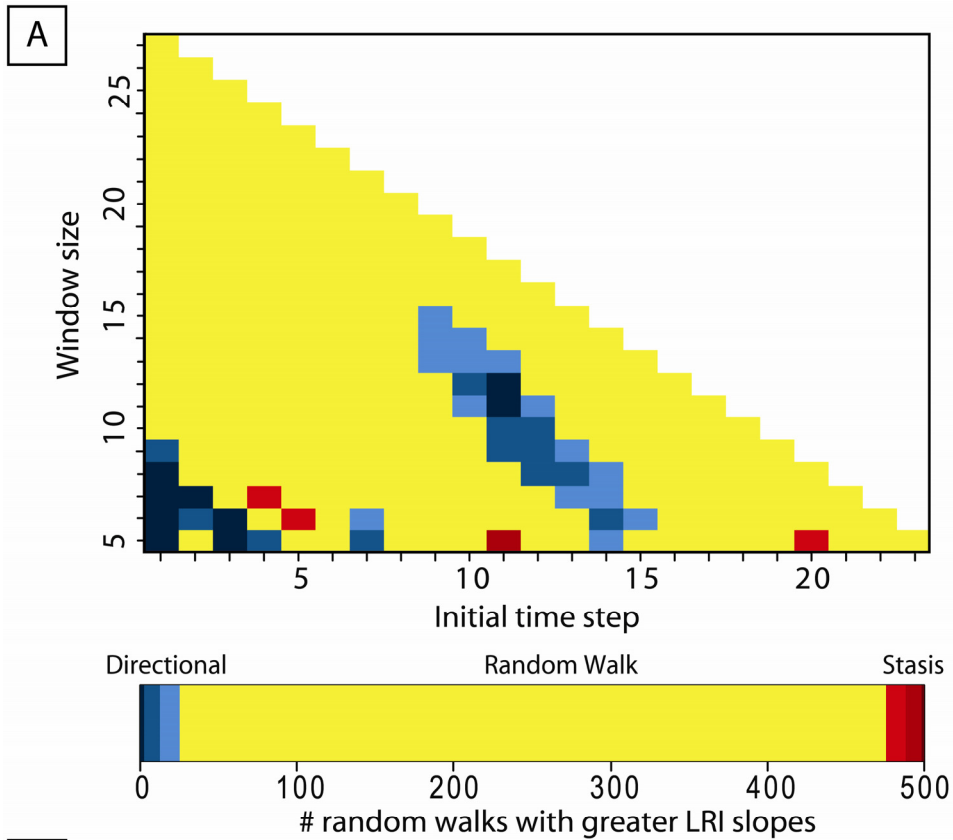


Figure 4.8 Log-rate-interval (LRI) test results for the lower second molar (m2) crown area time series. A) Moving window LRI results organized by initial time step and window size for all subsets of the m2 crown area time series. See caption for Fig. 4.6 for explanation. B) Stratigraphic plots exhibiting moving window LRI results. Two shifting points in evolutionary dynamics are indicated by the LRI results. Onset of directional selection for larger m2 sizes occurs at the 1620-1630 m interval following a segment of evolutionary stasis during the majority of Wa-1 time. At the 1910 m level, the directional trend reverses, favoring smaller m2 crown areas for the remainder of the time series.

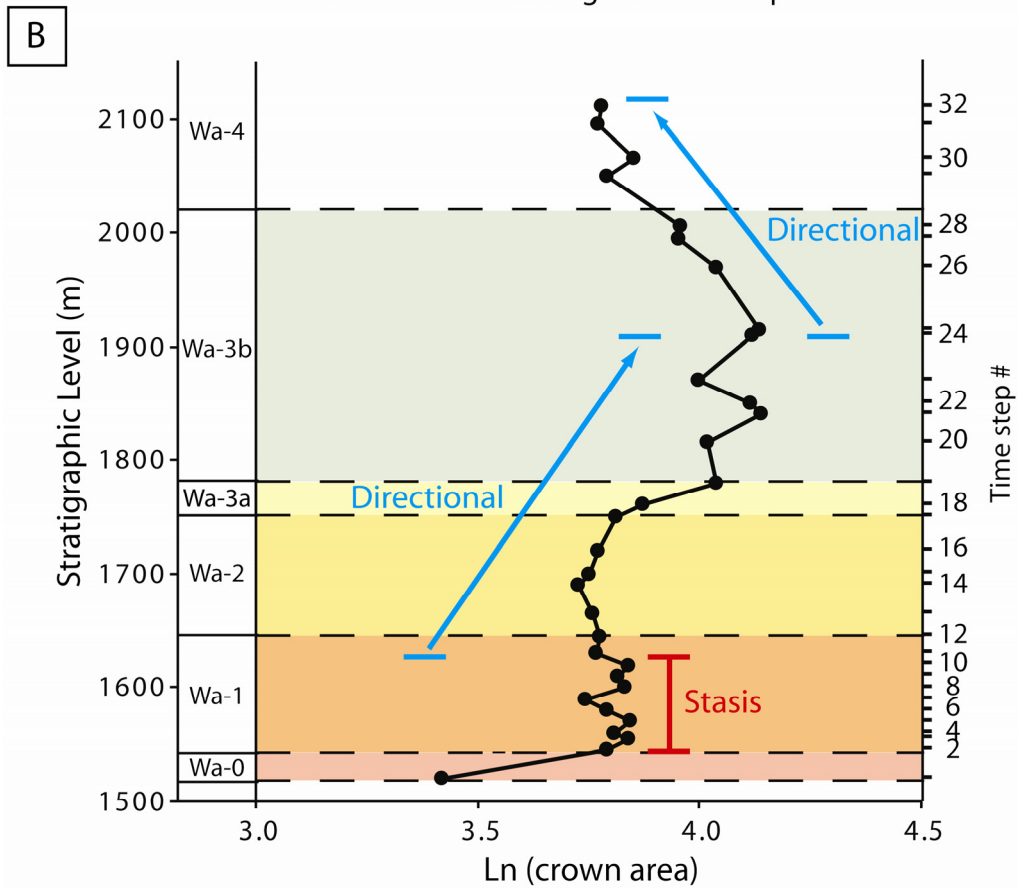
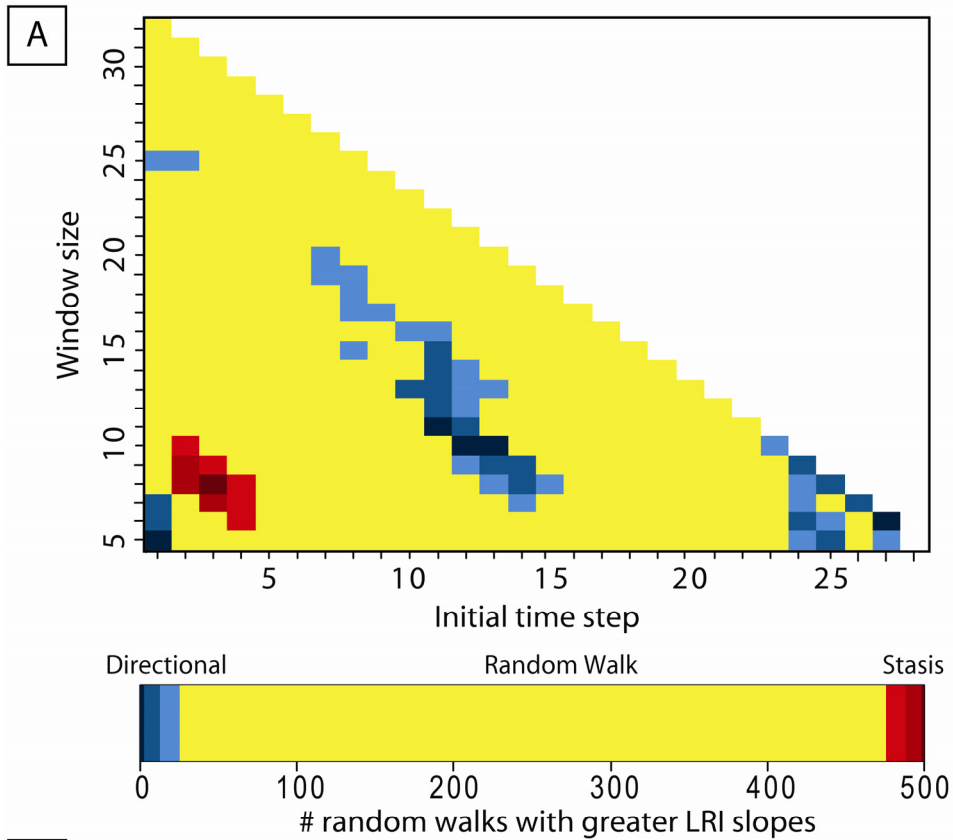


Figure 4.9 Log-rate-interval (LRI) test results for the lower third molar (m3) crown area time series. A) Moving window LRI results organized by initial time step and window size for all subsets of the m3 crown area time series. See caption for Fig. 4.6 for explanation. B) Stratigraphic plots exhibiting moving window LRI results. The heterogeneous evolutionary dynamics exhibited by the m3 LRI results are consistent with those of the m2 crown area time series, with the exception of a much longer stasis segment that spans the Wa-1 through Wa-3a biozones. The overlap midpoint of the stasis segment and the lower directional segment in the m3 time series occurs at the 1695 m level, relatively close to the shift point observed in the m1 series (1700-1720 m).

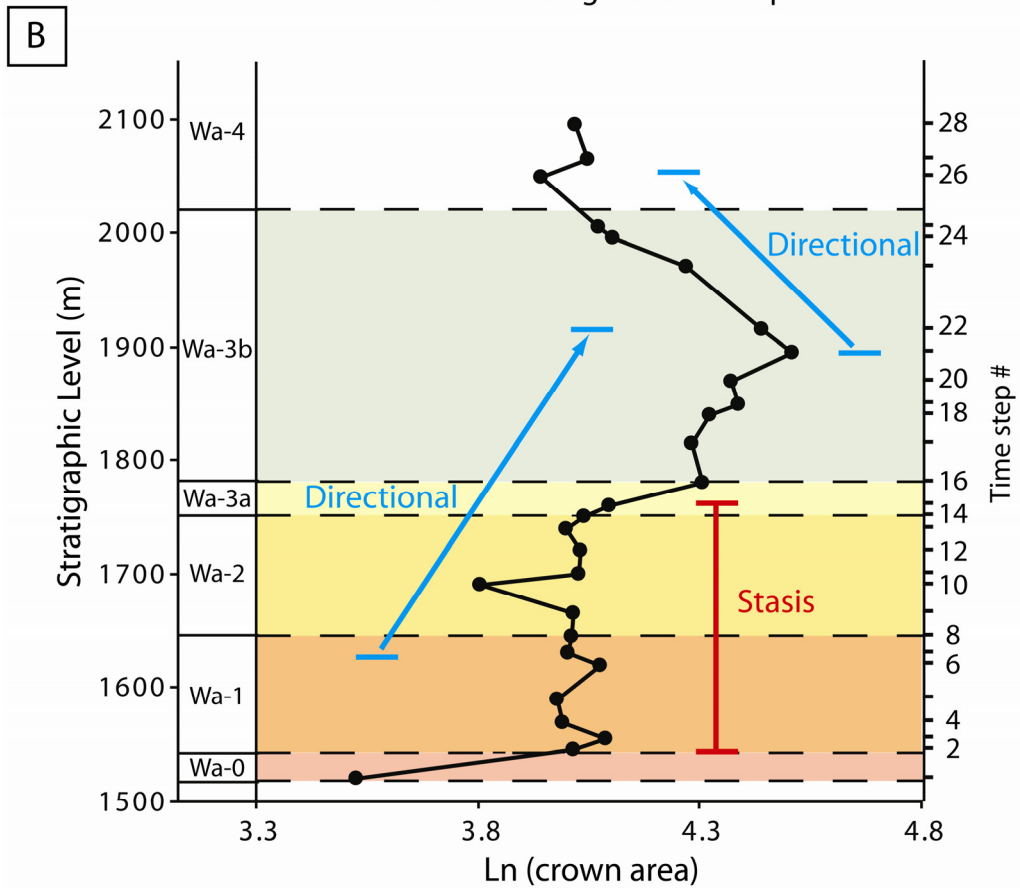
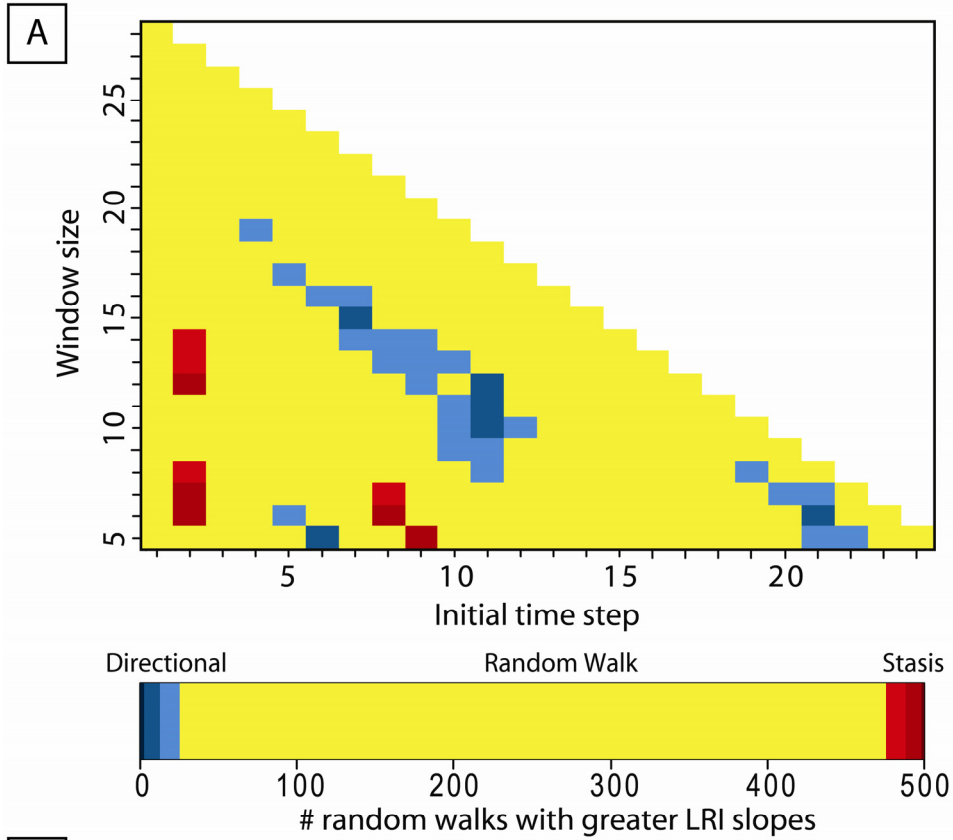


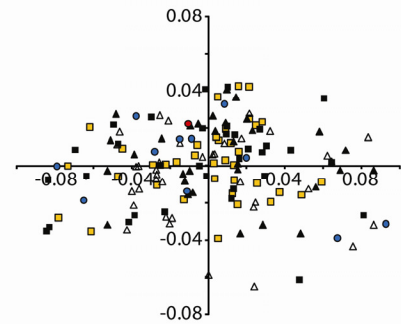
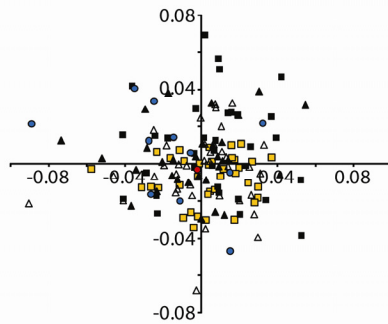
Figure 4.10 PC2 scores versus PC1 scores for predicted unworn buccal and lingual shapes for the lower fourth premolar (p4) and the first through third lower molars (m1-3) of Clarks Fork and northwestern Bighorn Basin *Hyracotherium* taxa. Principal components results show no separation at all temporal resolutions, indicating no change in tooth shape with time. The only exception is m3 lingual shape in which Wa-0 and Wa-4 taxa separate along the PC1 axis with Wa-1 through Wa-3 taxa equally distributed along PC1.

p4

Buccal view

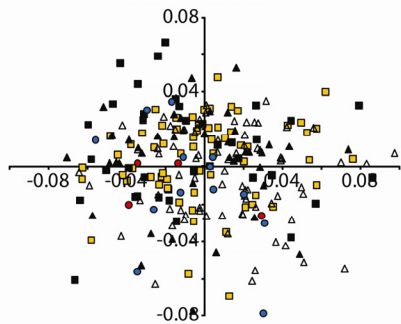
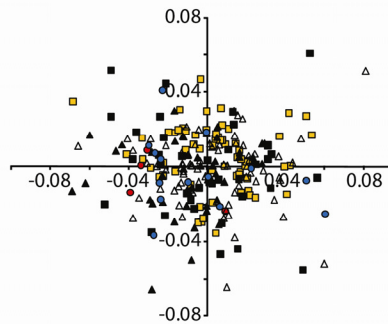
Lingual view

PC2 score



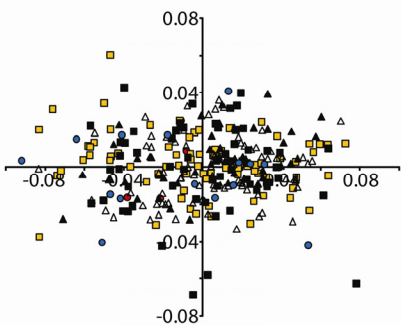
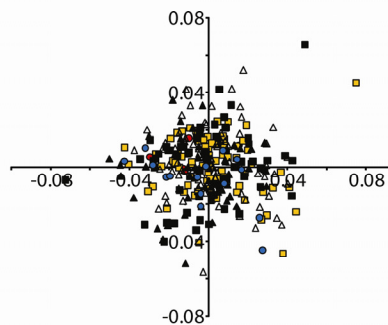
m1

PC2 score



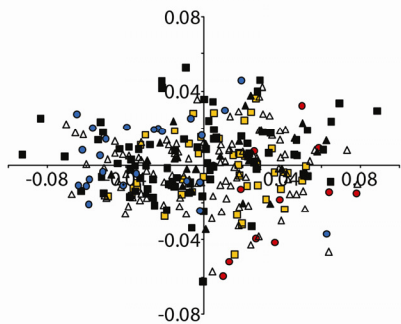
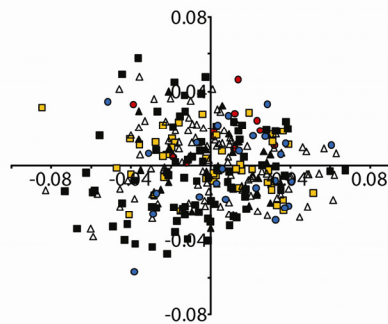
m2

PC2 score



m3

PC2 score



PC1 score

PC1 score





Figure 4.11 Principal components results for lower third molar lingual shape in *Hyracotherium*. A) PC2 scores versus PC1 scores for lower third molar lingual shape showing the separation between Wa-0 (black squares) and Wa-4 (red triangles) *Hyracotherium* taxa along PC1. Open circles represent PC scores for Wa-1 – Wa-3 taxa. Wa-0 taxa (*Hyracotherium sandrae*) are restricted to positive PC1 scores whereas Wa-4 taxa (*Hyracotherium pernix*) possess negative PC1, with the exception of 3 outliers. B) The dimension of variance described by PC1 is associated with the inclination of the entoconid and the height of the hypoconucristid relative to the other lingual cusps. Positive PC1 scores are associated with posteriorly inclined entoconids and short hypoconucristids as shown with the *Hyracotherium sandrae* specimen. Negative PC1 scores represent vertical entoconids and high hypoconucristids as shown with the *Hyracotherium pernix* specimen.

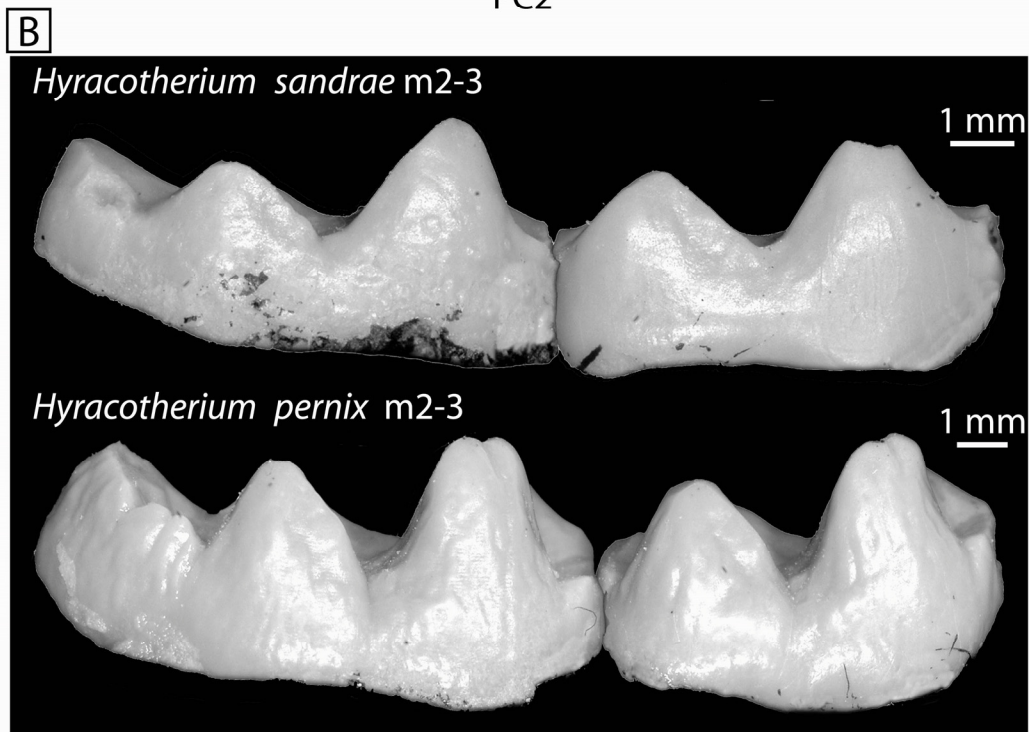
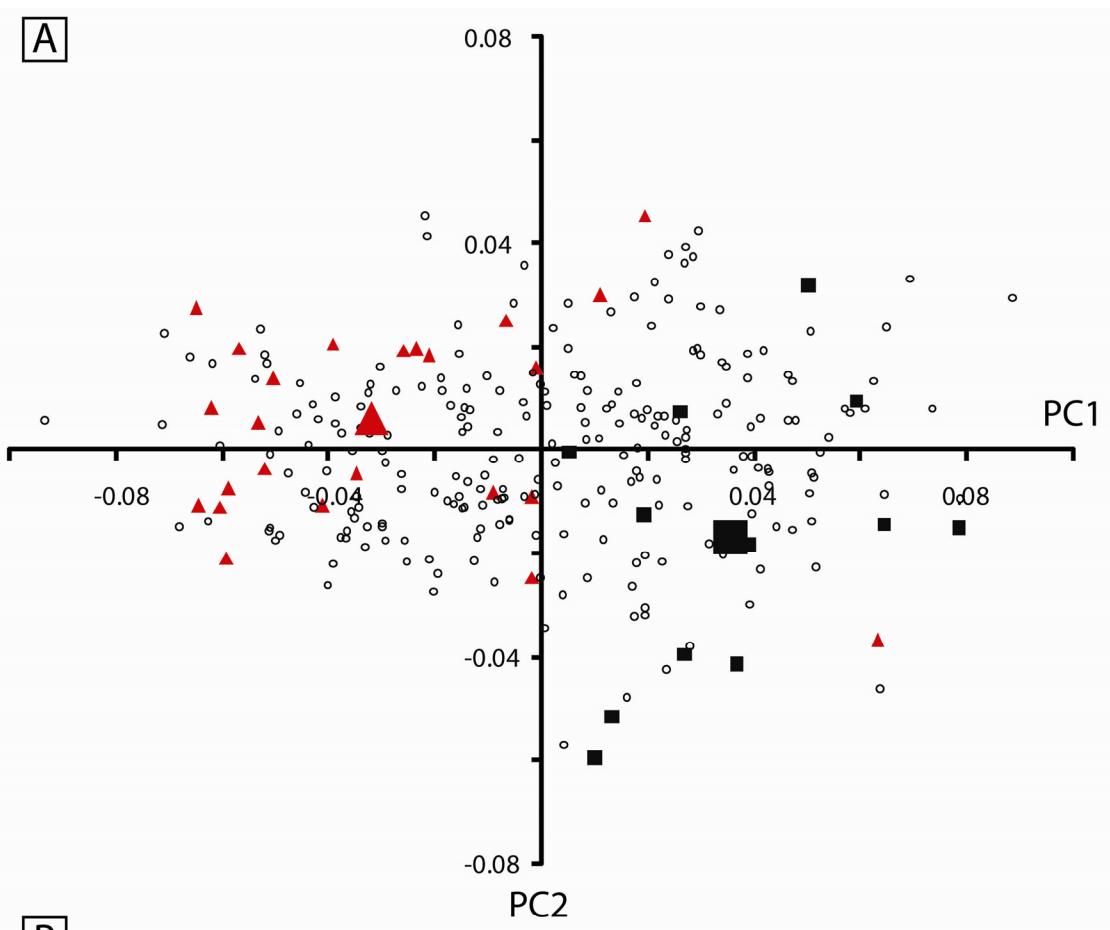
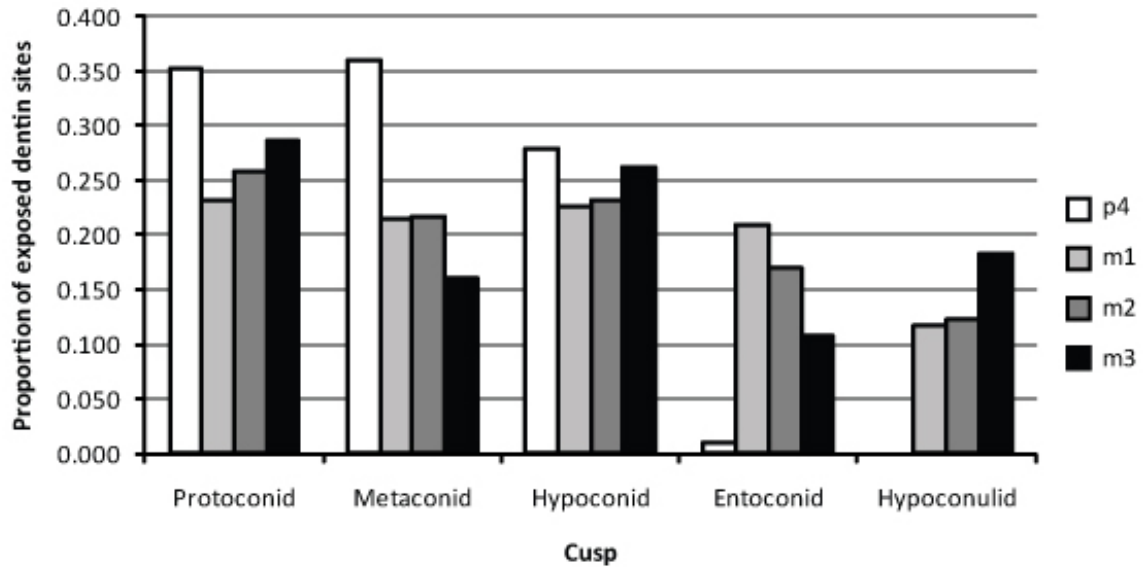


Figure 4.12 Bar graph showing the cusp distribution of exposed dentin sites among the lower fourth premolar (p4) and the first through third lower molars (m1-3) in the Clarks Fork and northwestern Bighorn Basin *Hyracotherium* taxa. The trigonid bears the majority of exposed dentin sites at the p4 position. Exposed dentin sites are more equally distributed among cusps of the trigonid and talonid at the m1 and m2 positions, although m2 exhibits slight asymmetry between the buccal and lingual sides. The lower third molar exhibits marked asymmetry between buccal and lingual sides of the tooth.



## References

- Bookstein, F. L. 1987. Random-walk and the existence of evolutionary rates. *Paleobiology*, v. 13, p. 446-464.
- 1988. Random-walk and the biometrics of morphological characters. *Evolutionary Biology*, v. 23, p. 398.
- Clyde, W. C. 2001. Mammalian Biostratigraphy of the McCullough Peaks area in the northern Bighorn Basin. *In* P. D. Gingerich, ed. *Paleocene-Eocene Stratigraphy and Biotic Change in the Bighorn and Clarks Fork Basins, Wyoming*. University of Michigan Papers on Paleontology 33: 109-126.
- Clyde, W. C. and P. D. Gingerich. 1994. Rates of evolution in the dentition of early Eocene *Cantius*: Comparison of size and shape. *Paleobiology*, v. 20, p. 506-522.
- Chew, A. 2005. Biostratigraphy, paleoecology, and synchronized evolution in the early Eocene mammalian fauna of the central Bighorn Basin, Wyoming. Ph.D. dissertation. Johns Hopkins University.
- Chew, A. E. 2009. Paleoecology of the early Eocene Willwood mammal fauna from the central Bighorn Basin, Wyoming. *Paleobiology*, v. 35, p. 13-31.
- Froehlich, D. J. 2002. Quo vadis eohippus? The systematic and taxonomy of the early Eocene equids (Perissodactyla): *Zoological Journal of the Linnean Society*, v. 134, p. 141-256.
- Gingerich, P. D. 1991. Systematics and evolution of early Eocene Perissodactyla (Mammalia) in the Clarks Fork Basin, Wyoming: Contributions from the Museum of Paleontology, University of Michigan, v. 28, p. 181-213.
- 1993. Quantification and comparison of evolutionary rates. *American Journal of Science* 293A: 453-478.
- 2003. Mammalian responses to climate change at the Paleocene-Eocene boundary: Polecat Bench record in the northern Bighorn Basin, Wyoming. *In* Gingerich, P. D., Schmitz, B., Thomas, E., and Wing, S. L., eds., *Causes and consequences of globally warm climates in the early Paleogene*: Geological Society of America Special Paper, v. 369, p. 463-478.
- Greaves, W. S. 2000. Location of the vector of jaw muscle force in mammals. *Journal of Morphology*, v. 243, p. 293-299.

- Hansen, T. F. and G. P. Wagner. 2001. Modeling genetic architecture: A multilinear theory of gene interaction. *Theoretical Population Biology*, v. 59, p. 61-86.
- Hansen, T. F. and D. Houle. 2004. Evolvability, stabilizing selection, and the problem of stasis. *In* M. Pigliucci and K. Preston, eds. *Phenotypic integration: Studying the ecology and evolution of complex phenotypes*. Oxford University Press, Oxford, p. 130-150.
- Herring, S. W. 1985. Morphological correlates of masticatory patterns in peccaries and pigs. *Journal of Mammalogy*, v. 66, p. 603-617.
- Janis, C. M. and M. Fortelius. 1988. On the means whereby mammals achieve increased functional durability of their dentitions, with special reference to limiting factors. *Biological Reviews*, v. 63, p. 197-230.
- Kaiser, T. M. and M. Fortelius. 2003. Differential mesowear in occluding upper and lower molars: Opening mesowear analysis for lower molars and premolars in hypsodont horses. *Journal of Morphology*, v. 258, p. 67-83.
- Piras, P., F. Marcolini, P. Raia, M. T. Curcio, and T. Kotsakis. 2009. Testing evolutionary stasis and trends in first lower molar shape of extinct Italian populations of *Terricola savii* (Arvicolidae, Rodentia) by means of geometric morphometrics. *Journal of Evolutionary Biology* 22: 179-191.
- Radinsky, L. 1969. The early evolution of the Perissodactyla. *Evolution*, v. 23, p. 308-328.
- Raup, D. M. and R. E. Crick. 1981. Evolution of single characters in the Jurassic ammonite *Kosmoceras*. *Paleobiology*, v. 7, p. 200-215.
- Salazar-Ciudad, I. and J. Jernvall. 2002. A gene network model accounting for development and evolution of mammalian teeth. *Proceedings of the National Academy of Science*, v. 99, p. 8116-8120.
- Schankler, D. 1980. Faunal zonation of the Willwood Formation in the central Bighorn Basin, Wyoming. *In* P. D. Gingerich, ed. *Early Cenozoic paleontology and stratigraphy of the Bighorn Basin, Wyoming*. University of Michigan Papers on Paleontology, v. 24, p. 99-114.
- Sheets, H. D. and C. E. Mitchell. 2001. Why the null matters: Statistical tests, random walks and evolution. *Genetica* 112: 105-125.
- Spencer, M. A. 1998. Force production in the primate masticatory system: Electromyographic tests of biomechanical hypotheses. *Journal of Human Evolution*, v. 34, p. 25-54.

- Weijs, W. A. 1980. Biomechanical models and the analysis of form: A study of the mammalian masticatory apparatus. *American Zoologist*, v. 20, p. 707-719.
- Wood, A. R., M. J. Kraus, and P. D. Gingerich. 2008. Downslope fossil contamination: Mammal-bearing fluvial conglomerates and the Paleocene-Eocene faunal transition (Willwood Formation, Bighorn Basin, Wyoming). *Palaios* 23: 380-390.
- Wood, A. R., M. L. Zelditch, A. N. Rountrey, T. P. Eiting, H. D. Sheets, and P. D. Gingerich. 2007. Multivariate stasis in the dental morphology of the Paleocene-Eocene condylarth *Ectocion*. *Paleobiology*, v. 33, p. 248-260.
- Workman, M. S., L. J. Leamy, E. J. Routman, and J. M. Cheverud. 2002. Analysis of quantitative trait locus effects on the size and shape of mandibular molars in mice. *Genetics*, v. 160, p. 1573-1586.

## Chapter 5

### ***Hyracotherium* Evolution within the Context of Climatic and Environmental Change: Summary and Conclusions**

The objective of this dissertation was to document and study high-resolution time series of *Hyracotherium* morphology in the Clarks Fork and northwestern Bighorn Basins, Wyoming, during the early-middle Wasatchian (earliest Eocene). This objective was achieved in the context of lower dental morphology (Chapter 4), facilitated by understanding and mitigating the biases imposed by dental wear (Chapter 3). The value of a post-cranial morphological time series derived from isolated elements is questionable without a comprehensive understanding of the post-cranial functional morphology in *Hyracotherium*. The post-cranial description of *Hyracotherium grangeri* (Chapter 2) provides a framework for such future work.

The evolutionary dynamics of *Hyracotherium* lower dental morphology were investigated in Chapter 4, but this data was not interpreted within the context of available paleoclimatic/paleoenvironmental proxies. Thus, the purpose of this chapter is to make preliminary comparisons between the proxies introduced in Chapter 1 and the time series of lower dental size and shape presented in Chapter 4. This chapter will conclude with a summary of main conclusions from previous chapters.

The similarity between time series of paleoclimatic/paleoenvironmental proxies and morphology can be quantitatively assessed via cross-correlation, assuming that temporal resolution is comparable in each time series and the data were sampled at regular intervals (Shumway and Stoffer, 2006). The question of interest is whether the patterns within each time series are similar, meaning that the latter assumption can be relaxed if data points in each time series were sampled from the same stratigraphic levels. Out of the three time series of paleoclimatic/paleoenvironmental proxies shown in Fig. 1.2, only the stable carbon isotope record of Koch et al. (1995) fulfills this condition. The stable carbon isotope values in their study were measured from pedogenic carbonates sampled from the same localities as dental material presented here.

Any significant cross-correlations between the stable carbon isotope time series and morphological series cannot be interpreted as causal relationships. Soil CO<sub>2</sub>, the source of carbon in pedogenic carbonates, is a mixture of atmospheric CO<sub>2</sub> and CO<sub>2</sub> from plant decomposition and root respiration (Bowen et al., 2001). Consequently, changes in carbon isotopic compositions of pedogenic carbonates reflect broad environmental perturbations potentially resulting from changes in atmospheric CO<sub>2</sub> isotopic composition and concentration as well as changes in floral communities. Thus, any observed correlations between the isotopic and morphological time series will be interpreted to result from common, underlying causal events.

## **Methods**

Only morphological time series exhibiting variable morphology through time were compared to the stable carbon isotope time series (i.e. p4 – m3 dental size time



series and the time series of PC1 scores derived from m3 lingual shape). All other morphological time series found to exhibit evolutionary stasis in Chapter 4 were excluded. Each time series was subjected to a test of stationarity prior to being analyzed for significant cross-correlations. A stationary time series is defined here as a time series with constant mean and variance (Shumway and Stoffer, 2006).

The significance of each cross-correlation was determined via a resampling test. A distribution of correlation coefficients was produced by resampling the stable carbon isotope time series with replacement 1000 times and recalculating the correlation coefficient between the resampled isotope time series and the unaltered morphological time series. If the observed correlation coefficient falls outside the two-sided confidence interval, then it can be concluded that the two time series are significantly similar.

The large carbon isotope excursion evident in the Wa-0 interval (1520 m level) could potentially overwhelm the cross-correlation calculation, leading to an erroneous high correlation between the carbon isotope time series and morphological time series. Thus, each cross-correlation was recalculated after removal of data derived from the 1520 m level.

## **Results**

The correlations between the stable carbon isotope time series and the three molar size time series are significant, although low in the case of m1 and m2 size (Table 5.1). Each significant correlation coefficient is positive, indicating that, as the stable carbon isotope values become more positive (heavier), molar size increases. This relationship is strongest for m3 size, which is also the morphological time series that exhibits the

greatest overall excursion in size. Removal of the 1520 m level data produces lower correlation coefficients between each molar size time series and the carbon isotope series. Only the m3 size time series coefficient remains significant after removal of Wa-0 data.

## **Discussion**

The weak, yet significant correlations between molar size and stable carbon isotopic series suggest that the climatic/environmental factors responsible for perturbations in soil CO<sub>2</sub> composition also exerted selective pressures on dental size in *Hyracotherium*. As expected, the low correlations indicate an indirect link between pedogenic carbonate isotopic composition and morphology. Reduction of correlation coefficients after removal of the Wa-0 data suggests either a nonlinear relationship between pedogenic carbon isotopes and molar/body size or presence of complicating factors during the Wa-0 biozone not present in succeeding intervals. Changes in plant composition and reproductive traits during the Eocene, however, may provide a link between these two records across all intervals.

Koch et al. (1995) minimized the contribution of atmospheric CO<sub>2</sub> to the isotopic composition of pedogenic carbonates by sampling carbonate nodules at least 30 cm below the top of each paleosol package. Consequently, their stable carbon isotope record should mainly reflect the isotopic composition of soil CO<sub>2</sub> derived from plant materials buried and decomposed in these Eocene soils. The C3 plant material of the early Eocene should track changes in isotopic composition of atmospheric CO<sub>2</sub> during that time (Arens et al., 2000), further reflecting changes to the regional and possibly global carbon cycles.

Changes in the carbon cycle result from changes in sequestration of carbon in both terrestrial and marine reservoirs. Increased burial of organic carbon in both terrestrial and marine reservoirs leads to lower atmospheric pCO<sub>2</sub> levels (Schimel, 1995; Kump and Arthur 1999) and positive excursions in δ<sup>13</sup>C values in remaining atmospheric CO<sub>2</sub> and organic compounds. Changes in terrestrial reservoirs are likely to coincide with alterations in terrestrial ecosystem characteristics, particularly evident in the composition of floral communities (Schimel, 1995). The lack of major flora turnover during the Wa-1 through Wa-4 biozones (Wing, 1998) suggests no major perturbations in terrestrial carbon reservoirs in the Clarks Fork and Bighorn Basins. There is evidence, however, of high levels of organic carbon burial in the marine record following the Paleocene-Eocene Thermal Maximum (Knies et al., 2008). Furthermore, boron isotope estimates of atmospheric pCO<sub>2</sub> levels provide independent evidence for a significant drop in pCO<sub>2</sub> following the Paleocene-Eocene Thermal Maximum (Pearson and Palmer, 2000) consistent with the more positive δ<sup>13</sup>C values recorded in Bighorn Basin pedogenic carbonates.

Atmospheric pCO<sub>2</sub> levels have been found to differentially affect the reproductive and structural components of plants, consequently affecting the types and amount of nutrition available from plants under varying pCO<sub>2</sub> conditions. Several studies have found an inverse relationship between nutritional quality of structural plant components (e.g. leaves and stems) and pCO<sub>2</sub> levels, such that the ratio of indigestible cellulose to protein was higher in structural components grown under elevated pCO<sub>2</sub> levels (Buse et al., 1998; Stiling and Cornelissen, 2007). Plant reproductive rates, however, increase

under elevated pCO<sub>2</sub> conditions, leading to the production of more fruit and seeds (Jackson et al., 1994; Jablonski et al., 2002).

It is possible that as pCO<sub>2</sub> levels dropped during the early-middle Wasatchian, the availability of fruit and seeds decreased while the nutritional quality of leaves increased, causing a shift in the proportion of fruits and leaves in the diets of herbivores. The nutritional quality of ingested plant material is relevant to differences in body size among mammalian herbivores. Larger bodied herbivores typically feed on foods of lower nutritional quality than smaller herbivores (Taylor and Murray, 1987), possibly due to their lower metabolic requirements or the ability of their longer gastrointestinal tracts to more efficiently extract nutrients (Clauss et al., 2003). Thus, the *Hyracotherium* lineage may have experienced selective pressures for larger body sizes to compensate for the change in fruit availability and greater intake of foliage.

Figure 5.1 shows that a shift in evolutionary dynamics in molar size coincides with a shift in optimal m3 lingual shape near the 1900 m stratigraphic level. At this level, the directional trend of increasing molar size is replaced by a directional trend of decreasing molar size. The shift in optimal m3 lingual shape involves a change in orientation of the m3 entoconid such that it more closely resembles the condition exhibited by m1 and m2 lingual shape (Fig. 4.10), possibly aligning the m3 hypolophid with those of m1 and m2 and lengthening the area of occlusion devoted to transverse shearing. The directional trend in decreasing molar size may be explained by greater availability of fruit after the 1900 m stratigraphic level. The concurrent change in m3 shape, however, suggests that the *Hyracotherium* dentition may have evolved the ability to process more foliage per chewing stroke, increasing the ability to derive nutrients from

foliage. Higher digestive efficiency may have reduced selective pressures for larger body sizes.

Shifts in evolutionary dynamics shown in Fig. 5.1 distinguish specific intervals in which the types or relative intensities of selective pressures experienced by the *Hyracotherium* lineage changed during the early Eocene. The first shift occurs across the Wa-0/Wa-1 boundary coincident with the climatic recovery following the PETM. The second shift in which evolutionary dynamics of dental size shifts from stasis to a directional trend of increasing size occurs within the Wa-2 – Wa-3a interval. The third shifting point at the 1900 m stratigraphic level was described in the preceding paragraph.

Future work involving intensive sampling of morphologies and paleoclimatic/paleoenvironmental proxies should be focused at these intervals in order to better characterize the selective pressures affecting the evolution of *Hyracotherium* and other taxa. Such work should include microwear analysis to detect differences in dietary preferences and high-resolution carbon isotopic analysis of bulk organic carbon and biomarkers such as leaf-wax lipids (e.g. Smith et al., 2007) to better quantify changing environmental conditions. Furthermore, work involving temperature proxies, such as isotopic composition of pedogenic hematite, should be performed at these intervals at high-resolution to better resolve temperature changes expected with decrease pCO<sub>2</sub> levels. Stable isotopic analysis of enamel from each interval's fauna could be conducted to detect potential changes in forest structure and resource partitioning among the mammalian taxa (e.g. Secord et al., 2008).

## Overall conclusions

Some of the more important conclusions of this dissertation can be summarized as follows:

1) The posterior thorax and lumbus of *Hyracotherium grangeri* is divided into anterior facultatively and posterior obligately dorsostable regions. The facultatively dorsostable region (T15-L3) is characterized by robust, cranially-inclined neural processes, well-developed attachment sites for epaxial musculature, and zygapophyseal articulations that limit motion to the sagittal plane. The dorsostable region (L3-S1) is characterized by vertical neural processes, a reduction in epaxial musculature sites, and the presence of embracing zygapophyses. [Chapter 2]

2) The range of motion available between distal and proximal articulations of the fore- and hindlimbs in *Hyracotherium grangeri* differ substantially. The rounded humeral and femoral heads indicate that the shoulder and hip joints were capable of a wide range of motions. The hinge-like joints of the wrist, knee, and ankle would limit motion to the parasagittal plane. Motion at the elbow is limited to a plane oblique to the parasagittal plane, such that in flexion the manus is oriented in line with the humerus and in extension the manus is oriented closer to the midline. [Chapter 2]

3) The post-cranial functional morphology of *Hyracotherium* suggests that locomotion in these early equids was not as similar to that of modern Equids as

previously suggested. The highly flexed neutral posture of the knee and presence of a large gastrocnemius sesamoid implies that considerable propulsive force was generated by extension of the knee and ankle in addition to extension of the hip. The flexible hip and shoulder joints were likely needed for greater maneuverability in the complicated and uneven terrain present in *Hyracotherium*'s forest habitat. The facultatively dorsostable region of the vertebral column would facilitate dynamic positioning of the center of mass during acceleration. The obligate dorsostable region would have minimized the efforts of epaxial musculature in preventing pelvic torsion, maximizing the energetic efficiency of vertebral stabilization. [Chapter 2]

4) The positional and overall wear indices are continuous, quantitative measurements of dental wear, calculated via multivariate analysis of dental morphology directly affected by wear. The suites of measurements used to derive the positional indices differ between each tooth position, reflecting differences in how each tooth is used during mastication. The overall wear index can be applied to all tooth positions for comparative purposes, but the explanatory power of the overall index is lower than that of the positional indices. [Chapters 3 & 4]

5) Dental wear accounts for a significant and substantial proportion of variance in dental shape among *Hyracotherium* taxa, which can be removed via regression to predict unworn morphologies. Regression coefficients derived from multivariate regression of shape data onto the wear index can be used to predict dental

morphologies at any level of wear. Regression residuals should reflect intra-specific variation and wear events unique to individuals (e.g. cusp breakage, malocclusion, etc). Prediction of unworn dental morphologies was used to increase sample sizes for test of evolutionary dynamics and to mitigate the bias imposed by dental wear. [Chapters 3 & 4]

6) Sampling teeth of various amounts of dental wear for statistical tests of evolutionary dynamics asymmetrically affects the ability to detect directional and static trends in dental morphology. Dental wear imposes a time-independent dimension of variation on morphological time series of dental shape. The ability of statistical tests to identify time series of evolutionary stasis is not hindered by dental wear, because phenotypic variation is already time-independent in these time series. The time-dependent variation in directional time series is diluted by the variation imposed by dental wear, such that the ability to detect directional trends depends on the relative proportions of each type of variation. [Chapter 3]

7) *Hyracotherium sandrae*, *H. grangeri*, *H. aemulor*, and *H. pernix* appear to constitute a single lineage of early Eocene equids in the Clarks Fork and northwestern Bighorn Basins. Diagnostic characters, such as the presence/absence of an anterior trigonid fovea or p4 entoconid, proposed by other authors were found to be equally distributed across all taxa and stratigraphic levels. These characters represent highly variable morphologies and are not informative for resolving early equid taxonomy. [Chapter 4]



8) The trajectories of dental shape change with increasing dental wear were not significantly different between *Hyracotherium grangeri* and *Hyracotherium aemulor*, suggesting no differences in occlusion or masticatory motion during feeding. The relative contribution of each cheek tooth to mastication, however, did vary between the species suggesting differences in the position of maximum occlusal force. Repositioning of maximum occlusal force could have been facilitated by changes in the geometry of masticatory muscles across this species transition. [Chapter 4]

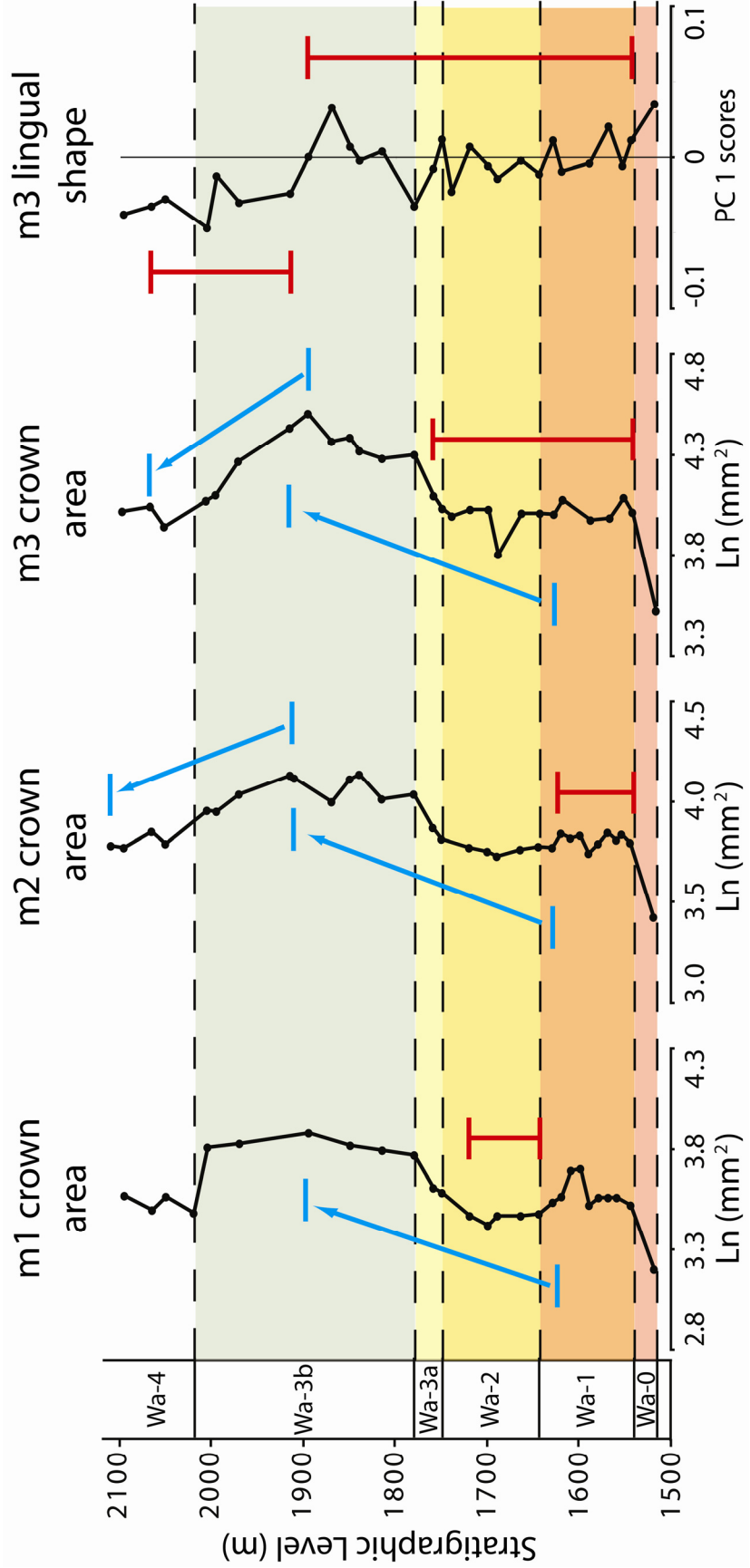
9) Time series of dental size in the *Hyracotherium* lineage exhibit heterogeneous evolutionary dynamics with segments of directional and static trends that significantly differ from random processes. The evolutionary dynamics in tooth size are relatively consistent among the different tooth positions, which is indicative of changing selective pressures on overall body size. [Chapter 4]

10) Time series of dental shape in the *Hyracotherium* lineage exhibit homogeneous evolutionary stasis across the sampled interval, with the exception of m3 lingual shape. The m3 lingual shape time series displays a shift in optimal morphology during the Wa-3b biozones that may have provided greater occlusal area for shearing during mastication. This shift in m3 lingual shape is coincident with an evolutionary shift in body size, suggesting that dental size and shape may evolve at different rates in response to the same selective pressures. [Chapter 4]

Table 5.1 Cross-correlation results between the pedogenic carbonate isotopic time series and morphological time series of dental size and shape. Removal of Wa-0 data associated with the Paleocene-Eocene Thermal Maximum (PETM) leads to lower correlation coefficients, indicating either a nonlinear relationship between the environment and morphological time series or the presence of unknown complicating factors during the PETM.

<b>Total time series</b>		
<b>Morphological time series</b>	<b>Correlation coefficient r</b>	<b>Significance level</b>
p4 crown area	0.43	p > 0.05
m1 crown area	<b>0.48</b>	<b>p &lt; 0.05</b>
m2 crown area	<b>0.46</b>	<b>p &lt; 0.05</b>
m3 crown area	<b>0.79</b>	<b>p &lt; 0.01</b>
m3 lingual PC1 scores	-0.28	p > 0.05
<b>Time series w/o Wa-0 interval</b>		
<b>Morphological time series</b>	<b>Correlation coefficient r</b>	<b>Significance level</b>
p4 crown area	0.09	p > 0.05
m1 crown area	0.33	p > 0.05
m2 crown area	0.26	p > 0.05
m3 crown area	<b>0.50</b>	<b>p &lt; 0.05</b>
m3 lingual PC1 scores	0.19	p > 0.05

Figure 5.1 Comparison of morphological time series of dental size and shape in the *Hyracotherium* lineage exhibiting heterogeneous evolutionary dynamics. Three shifts in evolutionary dynamics are evident in each time series. The first shift occurs at the Wa-0/Wa-1 boundary coincident with the climatic recovery following the PETM. The second shift occurs within the Wa-2 – Wa-3a intervals during which tooth size shifted from a static morphology to a directional trend of increasing size. The third shift occurs near the 1900 m stratigraphic level where a shift in optimal m3 shape coincides with a reversal in tooth/body size trends. Red and blue brackets indicate evolutionary stasis and directional change, respectively.



## References

- Arens, N. C., A. H. Jahren, and R. Amundson. 2000. Can C3 plants faithfully record the carbon isotopic composition of atmospheric carbon dioxide? *Paleobiology* 26: 137-164.
- Bowen, G. J., P. L. Koch, P. D. Gingerich, R. D. Norris, S. Bains, and R. M. Corfield. 2001. Refined isotope stratigraphy across the continental Paleocene-Eocene boundary on Polecat Bench in the northern Bighorn Basin. *In* P. D. Gingerich, ed. *Paleocene-Eocene stratigraphy and biotic change in the Bighorn and Clarks Fork Basins, Wyoming*. University of Michigan Papers on Paleontology 33: 73-88.
- Buse, A., J. E. G. Good, S. Dury, and C. M. Perrins. 1998. Effects of elevated temperature and carbon dioxide on the nutritional quality of leaves of oak (*Quercus robur* L.) as food for the winter moth (*Operophtera brumata* L.). *Functional Ecology* 12: 742-749.
- Clauss, M., R. Frey, B. Kiefer, M. Lechner-Doll, W. Loehlein, C. Polster, G. E. Rossner, and W. J. Streich. 2003. The maximum attainable body size of herbivorous mammals: Morphophysiological constraints on foregut and adaptations of hindgut fermenters. *Oecologia* 136: 14-27.
- Jablonski, L. M., X. Wang, and P. S. Curtis. 2002. Plant reproduction under elevated CO<sub>2</sub> conditions: A meta-analysis of reports of 79 crop and wild species. *New Phytologist* 156: 9-26.
- Jackson, R. B., O. E. Sala, C. B. Field, and H. A. Mooney. 1994. CO<sub>2</sub> alters water use, carbon gain, and yield for the dominant species in a natural grassland. *Oecologia* 98: 257-262.
- Knies, J., U. Mann, B. N. Popp, R. Stein, and H.-J. Brumsack. 2008. Surface water productivity and paleoceanographic implications in the Cenozoic Arctic Ocean. *Paleoceanography* 23: 1-12.
- Koch, P. L., J. C. Zachos, and D. L. Dettman. 1995. Stable isotope stratigraphy and paleoclimatology of the Paleogene Bighorn Basin (Wyoming, USA). *Palaeogeography, Palaeoclimatology, Palaeoecology* 115: 61-89.
- Kump, L. R. and M. A. Arthur. 1999. Interpreting carbon-isotope excursions: carbonates and organic matter. *Chemical Geology* 161: 181-198.
- Pearson, P. N. and M. R. Palmer. 2000. Atmospheric carbon dioxide concentrations over the past 60 million years. *Nature* 406: 695-699.

- Schimel, D. S. 1995. Terrestrial ecosystems and the carbon cycle. *Global Change Biology* 1: 77-91.
- Secord, R., S. L. Wing, and A. Chew. 2008. Stable isotopes in early Eocene mammals as indicators of forest canopy structure and resource partitioning. *Paleobiology* 34: 282-300.
- Shumway, R. H. and D. S. Stoffer. 2006. Time series analysis and its applications with R examples. 2<sup>nd</sup> Ed. Springer, New York.
- Smith, F. A., S. L. Wing, and K. H. Freeman. 2007. Magnitude of the carbon isotope excursion at the Paleocene-Eocene thermal maximum: The role of plant community change. *Earth and Planetary Science Letters* 262: 50-65.
- Stiling, P. and T. Cornelissen. 2007. How does elevated carbon dioxide (CO<sub>2</sub>) affect plant-herbivore interactions? A field experiment and meta-analysis of CO<sub>2</sub>-mediated changes on plant chemistry and herbivore performance. *Global Change Biology* 13: 1823-1842.
- Taylor, St. C. S. and J. I. Murray. 1987. Genetic aspects of mammalian survival and growth in relation to body size. Pp. 487-533 *in* J. B. Hacker and J. H. Ternouth, eds. *The Nutrition of Herbivores*. Academic Press, Orlando.
- Wing, S. L. 1998. Late Paleocene – early Eocene floral and climatic change in the Bighorn Basin, Wyoming. Pp. 380-400 *in* M.-P. Aubry, S. G. Lucas, and W. A. Berggren, eds. *Late Paleocene – Early Eocene Biotic and Climatic Events in the Marine and Terrestrial Records*. Columbia University Press, New York.

## Appendix 1

### R Code for Dental Wear Index Search Program

```
data=read.table(file.choose()) #Input data with variables arranged in columns.
                                #Dependent variable in first column.

numVar=ncol(data)-1
Rsquared=0 #Empty variables to be filled with search results.
Rsquared2=0 #R2 values of top ranking models.
Rsquared3=0
Rsquared4=0
Rsquared5=0
variables = 0 #Suite of measurements associated with top ranking models.
variables2 = 0
variables3 = 0
variables4 = 0
variables5 = 0
log = 0 #Log of R2 values to be ranked by search.

for (v in 2:(numVar-1)){
possible=combn((2:(numVar+1)),v) #Creates all possible combinations of variable indices.
numModels=ncol(possible)
for (i in 1:numModels){
mat=matrix(0,nrow(data),v)
for (d in 1:v){
mat[,d]=data[,possible[d,i]] #Defines the suite of measurements to be included in PCA.
}
pca=princomp(mat,cor=TRUE) #Principal components analysis of given suite of measurements.
model=lm(data[,1]~pca$scores[,1])
r2=(sum((fitted(model)-mean(data[,1]))^2))/sum((data[,1]-mean(data[,1]))^2)
log = c(log,r2)
if (r2>Rsquared) #Next 20 lines iteratively ranks models by
#R2 values as they are created.

variables<-as.vector(possible[,i]) else
if (r2>Rsquared2)
variables2<-as.vector(possible[,i]) else
if (r2>Rsquared3)
variables3<-as.vector(possible[,i]) else
if (r2>Rsquared4)
variables4<-as.vector(possible[,i]) else
if (r2>Rsquared5)
variables5<-as.vector(possible[,i])
if (r2>Rsquared)
Rsquared<-r2 else
```

```
if (r2>Rsquared2)
Rsquared2<-r2 else
if (r2>Rsquared3)
Rsquared3<-r2 else
if (r2>Rsquared4)
Rsquared4<-r2 else
if (r2>Rsquared5)
Rsquared5<-r2
}
}
RsquaredResults=matrix(0,5,1)
RsquaredResults[1,]=Rsquared
RsquaredResults[2,]=Rsquared2
RsquaredResults[3,]=Rsquared3
RsquaredResults[4,]=Rsquared4
RsquaredResults[5,]=Rsquared5
```

```
RsquaredResults
list(variables,variables2,variables3,variables4,variables5)
```

#Output of search results.

## Appendix 2

### R Code for Directional Selection Simulation Including Excursion and Angular Test

```
data=data.matrix(read.table(file.choose())) #Data in x1,y1,x2,y2...xn,yn format. Specimens in rows. No CS.
refShape=data.matrix(read.table(file.choose())) #Reference shape input.
indepX=as.vector(t(read.table(file.choose()))) #Wear index in a single column.

minWear=min(indepX)
maxWear=max(indepX)
wearDivision=20 #Number of subdivisions of wear index values.
wearIncr=(maxWear-minWear)/wearDivision #Width of wear index subdivisions.
numRuns=500 #Number of simulated random walks.
stdev=0.00001 #Standard deviation of shape coordinates.
strength=0.6 #Scalar multiplier of vector of directional change (i.e. selection strength).
numSteps=21 #Number of time steps in simulated time series.
numSeries=20 #Number of directional time series to simulate.

refShape=refShape[, -ncol(refShape)]
a=seq(1, length(refShape)-1, by=2)
b=seq(2, length(refShape), by=2)

theta=0.5*abs(atan((-2*(refShape[c(a)]%*%refShape[c(b)]))/(sum(refShape[c(a)]^2)-
sum(refShape[c(b)]^2)))) #Principal axis rotation angle.
ct=cos(theta)
st=sin(theta)
temp=refShape[c(a)]*ct-refShape[c(b)]*st
refShape[c(b)]=refShape[c(a)]*st+refShape[c(b)]*ct #Rotation of reference shape to its principal axis.
refShape[c(a)]=temp

for (i in 1:(nrow(data))) { #Rotation of shape data to reference shape principal axis.
  temp=data[i,c(a)]*ct-data[i,c(b)]*st
  data[i,c(b)]=data[i,c(a)]*st+data[i,c(b)]*ct
  data[i,c(a)]=temp
}

Rmatrix=matrix(0,ncol(data)/2,ncol(data)/2) #Definition of R matrix, pairwise Procrustes distance
#between landmarks in the reference shape.

for (i in 1:(ncol(data)/2)) {
  Rmatrix[i,]=(((refShape[a[i]]-refShape[seq(1,length(refShape)-1,by=2)])^2)+((refShape[b[i]]-
refShape[seq(2,length(refShape),by=2)])^2))^0.5
}

Umatrix=round(((Rmatrix)^2)*log(Rmatrix^2),digits=12)
diag(Umatrix)=0
newU=matrix(0,(ncol(data)/2)+3,(ncol(data)/2)+3) #L matrix used in thin plate spline interpolation.
newU[1:(ncol(data)/2),1:(ncol(data)/2)]=Umatrix
newU[(ncol(data)/2)+1,1:(ncol(data)/2)]=1
newU[1:(ncol(data)/2),(ncol(data)/2)+1]=1
newU[(ncol(data)/2)+2,1:(ncol(data)/2)]=refShape[c(a)]
```



```

newU[1:(ncol(data)/2),(ncol(data)/2)+2]=refShape[c(a)]
newU[(ncol(data)/2)+3,1:(ncol(data)/2)]=refShape[c(b)]
newU[1:(ncol(data)/2),(ncol(data)/2)+3]=refShape[c(b)]

invL=round(solve(newU),digits=10) #Eigen analysis of inverted L matrix.
EigenL=eigen(invL[1:(ncol(data)/2),1:(ncol(data)/2)])

diffMatrix0=(t(data)-(refShape)) #Matrix of shape differences between specimens and reference shape.
diffMatrix=diffMatrix0
diffMatrix[,1:(ncol(data)/2)]=diffMatrix0[,c(a)]
diffMatrix[((ncol(data)/2)+1):(ncol(data))]=diffMatrix0[,c(b)]
Pmatrix=matrix(0,ncol(data),ncol(data)-4) #Definition of principal warp matrix.
Pmatrix[1:(ncol(data)/2),1:(ncol(data)/2-3)]=EigenL$vectors[,1:(ncol(data)/2-3)]
Pmatrix[((ncol(data)/2)+1):nrow(Pmatrix),((ncol(data)/2-3)+1):(ncol(Pmatrix)-2)]=EigenL$vectors[,1:(ncol(data)/2-3)]
gamma=sum(refShape[c(b)]^2)
alpha=sum(refShape[c(a)]^2)
Pmatrix[1:(ncol(data)/2),(ncol(Pmatrix)-1)]=((alpha/gamma)^0.5)*refShape[c(b)]
Pmatrix[1:(ncol(data)/2),(ncol(Pmatrix))]=(-1*(gamma/alpha)^0.5)*refShape[c(a)]
Pmatrix[((ncol(data)/2)+1):(nrow(Pmatrix)),(ncol(Pmatrix)-1)]=((gamma/alpha)^0.5)*refShape[c(a)]
Pmatrix[((ncol(data)/2)+1):(nrow(Pmatrix)),(ncol(Pmatrix))]=((alpha/gamma)^0.5)*refShape[c(b)]

pwScores=as.matrix(diffMatrix)%*%Pmatrix #Calculation of partial warp and uniform component scores.

slopes=c(rep(0,ncol(pwScores)))
intercepts=c(rep(0,ncol(pwScores)))
residuals=matrix(0,nrow(data),ncol(pwScores))

for (i in 1:(ncol(pwScores))) { #Multivariate regression of partial warp scores onto wear index.
  model=lm(pwScores[,i]~indepX)
  slopes[i]=model$coefficients[2]
  intercepts[i]=model$coefficients[1]
  residuals[,i]=model$residuals
}

library(sn)
dp=c(-1.2047,2.0662,6.8654) #Parameters for skew normal distribution.

popWear=c(rsn(1000,dp[1],dp[2],dp[3])) #Skew normal distribution of wear index values.
popWear=sort(popWear)
numCrazy=length(c(which(popWear<minWear))) #Truncation of unrealistic wear index values.
popWear[(1:numCrazy)]=minWear

wearShape=matrix(0,numSteps,ncol(data))
simResults=matrix(0,(numSeries*(wearDivision+1)),8) #Definition of empty result matrix.

for (h in 1:numSeries) { #Generation of simulated directional time series.
  dirShape=matrix(0,(numSteps-1),ncol(residuals))
  for (d in 1:(numSteps-1)) {
    dirShape[d,]=residuals[135,]*(strength/(numSteps-1))*d+c(rnorm(ncol(residuals),0,stdev))
  } #residuals[135,] is the set of residuals corresponding to the target shape.
  for (z in 1:(wearDivision+1)) {
    simResults[((z-1)*numSeries)+h,1]=(minWear+((z-1)*wearIncr))
    simResults[((z-1)*numSeries)+h,2]=h
  }
}

```

```

stepWear0=mean(c(sample(popWear[1:max(c(which(popWear<=( minWear+((z-
1)*wearIncr)))]),20,replace=TRUE))) #Amount of dental wear sampled at step 1.
unwornMean=(stepWear0*slopes)+intercepts
unwornMean=unwornMean%*%t(Pmatrix)
tempX=unwornMean[c(1:(ncol(data)/2))]
tempY=unwornMean[c(((ncol(data)/2)+1):(ncol(data)))]
unwornMean[c(a)]=tempX
unwornMean[c(b)]=tempY
unwornMean=unwornMean+refShape #Mean shape at step 1.

for (q in 1:(nrow(wearShape)-1)){
  wearShape[1,]=unwornMean
  stepWear=mean(c(sample(popWear[1:max(c(which(popWear<=( minWear+((z-
1)*wearIncr)))]),20,replace=TRUE))) #Dental wear at step q.
  stepWear=(stepWear*slopes)+intercepts+dirShape[q,]
  stepWear=stepWear%*%t(Pmatrix)
  tempX=stepWear[c(1:(ncol(wearShape)/2))]
  tempY=stepWear[c(((ncol(wearShape)/2)+1):ncol(wearShape))]
  stepWear[c(a)]=tempX
  stepWear[c(b)]=tempY
  wearShape[q+1,]=stepWear+refShape #Mean shape at step q.
}

ProDistMatrix=matrix(0,nrow(wearShape),nrow(wearShape))
change=matrix(0,numSteps-1,ncol(wearShape))
changeDist=c(rep(0,numSteps-1))
angleChange=c(rep(0,numSteps-2))

for (i in 1:(numSteps-1)) { #Procrustes distance between adjacent time steps.
  change[i,]=as.matrix(wearShape[i+1,]-wearShape[i,])
  changeDist[i]=(sum(change[i,]^2))^0.5
}
for (t in 1:(numSteps-2)){ #Angle between vectors of shape change between consecutive steps.
  unitVect1=change[t,]/(sum(change[t,]^2)^0.5)
  unitVect2=change[t+1,]/(sum(change[t+1,]^2)^0.5)
  angleChange[t]=(180/3.14159)*(acos(round((sum(unitVect1*unitVect2))/((sum(unitVect1^2)^0.5
)*(sum(unitVect2^2)^0.5))),digits=10)))
}
avgAngle=mean(angleChange) #Observed average angle of shape change.

scaleChange=max(changeDist)/changeDist

Procrustes=function(x){ #Function performs Procrustes superimposition.
  a=seq(1,ncol(x)-1,by=2)
  b=seq(2,ncol(x),by=2)
  for (i in 1:(nrow(x))){
    x[i,c(a)]=x[i,c(a)]-mean((x[i,c(a)]))
    x[i,c(b)]=x[i,c(b)]-mean((x[i,c(b)]))
    x[i,]=x[i,]/(sum(x[i,]^2)^0.5)
  }
  meanShape=x[1,]
  xd=1
  while(xd>1e-12){

```

```

    for (i in 1:nrow(x)){
      theta=-atan(-1*(x[i,c(a)]/meanShape[c(b)]-
meanShape[c(a)]/x[i,c(b)])/(meanShape[c(a)]/x[i,c(a)]+meanShape[c(b)]/x[i,c(a)]))
      b1=cos(theta)
      b2=sin(theta)
      temp=(x[i,c(a)]*b1)-(b2*x[i,c(b)])
      x[i,c(b)]=(x[i,c(b)]*b1)+(b2*x[i,c(a)])
      x[i,c(a)]=temp
      x[i,]=x[i,]/(sum(x[i,]^2)^0.5)
    }
    xrefold=meanShape
    for (m in 1:ncol(x)){
      meanShape[m]=mean(x[,m])
    }
    meanShape=meanShape/(sum(meanShape^2)^0.5)
    xd=sum((meanShape-xrefold)^2)^0.5
    xd
    #points(x[1,c(a)],x[1,c(b)],col="red")
  }

  theta=0.5*abs(atan((-2*(meanShape[c(a)]/meanShape[c(b)])/(sum(meanShape[c(a)]^2)-
sum(meanShape[c(b)]^2))))
  ct=cos(theta)
  st=sin(theta)
  temp=meanShape[c(a)]*ct-meanShape[c(b)]*st
  meanShape[c(b)]=meanShape[c(a)]*st+meanShape[c(b)]*ct
  meanShape[c(a)]=temp

  for (i in 1:(nrow(x))){
    temp=x[i,c(a)]*ct-x[i,c(b)]*st
    x[i,c(b)]=x[i,c(a)]*st+x[i,c(b)]*ct
    x[i,c(a)]=temp
  }
}

Procrustes(wearShape)
for (i in 1:nrow(wearShape)){
  for (j in 1:nrow(wearShape)){
    ProDistMatrix[i,j]=(sum((wearShape[i,]-wearShape[j,])^2))^0.5
  }
}

ObsMaxExcursion=max(ProDistMatrix) #Observed maximum excursion in simulated time series.
randWalk=wearShape
MaxRand=c(rep(0,numRuns))
runAngle=c(rep(0,numSteps-2))
avgRandAngle=c(rep(0,numRuns))
runChange=matrix(0,numSteps-1,ncol(wearShape))
RandDistMatrix=matrix(0,nrow(wearShape),nrow(wearShape))

for (i in 1:numRuns){
  for (k in 1:(numSteps-1)){
    s=(sample(c(1:(nrow(wearShape)-1))),1,replace=TRUE))
    randWalk[k+1,]=as.matrix(randWalk[k,]+(sample(c(-1,1),1)*change[s,])*
runif(1,min=0,max=scaleChange[s]))
    for (w in 1:(numSteps-1)) {

```

```

        runChange[w,]=as.matrix(randWalk[w+1,]-randWalk[w,])
        }
        for (t in 1:(numSteps-2)){
            unitVect1=runChange[t,]/(sum(runChange[t,]^2)^0.5)
            unitVect2=runChange[t+1,]/(sum(runChange[t+1,]^2)^0.5)
            runAngle[t]=(180/3.14159)*(acos(round((sum(unitVect1*unitVect2))/((sum(unitVect1^2)^0.5)*
            (sum(unitVect2^2)^0.5)),digits=10)))
        }
        avgRandAngle[i]=mean(runAngle)           #Average angle of shape change in random time series.
    }
}
Procrustes(randWalk)
for (l in 1:nrow(wearShape)){           #Matrix of pairwise Procrustes distance between steps in random series.
for (j in 1:nrow(wearShape)){
    RandDistMatrix[l,j]=(sum((randWalk[l,]-randWalk[j,])^2)^0.5
}
}
    MaxRand[i]=max(RandDistMatrix)           #Maximum excursion in random time series.
}

sortedMax=sort(MaxRand)
numGreater=length(c(which(sortedMax > ObsMaxExcursion)))
numLess=length(c(which(sortedMax < ObsMaxExcursion)))

sortedAngle=sort(avgRandAngle)
angGreater=length(c(which(sortedAngle > avgAngle)))
angLess=length(c(which(sortedAngle < avgAngle)))

simResults[((z-1)*numSeries)+h,4]=numGreater
simResults[((z-1)*numSeries)+h,5]=numLess
simResults[((z-1)*numSeries)+h,3]=ObsMaxExcursion

simResults[((z-1)*numSeries)+h,8]=angGreater
simResults[((z-1)*numSeries)+h,7]=angLess
simResults[((z-1)*numSeries)+h,6]=avgAngle

}
}

#Format of simResults by column:
#1) Maximum wear index value sampled
#2) Time series number
#3) Observed maximum excursion
#4) Number of random walks with greater excursion
#5) Number of random walks with smaller excursion
#6) Observed average angle between consecutive time steps
#7) Number of random walks with smaller average angle
#8) Number of random walks with greater average angle

```

## Appendix 3

### R Code for Stasis Simulation Module

Note: Colored fonts correspond to modules in Appendix 2 code that need to be replaced in order to simulate time series of evolutionary stasis.

```
data=data.matrix(read.table(file.choose())) #Data in x1,y1,x2,y2...xn,yn format. Specimens in rows. No CS.
refShape=data.matrix(read.table(file.choose())) #Reference shape input.
indepX=as.vector(t(read.table(file.choose()))) #Wear index in a single column.
stasisSample=as.vector(t(read.table(file.choose()))) #Vector of specimen indices corresponding to row
                                                    #in original data file.

minWear=min(indepX)
maxWear=max(indepX)
wearDivision=20 #Number of subdivisions of wear index values.
wearIncr=(maxWear-minWear)/wearDivision #Width of wear index subdivisions.
numRuns=500 #Number of simulated random walks.
stdev=0.00001 #Standard deviation of shape coordinates.
numSteps=21 #Number of time steps in simulated time series.
numSeries=20 #Number of directional time series to simulate.

wearShape=matrix(0,numSteps,ncol(data))
stDevMatrix=matrix(0,numSteps,ncol(residuals))
simResults=matrix(0,(numSeries*(wearDivision+1)),8) #Definition of empty result matrix.

for (h in 1:numSeries){ #Generation of simulated stasis time series.
  stasisShape=matrix(0,numSteps,ncol(residuals))
  for (T in 1:numSteps){
    stDevMatrix[T,]=c(rnorm(ncol(residuals),0,stdev))
  }
  for (d in 1:(numSteps)){
    stasisShape[d,]=residuals[(sample(stasisSample,1)),]+stDevMatrix[d,]
  }
}

for (z in 1:(wearDivision+1)){
  simResults[((z-1)*numSeries)+h,1]=(minWear+((z-1)*wearIncr))
  simResults[((z-1)*numSeries)+h,2]=h
  stepWear0=mean(c(sample(popWear[1:max(c(which(popWear<=( minWear+((z-1)*wearIncr)))]),20,replace=TRUE)]),20,replace=TRUE))) #Amount of dental wear sampled at step 1.
  unwornMean=(stepWear0*slopes)+intercepts
  unwornMean=unwornMean%%t(Pmatrix)
```

```

tempX=unwornMean[c(1:(ncol(data)/2))]
tempY=unwornMean[c(((ncol(data)/2)+1):(ncol(data)))]
unwornMean[c(a)]=tempX
unwornMean[c(b)]=tempY
unwornMean=unwornMean+refShape #Mean shape at step 1.
wearShape[1,]=unwornMean

for (q in 1:(nrow(wearShape)-1)){
  stepWear=mean(c(sample(popWear[1:max(c(which(popWear<=( minWear+((z-
1)*wearIncr)))]),20,replace=TRUE))) #Dental wear at step q.
  stepWear=(stepWear*slopes)+intercepts+stasisShape[q,]
  stepWear=stepWear%*%t(Pmatrix)
  tempX=stepWear[c(1:(ncol(wearShape)/2))]
  tempY=stepWear[c(((ncol(wearShape)/2)+1):ncol(wearShape))]
  stepWear[c(a)]=tempX
  stepWear[c(b)]=tempY
  wearShape[q+1,]=stepWear+refShape #Mean shape at step q.
}

```

## Appendix 4

### R Code for Directional Dental Wear and Directional Selection Simulation Module

Note: Colored fonts correspond to modules in Appendix 2 code that need to be replaced in order to simulate time series with directionally changing dental wear.

```
wearSt=20                                #Scalar multiplier of vector describing directional trend in trajectory
                                          #of shape change with increasing wear.
wearChange=c(rep(0,ncol(pwScores)))      #Next 35 lines define directional trend in trajectory
wearChange=abs(slopes)/(slopes*10000)    #of shape change with increasing wear.
wearChange[1]=1e-04
wearChange[2]=-1e-05
wearChange[3]=1e-05
wearChange[4]=-1e-05
wearChange[5]=-1e-03
wearChange[6]=-1e-05
wearChange[7]=-1e-04
wearChange[8]=1e-03
wearChange[9]=1e-03
wearChange[10]=1e-04
wearChange[11]=1e-03
wearChange[12]=-1e-03
wearChange[13]=1e-04
wearChange[14]=-1e-03
wearChange[15]=1e-03
wearChange[16]=1e-03
wearChange[17]=1e-03
wearChange[18]=-1e-04
wearChange[19]=-1e-04
wearChange[20]=-1e-04
wearChange[21]=1e-04
wearChange[22]=-1e-04
wearChange[23]=1e-04
wearChange[6:29]=0
wearChange[28]=-1e-04
wearChange[29]=0
wearChange[30]=1e-03
wearChange[31]=-1e-04
wearChange[32]=1e-03
wearChange[33]=1e-04
wearChange[34]=-1e-03
wearChange[35]=1e-05
wearChange[36]=-1e-04
```

```

wearShape=matrix(0,numSteps,ncol(data))
simResults=matrix(0,(numSeries*(wearDivision+1)),8) #Definition of empty result matrix.

for (h in 1:numSeries){ #Generation of simulated directional time series.
  dirShape=matrix(0,(numSteps-1),ncol(residuals))
  for (d in 1:(numSteps-1)){
    dirShape[d,]=residuals[135,]*(strength/(numSteps-1))*d+c(rnorm(ncol(residuals),0,stdev))
  }
for (z in 1:(wearDivision+1)){
  simResults[((z-1)*numSeries)+h,1]=(minWear+((z-1)*wearIncr))
  simResults[((z-1)*numSeries)+h,2]=h
  stepWear0=mean(c(sample(popWear[1:max(c(which(popWear<=( minWear+((z-
1)*wearIncr)))]),20,replace=TRUE))) #Amount of dental wear sampled at step 1.
  unwornMean=(stepWear0*slopes)+intercepts
  unwornMean=unwornMean%*%t(Pmatrix)
  tempX=unwornMean[c(1:(ncol(data)/2))]
  tempY=unwornMean[c(((ncol(data)/2)+1):(ncol(data)))]
  unwornMean[c(a)]=tempX
  unwornMean[c(b)]=tempY
  unwornMean=unwornMean+refShape #Mean shape at step 1.

for (q in 1:(nrow(wearShape)-1)){
  wearShape[1,]=unwornMean
  stepWear=mean(c(sample(popWear[1:max(c(which(popWear<=( minWear+((z-
1)*wearIncr)))]),20,replace=TRUE))) #Dental wear at step q.
  stepWear=(stepWear*(slopes+((q/wearSt)*wearChange)))+(intercepts+(minWear*-
1*((q/wearSt)*wearChange))+dirShape[q,]
  stepWear=stepWear%*%t(Pmatrix)
  tempX=stepWear[c(1:(ncol(wearShape)/2))]
  tempY=stepWear[c(((ncol(wearShape)/2)+1):ncol(wearShape))]
  stepWear[c(a)]=tempX
  stepWear[c(b)]=tempY
  wearShape[q+1,]=stepWear+refShape #Mean shape at step q.
}
}

```



## Appendix 5

### R Code for Directional Dental Wear and Stasis Simulation Module

Note: Colored fonts correspond to modules in Appendix 2 code that need to be replaced in order to simulate time series with directionally changing dental wear.

```
wearSt=20                                #Scalar multiplier of vector describing directional trend in trajectory
                                           #of shape change with increasing wear.
wearChange=c(rep(0,ncol(pwScores)))        #Next 35 lines define directional trend in trajectory
wearChange=abs(slopes)/(slopes*10000)     #of shape change with increasing wear.
wearChange[1]=1e-04
wearChange[2]=-1e-05
wearChange[3]=1e-05
wearChange[4]=-1e-05
wearChange[5]=-1e-03
wearChange[6]=-1e-05
wearChange[7]=-1e-04
wearChange[8]=1e-03
wearChange[9]=1e-03
wearChange[10]=1e-04
wearChange[11]=1e-03
wearChange[12]=-1e-03
wearChange[13]=1e-04
wearChange[14]=-1e-03
wearChange[15]=1e-03
wearChange[16]=1e-03
wearChange[17]=1e-03
wearChange[18]=-1e-04
wearChange[19]=-1e-04
wearChange[20]=-1e-04
wearChange[21]=1e-04
wearChange[22]=-1e-04
wearChange[23]=1e-04
wearChange[6:29]=0
wearChange[28]=-1e-04
wearChange[29]=0
wearChange[30]=1e-03
wearChange[31]=-1e-04
wearChange[32]=1e-03
wearChange[33]=1e-04
wearChange[34]=-1e-03
wearChange[35]=1e-05
wearChange[36]=-1e-04
```

```

wearShape=matrix(0,numSteps,ncol(data))
stDevMatrix=matrix(0,numSteps,ncol(residuals))
simResults=matrix(0,(numSeries*(wearDivision+1)),8) #Definition of empty result matrix.

for (h in 1:numSeries){ #Generation of simulated stasis time series.
  stasisShape=matrix(0,numSteps,ncol(residuals))
  for (T in 1:numSteps){
    stDevMatrix[T,]=c(rnorm(ncol(residuals),0,stdev))
  }
  for (d in 1:(numSteps)){
    stasisShape[d,]=residuals[(sample(stasisSample,1),)+stDevMatrix[d,]]
  }
for (z in 1:(wearDivision+1)){
  simResults[((z-1)*numSeries)+h,1]=(minWear+((z-1)*wearIncr))
  simResults[((z-1)*numSeries)+h,2]=h
  stepWear0=mean(c(sample(popWear[1:max(c(which(popWear<=( minWear+((z-
1)*wearIncr)))]),20,replace=TRUE))) #Amount of dental wear sampled at step 1.
  unwornMean=(stepWear0*slopes)+intercepts
  unwornMean=unwornMean%>%t(Pmatrix)
  tempX=unwornMean[c(1:(ncol(data)/2))]
  tempY=unwornMean[c(((ncol(data)/2)+1):(ncol(data)))]
  unwornMean[c(a)]=tempX
  unwornMean[c(b)]=tempY
  unwornMean=unwornMean+refShape #Mean shape at step 1.
  wearShape[1,]=unwornMean

for (q in 1:(nrow(wearShape)-1)){
  stepWear=mean(c(sample(popWear[1:max(c(which(popWear<=( minWear+((z-
1)*wearIncr)))]),20,replace=TRUE))) #Dental wear at step q.
  stepWear=(stepWear*(slopes+((q/wearSt)*wearChange)))+(intercepts+(minWear*-
1*((q/wearSt)*wearChange))+stasisShape[q,])
  stepWear=stepWear%>%t(Pmatrix)
  tempX=stepWear[c(1:(ncol(wearShape)/2))]
  tempY=stepWear[c(((ncol(wearShape)/2)+1):ncol(wearShape))]
  stepWear[c(a)]=tempX
  stepWear[c(b)]=tempY
  wearShape[q+1,]=stepWear+refShape #Mean shape at step q.
}
}

```

## Appendix 6

### R Code for Variance Test of Directional Selection Module

Note: Colored fonts correspond to modules in Appendix 2 code that need to be replaced in order to perform variance test on directional selection simulations.

```
data=data.matrix(read.table(file.choose())) #Data in x1,y1,x2,y2...xn,yn format. Specimens in rows. No CS.
refShape=data.matrix(read.table(file.choose())) #Reference shape input.
indepX=as.vector(t(read.table(file.choose()))) #Wear index in a single column.

minWear=min(indepX)
maxWear=max(indepX)
wearDivision=20 #Number of subdivisions of wear index values.
wearIncr=(maxWear-minWear)/wearDivision #Width of wear index subdivisions.
numRuns=500 #Number of simulated random walks.
stdev=0.00001 #Standard deviation of shape coordinates.
strength=0.6 #Scalar multiplier of vector of directional change (i.e. selection strength).
numSteps=21 #Number of time steps in simulated time series.
numSeries=20 #Number of directional time series to simulate.

stDevMatrix=matrix(0,20,ncol(residuals))
simResults=matrix(0,(numSteps*numSeries*(wearDivision+1)),7) #Definition of empty result matrix.
for (h in 1:numSeries){
  simResults[(((numSteps*(wearDivision+1))*(h-1))+1):(((numSteps*(wearDivision+1))*(h-1))+
  (numSteps*(wearDivision+1))),1]=h

  for (z in 1:(wearDivision+1)){
    simResults[(((h-1)*(numSteps*(wearDivision+1)))+(z-1)*numSteps)+1):(((h-1)*
    (numSteps*(wearDivision+1)))+(z-1)*numSteps+numSteps),2]=(minWear+((z-1)*wearIncr))
    wearShape=(array(0,dim=c(20,ncol(data),numSteps)))
    for (v in 1:numSteps){
      simResults[(((z-1)*numSteps)+(h-1)*(numSteps*(wearDivision+1)))+v),3]=v
      wearValues=c(sample(popWear[1:max(c(which(popWear<=( minWear+((z-1)*wearIncr)))]),20,replace=TRUE))
      #Sample 20 wear values.
      for (d in 1:20){
        stDevMatrix[d,]=c(rnorm(ncol(pwScores),0,stdev)) #Random deviations from mean shape.
      }
    }
  }
  for (q in 1:20){
    stepWear=wearValues[q]
    stepResid=(residuals[135,]*((strength*v)/numSteps))+(stDevMatrix[q,])
    stepWear=(stepWear*slopes)+intercepts+stepResid #See *note below
    stepWear=stepWear%*%t(Pmatrix)
```

```

tempX=stepWear[c(1:(ncol(data)/2))]
tempY=stepWear[c(((ncol(data)/2)+1):ncol(data))]
stepWear[c(a)]=tempX
stepWear[c(b)]=tempY
wearShape[q,,v]=stepWear+refShape #Shape of individual q at time step v.
}
simResults[(((z-1)*numSteps)+((h-1)*(numSteps*(wearDivision+1))+v),4]=sum(diag(var(wearShape[,v])))
} #Interval variance calculation.
test=matrix(0,20*numSteps,ncol(data))
for (R in 1:numSteps){
test[(((R-1)*20)+1):(((R-1)*20)+20),]=wearShape[,R]
}
simResults[(((z-1)*numSteps)+((h-1)*(numSteps*(wearDivision+1))+v),5]=sum(diag(var(test)))
} #Total variance calculation.

for (J in 1:numSteps){
bootStrap=matrix(0,numRuns,1)
for (i in 1:numRuns){
resampInt=matrix(0,20,ncol(data))
resampTot=matrix(0,20,ncol(data))
sampVector1=sample(c(1:20),20,replace=TRUE)
sampVector2=sample(c(1:20),20,replace=TRUE)
sampVector3=sample(c(1:numSteps),20,replace=TRUE)
for (S in 1:20){
resampInt[S,]=wearShape[sampVector1[S],,J]
resampTot[S,]=wearShape[sampVector2[S],,sampVector3[S]]
}
bootStrap[i,]=sum(diag(var(resampTot)))-sum(diag(var(resampInt)))
} #Difference between resampled total variance and resampled interval variance
sortedBoots=sort(bootStrap)
simResults[(((z-1)*numSteps)+((h-1)*(numSteps*(wearDivision+1))+J),6]=sortedBoots[round(((numRuns*.025)),digits=0)]
simResults[(((z-1)*numSteps)+((h-1)*(numSteps*(wearDivision+1))+J),7]=sortedBoots[round((numRuns-
(numRuns*.025)),digits=0)]
}
}
}
}

```

\*Note: Replace this line with the following to perform the variance test on directional #selection simulations with directional wear (without #):

```

#stepWear=(stepWear*(slopes+((q/wearSt)*wearChange)))+(intercepts+(minWear*-
#1*((q/wearSt)*wearChange))+stepResid

```

#Format of simResults by column:

- #1) Time series number
- #2) Maximum wear index value sampled
- #3) Time step number
- #4) Variance of time step
- #5) Variance of total observed time series
- #6) Lower CI bound of difference between total and interval variance
- #7) Upper CI bound of difference between total and interval variance

## Appendix 7

### R Code for Variance Test of Stasis Module

Note: Colored fonts correspond to modules in Appendix 2 code that need to be replaced in order to perform variance test on directional selection simulations.

```
data=data.matrix(read.table(file.choose())) #Data in x1,y1,x2,y2...xn,yn format. Specimens in rows. No CS.
refShape=data.matrix(read.table(file.choose())) #Reference shape input.
indepX=as.vector(t(read.table(file.choose()))) #Wear index in a single column.
stasisSample=as.vector(t(read.table(file.choose()))) #Vector of specimen indices corresponding to row
#in original data file.

minWear=min(indepX)
maxWear=max(indepX)
wearDivision=20 #Number of subdivisions of wear index values.
wearIncr=(maxWear-minWear)/wearDivision #Width of wear index subdivisions.
numRuns=500 #Number of simulated random walks.
stdev=0.00001 #Standard deviation of shape coordinates.
numSteps=21 #Number of time steps in simulated time series.
numSeries=20 #Number of directional time series to simulate.

seriesResidualIndex=matrix(0,numSteps,20)
stDevMatrix=matrix(0,20,ncol(residuals))
simResults=matrix(0,(numSteps*numSeries*(wearDivision+1)),7) #Definition of empty result matrix.

for (h in 1:numSeries){
  simResults[(((numSteps*(wearDivision+1))*(h-1))+1):(((numSteps*(wearDivision+1))*(h-1))+
  (numSteps*(wearDivision+1))),1]=h
  for (d in 1:numSteps){
    seriesResidualIndex[d,]=sample(stasisSample,20,replace=TRUE)
  }
  for (z in 1:(wearDivision+1)){
    simResults[(((h-1)*(numSteps*(wearDivision+1)))+(z-1)*numSteps)+1):(((h-1)*
    (numSteps*(wearDivision+1)))+(z-1)*numSteps+numSteps),2]=(minWear+((z-1)*wearIncr))
    wearShape=(array(0,dim=c(20,ncol(data),numSteps)))
  }
  for (v in 1:numSteps){
    simResults[(((z-1)*numSteps)+(h-1)*(numSteps*(wearDivision+1)))+v),3]=v
    wearValues=c(sample(popWear[1:max(c(which(popWear<=( minWear+(z-1)*wearIncr)))]),20,replace=TRUE)]) #Sample 20 wear values.
    for (d in 1:20){
      stDevMatrix[d,]=c(rnorm(ncol(residuals),0,stdev)) #Random deviations from mean shape.
```

```

}
for (q in 1:20){
  stepWear=wearValues[q]
  stepWear=(stepWear*slopes)+intercepts+(residuals[(seriesResidualIndex[v,q]),]+
  stDevMatrix[q,]) #See *note below
  stepWear=stepWear%*%t(Pmatrix)
  tempX=stepWear[c(1:(ncol(data)/2))]
  tempY=stepWear[c(((ncol(data)/2)+1):ncol(data))]
  stepWear[c(a)]=tempX
  stepWear[c(b)]=tempY
  wearShape[q,v]=stepWear+refShape #Shape of individual q at time step v.
}
simResults[(((z-1)*numSteps)+((h-
1)*(numSteps*(wearDivision+1))+v),4]=sum(diag(var(wearShape[,v])))
} #Interval variance calculation.
test=matrix(0,20*numSteps,ncol(data))
for (R in 1:numSteps){
  test[(((R-1)*20)+1):(((R-1)*20)+20),]=wearShape[,R]
}
simResults[(((z-1)*numSteps)+((h-1)*(numSteps*(wearDivision+1))+v),5)=sum(diag(var(test)))
} #Total variance calculation.

for (J in 1:numSteps){
bootStrap=matrix(0,numRuns,1)
for (i in 1:numRuns){
  resampInt=matrix(0,20,ncol(data))
  resampTot=matrix(0,20,ncol(data))
  sampVector1=sample(c(1:20),20,replace=TRUE)
  sampVector2=sample(c(1:20),20,replace=TRUE)
  sampVector3=sample(c(1:numSteps),20,replace=TRUE)
  for (S in 1:20){
    resampInt[S,]=wearShape[sampVector1[S],,J]
    resampTot[S,]=wearShape[sampVector2[S],,sampVector3[S]]
  }
  bootStrap[i,]=sum(diag(var(resampTot)))-sum(diag(var(resampInt)))
} #Difference between resampled total variance and resampled interval variance.
sortedBoots=sort(bootStrap)
simResults[(((z-1)*numSteps)+((h-
1)*(numSteps*(wearDivision+1))+J),6]=sortedBoots[round(((numRuns*.025)),digits=0)]
simResults[(((z-1)*numSteps)+((h-
1)*(numSteps*(wearDivision+1))+J),7]=sortedBoots[round((numRuns-
(numRuns*.025)),digits=0)]
}
}
}

```

#\*Note: Replace this line and line above with the following to perform the variance test  
 #on stasis simulations with directional wear:

```

#stepWear=(stepWear*(slopes+((q/wearSt)*wearChange)))+(intercepts+(minWear*-
#1*((q/wearSt)*wearChange)))+(residuals[(seriesResidualIndex[v,q]),]+stDevMatrix[q,])

```

## Appendix 8

### R Code for Monte Carlo LRI Test for Directional Selection Simulation Module

Note: Colored fonts correspond to modules in Appendix 2 code that need to be replaced in order to perform Monte Carlo LRI on directional selection simulations.

```
wearShape=matrix(0,numSteps,ncol(data))
simResults=matrix(0,(numSeries*(wearDivision+1)),5) #Definition of empty result matrix.

for (h in 1:numSeries){ #Generation of simulated directional time series.
  dirShape=matrix(0,(numSteps-1),ncol(residuals))
  for (d in 1:(numSteps-1)){
    dirShape[d,]=residuals[135,]*(strength/(numSteps-1))*d+c(rnorm(ncol(residuals),0,stdev))
  }
  for (z in 1:(wearDivision+1)){
    simResults[((z-1)*numSeries)+h,1]=(minWear+((z-1)*wearIncr))
    simResults[((z-1)*numSeries)+h,2]=h
    stepWear0=mean(c(sample(popWear[1:max(c(which(popWear<=( minWear+((z-1)*wearIncr)))]),20,replace=TRUE)))]
    unwornMean=(stepWear0*slopes)+intercepts
    unwornMean=unwornMean%>%t(Pmatrix)
    tempX=unwornMean[c(1:(ncol(data)/2))]
    tempY=unwornMean[c(((ncol(data)/2)+1):(ncol(data)))]
    unwornMean[c(a)]=tempX
    unwornMean[c(b)]=tempY
    unwornMean=unwornMean+refShape

    for (q in 1:(nrow(wearShape)-1)){
      wearShape[1,]=unwornMean
      stepWear=mean(c(sample(popWear[1:max(c(which(popWear<=( minWear+((z-1)*wearIncr)))]),20,replace=TRUE)))]
      stepWear=(stepWear*slopes)+intercepts+dirShape[q,]
      stepWear=stepWear%>%t(Pmatrix)
      tempX=stepWear[c(1:(ncol(wearShape)/2))]
      tempY=stepWear[c(((ncol(wearShape)/2)+1):ncol(wearShape))]
      stepWear[c(a)]=tempX
      stepWear[c(b)]=tempY
      wearShape[q+1,]=stepWear+refShape
    }

    ProDistMatrix=matrix(0,nrow(wearShape),nrow(wearShape))
    change=matrix(0,numSteps-1,ncol(wearShape))
    changeDist=c(rep(0,numSteps-1))
  }
}
```

```

angleChange=c(rep(0,numSteps-2))

for (i in 1:(numSteps-1)) {
  change[i,]=as.matrix(wearShape[i+1,]-wearShape[i,])
  changeDist[i]=(sum(change[i,]^2))^0.5
}
for (t in 1:(numSteps-2)){
  unitVect1=change[t,]/(sum(change[t,]^2)^0.5)
  unitVect2=change[t+1,]/(sum(change[t+1,]^2)^0.5)
  angleChange[t]=(180/3.14159)*(acos(round((sum(unitVect1*unitVect2))/((sum(unitVect1^2)^0.5)
)*(sum(unitVect2^2)^0.5))),digits=10))
}
avgAngle=mean(angleChange)

scaleChange=max(changeDist)/changeDist

Procrustes=function(x){
  a=seq(1,ncol(x)-1,by=2)
  b=seq(2,ncol(x),by=2)
  for (i in 1:(nrow(x))){
    x[i,c(a)]=x[i,c(a)]-mean((x[i,c(a)]))
    x[i,c(b)]=x[i,c(b)]-mean((x[i,c(b)]))
    x[i,]=x[i,]/(sum(x[i,]^2)^0.5)
  }
  meanShape=x[1,]
  xd=1

  while(xd>1e-12){
    for (i in 1:nrow(x)){
      theta=-(atan(-1*(x[i,c(a)]/meanShape[c(b)]-
meanShape[c(a)]/x[i,c(b)])/(meanShape[c(a)]/x[i,c(a)]+meanShape[c(b)]/x[i,c(a)])))
      b1=cos(theta)
      b2=sin(theta)
      temp=(x[i,c(a)]*b1)-(b2*x[i,c(b)])
      x[i,c(b)]=(x[i,c(b)]*b1)+(b2*x[i,c(a)])
      x[i,c(a)]=temp
      x[i,]=x[i,]/(sum(x[i,]^2)^0.5)
    }
    xrefold=meanShape
    for (m in 1:ncol(x)){
      meanShape[m]=mean(x[,m])
    }
    meanShape=meanShape/(sum(meanShape^2)^0.5)
    xd=sum((meanShape-xrefold)^2)^0.5
    xd
  }

  theta=0.5*abs(atan((-2*(meanShape[c(a)]/meanShape[c(b)])/(sum(meanShape[c(a)]^2)-
sum(meanShape[c(b)]^2))))
  ct=cos(theta)
  st=sin(theta)
  temp=meanShape[c(a)]*ct-meanShape[c(b)]*st
  meanShape[c(b)]=meanShape[c(a)]*st+meanShape[c(b)]*ct
  meanShape[c(a)]=temp

  for (i in 1:(nrow(x))){

```



```

temp=x[i,c(a)]*ct-x[i,c(b)]*st
x[i,c(b)]=x[i,c(a)]*st+x[i,c(b)]*ct
x[i,c(a)]=temp
}
}

Procrustes(wearShape)
stepMatrix=matrix(0,nrow(ProDistMatrix),ncol(ProDistMatrix))
rateMatrix=matrix(0,nrow(ProDistMatrix),ncol(ProDistMatrix))
for (i in 1:nrow(wearShape)){
for (j in 1:nrow(wearShape)){
ProDistMatrix[i,j]=((sum((wearShape[i,]-wearShape[j,])^2))^0.5)
stepMatrix[i,j]=(abs(j-i))
rateMatrix[i,j]=log(ProDistMatrix[i,j]/stepMatrix[i,j])
stepMatrix[i,j]=log(stepMatrix[i,j])
}
}
diag(rateMatrix)=NA
diag(stepMatrix)=NA
sampleRate=c(rateMatrix[1,2: numSteps],rateMatrix[2,3: numSteps])
sampleInt=c(stepMatrix[1,2: numSteps],stepMatrix[2,3: numSteps])

for (g in 1:(numSteps-2)){
sampleRate=c(sampleRate,rateMatrix[g+2,(g+2): numSteps])
sampleInt=c(sampleInt,stepMatrix[g+2,(g+2): numSteps])
}
model=lm(sampleRate~sampleInt)
observedSlope=as.numeric(model$coefficients[2]) #Observed LRI slope.
simResults[((z-1)*numSeries)+h,3]=observedSlope

randWalk=wearShape
RandDistMatrix=matrix(0,nrow(wearShape),nrow(wearShape))
slopeVect=c(rep(0,numRuns))

for (l in 1:numRuns){ #Generation of random time series.
for (k in 1:(numSteps-1)){
s=(sample(c(1:(nrow(wearShape)-1))),1,replace=TRUE))
randWalk[k+1,]=as.matrix(randWalk[k,]+(sample(c(-1,1),1)*change[s,]*runif(1,min=0,max=scaleChange[s])))
}
}

Procrustes(randWalk)
stepMatrix=matrix(0,nrow(RandDistMatrix),ncol(RandDistMatrix))
rateMatrix=matrix(0,nrow(RandDistMatrix),ncol(RandDistMatrix))
for (i in 1:nrow(wearShape)){
for (j in 1:nrow(wearShape)){
RandDistMatrix[i,j]=((sum((randWalk[i,]-randWalk[j,])^2))^0.5)
stepMatrix[i,j]=(abs(j-i))
rateMatrix[i,j]=log(RandDistMatrix[i,j]/stepMatrix[i,j])
stepMatrix[i,j]=log(stepMatrix[i,j])
}
}
diag(rateMatrix)=NA
diag(stepMatrix)=NA
sampleRate=c(rateMatrix[1,2:numSteps],rateMatrix[2,3:numSteps])
sampleInt=c(stepMatrix[1,2: numSteps],stepMatrix[2,3: numSteps])

```

```

for (g in 1: (numSteps-2)){
sampleRate=c(sampleRate,rateMatrix[g+2,(g+2): numSteps])
sampleInt=c(sampleInt,stepMatrix[g+2,(g+2): numSteps])
}
model=lm(sampleRate~sampleInt)
slopeVect[1]=as.numeric(model$coefficients[2])
}

slopeVect=sort(slopeVect)

numGreater=length(c(which(slopeVect > observedSlope)))
numLess=length(c(which(slopeVect < observedSlope)))

simResults[((z-1)*numSeries)+h,4]=numGreater
simResults[((z-1)*numSeries)+h,5]=numLess
}
}

#Format of simResults by column:
#1) Maximum wear index value sampled
#2) Time series number
#3) Observed LRI slope
#4) Number of random walks with greater LRI slope
#5) Number of random walks with smaller LRI slope

```

#LRI slope of random time series.

## Appendix 9

### R Code for Monte Carlo LRI Test for Stasis Simulation Module

Note: Colored fonts correspond to modules in Appendix 2 code that need to be replaced in order to perform Monte Carlo LRI on stasis simulations.

```
data=data.matrix(read.table(file.choose())) #Data in x1,y1,x2,y2...xn,yn format. Specimens in rows. No CS.
refShape=data.matrix(read.table(file.choose())) #Reference shape input.
indepX=as.vector(t(read.table(file.choose()))) #Wear index in a single column.
stasisSample=as.vector(t(read.table(file.choose())))

minWear=min(indepX)
maxWear=max(indepX)
wearDivision=20 #Number of subdivisions of wear index values.
wearIncr=(maxWear-minWear)/wearDivision #Width of wear index subdivisions.
numRuns=500 #Number of simulated random walks.
stdev=0.00001 #Standard deviation of shape coordinates.
numSteps=21 #Number of time steps in simulated time series.
numSeries=20 #Number of directional time series to simulate.

wearShape=matrix(0,numSteps,ncol(data))
stDevMatrix=matrix(0,numSteps,ncol(residuals))
simResults=matrix(0,(numSeries*(wearDivision+1)),5) #Definition of empty result matrix.

for (h in 1:numSeries){ #Generation of simulated stasis time series.
  stasisShape=matrix(0,numSteps,ncol(residuals))
  for (T in 1:numSteps){
    stDevMatrix[T,]=c(rnorm(ncol(residuals),0,stdev))
  }
  for (d in 1:numSteps){
    stasisShape[d,]=residuals[(sample(stasisSample,1),)+stDevMatrix[d,]]
  }
  for (z in 1:(wearDivision+1)){
    simResults[((z-1)*numSeries)+h,1]=(minWear+((z-1)*wearIncr))
    simResults[((z-1)*numSeries)+h,2]=h
    stepWear0=mean(c(sample(popWear[1:max(c(which(popWear<=(minWear+((z-1)*wearIncr))))],20,replace=TRUE)])) #Amount of dental wear sampled at step 1.
    unwornMean=(stepWear0*slopes)+intercepts
    unwornMean=unwornMean%*%t(Pmatrix)
    tempX=unwornMean[c(1:(ncol(data)/2))]
    tempY=unwornMean[c(((ncol(data)/2)+1):(ncol(data)))]
    unwornMean[c(a)]=tempX
  }
}
```

```

unwornMean[c(b)]=tempY
unwornMean=unwornMean+refShape
wearShape[1,]=unwornMean #Mean shape at step 1.

for (q in 1:(nrow(wearShape)-1)){
  stepWear=mean(c(sample(popWear[1:max(c(which(popWear<=( minWear+((z-
1)*wearIncr)))]),20,replace=TRUE))) #Dental wear sampled at step q.
  stepWear=(stepWear*slopes)+intercepts+stasisShape[q,]
  stepWear=stepWear%%%(Pmatrix)
  tempX=stepWear[c(1:(ncol(wearShape)/2))]
  tempY=stepWear[c(((ncol(wearShape)/2)+1):ncol(wearShape))]
  stepWear[c(a)]=tempX
  stepWear[c(b)]=tempY
  wearShape[q+1,]=stepWear+refShape #Mean shape at step q.
}

ProDistMatrix=matrix(0,nrow(wearShape),nrow(wearShape))
change=matrix(0,numSteps-1,ncol(wearShape))
changeDist=c(rep(0,numSteps-1))
angleChange=c(rep(0,numSteps-2))

for (i in 1:(numSteps-1)) { #Procrustes distance between adjacent time steps.
  change[i,]=as.matrix(wearShape[i+1,]-wearShape[i,])
  changeDist[i]=(sum(change[i,]^2))^0.5
}
for (t in 1:(numSteps-2)){ #Angle between vectors of shape change between consecutive steps.
  unitVect1=change[t,]/(sum(change[t,]^2)^0.5)
  unitVect2=change[t+1,]/(sum(change[t+1,]^2)^0.5)
  angleChange[t]=(180/3.14159)*(acos(round((sum(unitVect1*unitVect2))/((sum(unitVect1^2)^0.5)
)*(sum(unitVect2^2)^0.5))),digits=10))
}
avgAngle=mean(angleChange) #Observed average angle of shape change.

scaleChange=max(changeDist)/changeDist

Procrustes=function(x) { #Function performs Procrustes superimposition.
  a=seq(1,ncol(x)-1,by=2)
  b=seq(2,ncol(x),by=2)
  for (i in 1:(nrow(x))){
    x[i,c(a)]=x[i,c(a)]-mean((x[i,c(a)]))
    x[i,c(b)]=x[i,c(b)]-mean((x[i,c(b)]))
    x[i,]=x[i,]/(sum(x[i,]^2)^0.5)
  }
  meanShape=x[1,]
  xd=1

  while(xd>1e-12){
    for (i in 1:nrow(x)){
      theta=-(atan(-1*(x[i,c(a)]%%meanShape[c(b)]-meanShape[c(a)]%%x[i,c(b)]/
(meanShape[c(a)]%%x[i,c(a)]+meanShape[c(b)]%%x[i,c(a)])))
      b1=cos(theta)
      b2=sin(theta)
      temp=(x[i,c(a)]*b1)-(b2*x[i,c(b)])
      x[i,c(b)]=(x[i,c(b)]*b1)+(b2*x[i,c(a)])
      x[i,c(a)]=temp
      x[i,]=x[i,]/(sum(x[i,]^2)^0.5)
    }
  }
}

```

```

    }
    xrefold=meanShape
    for (m in 1:ncol(x)){
      meanShape[m]=mean(x[,m])
    }
    meanShape=meanShape/(sum(meanShape^2)^0.5)
    xd=sum((meanShape-xrefold)^2)^0.5
    xd
  }

  theta=0.5*abs(atan((-2*(meanShape[c(a)]%*%meanShape[c(b)]))/(sum(meanShape[c(a)]^2)-
sum(meanShape[c(b)]^2))))
  ct=cos(theta)
  st=sin(theta)
  temp=meanShape[c(a)]*ct-meanShape[c(b)]*st
  meanShape[c(b)]=meanShape[c(a)]*st+meanShape[c(b)]*ct
  meanShape[c(a)]=temp

  for (i in 1:(nrow(x))){
    temp=x[i,c(a)]*ct-x[i,c(b)]*st
    x[i,c(b)]=x[i,c(a)]*st+x[i,c(b)]*ct
    x[i,c(a)]=temp
  }
}

Procrustes(wearShape)
stepMatrix=matrix(0,nrow(ProDistMatrix),ncol(ProDistMatrix))
rateMatrix=matrix(0,nrow(ProDistMatrix),ncol(ProDistMatrix))
for (i in 1:nrow(wearShape)){
  for (j in 1:nrow(wearShape)){
    ProDistMatrix[i,j]=((sum((wearShape[i,]-wearShape[j,])^2))^0.5)
    stepMatrix[i,j]=(abs(j-i))
    rateMatrix[i,j]=log(ProDistMatrix[i,j]/stepMatrix[i,j])
    stepMatrix[i,j]=log(stepMatrix[i,j])
  }
}
diag(rateMatrix)=NA
diag(stepMatrix)=NA
sampleRate=c(rateMatrix[1,2:numSteps],rateMatrix[2,3:numSteps])
sampleInt=c(stepMatrix[1,2:numSteps],stepMatrix[2,3:numSteps])

for (g in 1:(numSteps-2)){
  sampleRate=c(sampleRate,rateMatrix[g+2,(g+2):numSteps])
  sampleInt=c(sampleInt,stepMatrix[g+2,(g+2):numSteps])
}
model=lm(sampleRate~sampleInt)
observedSlope=as.numeric(model$coefficients[2]) #Observed LRI slope.
simResults[((z-1)*numSeries)+h,3]=observedSlope

randWalk=wearShape
RandDistMatrix=matrix(0,nrow(wearShape),nrow(wearShape))
slopeVect=c(rep(0,numRuns))

for (l in 1:numRuns){ #Generation of random time series.
  for (k in 1:(numSteps-1)){
    s=(sample((c(1:(nrow(wearShape)-1))),1,replace=TRUE))

```

```

        randWalk[k+1,]=as.matrix(randWalk[k,]+(sample(c(-
        1,1),1)*change[s,]*runif(1,min=0,max=scaleChange[s])))
    }
Procrustes(randWalk)
stepMatrix=matrix(0,nrow(RandDistMatrix),ncol(RandDistMatrix))
rateMatrix=matrix(0,nrow(RandDistMatrix),ncol(RandDistMatrix))
for (i in 1:nrow(wearShape)){
for (j in 1:nrow(wearShape)){
    RandDistMatrix[i,j]=((sum((randWalk[i,]-randWalk[j,])^2))^0.5)
    stepMatrix[i,j]=(abs(j-i))
    rateMatrix[i,j]=log(RandDistMatrix[i,j]/stepMatrix[i,j])
    stepMatrix[i,j]=log(stepMatrix[i,j])
}
}
diag(rateMatrix)=NA
diag(stepMatrix)=NA
sampleRate=c(rateMatrix[1,2:numSteps],rateMatrix[2,3:numSteps])
sampleInt=c(stepMatrix[1,2:numSteps],stepMatrix[2,3:numSteps])

for (g in 1:(numSteps-2)){
sampleRate=c(sampleRate,rateMatrix[g+2,(g+2):numSteps])
sampleInt=c(sampleInt,stepMatrix[g+2,(g+2):numSteps])
}
model=lm(sampleRate~sampleInt)
slopeVect[1]=as.numeric(model$coefficients[2])
}

slopeVect=sort(slopeVect)

numGreater=length(c(which(slopeVect > observedSlope)))
numLess=length(c(which(slopeVect < observedSlope)))

simResults[((z-1)*numSeries)+h,4]=numGreater
simResults[((z-1)*numSeries)+h,5]=numLess
}
}

```

#LRI slope of random time series.

## Appendix 10

### R Code for “Moving Window” LRI Test Module

```
data=read.table(file.choose())      #Input data with 2 columns: 1) Time or strat level and 2) Morphology.
library(MASS)
x=1
numRuns=500                          #Number of simulated random walks.
sumRow=0
for (t in 5:nrow(data)){              #Calculation of number of time series subsets to be analyzed.
  sumRow=sumRow+(nrow(data)-(t-1))
}
Results=matrix(0,sumRow,5)
seqMorph=matrix(0,(nrow(data)-1),1)
for (i in 1:(nrow(data)-1)){         #Morphological difference between all consecutive time steps.
  seqMorph[i,1]=abs(data[i+1,2]-data[i,2])
}
for (q in 1:(nrow(data)-4)){
  window=4+q
tempResults=matrix(0,(nrow(data)-(window-1)),5)
winData=matrix(0,window,2)

for (p in 1:((nrow(data)-(window-1)))){
  winData=data[p:(p+(window-1)),]    #Definition of subset p to be tested.
  pairMat=matrix(0,(sum(seq(1,window,by=1))-window),2)
  pairInt=matrix(0,window,window)
  pairMorph=matrix(0,window,window)

for (i in 1:window){
for (j in 1:window){
  pairInt[i,j]=abs(winData[j,1]-winData[i,1])      #Pairwise interval length in time series subset.
  pairMorph[i,j]=abs(winData[j,2]-winData[i,2])
}
}
}
a=c(pairInt[1,2:window])
b=c(pairMorph[1,2:window])
for (l in 2:(window-1)){
  a=c(a,pairInt[1,(l+1):window])
```

```

        b=c(b,pairMorph[1,(l+1):window])
    }
    pairMat[,1]=log(a)
    temp=b/a
    pairMat[,2]=log(temp)
    model=rlm(pairMat[,2]~pairMat[,1]) #Robust linear regression model.
    obsSlope=model$coefficients[2] #Observed LRI slope.
    randSlope=matrix(0,numRuns,1)
    for (h in 1:numRuns){
        randWalk=matrix(0>window,2)
        randWalk[,1]=winData[,1]
        randWalk[,2]=winData[,2]
        for (g in 2>window){ #Generation of random time series.
            randWalk[g,2]=randWalk[g-1,2]+sample(c(-1,1),1)*runif(1,0,max(seqMorph))
        }
        randMat=matrix(0,(sum(seq(1>window,by=1))-window),2)
        randInt=matrix(0>window>window)
        randMorph=matrix(0>window>window)
        for (i in 1>window){
            for (j in 1>window){
                randInt[i,j]=abs(randWalk[j,1]-randWalk[i,1])
                randMorph[i,j]=(abs(randWalk[j,2]-randWalk[i,2]))
            }
        }
        a=c(randInt[1,2:(nrow(randWalk))])
        b=c(randMorph[1,2:(nrow(randWalk))])
        for (l in 2:(nrow(randWalk)-1)){
            a=c(a,randInt[l,(l+1):(nrow(randWalk))])
            b=c(b,randMorph[l,(l+1):(nrow(randWalk))])
        }
        randMat[,1]=log(a)
        temp=b/a
        randMat[,2]=log(temp)
    model=rlm(randMat[,2]~randMat[,1]) #LRI slope for random walk.
    randSlope[h,1]=model$coefficients[2]
    }
    sortRand=sort(randSlope)
    numGreater=length(c(which(sortRand>obsSlope)))
    numLess=length(c(which(sortRand<obsSlope)))
    tempResults[p,1]=p
    tempResults[p,2]=(p+(window-1))
    tempResults[p,3]=obsSlope
    tempResults[p,4]=numGreater
    tempResults[p,5]=numLess
    }
    Results[x:(x+(nrow(tempResults)-1))]=tempResults
    x=x+nrow(tempResults)
    }
    Results

#Results format by column:
#1) Initial time step in window
#2) Final time step in window
#3) Observed LRI slope
#4) Number of random walks with greater LRI slope
#5) Number of random walks with smaller LRI slope

```